CORTICO-CORTICAL AND HIPPOCAMPAL-CORTICAL INTERACTIONS IN MOUSE MODELS OF ALZHEIMER'S DISEASE

SURJEET SINGH
Master of Engineering, **Thapar University, 2010**

A thesis submitted
in partial fulfilment of the requirements for the degree of

DOCTOR OF PHILOSOPHY

in

NEUROSCIENCE

Department of Neuroscience
University of Lethbridge
LETHBRIDGE, ALBERTA, CANADA

CORTICO-CORTICAL AND HIPPOCAMPAL-CORTICAL INTERACTIONS IN MOUSE MODELS OF ALZHEIMER'S DISEASE

SURJEET SINGH

Date of Defence: July 21, 2021

Dr. R. Sutherland	Professor	Ph.D.
Dr. M. Mohajerani	Associate Professor	Ph.D.
Thesis Co-Supervisors		
Dr. A. Gruber	Associate Professor	Ph.D.
Thesis Examination Committee Member		
Dr. M. Tatsuno	Associate Professor	Ph.D.
Internal External Examiner		
Department of Neuroscience,		
Faculty of Arts and Science.		
Dr. A. Chan	Assistant Professor	Ph.D.
External Examiner		
Department of Psychiatry,		
University of Alberta.		
Dr. I. Whishaw	Professor	Ph.D.
Chair, Thesis Examination Committee		

DEDICATION

To my wife Dr. Harpreet Kaur and my parents.

ABSTRACT

Alzheimer's disease (AD) is a neurodegenerative disease which is pathologically characterized by extracellular deposition of amyloid beta (Aβ) plaques, intracellular deposition of neurofibrillary tangles (NFT) caused by hyperphosphorylated tau protein, neuroinflammation, and progressive neuron loss. Brain regions involved in memory processing, such as hippocampus and the neocortex, are affected in the early stages of disease pathology. Using in vivo mesoscale wide-field voltage imaging and local field potential (LFP) recording from CA1 region of the hippocampus in 6- and 12-month-old (1) knock-in ($App^{NL\text{-}G\text{-}F}$) and (2) transgenic (5xFAD) mouse model of AD, this study is aimed at understanding how cortico-cortical and hippocampal-cortical interactions are affected by AD. Aberrant sensory evoked cortical activity and resting state cortical functional connectivity were observed in AD and sharp wave ripples (SWRs), which subserve important aspects of hippocampal-cortical interactions are disrupted in AD. Further, gradual cerebral hypoperfusion exacerbate AD pathology and network dysfunctions.

ACKNOWLEDGEMENTS

First and above all, I want to thank the divine spirit that is pervading everywhere for keeping me on the path of righteousness, keeping me sane, providing protection, patience, and courage to navigate through good and bad times in this journey called PhD.

My utmost gratitude to my PhD supervisors Drs. Robert J. Sutherland and Majid H. Mohajerani, who believed in me and provided me this opportunity to quench my thirst for scientific exploration. I want to thank you for giving me freedom to pursue multiple projects, this helped me grow as a young scientist and decide my future direction. I know it has not been an easy journey with unique scientific and personal challenges, I appreciate your patience and support.

I want to thank my supervisory committee members Drs. Aaron J. Gruber and Artur Luczak for their suggestions which significantly improved this work. My sincere thanks to Dr. Ian Q. Whishaw who has been a fatherly figure, a mentor, and a friend. Your deep scientific reasoning and experience helped in shaping my line of thought and sharpening many of my insights. You are a person who I look up to, you inspire me to be a good scientist and a good human being. I have really enjoyed working with you and I hope to continue this collaboration in future.

One thing I liked at CCBN was the opportunity to interact with amazing faculty members who not only shared their scientific wisdom but also were a source of inspiration. I want to thank Drs. Robert McDonald, Bryan Kolb, Masami Tatsuno, Sergio Pellis, Robbin Gibb, Matthew Tata, and David Euston

I had the privilege of working with some amazing peers who were great mentors, friends and some were like family. It's a long list of people I want to thank so I begin with people with academic seniority first: Drs. Dun Mao, Hardeep Ryait, Edgar

Bermudez Contreras, Jogender Mehla, Samsoon Inayat, Zahra Jafari, Jamshid Faraji, Michael Kyweriga, Ingrid De Miranda Esteves, Sergey Chekhov, Jianjun Sun, Maurice Needham, Volodymyr Turchenko, Sorina Truica, Keiko McCreary, Brendan McAllister, Justin Q. Lee, Mirela Ambeskovic, Reza Torabi.

I want to thank my fellow graduate students and undergrads with whom I have shared moments of deep anxiety and excitement: Haoran Chang, Ritwik Das, Zahra Rezaei, Qandeel, Rachel Stark, Jackson Ham, Tanzi Hover, Shweta Soni, Aubrey Demchuk, John Walkey, Zak Stinson, Hadil Karem, Sienna Randolph, Kathleen Ward, Clifford Donovan, Behroo Mirza Agha, Candace Burke, Jarret McKinnon, Mojtaba Nazari, Victorita Ivan, Megan Torry, Catherine Laskowski, Rui Pais, Kartik Iyer, Saeedeh Hashemnia, Navvab Afrashteh, Javad Karimi, Abigail Nixon, Valerié Lapointe, Scott Deibel, Darryl Gidyk, Ellie Fraser, Deryn LeDuke, Rebecca McHugh, Kate Chua, Bryant Young, Sam Drescher, Sean Lacoursiere.

Five years ago, when I left my career as a public servant and embarked upon the journey of graduate school. With no background in neuroscience, I was moving into an uncharted territory. One person who made it all seem easy was my wife Dr. Harpreet Kaur, without her support I had no chance to thrive in my doctoral program. In fact, she is the reason why I decided to pursue a career in neuroscience, believe me her enthusiasm and love for research is contagious. These past five years have not been an easy ride, both academically and personally. But you have always been a true and great supporter. Thanks again for sticking by my side, even when I was irritable and depressed due to workload. I feel that what we both learned a lot about life and strengthened our commitment and determination to each other.

I want to extend my regards to my mom, dad, and my brother Amarjit Singh. You were the first community that encouraged me for pursuing my passion for research,

without your support, patience and compromises it would not have been easy to reach this milestone. I would like to acknowledge the support and encouragement I received from my parents-in-law, sister-in-law Navdeep and brother-in-law Lovepreet.

I also want to thank some of my friends who are like family to me and made my stay in Lethbridge enjoyable. I want to thank Sam, Qandeel and Noah for their love and care. Sam, I will miss our regular walk in the park and intellectual discussions, thank you for the motivation and your guidance. I want to thank Jyote, Bal uncle and Jass aunty for considering me as part of their family. I want to thank Leo, Layla, Erika, Matt, Rebecca, Sandra, Edgar, Jenna, Rafi, Diego, Sergey, Aubrey, Megan, Michael, Mimoza and her Kosovo group, Patricio (aka D.J. Tizio), Andres, Ammy, Clémence, Rachana, Pooja, Jocelyn, Sorina, Vicky, Jenn, and many more with whom I spent fun time travelling, camping, sala-dancing, potluck, drinks etc. I want to thank Haoran, Ritwik and Vicky for the late night and early morning company to Tim Hortons.

I deeply appreciate the help of non-teaching staff members, for their cooperation throughout the period. Special thanks to Naomi Cramer and Amanda Mauthe-Kaddoura for administrative support. I want to thank Janelle Fyfe from school of graduate studies for her help during my thesis submission. I am also thankful to the animal care staff members Karen, Moira, James, and Isabella for their help. I want to thank Di Shao for his help with animal breading and making sure I have the right animals at right time.

No words would suffice to express my sincere thanks to those innocent creatures who sacrificed their lives without which this study would not have been possible.

TABLE OF CONTENTS

LIST OF TABLES

LIST OF FIGURES

LIST OF ABBREVIATIONS

AD	Alzheimer’s disease	IADRP	International Alzheimer's and Related Dementias Research Portfolio
AC	Ameroid constrictor	Iba1	Ionized calcium binding adaptor molecule 1
Ach	Acetylcholine	IR	Investigation ratio
AChE	Acetylcholinesterase	LFP	Local field potential
AFM	Atomic force microscopy	LOAD	Late onset Alzheimer’s disease
AI	Asymmetry Index	mAChRs	Acetylcholine muscarinic receptors
AMPA	Amino-3-hydroxy-5-methyl-4-isoxazolepropionic acid	MAPT	Microtubule Associated Protein Tau
ANCOVA	Analysis of covariance	MRI	Magnetic resonance imaging
ANOVA	Analysis of variance	MWT	Morris Water Task
APOE-ε4	Apolipoprotein E- ε4	nAChRs	Acetylcholine nicotinic receptors
APP	Amyloid precursor protein	NeuN	Neuronal nuclear protein
Aβ	Amyloid beta	NFT	Neurofibrillary tangles
BACE 1	β-site APP cleaving enzyme	NGS	Normal goat serum
BB	Balance Beam	NIA	National Institute on Aging
BOLD	Blood-oxygen-level-dependent	NMDA	N-methyl-D-aspartate receptor
CA1	Cornu Ammonis Area 1	NMR	Nuclear magnetic resonance
CADRO	Common Alzheimer's and Related Dementias Research Ontology	NoH	Non-occluded hemisphere
CBF	Cerebral blood flow	NOR	Novel Object Recognition
CCA	Common carotid artery	OH	occluded hemisphere
CCD	Charge-coupled device	PAS	Peripheral anionic site
CD	Circular Dichroism	PBS	Phosphate-buffered saline
ChAT	Choline acetyltransferase	PCC	Posterior cingulate cortex
CNS	Central nervous system	PET	Positron emission tomography
CPC	Clinicopathologic correlation	PFA	Paraformaldehyde
CSHA	Canadian Study of Health and Aging	PFC	Prefrontal cortex
CTFα	C-terminal fragment alpha	PHF	Paired helical filament
CTFβ	C-terminal fragment beta	PS1	Presenilin 1
DMN	Default mode network	PS2	Presenilin 2
EC	Entorhinal cortex	PV	Parvalbumin
EEG	Electroencephalography	ROI	Regions of interest

EM	Electron microscopy	RSC	Retrosplenial cortex
EOAD	Early onset Alzheimer’s disease	rs-fMRI	Resting state functional MRI
FAD	Familial Alzheimer's Disease	SAD	Sporadic Alzheimer’s disease
FC	Functional connectivity	sAPPα	Soluble ectodomain of Amyloid precursor protein
FcOIS	Functional connectivity optical intrinsic signal	sAPPβ	Soluble APPβ fragment
FDA	Food and Drug Administration	SWR/SWRs	Sharp wave ripple/s
FL	Forelimb	SWS	Slow-wave sleep
FTIR	Fourier Transform Infrared Spectroscopy	TBS	Tris-buffered saline
GABA	Gamma-aminobutyric acid	UCAgO	Unilateral common carotid artery gradual occlusion
GFAP	Glial fibrillary acidic protein	VCI	Vascular cognitive impairment
GLME	Generalized linear mixed-effects	VGluT	vesicular glutamate transporter
GluRs	Glutamate receptor	VSDI	Voltage sensitive dye imaging
GPCRs	G-protein coupled receptors	w.r.t.	With respect to
HL	Hindlimb		
HP	Hypoperfusion		
HPC	Hippocampus		

Chapter 1 : Introduction to Alzheimer's Disease Pathology and Oscillations in the Brain.

> *"All the world's a stage, And all the men and women merely players;*
> *They have their exits and their entrances, And one man in his time plays many parts,*
> *His acts being seven ages. ....*
> *.... Last scene of all, That ends this strange eventful history,*
> *Is second childishness and mere oblivion, Sans teeth, sans eyes, sans taste,* ***sans everything****."*
>
> — William Shakespeare
> As You Like It (1599)
> (Jaques, Act 2 Scene 7)

Introduction

Alzheimer's disease (AD) was described as "presenile dementia" in 1906 by a German psychiatrist Alois Alzheimer. He examined the post-mortem brain of his 55-year old female patient named Auguste Deter and found numerous small, miliary foci, which now are recognized as senile or neuritic plaques (Sery et al., 2013). Alzheimer noted the presence of two distinctive pathologies in his patient's brain: abnormal intracellular aggregates or neurofibrillary tangles, which were later shown to be composed of hyperphosphorylated and cleaved forms of the microtubule-associated protein tau, and neuritic plaques, which he called miliary foci were dystrophic neuronal processes surrounding a "special substance in the cortex" (Alzheimer et al., 1995; O'Brien and Wong, 2011). This abnormal accumulation of amyloid-β protein (Aβ) in senile plaques and hyperphosphorylated tau protein in neurofibrillary tangles are now considered as the hallmarks of AD pathology (Karantzoulis and Galvin, 2011).

There are many different forms of dementia. Typically, age-related dementias are irreversible conditions resulting in progressive cognitive decline and loss of neural tissue. Dementia refers to a set of difficulties with memory, language, problem-solving and other thinking skills (cognitive abilities) that progressively and adversely affect a

person's ability to perform everyday activities (Alzheimer's Association Report (2020)). AD is the most common form of dementia and accounts for total 60-80% of dementia cases. It usually begins in late life and results in a progressive loss of most abilities. Vascular dementia is the second most common cause of dementia and accounts for at least 20% of cases and occurs because of microscopic bleeding and blood vessel blockage in the brain (Iadecola, 2013). Other common forms of dementia include Lewy body dementia, Parkinson's disease with dementia, frontotemporal lobar degeneration and normal pressure hydrocephalus, with each of these accounting for between 5 and 10% of cases (Braak and Braak, 1998).

There are several forms of AD. The most common are sporadic AD (SAD) which typically occurs after the age of 60–65 years and familial AD (FAD) which appears at an early age (<60 years), FAD accounts for ~5% of total AD cases (Minati et al., 2009; Dorszewska et al., 2016). FAD is generally associated with a family history and mutation in one of three genes: (1) Amyloid precursor protein (APP) on chromosome 21, (2) presenilin 1 (PS1) on chromosome 14 and (3) presenilin 2 (PS2) on chromosome 1, resulting in abnormal processing of APP resulting in an early onset of disease. Apart from mutation in these genes, another genetic risk factor is apolipoprotein E gene (APOE 4ε allele), which is associated with increased risk for AD (Liu et al., 2013). AD is further divided into 2 subtypes based on the age of onset or time of appearance of first symptom of disease. Early onset AD (EOAD) accounts for approximately 1% to 6% of all cases and ranges roughly from 30 years to 60 or 65 years and late onset AD (LOAD) appears at later than 60 or 65 years of age (Bekris et al., 2010).

Epidemiology

Worldwide, nearly 50 million people are suffering from dementia, more than the total population of Canada, making the disease a global health crisis. More than half a million Canadians are living with dementia and one in five Canadian have cared for someone living with dementia (https://alzheimer.ca/). The estimated number of people with AD is projected to reach 82 million in 2020 and 152 million in year 2050 worldwide (Alzheimer's Association Report (2020)) . The Canadian Study of Health and Aging estimated that by 2021 there will be 592,000 individuals living with dementia in Canada, and about two-third of them will be women (Canadian Study of Health and Aging Working Group (1994)). It is estimated that the prevalence will increase significantly to 986,000 by 2033 (Adlimoghaddam et al., 2018). Despite ageing being the biggest risk factor for Alzheimer's disease, more than 70,000 of those living with dementia are under the age of 65 (Chang et al., 2015).

Table 1.1: Projection of dementia statistics in Canada.
(adapted from (Adlimoghaddam et al., 2018))

Year	60-74 years	75-84 years	85+ years	Total Cases
2014	74,428	189,126	220,39	483,953
2033	114,940	390,246	481,768	986,954

Hypothesis

The etiology of AD is highly complex and multifactorial, and several hypotheses have been proposed so far and several biochemical perturbations are suggested to play a role in AD. They include the cholinergic hypothesis, amyloid hypothesis, tau propagation hypothesis, mitochondrial cascade hypothesis, neurovascular hypothesis, calcium homeostasis hypothesis, inflammatory hypothesis, metal ion hypothesis, and lymphatic system hypothesis (Liu et al., 2019b). The causative hypotheses include oxidative stress and the involvement of peripheral systems in AD. National Institute on

Aging (NIA) in collaboration with Alzheimer's Association have developed an International Alzheimer's and Related Dementias Research Portfolio that utilizes Common Alzheimer's and Related Dementias Research Ontology. It is a three-tiered classification system that identifies the above-mentioned AD hypothesis as potential targets from early-stage to late-stage clinical drug development (Refolo et al., 2012; Cummings et al., 2020).

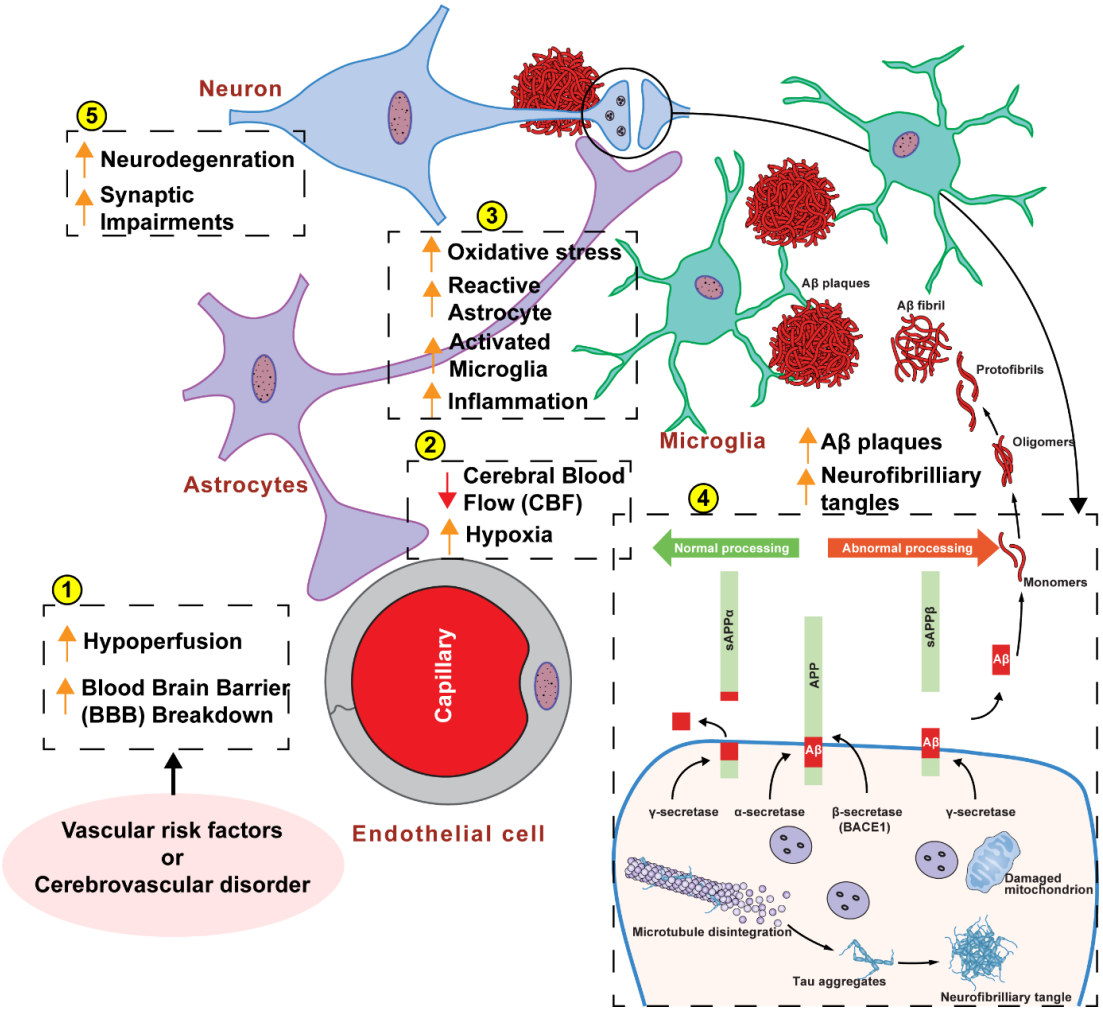

Figure 1.1: A unified hypothesis of Alzheimer's disease pathology.
Multiple underlying mechanism have been proposed and tested to study AD pathology in the past few decades. Here, we present possible some well explored domains of AD pathology, including amyloid plaques, neurofibrillary tangles, vascular abnormalities, and increased neuroinflammation. These hypotheses of AD are not mutually exclusive, in fact AD is now known to be a multifactorial disease encompassing factors shown in this figure. (1-2) explain vasculature risk factors in which reduction in blood flow may cause hypoxia leading to over production of Aβ and this leads to a vicious cycle causing neuro degeneration, inflammation, oxidative stress, and cognitive deficits. (3) low concentration of amyloid β may increase inflammatory markers which in turn will increase activated microglia and reactive astrocytes leading to increased calcium influx, synaptic loss, mitochondrial damage, reduced glutamate reuptake. (4) represents classical hallmarks of AD pathology: extracellular deposits of Aβ and

intracellular aggregation of tau protein. Again, this abnormal aggregation leads to synaptic dysfunction, inflammation, and, ultimately, cell death (5). (Singh et al. Unpublished)

Fig 1.1 presents the key aspects of AD pathology and how multiple factors my initiate or exacerbate AD pathology eventually leading to neuronal loss. Abnormal processing of amyloid precursor protein causes Aβ plaque formation which increases with age and leads to downstream effects such as increased inflammation, loss of synaptic functions, altered neuronal ionic homeostasis and oxidative injury, neurotransmitter deficits, hyper-phosphorylation of tau / neurofibrillary tangles and cell death. In addition, vasculature risk factors such as cerebral hypoperfusion may exacerbate the disease pathology.

Amyloid beta hypothesis

There are three pathological hallmarks of AD, deposition of amyloid fibrils composed of the amyloid-beta (Aβ) peptide, neurofibrillary tangles consisting of hyperphosphorylated tau protein, and neurodegeneration. Aβ is a 4.2-kDa peptide, primarily 40 or 42 amino acids in length that was first isolated and purified by Glenner & Wong in 1984 (Glenner and Wong, 1984). The relationship between the amount of neocortical Aβ plaques in the brains of elderly subjects and the risk of dementia was first demonstrated in seminal articles by Blessed et al. (Blessed et al., 1968). Clinicopathologic correlation (CPC) studies related to Alzheimer disease (AD) conducted in the past few decades have raised questions related to the hypothesis that AD neuropathologic changes (Aβ plaques and neurofibrillary tangles) correlate with clinical dementia (Nelson et al., 2012).

According to amyloid hypothesis, which was first proposed by John Hardy and David Allsop in year 1991, Aβ is the causative factor for AD and misfolded protein

accumulates or clumps to form deposits (senile plaques) in the brain. These trigger neurodegenerative processes that lead to the loss of memory and cognitive ability observed in Alzheimer's disease (Hardy and Allsop, 1991). They proposed that the pathological cascades in AD are Aβ deposition, tau phosphorylation, neurofibrillary tangles (NFT) formation, and neuronal death (Hardy and Higgins, 1992). The neuron specific APP isoform is cleaved by various secretases including α-, β-, and γ-secretases, cleavage by α-secretase releases the soluble ectodomain of APP, termed sAPPα, and a membrane-tethered intracellular C-terminal fragment, called CTFα or C83. Cleavage by β-secretase also known as BACE 1 (or β-site APP cleaving enzyme) yields a slightly shorter soluble APPβ fragment (sAPPβ) and a correspondingly longer CTFβ or C99 (Nhan et al., 2015). The APP-CTFs produced from α, β secretases are subsequently cleaved by γ-secretase to generate either a 3 kDa product (non-toxic p3, from APP-CTFα) or Aβ (Aβ1–40/42 from APP-CTFβ), and the APP intracellular domain (Zheng and Koo, 2011). Aβ peptides contain several alloforms with varying sequences of amino acids, based on the cleavage sites of γ−secretase with Aβ40 as the most abundant species and Aβ42 as the most amyloidogenic and toxic species. Numerous biophysical tools and techniques including nuclear magnetic resonance (NMR), Circular Dichroism, X-ray fiber diffraction, atomic force and electron microscopy, Fourier Transform Infrared Spectroscopy (FTIR) have contributed to a better understanding of structure of Aβ. The Aβ monomers formed can aggregate into different forms such as oligomers, protofibrils and amyloid fibrils, all having different solubility properties. Which form of the Aβ peptide is more toxic over the other is still controversial. There is evidence suggesting that APP undergo posttranslational modifications, including N-glycosylation, O-glycosylation, ubiquitination, and phosphorylation, which may play a pivotal role in

AD pathogenesis by dysregulating APP processing and promoting Aβ generation (Lee et al., 2003; Schedin-Weiss et al., 2014; Menon et al., 2019).

Tau hypothesis

Tau protein is normally a highly soluble microtubule-associated protein (MAP), however it forms insoluble filaments that accumulate as neurofibrillary tangles in AD. Hence, the tau hypothesis states that excessive or abnormal phosphorylation of tau results in the transformation of normal adult tau into PHF-tau (paired helical filament) and neurofibrillary tangles. The main difference in tau and Aβ pathology is accumulation of hyperphosphorylated tau fibrillates intracellularly in form of tangles that results in neuron degeneration while the aggregation and fibrillation of Aβ peptide occurs extracellularly. Evidence suggests that tau accumulation occurs independent of Aβ, and it appears before the formation of Aβ plaques. Aβ may be a key initiator of a complex pathogenic cascade and triggers an exacerbation of tauopathy, which may in turn cause neuronal dysfunction and death (Johnson and Johnson, 1975; Musiek and Holtzman, 2015; Rayaprolu et al., 2021). Hence, there are still controversies about the importance of tau and Aβ as a potential therapeutic target for drug development. Studies also show a correlation between the tau levels and cognitive symptoms over the amyloid burden, suggesting the direct link of tau to AD progression (Hanseeuw et al., 2019). Tau can be modified by phosphorylation, glycation, isomerization etc. The abnormal post-translational modifications, especially the abnormally hyperphosphorylation, of tau and its aggregation into bundles of filaments has been proposed to be the main cause for the clinical expression of AD and related symptoms (Alonso et al., 2008; Iqbal et al., 2010). Normal brain tau contains 2–3 moles of phosphate per mole of the protein, which is soluble in nature, and appears to be optimal for its interaction with tubulin in

the promotion or stabilization of microtubule assembly (Kopke et al., 1993; Iqbal et al., 2010).

Neurotransmitter hypothesis

Increased Aβ is known to be associated with a derangement of neuronal activity in AD (Palop and Mucke, 2010). Moreover, neuronal activity is found to regulate the secretion of Aβ from neuronal cells (Kamenetz et al., 2003). Neurotransmitters are endogenous chemicals that carry messages or signals between neurons and hence play a central role in brain functions and neuronal activity. Neurotransmitters transmit the signals across the synapse (between the neurons) and neuromuscular junctions. Some neurotransmitters are endogenously synthesized from amino acids usually stored in the synaptic vesicles, beneath the membrane in the axon terminal. They are released into the synapse with the appropriate signal. The mechanisms responsible for the cognitive decline underlying AD are not well understood, but it is believed that accumulation of Aβ, neuronal apoptosis, inflammatory responses produces alterations in several neurotransmitters and their receptors that may account for the progression of cognitive decline (Xiong et al., 2004; Xu et al., 2012; Kinney et al., 2018). Evidences show the involvement of both cholinergic and glutamatergic neurotransmitters in the etiology of Alzheimer's disease (Francis, 2005). For example, Aβ oligomers has been shown to reduce glutamatergic synaptic transmission strength and plasticity (Chapman et al., 1999; Walsh et al., 2002).

Cholinergic Hypothesis of Alzheimer's Disease

Acetylcholine (ACh) is the main neurotransmitter in cholinergic neurons and is for modulating brain activity in such functions as attentional processing. It is also suggested to have a role in learning, memory, and cognitive functions (Hasselmo, 2006;

Haam and Yakel, 2017). ACh is synthesized from choline and acetyl-coenzyme A (Acetyl-CoA) in a chemical reaction that is catalyzed by choline acetyltransferase (ChAT). The inadequate synthesis of the ACh is suggested to be responsible for AD. Numerous studies have reported an alteration in cholinergic system in AD patients (Grothe et al., 2010; Grothe et al., 2012; Grothe et al., 2014). Moreover, the levels of choline acetyltransferase (ChAT), the enzyme necessary for synthesizing Ach, has been shown to be altered in AD (Davies and Maloney, 1976; Bird et al., 1983; Fu et al., 2004). ChAT activity is regulated by neuronal depolarization, influx of Ca^{2+} and phosphorylation of the enzyme by a wide variety of protein kinases such as protein kinase C (PKC), protein kinase A (PKA), protein kinase G, casein kinase II (CK2) and α-calcium/calmodulin dependent protein kinase II (α-CaM kinase) (Ferreira-Vieira et al., 2016). When released, ACh binds to a postsynaptic receptor, either a acetylcholine muscarinic receptors (mAChRs) or a Acetylcholine nicotinic receptors (nAChRs). The receptors are named for their differential selectivity for the xenobiotic compounds muscarine and nicotine, respectively. Excess of Ach rapidly degraded into choline and acetate by acetylcholinesterase (AChE) enzymes.

The “Cholinergic Hypothesis of Alzheimer’s Disease” links the dysregulation of the basal forebrain cholinergic neurotransmission, alteration in the levels of cholinergic markers such as Ach, choline, and ChAT, to the age-related cognitive decline of AD (Bartus et al., 1982; Bekdash, 2021). Several approaches have been proposed and tested for the treatment of cholinergic deficits in AD. These focus on using cholinesterase inhibitors that can increase ACh levels in the synaptic cleft to ameliorate cognitive symptoms, however the improvement is found to be limited. Donepezil, galantamine, rivastigmine are some of the most common cholinesterase inhibitors that are Food and Drug Administration (FDA) approved and used as a first-

line drug treatment for mild-to-moderate AD (Grossberg, 2003; Haake et al., 2020; Amat-Ur-Rasool et al., 2021). Tacrine is one of the first drugs to be widely marketed for the loss of memory and intellectual decline in Alzheimer's disease, however it is no longer available in market for AD due to concerns over its link to liver toxicity (LiverTox (2012)). Anti-cholinergic drugs can inhibit AChE via direct binding to the catalytic site or via binding to a peripheral anionic site (PAS) primarily composed of aromatic amino acids (Silva et al., 2020). Anticholinergic drugs have undesired side effects, and ultimately, only provide symptomatic rather than curative benefits.

GABAergic hypothesis of AD pathogenesis

Involvement of GABA (gamma-aminobutyric acid) dysfunction in the pathogenesis in the AD brain is comparatively a new hypothesis. It states that GABAergic system is an important contributor in the excitatory/inhibitory imbalance on neurotransmission associated with AD. GABA is considered as a primary inhibitory neurotransmitter in nervous system as it blocks, or inhibits, most brain signals by decreasing neuronal activity. A number of studies show decreased GABA concentrations in various cortical areas, including in the temporal, frontal, parietal and occipital cortices of post-mortem brain tissues from patients with AD (Arai et al., 1984; Ellison et al., 1986; Lowe et al., 1988; Govindpani et al., 2017). The GABAergic system has three main components: GABAergic neurons, GABA transmitters, and GABA receptors and malfunctions in one of these components can contribute to imbalance in the excitation/inhibition of neuronal activity. There are more than 20 distinct types of inhibitory neurons in the hippocampus and the neighbouring brain regions, each of which play distinct functional roles in dynamic regulations of brain states and in the context-dependent extraction of sensory information, cognitive function, and behavioral

output (Roux and Buzsaki, 2015; Callaway, 2016). Not much is known about the effects of Aβ, or APP on GABAergic transmission at the pre- and post-synaptic level. Few studies have shown the downregulation of GABA(A) receptors and weaken of synaptic inhibitions at post synapse in cortical neuron preparations (Ulrich, 2015). One study shows that Aβ-induced hyperexcitability of hippocampal inhibitory parvalbumin (PV) interneurons contributes to neuronal network dysfunction and memory impairment in APP/PS1 mice (Hijazi et al., 2020). APP is highly expressed in a subset of GABAergic interneurons in the mouse hippocampus. GABAergic interneurons are estimated to account for only 10–15% of the total neurons (Pelkey et al., 2017) and the selective deletion of GABA, but not glutamatergic neurons disrupts adult hippocampal neurogenesis (Wang et al., 2014). A recent study using APP knock-in mouse model ($App^{NL\text{-}G\text{-}F}$) finds that beta-site amyloid precursor protein cleaving enzyme 1 (BACE1) knock-out in GABAergic neurons resulted in the greatest reduction (75%) in plaque load, demonstrating the involvement of GABAergic neurons in AD (Rice et al., 2020).

Glutamatergic hypothesis in AD

Glutamate is the major excitatory neurotransmitter in the central nervous system and is known to play roles in learning and memory, neuronal development, and synaptic plasticity. About 70% of all excitatory synapses in the central nervous system (CNS) utilize glutamate as a neurotransmitter. Studies provide evidence that glutamatergic neurons located in the hippocampus and in the frontal, temporal and parietal cortex are severely affected in AD (Revett et al., 2013). An increased excitatory neuronal activity or disrupted glutamatergic neurotransmission in AD has been reported, supporting the hypothesis that enhanced glutamatergic transmission or degeneration of glutamatergic neurons or glutamate-mediate toxicity is responsible for memory impairment and cell

death (Gray and Patel, 1995; Francis, 2003; Kirvell et al., 2006). There are two major types of glutamate receptor (GluRs): ionotropic and metabotropic which further are characterized into several subfamilies including N-methyl-d-aspartate (NMDA), amino-3-hydroxy-5-methyl-4-isoxazolepropionic acid (AMPA), kainate receptors and G-protein coupled receptors (GPCRs). Some of these receptors have been found to bind to Aβ peptides, however N-methyl-D-aspartate receptor (NMDA) receptor followed by AMPA have been quite extensively studied in terms of its involvement in neurodegeneration mechanism in AD. Both receptors are highly expressed at synapses for glutamate and associated with lipid rafts. Exposure of the NMDA receptor to Aβ oligomers is known to promote endocytosis of the receptor as well as other signaling events associated with NMDA receptor trafficking (Lai and McLaurin, 2010). Numerous studies *in vivo* and *in vitro* indicate a role of glutamate excitotoxicity in delayed slowly evolving neurodegeneration (Wang and Reddy, 2017; Liu et al., 2019a). Aβ interaction with the plasma membrane results in increased vulnerability of the neurons to excitotoxicity. Aβ protein shown to enhance the glutamate neurotoxicity in cortical cultures via both NMDA and kainate receptor most likely by compromising the ability of the neurons to reduce intracellular calcium levels to normal limits (Mattson et al., 1992; Miguel-Hidalgo et al., 2002). Several studies show that glutamate toxicity in is associated with intense transient influx of Ca^{2+} that can trigger a cascade of events leading to mitochondrial functional impairments and simultaneous formation of reactive oxygen species or free radicals and programmed cell death (Kamat et al., 2013).

In vitro studies show the involvement of oligomeric forms of Aβ 1-42 in calcium mediated toxicity (Demuro et al., 2005). In addition to increasing the production of Aβ, amyloidogenic processing of APP may perturb neuronal calcium homeostasis by decreasing the production of a secreted form of APP (sAPPα) that activates potassium

channels, and by generating an APP intracellular domain that affects endoplasmic reticulum calcium release by regulating the expression of genes involved in calcium homeostasis (Furukawa et al., 1996; Leissring et al., 2002; Bezprozvanny and Mattson, 2008). Another recent study reports decreased density of the glutamate receptor subunit GluA1 and the vesicular glutamate transporter (VGluT) 1 in CA1 of aged C57BL/6 mice injected with Aβ1-42 compared to naïve controls, with no effects on GluA2, GluN1, GluN2A, and VGluT2 receptors (Yeung et al., 2020). These changes were brain region and layer specific, suggesting complex and spatial vulnerability of this pathway during development of AD neuropathology. Finally, synthetic Aβ oligomers also known to increase excitatory postsynaptic potentials (EPSCs), membrane depolarizations, and action potentials (Gilbert et al., 2016) of glutamate neurons.

Neurovascular hypothesis

The amyloid cascade hypothesis has dominated AD research in the past few decades. Recent studies suggest that the vascular system is also a major contributor to disease progression. Interestingly, vascular dysfunction and reduced cerebral blood flow (CBF) may occur prior to the accumulation and aggregation of Aβ plaques and hyperphosphorylated tau tangles (Meyer et al., 2000; de la Torre, 2002b, a). Autopsy findings in patients with dementia has revealed that AD with cerebrovascular disease (mixed dementia), is more common than the 'pure' conditions of AD and vascular cognitive impairment (VCI) (Snowdon et al., 1997; Esiri et al., 1999; Gold et al., 2007; Schneider et al., 2007; Launer et al., 2008; Schneider et al., 2009; Gorelick et al., 2011; Mazza et al., 2011; Kalaria et al., 2012; Toledo et al., 2013; Attems and Jellinger, 2014; Hattori et al., 2016; Dichgans and Leys, 2017; Feng et al., 2018; Girouard and Munter, 2018; Hartmann et al., 2018; Smith, 2018).

Large/small cerebral vasculature damage and vascular risk factors (e.g., hypertension, diabetes mellitus, atherosclerosis, smoking, hypercholesterolemia, homocysteinemia obesity) could cause cerebral hypoperfusion (McDonald, 2002; McDonald et al., 2010; Attems and Jellinger, 2014; Gardener et al., 2015; Daulatzai, 2017; van Veluw et al., 2017; Hartmann et al., 2018; Iadecola et al., 2019). The effect of chronic cerebral hypoperfusion on cognitive dysfunction and neurodegenerative processes is still unknown. Understanding the functional and pathogenic synergy between neurons, glia, and vascular cells could providing a mechanistic insight into how alterations in cerebral blood vessels exacerbated neuronal dysfunction and underlying cognitive impairment (Iadecola, 2010; Quaegebeur et al., 2011; Zlokovic, 2011). Preclinical animal models provide us an opportunity to study the contribution of vascular alterations to AD pathology and could be an important step in the development of new treatments for the prevention of AD.

Animal models of AD

Even though FAD consist of ~5% of total AD cases in humans, it is easier to study and model, as the causative genes of FAD: APP, PSEN1 and PSEN2 are known. In contrast, even though SAD accounts for ~95% of the total AD cases in humans, the etiology of SAD is poorly understood, thus it is hard to model. Therefore, most of the mouse models of AD are generated by inserting humanized mutant APP, PSEN1 and PSEN2 genes, which mimics some aspects of complex AD pathology, especially amyloidosis. Similarly, models of neurofibrillary tangles can be created by inserting mutant human Microtubule Associated Protein Tau (MAPT) gene that encodes Tau protein leads.

These mouse models are genetically unique. Because they carry specific sets of mutations that are found in the humans, this introduces substantial phenotypical variations (e.g. onset of amyloid plaques, neurofibrillary tangles, neurodegeneration, synaptic dysfunctions and cognitive deficits) not only with genotype but with age as well. Thus, how faithfully any model by itself recapitulates the diverse human pathology is questionable. This explains why some treatments that work in one animal model fail in another even before going to human trials. Therefore, it is important to study several models in parallel. Despite the issues linked with mouse models they are very useful in understanding certain aspects of AD pathology. It is important for us to choose the models carefully to address specific aims of any study. A comprehensive list of available mouse models is available at alzfourm.org (https://www.alzforum.org/research-models/alzheimers-disease).

In my studies a knock-in (App^{NL-G-F}) and a transgenic (5xFAD) mouse model of Alzheimer's disease were used. *App* knock-in mice (Saito et al., 2014) carry Swedish (KM670, 671NL), Arctic (E693G) and Beyreuther/Iberian mutations (I716F) ($App^{NL-G-F/NL-G-F}$). 5xFAD transgenic mice (Oakley et al., 2006) overexpress both mutant human amyloid beta (Aβ) precursor protein 695 (APP)) with the Swedish (K670N, M671L), Florida (I716V), and London (V717I) Familial Alzheimer's Disease (FAD) mutations and human PS1 harboring two FAD mutations, M146L and L286V.

Brain activity as biomarker of AD

Understanding early disruptions of brain dynamics in AD may help in identifying early markers of disease pathology. Magnetic resonance imaging (MRI), positron emission tomography (PET), and electroencephalography (EEG) have been used to study circuit dysfunctions in the brain of AD patients (Seab et al., 1988; Greicius

et al., 2004; Sheline et al., 2010). Resting state functional MRI (rs-fMRI) has become popular in the past two decades to study functional network disruptions in AD (Liu et al., 2008; Buckner et al., 2009; Chhatwal and Sperling, 2012; Sugarman et al., 2012; Weiner et al., 2012; Dennis and Thompson, 2014; Li et al., 2015; Asaad and Lee, 2018; Zott et al., 2018). More specifically rs-fMRI studies reveal decreased functional connectivity (FC) in the default mode network (DMN), a network hypothesized to be usually active during internal processes such as daydreaming, introspection and mind wandering; and deactivated during task execution or learning. In addition, DMN is hypothesized to be involved in several cognitive functions, including autobiographical memory, memory consolidation, and self-referential thought (Andrews-Hanna et al., 2007). DMN primarily consist of medial prefrontal cortex, posterior cingulate cortex/precuneus and angular gyrus, whether hippocampus is a part of this DMN is not clear. Most of the cortical hubs that are preferentially affected in AD are within regions of multimodal association cortex that are components of the DMN (Buckner et al., 2009). In a seminal paper, Mesulam discussed the importance of these multimodal regions of cortex in detail (Mesulam, 1998). It is hypothesized that these DMN regions may be more vulnerable because of their continuous high baseline activity and/or associated metabolism (Mevel et al., 2011; Simic et al., 2014). Using high resolution fMRI, regional vulnerability of lateral entorhinal cortex (LEC) has been shown to be linked with high basal metabolism suggesting that LEC dysfunction could spread to the neighbouring parietal cortex (Khan et al., 2014). Hyper- and hypo- functional connectivity has been shown to be a signature of early and late stages of AD pathology (Schultz et al., 2017). Interestingly in another study hyper- connectivity has been shown in healthy young Apolipoprotein E- ε4 (APOE-ε4) carriers and hypo- connectivity in AD patients (Koelewijn et al., 2019)

In rodent models of AD, rs-fMRI and task or stimulus related brain activity, has also been studied (Mueggler et al., 2003; Sanganahalli et al., 2013; Shah et al., 2013; Grandjean et al., 2014; Grandjean et al., 2016; Shah et al., 2016; Parent et al., 2017; Shah et al., 2018; Latif-Hernandez et al., 2019). Interestingly, these studies have presented diverse results showing either continuous reduction in functional connectivity from early stages (Grandjean et al., 2014) or transitions from hyper- to hypo-connectivity with age (Shah et al., 2016; Latif-Hernandez et al., 2019). This early and late-stage functional connectivity dissociation has also been shown in APP/PS1 mice using functional connectivity optical intrinsic signal (fcOIS) imaging technique (Bero et al., 2012).

At a circuit level, disruption of multiple brain rhythms such as gamma oscillations (Iaccarino et al., 2016; Nakazono et al., 2017; Nakazono et al., 2018; Etter et al., 2019; Chen et al., 2021), hippocampal sharp wave ripples (SWRs) (Gillespie et al., 2016; Jones et al., 2019; Benthem et al., 2020), theta–gamma coupling (Goutagny et al., 2013; Goodman et al., 2018) have been examined in mouse models of AD. Abnormal cellular level hyper- and hypo- activity has also been shown to be an early marker of AD pathology in these models (Busche et al., 2008; Busche et al., 2015b; Xu et al., 2015; Yamamoto et al., 2015; Nuriel et al., 2017; Busche et al., 2019; Marinković et al., 2019; Petrache et al., 2019).

Hippocampal sharp wave ripples (SWRs) are high frequency oscillatory (100-250 Hz) signals hypothesised to be involved in memory consolidation and retrieval (Buzsáki, 2015). Coordinated interplay between SWRs and cortical slow oscillations is strongly implicated in learning and memory (Schabus et al., 2004; Ulrich, 2016). Furthermore, there is a causal link of SWR in learning and memory (Girardeau et al.,

2009; Ego-Stengel and Wilson, 2010; Jadhav et al., 2012). HPC-SWRs and SWRs mediated hippocampal-cortical interaction has been shown to be disrupted in mouse models of AD (Ciupek et al., 2015; Gillespie et al., 2016; Iaccarino et al., 2016; Nicole et al., 2016; Jones et al., 2019; Jura et al., 2019; Benthem et al., 2020; Caccavano et al., 2020; Sanchez-Aguilera and Quintanilla, 2021). High vulnerability of hippocampus and multimodal association cortex to AD pathology makes them a target brain circuitry for treatment. Thus, it is important to understand how signatures of hippocampal and cortical activity changes with disease progression.

Thesis Objectives

Deposition of Aβ is the central event in AD pathology leading to tau deposition, and eventually neurodegeneration. This is an irreversible condition resulting in progressive cognitive decline and loss of neural tissue. How this progressive deposition of Aβ cause early disruptions of brain dynamics and subsequent information processing is still unknown. Understanding cortical-cortical and hippocampal-cortical interactions is important to identify biomarkers and mechanism of memory dysfunctions in Alzheimer's disease. Mouse models of AD provide us an opportunity to study these network interactions and subsequent dysfunctions *in-vivo* at a spatio-temporal scale which is not possible to study in humans.

Previous studies have reported *hyper*- and *hypo*- activity and connectivity associated with Aβ and tau pathology in rodent models of AD. However, very few studies have investigated widefield cortical dynamics alterations in mouse models of AD (Bero et al., 2012; Busche et al., 2015a; Kastanenka et al., 2017). Further, none of these studies has investigated network dysfunctions associated with AD pathology in terms of cortical evoked activity, cortical functional connectivity, and hippocampal-cortical

interactions in a strain specific and age dependent manner. Therefore, it is important to leverage the diverse mouse models available and investigate the common mechanisms of brain dynamics dysfunctions in AD. In this thesis, I have tested the following three hypotheses using a knock-in (App^{NL-G-F}) and a transgenic (5xFAD) mouse model of AD:

***Hypothesis 1*:** Progressive Aβ deposition may alter sensory-evoked and spontaneous cortical dynamics. (Cortico-cortical interactions: Chapter 2)

***Hypothesis 2*:** Progressive Aβ deposition may alter SWRs and SWRs-coupled cortical dynamics. (Hippocampal-cortical interactions: Chapter 3)

***Hypothesis 3*:** Chronic cerebral hypoperfusion may lead to accelerated Aβ pathology and alter sensory-evoked and spontaneous cortical dynamics. (Chronic cerebral hypoperfusion and cortico-cortical interactions: Chapter 4).

Chapter 2 : Alzheimer's disease pathology and Cortico-cortical interactions in mouse models of AD

Abstract

Abnormal hyper- and hypo- activity and connectivity has been reported in Alzheimer's disease. In this study I aimed to understand how sensory evoked and spontaneous cortical activity is altered at ages 6- and 12- month in a knock-in (*App*$^{NL\text{-}G\text{-}F}$) and a transgenic 5xFAD mouse model of AD. Histology analysis revealed differences in amyloid beta (Aβ) pathology in *App*$^{NL\text{-}G\text{-}F}$ and 5xFAD mice with age. Using *in vivo* mesoscale wide-field voltage imaging, I observed hyperactivity in sensory evoked cortical activations in 12-month-old 5xFAD mice. The velocity of signal propagation across the cortex was also increased with alterations in direction of signal flow. Interestingly sensory evoked cortical signal flow had a preferred direction towards higher-order multimodal areas. Further, analysis of resting state spontaneous cortical activity revealed a reduction in functional connectivity of 6- and 12-month AD groups. The reduction in functional connectivity was more prominent with age in *App*$^{NL\text{-}G\text{-}F}$ mice than 5xFAD mice. Interestingly, when the functional connectivity of 6-month-old *App*$^{NL\text{-}G\text{-}F}$ mice was compared to C57BL/6J mice I observed hyper- functional connectivity that changed to hypo- functional connectivity when compared at 12-month age. The results suggest that cortico-cortical interaction dysfunctions exist in AD and reduced functional connectivity can be used as a marker of disease progression. In addition, excitation-inhibition imbalance may lead cortical hyperactivity in late-stage AD.

Introduction

Increase in amyloid beta (Aβ) deposition leads to disease associated neuronal damage which eventually disrupts neuronal circuits. There is enough evidence of large-scale network disruptions in AD, alterations in network activity and connectivity are associated with Aβ deposition in humans and mouse models of AD. Brain imaging methods such as magnetic resonance imaging (MRI) and positron emission tomography (PET), and electroencephalography (EEG) has been extensively used to study circuit dysfunctions in the brains of AD patients. For example, by injecting radioactive compounds such as 18-flourodeoxyglucose, PET studies have shown reduction of brain metabolism in AD patients (Greicius et al., 2004; Sheline et al., 2010). In addition to PET imaging, MRI scans have identified brain atrophy, which have validated pathological observations in post-mortem brains, including atrophy in the hippocampus (Seab et al., 1988).

Resting state functional MRI (fMRI) which measures changes in blood-oxygen-level-dependent (BOLD) signal, has become popular in the past two decades for studying functional network disruptions in AD (Liu et al., 2008; Chhatwal and Sperling, 2012; Sugarman et al., 2012; Weiner et al., 2012; Dennis and Thompson, 2014; Li et al., 2015; Asaad and Lee, 2018; Zott et al., 2018). These studies have focused on two main aspects of brain network activity: (1) resting state brain activity (rs-fMRI) and (2) task or stimulus related brain activity.

rs-fMRI studies in AD patients have revealed decreased functional connectivity in the default mode network (DMN), a network hypothesized to be usually active during internal processes such as daydreaming, introspection and mind wandering. This network usually gets deactivated during task execution or learning. DMN included

primarily consist of medial prefrontal cortex, posterior cingulate cortex/precuneus and angular gyrus. Whether the hippocampus is a part of this DMN is not yet clear. Studies combining rs-FMRI and PET tracers for Aβ (Pittsburgh Compound B (PiB)-PET) and tau (AV1451-PET) have revealed how the brain network dysfunction emerges with disease progression. In a recent study, hyper- connectivity is observed in amyloid-positive patients when neocortical tau levels are low and hypo- connectivity is observed in the same patients when tau levels increase with disease progression (Schultz et al., 2017). Hyper- and hypo- connectivity has also been shown in young APOE-ε4 carriers and AD patients respectively (Koelewijn et al., 2019). Decreased cortical functional connectivity has also been shown in animal models of AD (Bero et al., 2012; Busche et al., 2015a). Aberrant hyperexcitation related to intrinsic firing has been observed in AD and several studies suggest that impaired spontaneous excitation and inhibition and an increasing state of hyperexcitability originates from entorhinal cortex (EC) and then appears in hippocampus (HPC) and other cortical areas as the disease progresses (Khan et al., 2014).

Abnormal hyper- and hypo- activity and connectivity has been reported in mouse models of AD and is considered to be an early marker of AD pathology (Busche et al., 2008; Palop and Mucke, 2010; Busche et al., 2012; Grienberger et al., 2012; Busche et al., 2015b; Xu et al., 2015; Yamamoto et al., 2015; Maatuf et al., 2016; Kastanenka et al., 2017; Nuriel et al., 2017; Brown et al., 2018; Busche et al., 2019; Marinković et al., 2019; Petrache et al., 2019; Zott et al., 2019; Hector and Brouillette, 2021). This early hyperexcitation could be related to pro-inflammatory mediators, such as cytokines, reactive oxygen species and free radicals to name a few, released from the activated astrocytes and glial cells, which themselves have been shown to be altered morphologically in AD (Olabarria et al., 2010; Rodríguez et al., 2010). Seizure like

activity or hyperactivity may be caused by excitation inhibition imbalance. In a study by (Busche et al., 2008; Busche et al., 2015a) decreased GABAergic inhibition rather than increased glutamatergic transmission was shown to be associated with hyperactive neurons in cortical circuits of APP23xPS45 mice. However, later in a study by the same group (Zott et al., 2019) and in the same animal model, it was shown that hyperactivation is initiated by the suppression of glutamate reuptake. Further, hyperactivity in AD is also pathologically manifested by loss of interneurons. In a recent study persistent synaptic hyperexcitation and reduced inhibition has been shown in CA1 neurons of 10-18 month old $App^{NL\text{-}F/NL\text{-}F}$ mice. Finally, an increased reduction in the number of parvalbumin-containing (PV) interneurons in lateral entorhinal cortex (LEC) has been shown as compared to other cortical areas (Petrache et al., 2019).

Current literature suggests that abnormal processing of amyloid beta (Aβ) leads to downstream effects causing AD pathology and aberrant brain dynamics. More specifically *hypo*- connectivity and *hyper*- activity in the cortex is expected to increase in an age dependent manner as the disease progresses. In this chapter using wide field voltage sensitive dye imaging in mouse cortex, I will address how the sensory evoked and spontaneous cortical activity is altered in an age and strain specific manner in a knock-in ($App^{NL\text{-}G\text{-}F}$) and a transgenic (5xFAD) mouse model of AD.

Materials and Methods

Animals and Experimental Design

Naïve male and female pairs of C57BL/6J and *App* knock-in mice (Saito et al., 2014; Mehla et al., 2019) carrying Swedish (KM670, 671NL), Arctic (E693G) and Beyreuther/Iberian mutations (I716F) ($App^{NL\text{-}G\text{-}F/NL\text{-}G\text{-}F}$) (25-30 g) bred in a pathogen free facility were used. The *App* knock-in mice were gifted by RIKEN Center for Brain

Science, Japan. For another experimental group naïve male and female pairs of C57BL/6J and 5xFAD transgenic mice (Oakley et al., 2006; Jawhar et al., 2012) overexpressing both mutant human amyloid beta (Aβ) precursor protein 695 (APP)) with the Swedish (K670N, M671L), Florida (I716V), and London (V717I) Familial Alzheimer's Disease (FAD) mutations and human PS1 harboring two FAD mutations, M146L and L286V, bred in the same facility were used. In addition to littermate controls another group of C57BL/6J mice was also used as a control. Mice were weaned at 3 to 4 weeks and genotyping of all mice was done by polymerase chain reaction using ear-notching method. Male and female mice were divided into 10 groups based on their genotype and age, the number of animal used per group in this study are shown in table 2.1.

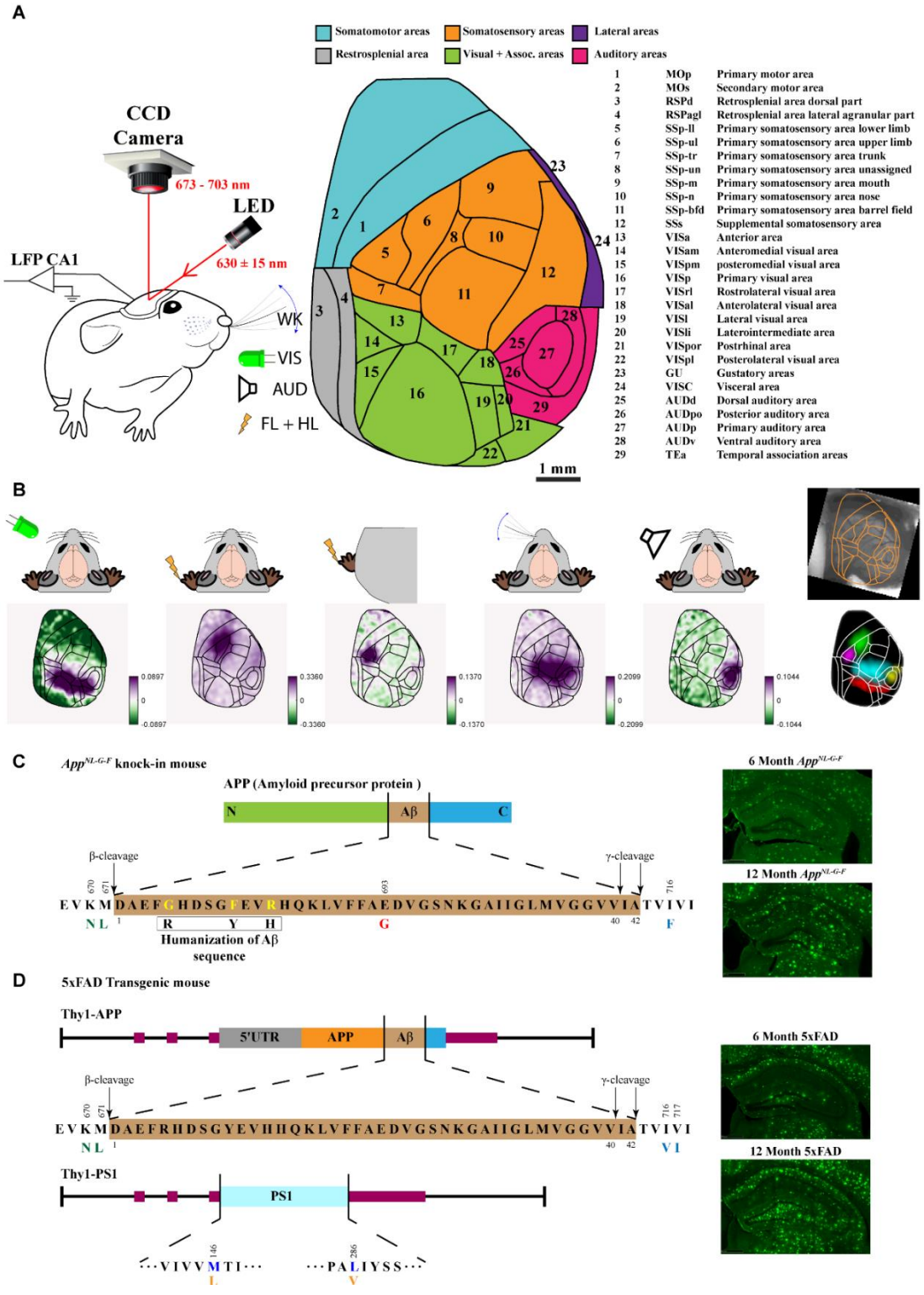

Figure 2.1: Understanding Cortical dynamics in Alzheimer's disease.
(A) Experimental setup for wide field voltage sensitive dye imaging (VSDI) in head fixed mice under urethane anaesthesia, with unilateral craniotomy, right hemisphere, 7×6 mm window; bregma: 2.5 to −4.5 mm, lateral: 0 to 6 mm. LFP electrode in ipsilateral dorsal CA1 inserted at an angle of ~58° from the vertical, ~2.5 mm lateral from the midline and tangent to the posterior side of the occipital suture and an approximate depth of 1.8 mm. We defined 29 cortical areas of interest in the imaging window based on the Allen common coordinate framework, which were then grouped into six functional subgroups: Somatomotor (Teal), Somatosensory

(Orange), Lateral (Purple), Retrosplenial (Gray), Visual + Association (Green), and Auditory areas (Pink). (B) Each mouse cortical imaging data was registered to 2D top view of Allen Mouse brain atlas (https://atlas.brain-map.org/) rotated laterally 30° to match the angle of the mouse head rotation in the VSD experiments. The registration was done based on regions identified by functional cortical mapping done with five different evoked sensory stimuli (contra-lateral stimulation): forelimb or hindlimb paw (1mA, 1 ms), whisker (1ms), auditory (1ms) and visual (1ms). (C-D) *App* knock-in mice carrying Swedish (KM670, 671NL), Arctic (E693G) and Beyreuther/Iberian mutations (I716F) ($App^{NL\text{-}G\text{-}F/NL\text{-}G\text{-}F}$) and 5xFAD transgenic mice overexpressing both mutant human amyloid beta (Aβ) precursor protein 695 (APP)) with the Swedish (K670N, M671L), Florida (I716V), and London (V717I) Familial Alzheimer's Disease (FAD) mutations and human PS1 harboring two FAD mutations, M146L and L286V, were used to study cortico-cortical and hippocampal-cortical interactions in mouse models of AD at 6 month and 12 month of age. It is important to note that amyloid beta (Aβ) pathology is significantly different in these animal models with respect to (w.r.t.) age and strain.

Table 2.1: Animal groups used in this study.

6 Month					12 Month				
C57BL/6J	***App*$^{+/+}$**	***App*$^{-/-}$**	**5xFAD^{+}**	**5xFAD^{-}**	**C57BL/6J**	***App*$^{+/+}$**	***App*$^{-/-}$**	**5xFAD^{+}**	**5xFAD^{-}**
n = 9	n = 7	n = 7	n = 9	n = 8	n = 6	n = 10	n = 6	n = 9	n = 6

Widefield voltage sensitive dye (VSD) imaging with simultaneous local field potential (LFP) recording from dorsal-CA1 of hippocampus was done on these animals at 6 and 12 months of age. Mice were housed 4-5 mice per cage with ad libitum access to standard rodent chow and water and maintained on a 12-hour light/dark cycle. Colony room temperature was maintained at 23°C ± 1 °C. All experimentation was completed during the light cycle at the same time each day. All experimental procedures were approved by the institutional animal care committee and performed in accordance with the standards set out by the Canadian Council for Animal Care.

Histology

Mice were deeply anaesthetized with an overdose of sodium pentobarbital, and transcardially perfused with phosphate-buffered saline (PBS) followed by 4% paraformaldehyde (PFA) in PBS. Brains were extracted and post-fixed overnight in 4% PFA in PBS at 4 °C. Brains were then transferred to a sucrose solution (30% sucrose, 0.02% sodium azide in PBS) and stored at 4 °C until sectioning.

Brains were cut into six series of 40 µm coronal sections using a freezing, sliding microtome (American Optical, Model #860). One series was used for double fluorescence immunolabeling of Aβ plaques and microglia or astrocytes, using the 4G8 antibody that is reactive to amino acid residues 17-24 of Aβ and an antibody against Iba1 or GFAP, respectively. A second series was used for double fluorescence immunolabeling of cholinergic neurons, using an antibody against choline acetyltransferase (ChAT), and NeuN-positive neurons. A third series was used for immunohistochemistry to label parvalbumin-positive interneurons.

All incubations and washes described below were performed at room temperature on a rotator, unless otherwise specified. Sections were mounted on charged microscope slides (Fisherbrand Superfrost Plus). Following immunolabeling, images for analysis were captured using a slide scanning microscope (NanoZoomer-RS, Hamamatsu).

Iba1/4G8/GFAP immunolabeling was performed on slide-mounted sections. The sections were submerged in cold 4% PFA for 4 min (without agitation), washed in tris-buffered saline (TBS), and then antigen retrieval was performed for approximately 10 min using 70% formic acid. After washing in TBS, the sections were permeabilized for 15 min in 0.1% TBS-X (i.e., TBS with 0.1% Triton X-100), blocked for 30 min in 0.1% TBS-X with 2% bovine serum albumin, and incubated for 2 days in blocking solution containing the primary antibodies (mouse anti-Aβ, 1:1000, BioLegend, 800701; rabbit anti-Iba1, 1:1000, Wako, 019-19741 and rabbit anti-GFAP,1:2000, Abcam, Ab7260). After washing, the sections were again permeabilized for 15 min, blocked for 30 min, and incubated overnight in blocking solution containing the secondary antibodies (goat anti-mouse Alexa Fluor 488, 1:1000, Abcam, ab150113;

goat anti-rabbit Alexa Fluor 594, 1:1000, Invitrogen, A-11037 and goat anti-rabbit Alexa Flour 594, 1:2000, Invitrogen, A11037). Finally, after washing in TBS, the slides were cover-slipped with Vectashield (Vector Laboratories, H-1000), sealed with nail polish, and stored at 4 °C in the dark until imaging.

ChAT/NeuN immunolabeling was also performed on slide-mounted sections. The sections were washed in TBS, blocked for 2 h in 0.3% TBS-X with 3% normal goat serum (NGS), and incubated for 24 h in 0.3% TBS-X containing the primary antibodies (rabbit anti-ChAT, 1:2000, Abcam, ab178850; mouse anti-NeuN, 1:400, Millipore, MAB377). The sections were then washed in 0.3% TBS-X and incubated for 25 h in 0.3% TBS-X containing the secondary antibodies (goat anti-mouse Alexa Fluor 488, 1:500, Abcam, ab150113; goat anti-rabbit Alexa Fluor 594, 1:500, Invitrogen, A-11037). Finally, after washing in 0.3% TBS-X followed by TBS, the slides were cover-slipped with Vectashield, sealed with nail polish, and stored at 4 °C in the dark until imaging.

Parvalbumin immunolabeling was performed on free floating sections. The sections were washed in PBS and then placed in 0.3% hydrogen peroxide in PBS for 25 min to block endogenous peroxidase activity. After washing in PBS, the sections were blocked for 1.5 h in 0.5% TBS-X with 5% NGS, followed by incubation for 2 days in 0.5% TBS-X containing the primary antibody (mouse anti-parvalbumin, 1:2000, Sigma-Aldrich, P3088). The sections were then washed in 0.5% TBS-X and incubated for 1.5 h in 0.5% TBS-X containing the secondary antibody (biotinylated goat anti-mouse, 1:500, Sigma-Aldrich, B7151). After washing in 0.5% TBS-X followed by PBS, the sections were incubated for 1 h in tertiary antibody solution, prepared from Reagent A + B of the Vectastain ABC-HRP Kit (Vector Laboratories, PK-4000) diluted 1:500

in PBS. After washing in PBS, colour was developed for 8-12 min in TBS containing 0.05% diaminobenzidine and 0.015% hydrogen peroxide. The sections were then washed in PBS, mounted to slides, and allowed to dry. The sections were dehydrated in an ascending series of ethanol baths, cleared with Hemo-De, and the slides were cover-slipped with Permount (Fisher Scientific, SP15-500).

Histology Analysis

Histology images were registered to the Allen CCF in a semi-automated approach to quantify Aβ plaques, microglia or astrocytes, cholinergic neurons (ChAT positive neurons) and Parvalbumin-positive interneurons, in different brain areas. We adapted the publicly available code (http://github.com/petersaj/AP_histology) for rigid and non-rigid histology alignment to Allen CCF and segmentation. Affine transform is used at the first level to register brain slices with Allen CCF, if on visual inspection there is a mismatch in alignment then we used non rigid cubic b-spline transform for registration (Rueckert et al., 1999).

Table 2.2: Abbreviation and full structure name of mouse brain regions analysed for histology data.

Abbreviation	*Full structure Name*	*Abbreviation*	*Full structure Name*
Brainstem nuclei		SSp-un	Primary somatosensory area, unassigned
TH	Thalamus	SSs	Supplemental somatosensory area
HY	Hypothalamus	GU	Gustatory areas
MBsen	Midbrain sensory related	VISC	Visceral area
MBmot	Midbrain motor related	AUDd	Dorsal auditory area
MBsta	Midbrain behavioral state related	AUDp	Primary auditory area
P	Pons	AUDpo	Posterior auditory area
MY	Medulla	AUDv	Ventral auditory area
Cerebral nuclei		VISal	Anterolateral visual area
STR	Striatum	VISam	Anteromedial visual area
PAL	Pallidum	VISl	Lateral visual area

Cortical subplate		VISp	Primary visual area
CLA	Claustrum	VISpl	Posterolateral visual area
EPd	Endopiriform nucleus, dorsal part	VISpm	Posteromedial visual area
EPv	Endopiriform nucleus, ventral part	VISli	Laterointermediate area
LA	Lateral amygdalar nucleus	VISpor	Postrhinal area
BLA	Basolateral amygdalar nucleus	ACAd	Anterior cingulate area, dorsal part
BMA	Basomedial amygdalar nucleus	ACAv	Anterior cingulate area, ventral part
PA	Posterior amygdalar nucleus	PL	Prelimbic area
Hippocampal formation		ILA	Infralimbic area
CA1	Field CA1	ORBl	Orbital area, lateral part
CA2	Field CA2	ORBm	Orbital area, medial part
CA3	Field CA3	ORBvl	Orbital area, ventrolateral part
DG	Dentate gyrus	AId	Agranular insular area, dorsal part
FC	Fasciola cinerea	AIp	Agranular insular area, posterior part
IG	Induseum griseum	AIv	Agranular insular area, ventral part
ENTl	Entorhinal area, lateral part	RSPagl	Retrosplenial area, lateral agranular part
ENTm	Entorhinal area, medial part, dorsal zone	RSPd	Retrosplenial area, dorsal part
PAR	Parasubiculum	RSPv	Retrosplenial area, ventral part
POST	Postsubiculum	VISa	Anterior area
PRE	Presubiculum	VISrl	Rostrolateral visual area
SUB	Subiculum	TEa	Temporal association areas
ProS	Prosubiculum	PERI	Perirhinal area
HATA	Hippocampo-amygdalar transition area	ECT	Ectorhinal area
APr	Area prostriata	**Olfactory areas**	
Isocortex		MOB	Main olfactory bulb
FRP	Frontal pole, cerebral cortex	AOB	Accessory olfactory bulb
MOp	Primary motor area	AON	Anterior olfactory nucleus
MOs	Secondary motor area	TT	Taenia tecta
SSp-n	Primary somatosensory area, nose	DP	Dorsal peduncular area

SSp-bfd	Primary somatosensory area, barrel field	PIR	Piriform area
SSp-ll	Primary somatosensory area, lower limb	NLOT	Nucleus of the lateral olfactory tract
SSp-m	Primary somatosensory area, mouth	COAa	Cortical amygdalar area, anterior part
SSp-ul	Primary somatosensory area, upper limb	COAp	Cortical amygdalar area, posterior part
SSp-tr	Primary somatosensory area, trunk	PAA	Piriform-amygdalar area
		TR	Postpiriform transition area

Surgery for craniotomy and VSDI

At 6 and 12 months of age, craniotomy for VSDI was performed as described previously (Mohajerani et al., 2010; Mohajerani et al., 2013; Kyweriga and Mohajerani, 2016). Mice were anesthetized with isoflurane (1.2–1.5%) for induction, followed by urethane for data collection (1.0-1.2 mg/kg, i.p). Mice were transferred on a metal plate that could be mounted onto the stage of the upright macroscope, and the skull was rotated laterally 30° and fastened to a steel plate. A tracheotomy was performed on mice to assist with breathing before starting the craniotomy. A 7×6 mm unilateral craniotomy (bregma 2.5 to −4.5 mm, lateral 0 to 6 mm) was made and the underlying dura was removed. Body temperature was maintained at 37 ± 0.2 °C degrees using a heating pad with a feedback thermistor.

For *in vivo* VSDI, RH1691 dye (Optical Imaging, New York, NY) was applied to the cortex for 30-45 min. For data collection, 12-bit images were captured with a charge-coupled device (CCD) camera (1M60 Pantera, Dalsa, Waterloo, ON) and E8 frame grabber with XCAP 3.9 imaging software (EPIX, Inc., Buffalo Grove IL). The voltage sensitive dye was excited with a red LED (Luxeon K2, 627 nm center), and

excitation filters 630 ± 15 nm (Mohajerani et al., 2010; Mohajerani et al., 2013; Chan et al., 2015; Karimi Abadchi et al., 2020). Images were taken through a macroscope composed of front-to-front video lenses (8.6 × 8.6 mm field of view, 67 μm per pixel). The depth of field of the imaging setup used was ~1 mm (Lim et al., 2012). To stimulate the forelimbs and hindlimbs, thin acupuncture needles (0.14 mm) were inserted into the paws, and a 1 mA, 1-ms electrical pulse was delivered. To stimulate a single whisker (C2), the whisker was attached to a piezoelectric device (Q220-A4-203YB, Piezo Systems, Inc., Woburn, MA) and given a single 1-ms tap using a square pulse. The whisker was moved at most 90 μm in an anterior-to-posterior direction, which corresponds to a 2.6° angle of deflection. A 1-ms pulse of green light was delivered as visual stimulation. A single 1-ms tone was used as auditory stimulation.

Local field potential (LFP) electrode

Teflon coated stainless steel wires (A-M Systems) with the thickness of 50 μm were used for the hippocampal LFP recordings. The HPC electrode was inserted at an angle of ~58 degrees from the vertical, ~2.5 mm lateral from the midline and tangent to the posterior side of the occipital suture and an approximate depth of 1.8 mm to record LFP activity from pyramidal layer of dorsal CA1.

VSD data pre-processing

VSDI of spontaneous cortical activity was recorded in the absence of visual, olfactory, tactile, or auditory stimulation during 15 min epochs with 10 ms (100 Hz) temporal resolution. Data was first denoised by applying singular-value decomposition and taking only the components with greatest associated singular values (top 50 components which explain 99.99% of the variance). The baseline of the optical signal (F_0) captured from each pixel in the imaging window was calculated using the *locdetrend* function in

the Choronux toolbox was used to fit a piecewise linear curve to the pixel time series using the local regression method (Mitra and Bokil, 2008). The fluorescence changes were quantified as $(F-F_0)/F_0 \times 100\%$; F represents the fluorescence signal at any given time and F_0 represents the average of fluorescence over all frames. A band pass filter was applied (0.5–6 Hz) FIR filter on the $\Delta F/F_0$ signal as most of the optical signal power is concentrated in low frequencies (Mohajerani et al., 2013).

VSD responses to sensory-evoked stimulation were calculated as the normalized difference to the average baseline estimated by fitting a fourth-degree polynomial ($\Delta F/F_0 \times 100$) using custom-written code in MATLAB 2019b (Mathworks). Average sensory evoked response was calculated from 20 trials of stimulation with an inter-stimulus interval of 10 s and 6.7 ms (150 Hz) temporal resolution.

VSDI registration

Each mouse cortical imaging data was registered to 2D top view of Allen Mouse brain atlas (https://atlas.brain-map.org/) rotated laterally 30° to match the angle of the mouse head rotation in the VSD experiments. The registration was done based on regions identified by functional cortical mapping done with five different evoked sensory stimuli (contra-lateral stimulation): forelimb or hindlimb paw (1mA, 1 ms), whisker (1ms), auditory (1ms) and visual (1ms). Matlab's *fitgeotrans* function was used to register VSDI data to reference map. Briefly, *figeotrans* function implements a 2D geometric transformation in which points from one Euclidean space are mapped to points in another Euclidean space. For instance, a geometric transform T that implements nonreflective similarity transformation that may include a rotation, a scaling, and a translation, will map a point with Cartesian coordinates (x, y) to another point with Cartesian coordinates (u, v) with the following rule:

$$[u\ v] = [x\ y\ 1]T$$

where, T is a 3-by-3 matrix that depends on four parameters namely, scale factor S, rotation angle θ, translation in x dimension t_x and translation in y dimension t_y.

$$T = \begin{bmatrix} S\cos\theta & -S\sin\theta & 0 \\ S\sin\theta & S\cos\theta & 0 \\ t_x & t_y & 1 \end{bmatrix}$$

I defined 29 cortical areas of interest in the imaging window based on the Allen common coordinate framework, this ensured that all mice had similar regions of interest that were comparable across animals. We then grouped the cortical surface into six functional subgroups (fig 1 A) according to the Allen CCF (Wang et al., 2020) and some recent studies using widefield optical imaging (Harris et al., 2019; Musall et al., 2019; Gilad and Helmchen, 2020; Gallero-Salas et al., 2021). Somatomotor areas (Teal): primary motor area (MOp), secondary motor area (MOs). Somatosensory areas (Orange): primary somatosensory area upper limb (SSp-ul), primary somatosensory area lower limb (SSp-ll), primary somatosensory area barrel field (SSp-bfd), primary somatosensory area nose (SSp-n), primary somatosensory area unassigned (SSp-un), primary somatosensory area trunk (SSp-tr), primary somatosensory area mouth (SSp-m), and supplemental somatosensory area (SSs). Lateral areas (Purple): visceral area (VISC) and gustatory areas (GU). Retrosplenial area (Gray): retrosplenial area lateral agranular part (RSPagl) and retrosplenial area dorsal part (RSPd). Visual + Association areas (Green): anteromedial visual area (VISam), laterointermediate area (VISli), posteromedial visual area (VISpm), postrhinal area (VISpor), primary visual area (VISp), lateral visual area (VISl), anterolateral visual area (VISal), posterolateral visual area (VISpl), anterior area (VISa), and rostrolateral visual area (VISrl). Auditory areas

(Pink): dorsal auditory area (AUDd), primary auditory area (AUDp), posterior auditory area (AUDpo), ventral auditory area (AUDv), and temporal association areas (TEa).

Spontaneous Data Analysis

Mohajerani et al. 2013 and others have shown that VSDI signal power is mostly concentrated in lower frequencies thus in our analysis we band pass filtered spontaneous data from 0.5 Hz to 6 Hz using a 400-order band pass FIR filter (Hamming window design). Average pixel values over time in 29 regions of interest from resting state (task-independent) spontaneous VSDI data was used to calculate zero-lag Pearson correlation between regions which is indicative of regional functional connectivity strength.

Network Analysis

Brain connectivity toolbox (Rubinov and Sporns, 2010) was used to calculate network properties such as characteristic path length, global efficiency, consensus partition and clustering coefficient. Weighted undirected network approach was used for our analysis where, network nodes were cortical ROIs and links were the magnitude of temporal correlation between ROIs obtained from spontaneous activity.

Evoked Data Analysis

Alteration in evoked population responses were compared based on the following five parameters: rise time, fall time, peak ΔF/F0, average speed, and direction of propagation. The rise-time was defined as the time taken for the signal to rise from 10% to 90% of the peak evoked activation in the contralateral hemisphere. Fall-time was defined as the time taken by the signal to fall from 90% to 10% of the peak evoked activation in contralateral hemisphere. Peak amplitude is the peak evoked change in fluorescence ($\Delta F/F_0$) in contralateral hemisphere. Average speed and direction of propagation was calculated using optical flow analysis as stated below.

Optical Flow Analysis

The direction of information flow is important for understanding the information integration over multiple brain areas. Optical flow analysis provides a novel approach to identify the velocity and directionality of information flow in the brain. Multiple algorithms such as Horn-Schunck (HS), Lucas-Kanade (LK), Temporospatial (TS) and Combined local-global (CLG) have been used in previous studies to quantify information propagation across mouse cortex in widefield optical imaging data (Mohajerani et al., 2013; Afrashteh et al., 2017; Karimi Abadchi et al., 2020). Here we used CLG (Bruhn et al., 2005; Jara et al., 2015) method to quantify optical flow of widefield VSDI data during evoked activations. The advantage of using CLG method over others is that it considers both local and global approaches, leading to dense flow fields that are robust against noise. We used the Matlab implementation of CLG method by Ce Liu (Liu, 2009) to quantify the direction of information flow during early phase of evoked activation (i.e. from stimulus onset to peak activation in the stimulated region).

Statistical Analysis

MATLAB 2019b was used for statistical analysis of sensory evoked and spontaneous cortical activity. A p value < 0.05 was considered statistically significant, adjusted p values reported. Two-Sample t-test was used to compare change in plaque pathology with age. One-, two- or three- way ANOVA followed by Bonferroni multiple comparison was used to determine the effects of age, age + genotype, age + genotype + region. Changes in functional connectivity matrix was reported after correcting for multiple comparisons using false discovery rate (fdr). The adjusted critical p-value (p < 0.05) was considered significant.

Results

Region selective increase in Aβ *plaques with age in* $App^{NL\text{-}G\text{-}F}$ *and 5xFAD mice*

Photomicrographs of immunohistochemistry staining of 4G8 (green, antibody is reactive to amino acid residues 17-24 of amyloid-beta (Aβ)) reveal amyloid plaque distribution in different brain regions of $App^{NL\text{-}G\text{-}F}$ mice fig 2.2 (E, G) and 5xFAD mice fig 2.2(F,H) at the age of 6 and 12 months. The Aβ plaque distribution in $App^{NL\text{-}G\text{-}F}$ mice is homogenous across cortical layers however, for 5xFAD they are mostly concentrated in deeper layers (Layer 5 and 6) with minimum plaques in Layer 1, 2/3 and 4. In hippocampus of $App^{NL\text{-}G\text{-}F}$ mice there is homogeneous distribution of plaques but for 5xFAD mice plaques were most concentrated in dentate and pyramidal layer of CA1. Further there were little to no plaques in striatum region (specifically caudoputamen) and in Hypothalamus regions of 6-month 5xFAD mice. However, by 12 months age plaques in these regions increased considerably with full blown plaque pathology in cortical subplate and piriform area. Changes in plaque load with age is quantified in fig 2.2 (I, J) for 5xFAD and $App^{NL\text{-}G\text{-}F}$, a significant increase in plaque pathology is observed across multiple brain areas, further, astrocytosis is significantly correlated with plaque load.

Effects of disease pathology on evoked cortical dynamics

Evoked VSD data was first registered to the reference map using methodology described earlier, further, peak cortical activations, rise time and fall time in 29 regions of interest (ROIs) was calculated. Regions that showed no significant change in amplitude or were not in imaging window of majority animals were excluded from analysis, thus there we less than 29 regions for each analysis. Optical flow analysis was used to study speed and direction of signal flow associated with evoked activation.

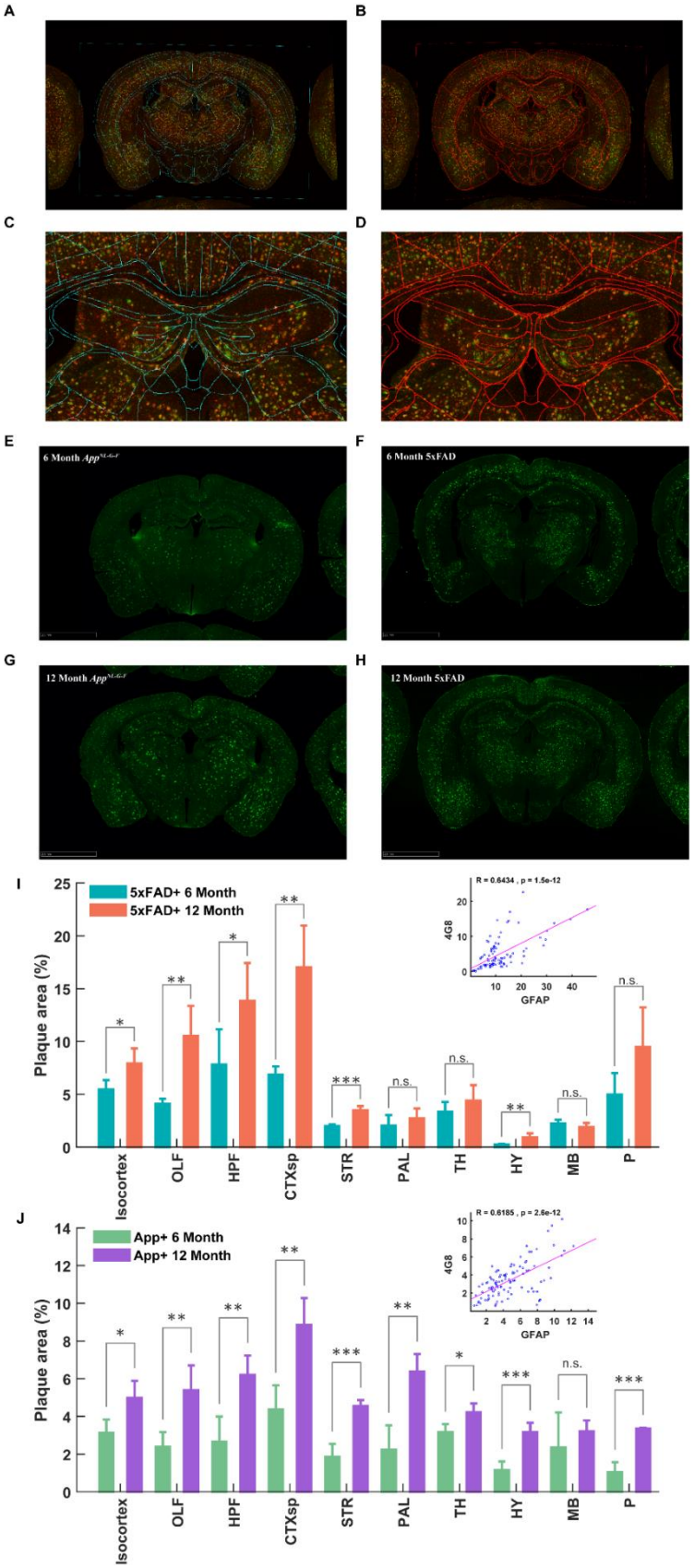

Figure 2.2: Histology slice registration and AD Pathology.
(A-D) Affine transform is used at the first level to register brain slices with Allen CCF, if on visual inspection there is a mismatch in alignment then we used non rigid cubic b-spline transform for registration. Photomicrographs of immunohistochemistry staining of 4G8 (green, antibody is reactive to amino acid residues 17-24 of amyloid-beta (Aβ)) reveal amyloid plaque

distribution in different brain regions of *App*$^{NL-G-F}$ mice (E,G) and 5xFAD mice(F,H) at the age of 6 and 12 months. The Aβ plaque distribution in *App*$^{NL-G-F}$ mice is homogenous across cortical layers however, for 5xFAD they are mostly concentrated in deeper layers (Layer 5 and 6) with minimum plaques in Layer 1, 2/3 and 4. In hippocampus of *App*$^{NL-G-F}$ mice there is homogeneous distribution of plaques but for 5xFAD mice plaques were most concentrated in dentate and pyramidal layer of CA1.

Table 2.3: p-values of two sample t-test comparing amyloid-beta (Aβ) plaques in brain of 5xFAD and *App*$^{NL-G-F}$ mice at 6- and 12-months age.

	Isocortex	OLF	HPF	CTXsp	STR	PAL	TH	HY	MB	P
5xFAD	0.02561	0.004528	0.04823	0.002337	0.000334	0.362087	0.275074	0.009405	0.241521	0.078978
App	0.017486	0.007756	0.005679	0.003418	0.000374	0.001986	0.015485	0.000936	0.411809	0.000119

Auditory Stimulus: To identify disease associated changes in auditory cortex, 1 ms auditory clicks were presented towards the contralateral ear. Interestingly auditory evoked cortical signal flow had a preferred direction towards higher-order multimodal areas (e.g., parietal associational area (ptA)) (fig 2.3A). A significant effect of age was observed in 5xFAD group for changes in direction, speed, and amplitude of activation, further a significant effect of genotype and interaction between age and genotype was observed for direction and amplitude of activation (see Table 2.4 5xFAD for detail statistics). A significant difference in the direction of propagation was observed in 6-month-old 5xFAD^{+} mice, further an increase in peak amplitude of activation and the speed of propagation was observed in 12-month-old 5xFAD^{+} mice, no changes were observed for rise-time and fall-time in all groups (fig 2.3). For App group significant effect of age was observed in direction of propagation and fall time, further a significant effect of genotype was observed for direction, amplitude, risetime, and fall time. There was significant interaction between age and genotype for direction, amplitude and fall time (see Table 2.4 App for detail statistics). A significant difference in direction and fall-time of cortical activation was observed for 12-month-old *App*$^{+/+}$ mice, further we observed an increase in evoked amplitude for 12-month-old *App*$^{+/+}$ mice (fig 2.4). For C57 group a significant effect of age was observed in direction, amplitude, rise-time, and fall-time of cortical activation (fig 2.5) (see Table 2.4 C57 for detail statistics).

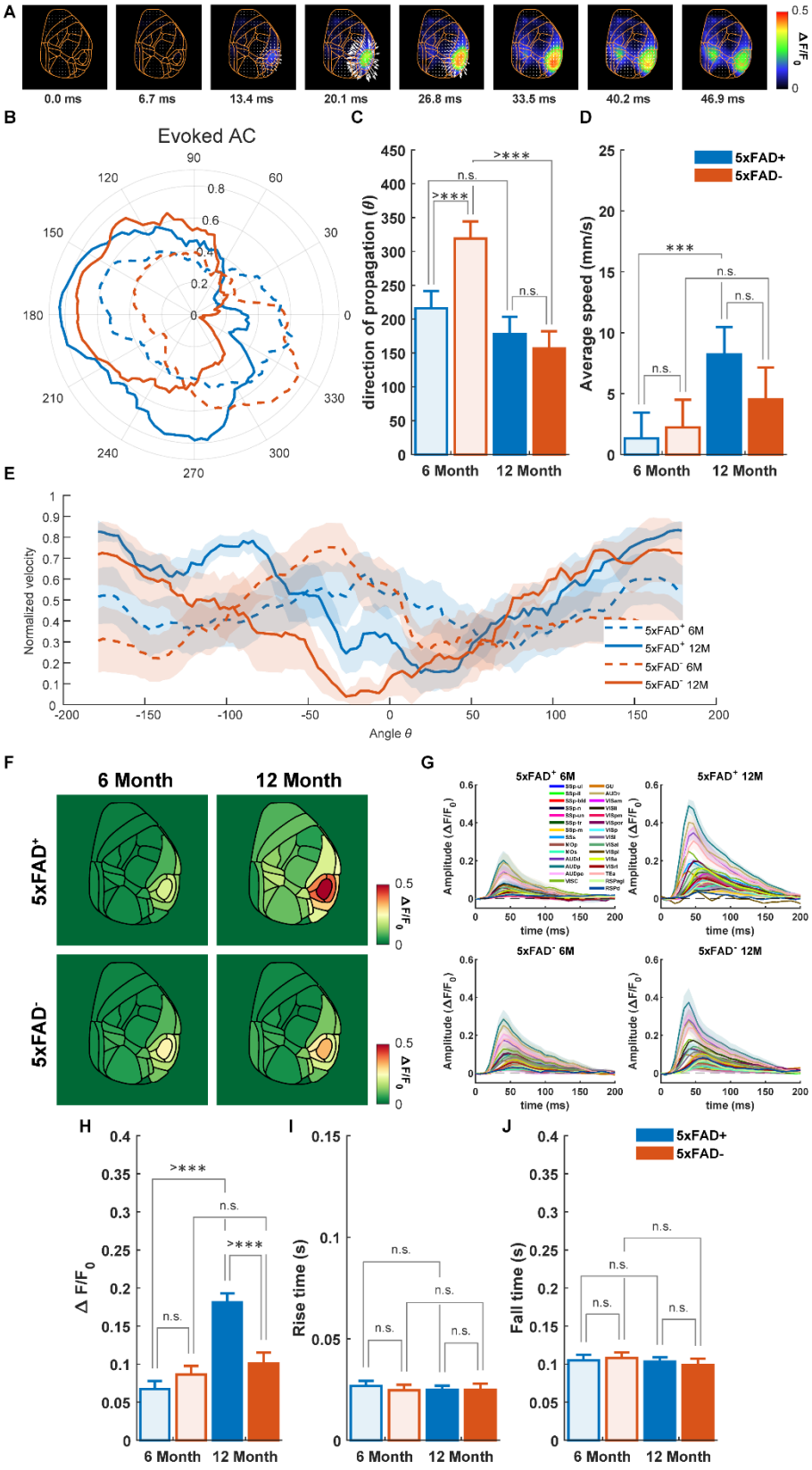

Figure 2.3: Auditory stimulus evoked cortical dynamics for 5xFAD mice.
(A) Montage of representative Auditory stimulus (1 ms) evoked cortical activity with overlaid velocity vector fields determined using Combined local-global (CLG) method for optical flow analysis. (B) polar plot and (E) mean ± S.E.M. of normalized velocity with respect to the angle/direction of signal flow. (C-D) Direction and speed of auditory evoked cortical signal propagation changes with genotype and age. (F) A spatial representation of region-wise peak

amplitude of evoked cortical activations. (G) time series representation of evoked cortical activations in multiple regions of interest (ROIs) shown in fig 2.1A. (H) Peak amplitude of cortical activation increases with age in 5xFAD^{+} mice suggesting hyperactivity associated with disease progression. (I-J) No changes in rise-time and fall-time of the signal was observed. (6-month-old: 5xFAD^{+}, n = 9; 5xFAD^{-}, n = 8 and 12-month-old: 5xFAD^{+}, n = 7; 5xFAD^{-}, n = 6). * = $p < 0.05$; ** = $p < 0.01$; *** = $p < 0.001$; >*** = $p < 0.001$.

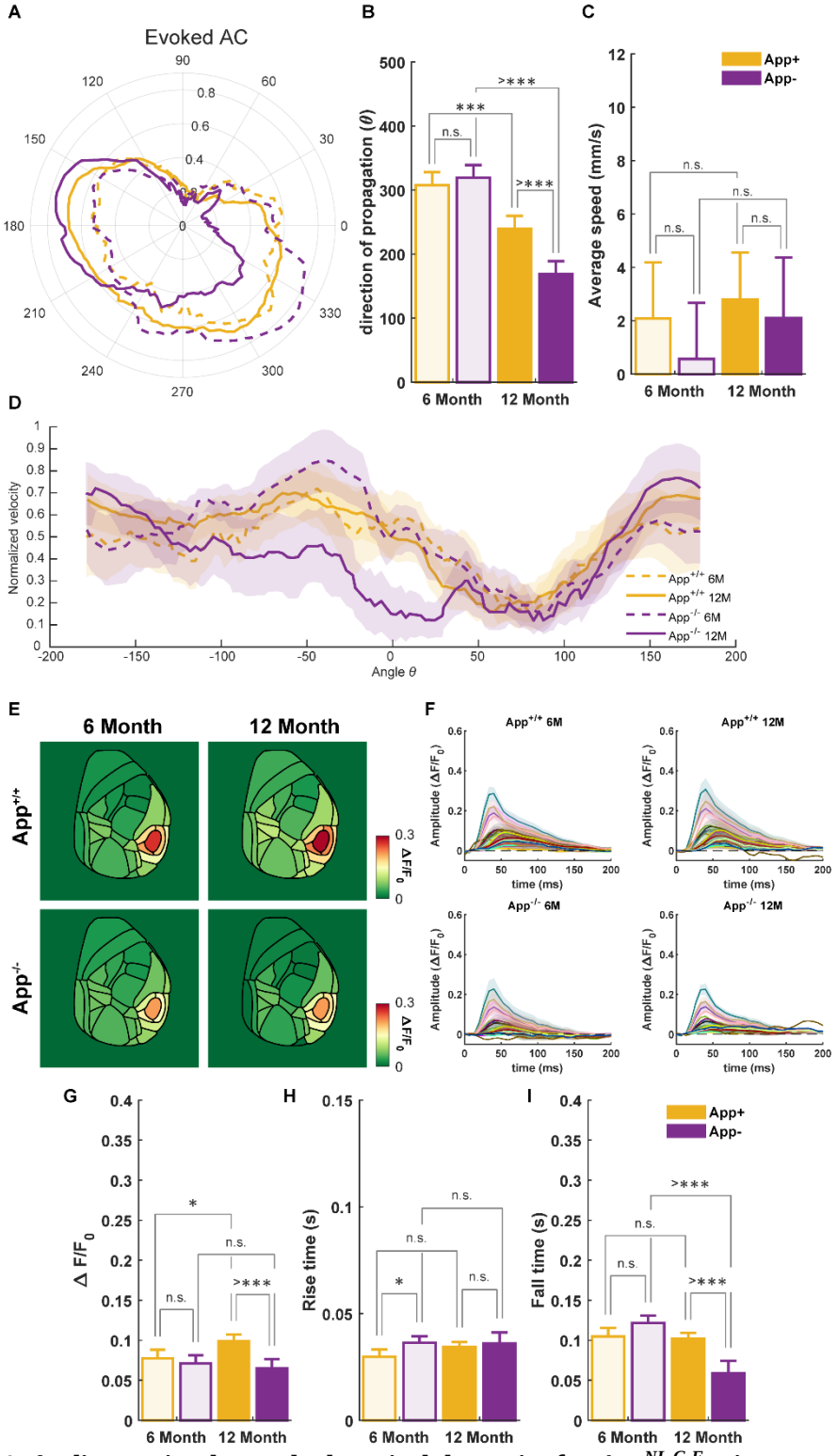

Figure 2.4: Auditory stimulus evoked cortical dynamics for *App*$^{NL-G-F}$ mice.
(A) polar plot and (D) mean ± S.E.M. of normalized velocity with respect to the angle/direction of signal flow. (B-C) Direction of auditory evoked cortical signal propagation changes with

genotype and age, However, no effect on speed of propagation in observed. (E) A spatial representation of region-wise peak amplitude of evoked cortical activations. (F) time series representation of evoked cortical activations in multiple regions of interest (ROIs) shown in fig 2.1A. (G) Peak amplitude of cortical activation increases with age in $App^{+/+}$ mice suggesting hyperactivity associated with disease progression. (H-I) $App^{+/+}$ mice had reduced rise-time suggesting quick activation after stimulus onset, however, reduced fall-time at 12 months suggest short period of activation for both $App^{+/+}$ and $App^{-/-}$ mice. (6-month-old: $App^{+/+}$, n = 7; $App^{-/-}$, n = 7 and $App^{+/+}$, n = 9; $App^{-/-}$, n = 6). * = $p < 0.05$; ** = $p < 0.01$; *** = $p < 0.001$; >*** = $p < 0.001$.

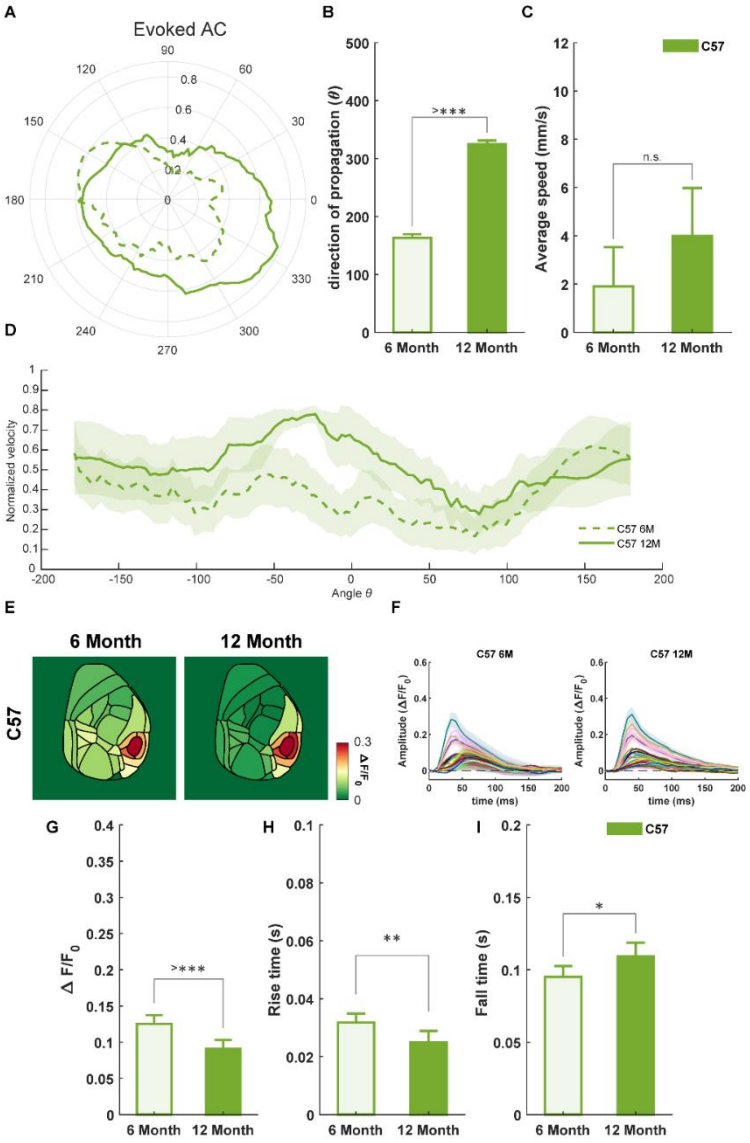

Figure 2.5: Auditory stimulus evoked cortical dynamics for C57 mice.
(A) polar plot and (D) mean ± S.E.M. of normalized velocity with respect to the angle/direction of signal flow. (B-C) Direction of auditory evoked cortical signal propagation changes with age, however, no significant effect on speed of propagation in observed. (E) A spatial representation of region-wise peak amplitude of evoked cortical activations. (F) time series representation of evoked cortical activations in multiple regions of interest (ROIs) shown in fig 2.1A. (G) Peak amplitude of cortical activation decreases with age in C57 mice. (H-I) C57 mice had reduced rise-time at 12 months age suggesting quick activation after stimulus onset, however, the fall-time increases suggesting prolonged activation. (6-month-old: C57BL/6J, n = 8 and 12-month-old: C57BL/6J, n = 6). * = $p < 0.05$; ** = $p < 0.01$; *** = $p < 0.001$; >*** = $p < 0.001$.

Table 2.4: ANOVA table for statistical comparison of direction of propagation, propagation speed, amplitude, rise time and fall time of Auditory evoked cortical activations.

5xFAD

Direction								**Speed**															
Source	Sum Sq.	d.f.	Singular?	Mean Sq.	F	Prob>F		Source	Sum Sq.	d.f.	Singular?	Mean Sq.	F	Prob>F									
Age	130594.2	1	0	130594.2	61.72569	3.63E-10		Age	159.6628	1	0	159.6628	15.70786	0.000488									
Genotype	21576.51	1	0	21576.51	10.19819	0.002483		Genotype	14.43578	1	0	14.43578	1.420213	0.243739									
Age*Genotype	50181.76	1	0	50181.76	23.71854	1.25E-05		Age*Genotype	39.93303	1	0	39.93303	3.928669	0.057733									
Error	101554.5	48	0	2115.719				Error	274.442	27	0	10.16452											
Total	303907	51	0					Total	507.0892	30	0												
Amplitude								**Rise Time**								**Fall Time**							
Source	Sum Sq.	d.f.	Singular?	Mean Sq.	F	Prob>F		Source	Sum Sq.	d.f.	Singular?	Mean Sq.	F	Prob>F		Source	Sum Sq.	d.f.	Singular?	Mean Sq.	F	Prob>F	
Regions	5.117091	27	0	0.189522	28.30488	1.23E-94		Regions	0.019045	27	0	0.000705	4.643488	1.95E-12		Regions	0.039974	27	0	0.001481	1.216357	0.212485	
Age	0.727762	1	0	0.727762	108.6904	8.45E-24		Age	4.89E-05	1	0	4.89E-05	0.321832	0.570818		Age	0.002574	1	0	0.002574	2.11488	0.146635	
Genotype	0.172275	1	0	0.172275	25.72915	5E-07		Genotype	0.000103	1	0	0.000103	0.677238	0.411016		Genotype	3.73E-05	1	0	3.73E-05	0.030613	0.861192	
Regions*Age	0.482508	27	0	0.017871	2.668965	1.17E-05		Regions*Age	0.002847	27	0	0.000105	0.69408	0.874431		Regions*Age	0.040503	27	0	0.0015	1.232446	0.198408	
Regions*Genotype	0.051453	27	0	0.001906	0.284609	0.99989		Regions*Genotype	0.006382	27	0	0.000236	1.555925	0.039394		Regions*Genotype	0.023155	27	0	0.000858	0.704566	0.864244	
Age*Genotype	0.474022	1	0	0.474022	70.79467	2.12E-16		Age*Genotype	0.000116	1	0	0.000116	0.76557	0.382101		Age*Genotype	0.001366	1	0	0.001366	1.122152	0.290076	
Error	4.827622	721	0	0.006696				Error	0.062587	412	0	0.000152				Error	0.501475	412	0	0.001217			
Total	12.04484	805	0					Total	0.093888	496	0					Total	0.60047	496	0				

App

Direction								**Speed**															
Source	Sum Sq.	d.f.	Singular?	Mean Sq.	F	Prob>F		Source	Sum Sq.	d.f.	Singular?	Mean Sq.	F	Prob>F									
Age	154952.5	1	0	154952.5	116.1109	2.08E-14		Age	9.16489	1	0	9.16489	1.187411	0.285849									
Genotype	11396.93	1	0	11396.93	8.540087	0.005284		Genotype	8.935281	1	0	8.935281	1.157663	0.291834									
Age*Genotype	21906.53	1	0	21906.53	16.41527	0.000185		Age*Genotype	1.225448	1	0	1.225448	0.15877	0.693545									
Error	64057.06	48	0	1334.522				Error	200.6779	26	0	7.718381											
Total	252313	51	0					Total	221.5982	29	0												
Amplitude								**Rise Time**								**Fall Time**							
Source	Sum Sq.	d.f.	Singular?	Mean Sq.	F	Prob>F		Source	Sum Sq.	d.f.	Singular?	Mean Sq.	F	Prob>F		Source	Sum Sq.	d.f.	Singular?	Mean Sq.	F	Prob>F	
Regions	2.541325	27	0	0.094123	19.0281	9.51E-67		Regions	0.046164	27	0	0.00171	8.902053	8.16E-26		Regions	0.02999	27	0	0.001111	0.63296	0.923781	
Age	0.010029	1	0	0.010029	2.027531	0.154907		Age	0.000263	1	0	0.000263	1.366815	0.243211		Age	0.059369	1	0	0.059369	33.83169	1.43E-08	
Genotype	0.069969	1	0	0.069969	14.14505	0.000183		Genotype	0.000926	1	0	0.000926	4.823389	0.028778		Genotype	0.009272	1	0	0.009272	5.283655	0.022157	
Regions*Age	0.016681	27	0	0.000618	0.124902	1		Regions*Age	0.003198	27	0	0.000118	0.616645	0.934681		Regions*Age	0.04939	27	0	0.001829	1.042413	0.410106	
Regions*Genotype	0.052907	27	0	0.00196	0.396137	0.99764		Regions*Genotype	0.003349	27	0	0.000124	0.645763	0.914462		Regions*Genotype	0.028102	27	0	0.001041	0.593122	0.948512	
Age*Genotype	0.035839	1	0	0.035839	7.245175	0.007275		Age*Genotype	0.000468	1	0	0.000468	2.436634	0.119498		Age*Genotype	0.066395	1	0	0.066395	37.83541	2.25E-09	
Error	3.541718	716	0	0.004947				Error	0.062805	327	0	0.000192				Error	0.573831	327	0	0.001755			
Total	6.473815	800	0					Total	0.120842	411	0					Total	0.784392	411	0				

C57

Direction								**Speed**															
Source	Sum Sq.	d.f.	Singular?	Mean Sq.	F	Prob>F		Source	Sum Sq.	d.f.	Singular?	Mean Sq.	F	Prob>F									
Age	170220.8	1	0	170220.8	1255.809	3.08E-22		Age	15.63596	1	0	15.63596	2.638323	0.128301									
Error	3253.121	24	0	135.5467				Error	77.0442	13	0	5.926477											
Total	173474	25	0					Total	92.68016	14	0												
Amplitude								**Rise Time**								**Fall Time**							
Source	Sum Sq.	d.f.	Singular?	Mean Sq.	F	Prob>F		Source	Sum Sq.	d.f.	Singular?	Mean Sq.	F	Prob>F		Source	Sum Sq.	d.f.	Singular?	Mean Sq.	F	Prob>F	
Regions	2.094698	27	0	0.077581	12.18083	1.34E-34		Regions	0.016976	24	0	0.000707	2.518167	0.000281		Regions	0.037515	24	0	0.001563	0.949832	0.534634	
Age	0.103178	1	0	0.103178	16.19975	7.17E-05		Age	0.002074	1	0	0.002074	7.384403	0.007197		Age	0.00916	1	0	0.00916	5.565714	0.019347	
Regions*Age	0.101935	27	0	0.003775	0.592761	0.948482		Regions*Age	0.009757	24	0	0.000407	1.447319	0.090377		Regions*Age	0.037657	24	0	0.001569	0.953409	0.529839	
Error	1.974433	310	0	0.006369				Error	0.052526	187	0	0.000281				Error	0.307746	187	0	0.001646			
Total	4.253013	365	0					Total	0.086529	236	0					Total	0.400196	236	0				

Forelimb Stimulus: To identify disease associated changes in forelimb somatosensory cortex, 1mA - 1 ms electrical stimulation was applied to contralateral forepaw. Interestingly forelimb evoked cortical signal flow had a preferred direction towards midline and higher-order multimodal areas, more specifically parietal associational area (ptA). Additionally, secondary activation was observed in supplementary somatosensory area (fig 2.6A). A significant effect of age was observed in 5xFAD group for changes in direction, speed, amplitude, rise-time, and fall-time of activation, further a significant effect of genotype and interaction between age and genotype was observed for direction and amplitude of activation (see Table 2.5 5xFAD for detail statistics). A significant difference in the direction of propagation was observed in 12-month-old 5xFAD^{+} mice, further an increase in peak amplitude of activation and the speed of propagation was observed in 12-month-old 5xFAD^{+} mice, no changes were observed for rise-time in all groups (fig 2.6). For App group significant effect of age was observed in direction of propagation, amplitude, rise-time, and fall-time, further a significant effect of genotype was observed for amplitude of activation. There was significant interaction between age and genotype for direction, amplitude and fall time (see Table 2.5 App for detail statistics). A significant difference in direction, rise-time and fall-time of cortical activation was observed for 6- and 12-month-old *App*$^{+/+}$ mice, further evoked amplitude for 6-month-old *App*$^{+/+}$ mice is significantly less w.r.t. control however it significantly increases with age for both diseased and control mice (fig 2.7). For C57 group a significant effect of age was observed in amplitude, rise-time, and fall-time of cortical activation, there was a decrease in amplitude and rise-time with age and increase in fall-time with age (fig 2.8) (see Table 2.5 C57 for detail statistics).

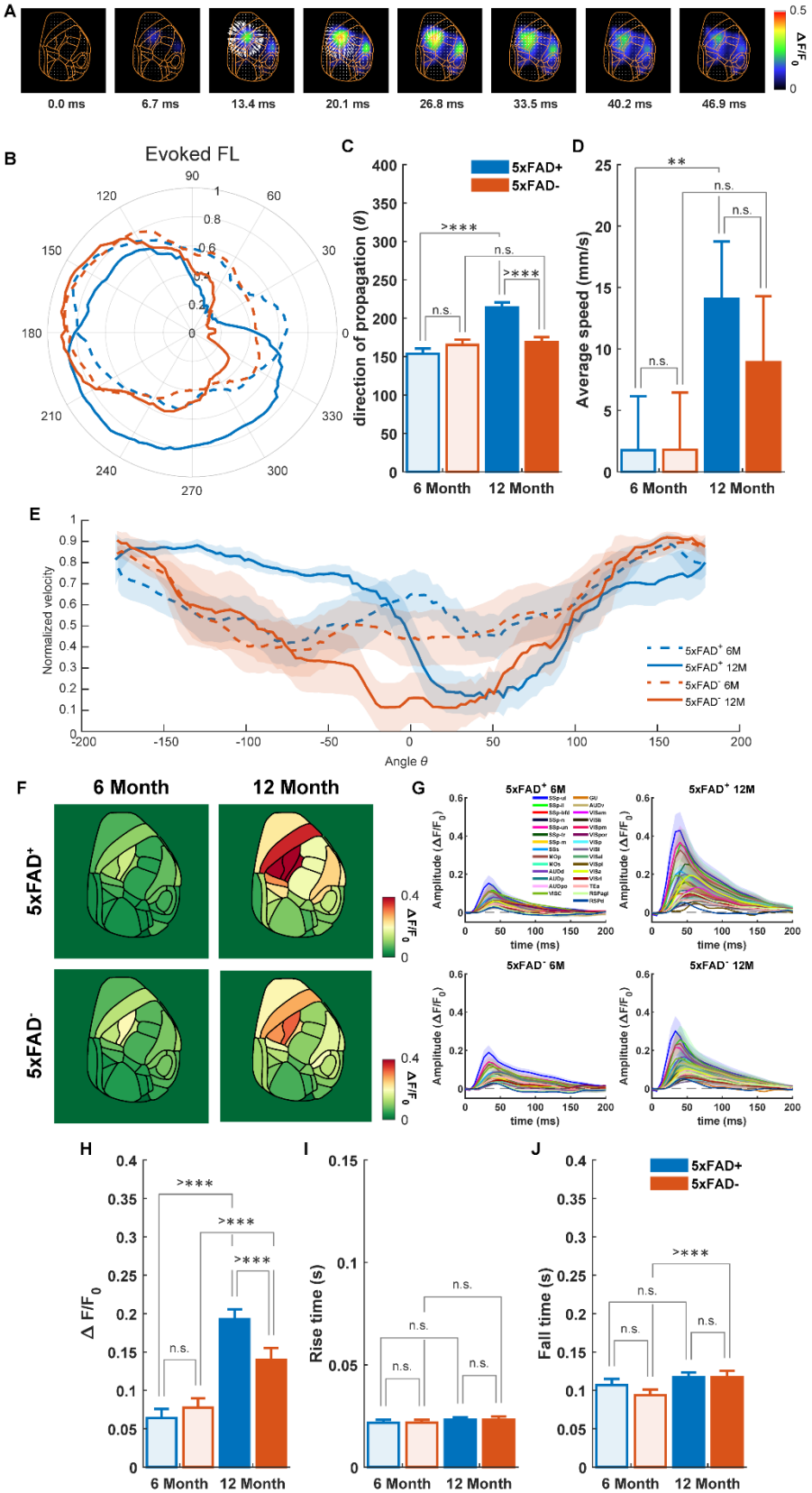

Figure 2.6: Forelimb stimulus evoked cortical dynamics for 5xFAD mice.
(A) Montage of representative forelimb stimulus (1mA, 1 ms) evoked cortical activity with overlaid velocity vector fields determined using Combined local-global (CLG) method for

optical flow analysis. (B) polar plot and (E) mean ± S.E.M. of normalized velocity with respect to the angle/direction of signal flow. (C-D) Direction and speed of forelimb evoked cortical signal propagation changes with age. (F) A spatial representation of region-wise peak amplitude of evoked cortical activations. (G) time series representation of evoked cortical activations in multiple regions of interest (ROIs) shown in fig 2.1A. (H) Peak amplitude of cortical activation increases with age in 5xFAD^{+} mice suggesting hyperactivity associated with disease progression. (I-J) No changes in rise-time of the signal was observed, however, fall-time increased with age. (6-month-old: 5xFAD^{+}, n = 9; 5xFAD^{-}, n = 8 and 12-month-old: 5xFAD^{+}, n = 7; 5xFAD^{-}, n = 6). * = $p < 0.05$; ** = $p < 0.01$; *** = $p < 0.001$; >*** = $p < 0.001$.

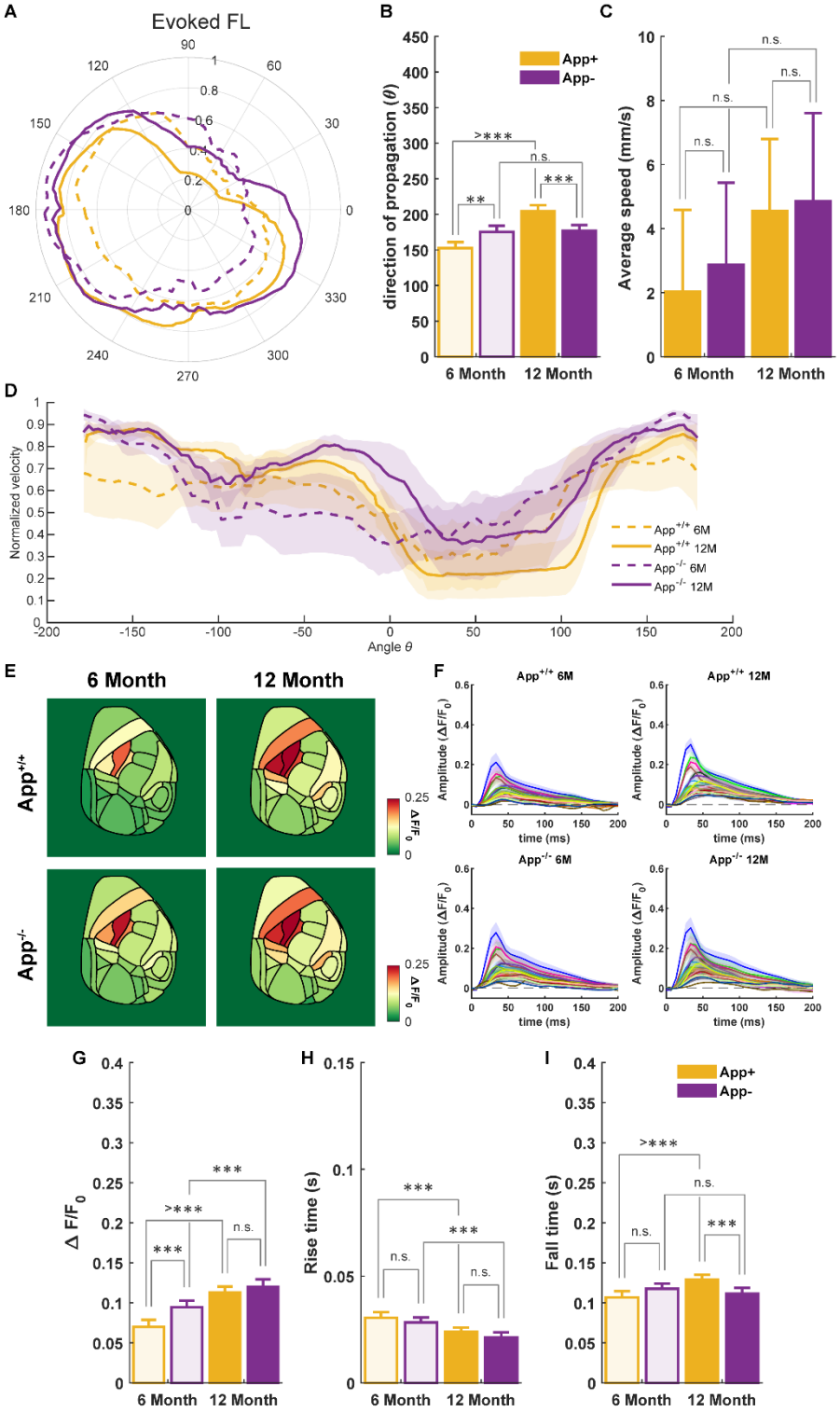

Figure 2.7: Forelimb stimulus evoked cortical dynamics for *App*$^{NL-G-F}$ mice.

(A) polar plot and (D) mean ± S.E.M. of normalized velocity with respect to the angle/direction of signal flow. (B-C) Direction of forelimb evoked cortical signal propagation changes with genotype and age, however, no effect genotype is observed on speed of propagation. (E) A spatial representation of region-wise peak amplitude of evoked cortical activations. (F) time series representation of evoked cortical activations in multiple regions of interest (ROIs) shown in fig 2.1A. (G) Peak amplitude of cortical activation in 6-month-old $App^{+/+}$ mice is significantly less w.r.t. control however it significantly increases with age for both diseased and control mice. (H-I) $App^{+/+}$ mice had reduced rise-time with age suggesting quick activation after stimulus onset, increased fall-time at 12 months suggest longer period of activation. (6-month-old: $App^{+/+}$, n = 7; $App^{-/-}$, n = 7 and $App^{+/+}$, n = 8; $App^{-/-}$, n = 6). * = $p < 0.05$; ** = $p < 0.01$; *** = $p < 0.001$; >*** = $p < 0.001$.

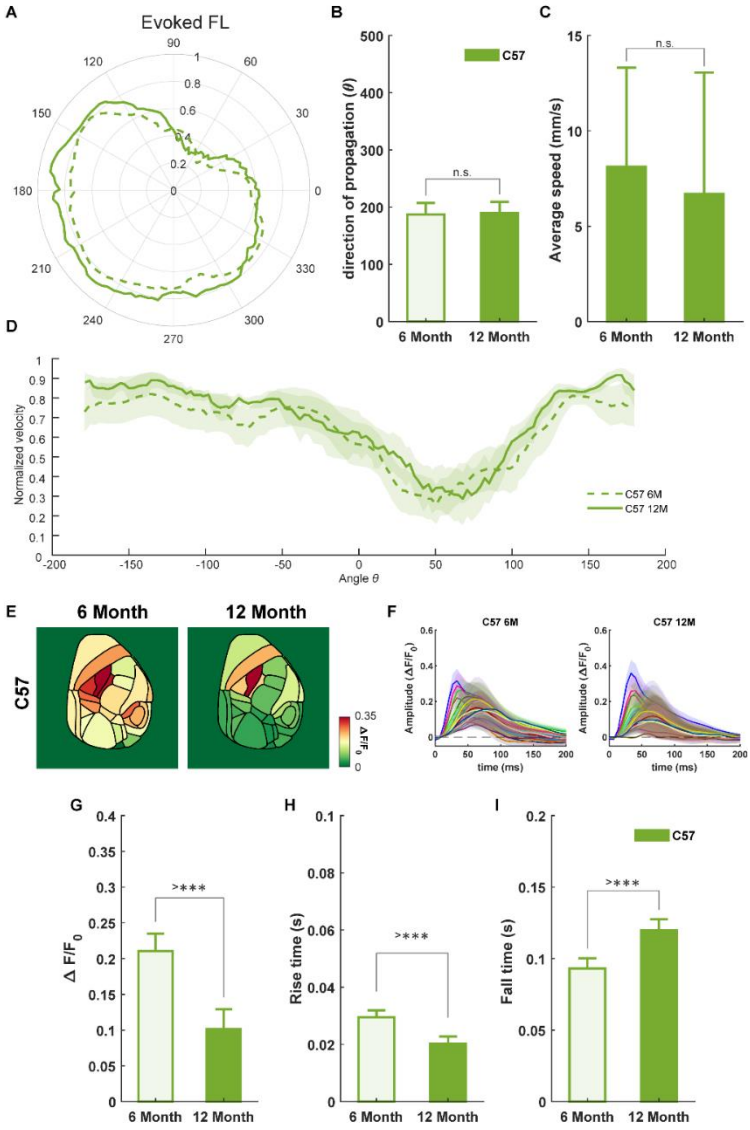

Figure 2.8: Forelimb stimulus evoked cortical dynamics for C57 mice.
(A) polar plot and (D) mean ± S.E.M. of normalized velocity with respect to the angle/direction of signal flow. (B-C) There no change in direction and speed of forelimb evoked cortical signal propagation with age. (E) A spatial representation of region-wise peak amplitude of evoked cortical activations. (F) time series representation of evoked cortical activations in multiple regions of interest (ROIs) shown in fig 2.1A. (G) Peak amplitude of cortical activation decreases with age in C57 mice. (H-I) C57 mice had reduced rise-time at 12 months age suggesting quick activation after stimulus onset, however, the fall-time increases suggesting prolonged activation. (6-month-old: C57BL/6J, n = 8 and 12-month-old: C57BL/6J, n = 6). * = $p < 0.05$; ** = $p < 0.01$; *** = $p < 0.001$; >*** = $p < 0.001$.

Table 2.5: ANOVA table for statistical comparison of direction of propagation, propagation speed, amplitude, rise time and fall time of Forelimb evoked cortical activations.

5xFAD

Direction								**Speed**															
Source	Sum Sq.	d.f.	Singular?	Mean Sq.	F	Prob>F		Source	Sum Sq.	d.f.	Singular?	Mean Sq.	F	Prob>F									
Age	13196.29	1	0	13196.29	87.47219	2.16E-12		Age	717.2309	1	0	717.2309	16.55095	0.000369									
Genotype	3627.429	1	0	3627.429	24.04458	1.12E-05		Genotype	49.82841	1	0	49.82841	1.149849	0.293072									
Age*Genotype	10428.52	1	0	10428.52	69.12594	7.41E-11		Age*Genotype	50.89652	1	0	50.89652	1.174497	0.288062									
Error	7241.408	48	0	150.8627				Error	1170.038	27	0	43.33474											
Total	34493.65	51	0					Total	2043.893	30	0												
Amplitude								**Rise Time**								**Fall Time**							
Source	Sum Sq.	d.f.	Singular?	Mean Sq.	F	Prob>F		Source	Sum Sq.	d.f.	Singular?	Mean Sq.	F	Prob>F		Source	Sum Sq.	d.f.	Singular?	Mean Sq.	F	Prob>F	
Regions	3.125046	27	0	0.115742	14.37344	5.41E-51		Regions	0.007713	27	0	0.000286	5.190988	7.61E-15		Regions	0.079245	27	0	0.002935	1.784712	0.009548	
Age	1.600885	1	0	1.600885	198.8054	4.75E-40		Age	0.000245	1	0	0.000245	4.443831	0.035522		Age	0.032359	1	0	0.032359	19.67659	1.13E-05	
Genotype	0.071939	1	0	0.071939	8.933766	0.002895		Genotype	1.25E-06	1	0	1.25E-06	0.022707	0.880282		Genotype	0.004631	1	0	0.004631	2.816018	0.093949	
Regions*Age	0.730368	27	0	0.027051	3.359278	3.27E-08		Regions*Age	0.001443	27	0	5.35E-05	0.971391	0.507725		Regions*Age	0.049648	27	0	0.001839	1.118146	0.312347	
Regions*Genotype	0.072838	27	0	0.002698	0.335012	0.999473		Regions*Genotype	0.002154	27	0	7.98E-05	1.449831	0.068523		Regions*Genotype	0.038877	27	0	0.00144	0.875573	0.648499	
Age*Genotype	0.213196	1	0	0.213196	26.47569	3.44E-07		Age*Genotype	1.33E-08	1	0	1.33E-08	0.000242	0.987593		Age*Genotype	0.00609	1	0	0.00609	3.703345	0.054867	
Error	5.805869	721	0	0.008053				Error	0.02768	503	0	5.5E-05				Error	0.827194	503	0	0.001645			
Total	12.08772	805	0					Total	0.040465	587	0					Total	1.053679	587	0				

App

Direction								**Speed**															
Source	Sum Sq.	d.f.	Singular?	Mean Sq.	F	Prob>F		Source	Sum Sq.	d.f.	Singular?	Mean Sq.	F	Prob>F									
Age	9132.091	1	0	9132.091	40.76439	6.46E-08		Age	35.74907	1	0	35.74907	3.133565	0.088892									
Genotype	76.6878	1	0	76.6878	0.342324	0.561232		Genotype	2.313633	1	0	2.313633	0.2028	0.656351									
Age*Genotype	8271.167	1	0	8271.167	36.92134	1.92E-07		Age*Genotype	0.51436	1	0	0.51436	0.045086	0.833568									
Error	10753.02	48	0	224.0213				Error	285.2109	25	0	11.40843											
Total	28232.97	51	0					Total	323.5028	28	0												
Amplitude								**Rise Time**								**Fall Time**							
Source	Sum Sq.	d.f.	Singular?	Mean Sq.	F	Prob>F		Source	Sum Sq.	d.f.	Singular?	Mean Sq.	F	Prob>F		Source	Sum Sq.	d.f.	Singular?	Mean Sq.	F	Prob>F	
Regions	1.923367	27	0	0.071236	22.40275	1.69E-76		Regions	0.024655	27	0	0.000913	4.639218	6.19E-13		Regions	0.080946	27	0	0.002998	1.724599	0.013616	
Age	0.20014	1	0	0.20014	62.9414	8.64E-15		Age	0.006369	1	0	0.006369	32.35552	2.06E-08		Age	0.009594	1	0	0.009594	5.518981	0.019154	
Genotype	0.042817	1	0	0.042817	13.46527	0.000262		Genotype	0.00073	1	0	0.00073	3.709332	0.05461		Genotype	0.00167	1	0	0.00167	0.960504	0.327479	
Regions*Age	0.075017	27	0	0.002778	0.873778	0.651556		Regions*Age	0.003976	27	0	0.000147	0.748202	0.818605		Regions*Age	0.021368	27	0	0.000791	0.455264	0.992441	
Regions*Genotype	0.006425	27	0	0.000238	0.07484	1		Regions*Genotype	0.004692	27	0	0.000174	0.882831	0.638076		Regions*Genotype	0.037355	27	0	0.001384	0.795868	0.759733	
Age*Genotype	0.014222	1	0	0.014222	4.472523	0.034803		Age*Genotype	1.08E-05	1	0	1.08E-05	0.054928	0.814785		Age*Genotype	0.030968	1	0	0.030968	17.81459	2.84E-05	
Error	2.187689	688	0	0.00318				Error	0.111407	566	0	0.000197				Error	0.983922	566	0	0.001738			
Total	4.508079	772	0					Total	0.151458	650	0					Total	1.172118	650	0				

C57

Direction								**Speed**															
Source	Sum Sq.	d.f.	Singular?	Mean Sq.	F	Prob>F		Source	Sum Sq.	d.f.	Singular?	Mean Sq.	F	Prob>F									
Age	32.63632	1	0	32.63632	0.025248	0.87508		Age	7.27114	1	0	7.27114	0.119433	0.735178									
Error	31023.2	24	0	1292.633				Error	791.4454	13	0	60.88041											
Total	31055.84	25	0					Total	798.7165	14	0												
Amplitude								**Rise Time**								**Fall Time**							
Source	Sum Sq.	d.f.	Singular?	Mean Sq.	F	Prob>F		Source	Sum Sq.	d.f.	Singular?	Mean Sq.	F	Prob>F		Source	Sum Sq.	d.f.	Singular?	Mean Sq.	F	Prob>F	
Regions	1.517862	27	0	0.056217	1.792064	0.010265		Regions	0.007608	27	0	0.000282	1.349192	0.121978		Regions	0.0213	27	0	0.000789	0.404358	0.996778	
Age	1.093848	1	0	1.093848	34.8692	8.61E-09		Age	0.006092	1	0	0.006092	29.16905	1.49E-07		Age	0.049408	1	0	0.049408	25.32502	9.03E-07	
Regions*Age	0.254137	27	0	0.009412	0.300047	0.999791		Regions*Age	0.006604	27	0	0.000245	1.171187	0.260935		Regions*Age	0.062265	27	0	0.002306	1.182045	0.250128	
Error	10.5717	337	0	0.03137				Error	0.054511	261	0	0.000209				Error	0.509199	261	0	0.001951			
Total	13.583	392	0					Total	0.075812	316	0					Total	0.642671	316	0				

Hindlimb Stimulus: To identify disease associated changes in hindlimb somatosensory cortex, 1mA - 1 ms electrical stimulation was applied to contralateral hindpaw. Interestingly hindlimb evoked cortical signal flow had a preferred direction towards midline and higher-order multimodal areas, more specifically parietal associational area (ptA). Additionally, secondary activation was observed in supplementary somatosensory area (fig 2.9A). A significant effect of age was observed in 5xFAD group for changes in direction, speed, amplitude, rise-time, and fall-time of activation, further a significant effect of genotype was observed for direction, amplitude of activation, rise-time and fall time. Significant interaction between age and genotype was observed for direction, amplitude, and rise-time (see Table 2.6 5xFAD for detail statistics). A significant difference in the direction of propagation was observed in 12-month-old 5xFAD^{+} mice, further an increase in peak amplitude of activation, fall-time and the speed of propagation was observed in 12-month-old 5xFAD^{+} mice, for 6-month 5xFAD^{+} mice the rise- and fall-time was significantly small suggesting quick activation and deactivation (fig 2.9). For App group significant effect of age was observed in direction of propagation, amplitude, and fall-time, further a significant effect of genotype was observed for direction and fall-time, no significant interaction between age and genotype was observed (see Table 2.6 App for detail statistics). A significant difference in direction of cortical activation was observed for 12-month-old mice, further there was significant increase in evoked amplitude for 12-month-old (fig 2.10). For C57 group a significant effect of age was observed in direction, amplitude, rise-time, and fall-time of cortical activation, there was a decrease in amplitude and rise-time with age and increase in fall-time with age (fig 2.11) (see Table 2.6 C57 for detail statistics).

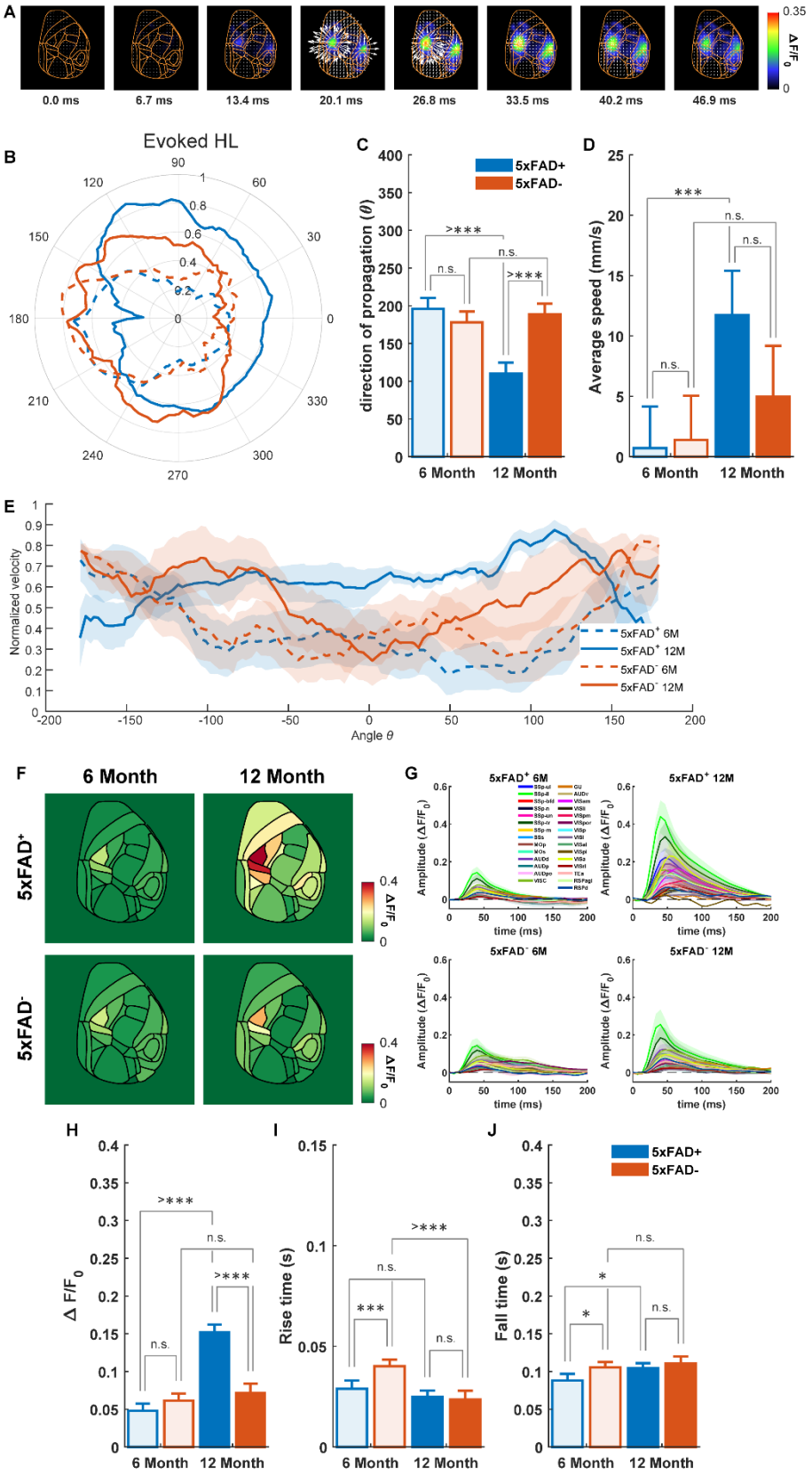

Figure 2.9:Hindlimb stimulus evoked cortical dynamics for 5xFAD mice.
(A) Montage of representative hindlimb stimulus (1mA, 1 ms) evoked cortical activity with overlaid velocity vector fields determined using Combined local-global (CLG) method for optical flow analysis. (B) polar plot and (E) mean ± S.E.M. of normalized velocity with respect to the angle/direction of signal flow. (C-D) Direction and speed of hindlimb evoked cortical signal propagation changes with age. (F) A spatial representation of region-wise peak amplitude

of evoked cortical activations. (G) time series representation of evoked cortical activations in multiple regions of interest (ROIs) shown in fig 2.1A. (H) Peak amplitude of cortical activation increases with age in 12-month-old 5xFAD^{+} mice suggesting hyperactivity associated with disease progression. (I-J) Rise- and fall-time was significantly small for 6-month 5xFAD^{+} mice the suggesting quick activation and deactivation. (6-month-old: 5xFAD^{+}, n = 9; 5xFAD^{-}, n = 8 and 12-month-old: 5xFAD^{+}, n = 7; 5xFAD^{-}, n = 6). * = $p < 0.05$; ** = $p < 0.01$; *** = $p < 0.001$; >*** = $p < 0.001$.

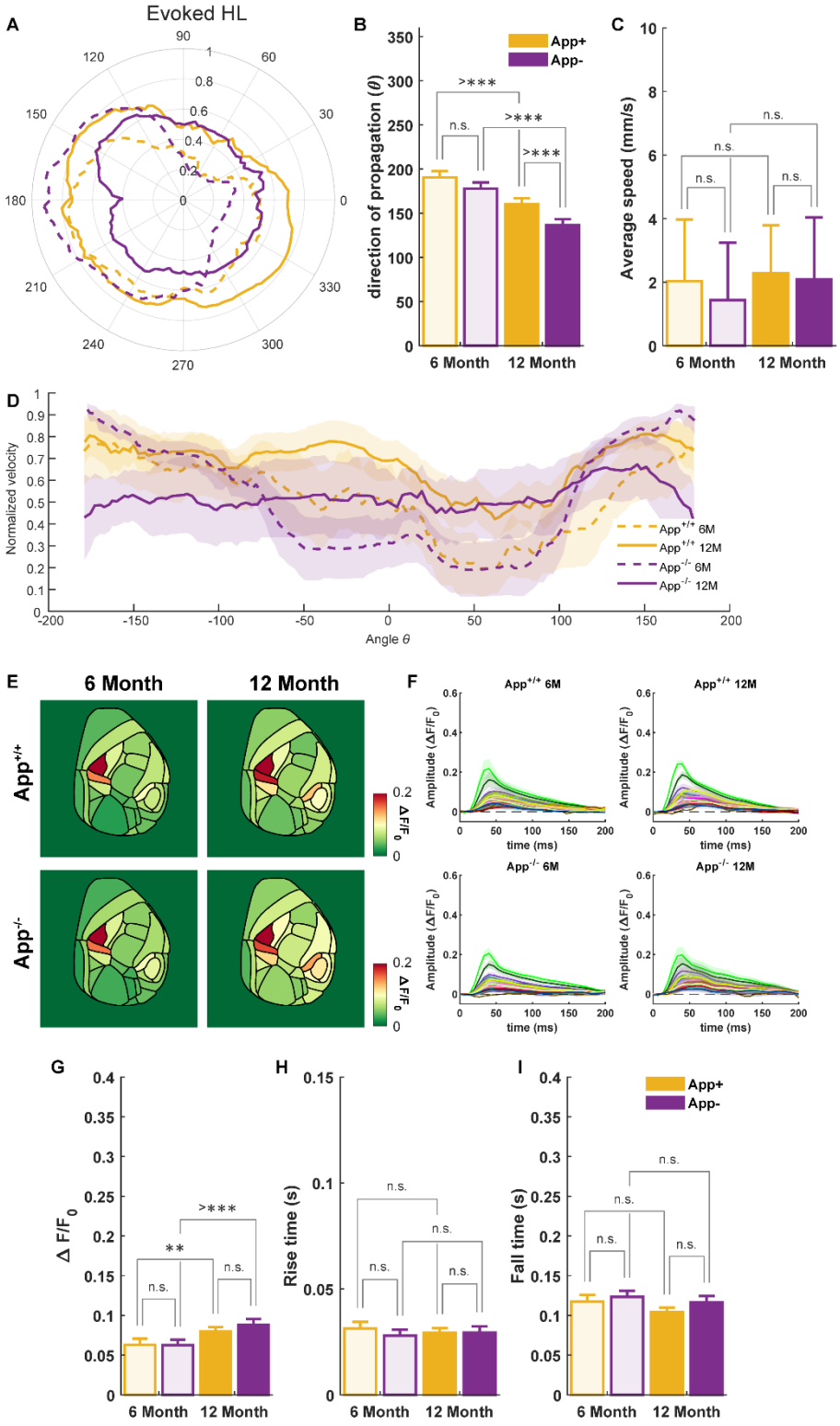

Figure 2.10: Hindlimb stimulus evoked cortical dynamics for *App*$^{NL-G-F}$ mice.

(A) polar plot and (D) mean ± S.E.M. of normalized velocity with respect to the angle/direction of signal flow. (B-C) Direction of hindlimb evoked cortical signal propagation changes with genotype and age, However, no effect on speed of propagation in observed. (E) A spatial representation of region-wise peak amplitude of evoked cortical activations. (F) time series representation of evoked cortical activations in multiple regions of interest (ROIs) shown in fig 2.1A. (G) Peak amplitude of cortical activation increases with age. (H-I) No significant change in rise- and fall- time is observed. (6-month-old: $App^{+/+}$, n = 7; $App^{-/-}$, n = 7 and $App^{+/+}$, n = 8; $App^{-/-}$, n = 6). * = $p < 0.05$; ** = $p < 0.01$; *** = $p < 0.001$; >*** = $p < 0.001$.

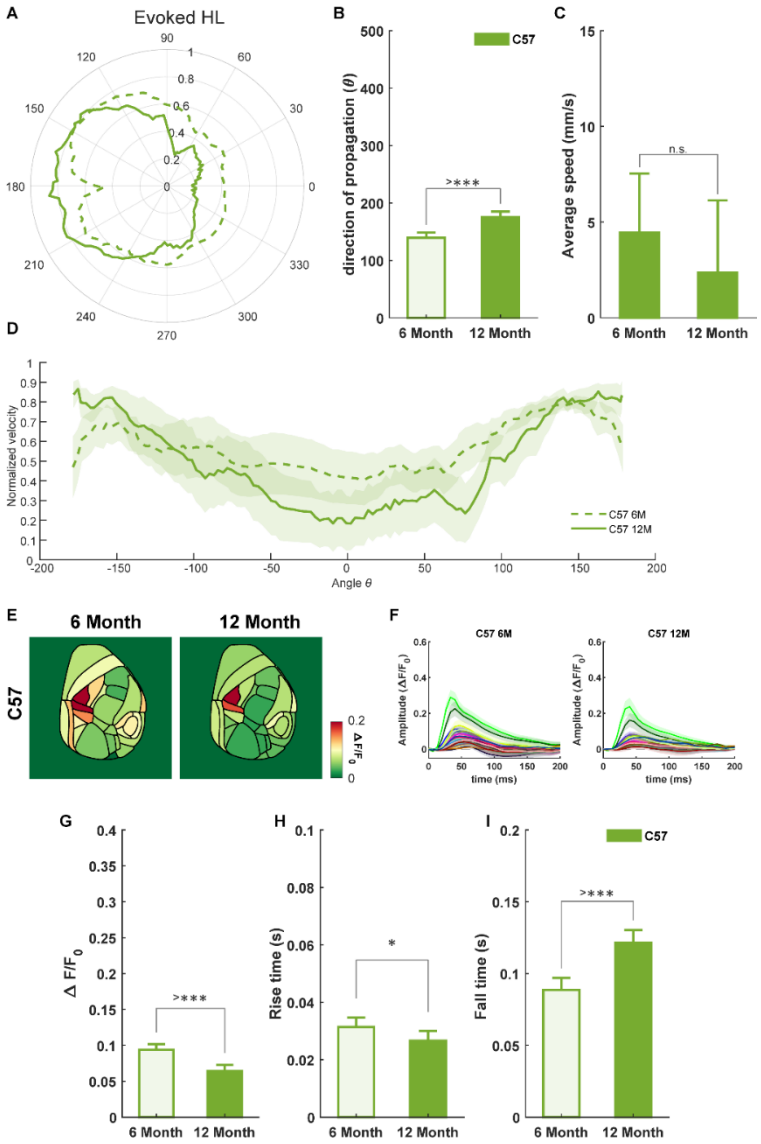

Figure 2.11: Hindlimb stimulus evoked cortical dynamics for C57 mice.
(A) polar plot and (D) mean ± S.E.M. of normalized velocity with respect to the angle/direction of signal flow. (B-C) Direction of hindlimb evoked cortical signal propagation changes with age, however, no significant effect on speed of propagation in observed. (E) A spatial representation of region-wise peak amplitude of evoked cortical activations. (F) time series representation of evoked cortical activations in multiple regions of interest (ROIs) shown in fig 2.1A. (G) Peak amplitude of cortical activation decreases with age in C57 mice. (H-I) C57 mice had reduced rise time at 12 months age suggesting quick activation after stimulus onset, however, the fall time increases suggesting prolonged activation. (6-month-old: C57BL/6J, n = 8 and 12-month-old: C57BL/6J, n = 6). * = $p < 0.05$; ** = $p < 0.01$; *** = $p < 0.001$; >*** = $p < 0.001$.

Table 2.6: ANOVA table for statistical comparison of direction of propagation, propagation speed, amplitude, rise time and fall time of hindlimb evoked cortical activations.

5xFAD

Direction								**Speed**															
Source	Sum Sq.	d.f.	Singular?	Mean Sq.	F	Prob>F		Source	Sum Sq.	d.f.	Singular?	Mean Sq.	F	Prob>F									
Age	18495.3	1	0	18495.3	27.16552	3.9E-06		Age	403.9019	1	0	403.9019	15.06554	0.000605									
Genotype	11788.8	1	0	11788.8	17.31515	0.00013		Genotype	70.01092	1	0	70.01092	2.611407	0.117724									
Age*Genotype	30146.37	1	0	30146.37	44.27838	2.49E-08		Age*Genotype	105.3078	1	0	105.3078	3.927979	0.057753									
Error	32680.19	48	0	680.8372				Error	723.8607	27	0	26.80966											
Total	93110.65	51	0					Total	1350.411	30	0												
Amplitude								**Rise Time**								**Fall Time**							
Source	Sum Sq.	d.f.	Singular?	Mean Sq.	F	Prob>F		Source	Sum Sq.	d.f.	Singular?	Mean Sq.	F	Prob>F		Source	Sum Sq.	d.f.	Singular?	Mean Sq.	F	Prob>F	
Regions	2.149678	27	0	0.079618	15.82593	4.2E-56		Regions	0.028092	27	0	0.00104	3.069265	8.06E-07		Regions	0.060608	27	0	0.002245	1.446931	0.071019	
Age	0.573802	1	0	0.573802	114.057	8.1E-25		Age	0.009692	1	0	0.009692	28.59026	1.47E-07		Age	0.010483	1	0	0.010483	6.757408	0.009666	
Genotype	0.209481	1	0	0.209481	41.63934	2.01E-10		Genotype	0.002367	1	0	0.002367	6.982317	0.008541		Genotype	0.01363	1	0	0.01363	8.785793	0.00321	
Regions*Age	0.646823	27	0	0.023956	4.761909	9.52E-14		Regions*Age	0.008963	27	0	0.000332	0.979267	0.49671		Regions*Age	0.035021	27	0	0.001297	0.836082	0.704371	
Regions*Genotype	0.117187	27	0	0.00434	0.862728	0.667687		Regions*Genotype	0.010381	27	0	0.000384	1.134216	0.295287		Regions*Genotype	0.021542	27	0	0.000798	0.514299	0.980607	
Age*Genotype	0.419268	1	0	0.419268	83.33953	6.84E-19		Age*Genotype	0.004109	1	0	0.004109	12.12114	0.000551		Age*Genotype	0.003304	1	0	0.003304	2.129844	0.145206	
Error	3.627234	721	0	0.005031				Error	0.141699	418	0	0.000339				Error	0.648473	418	0	0.001551			
Total	7.973331	805	0					Total	0.212904	502	0					Total	0.779165	502	0				

App

Direction								**Speed**															
Source	Sum Sq.	d.f.	Singular?	Mean Sq.	F	Prob>F		Source	Sum Sq.	d.f.	Singular?	Mean Sq.	F	Prob>F									
Age	16803.93	1	0	16803.93	109.8604	5.31E-14		Age	1.420706	1	0	1.420706	0.249743	0.621626									
Genotype	4338.25	1	0	4338.25	28.36253	2.64E-06		Genotype	1.04601	1	0	1.04601	0.183876	0.671735									
Age*Genotype	388.8049	1	0	388.8049	2.541921	0.117424		Age*Genotype	0.274967	1	0	0.274967	0.048336	0.82777									
Error	7341.941	48	0	152.9571				Error	142.2166	25	0	5.688664											
Total	28872.92	51	0					Total	145.2478	28	0												
Amplitude								**Rise Time**								**Fall Time**							
Source	Sum Sq.	d.f.	Singular?	Mean Sq.	F	Prob>F		Source	Sum Sq.	d.f.	Singular?	Mean Sq.	F	Prob>F		Source	Sum Sq.	d.f.	Singular?	Mean Sq.	F	Prob>F	
Regions	1.22905	27	0	0.04552	21.62514	3.25E-74		Regions	0.031449	27	0	0.001165	5.648675	1.82E-16		Regions	0.085141	27	0	0.003153	1.962985	0.002985	
Age	0.074275	1	0	0.074275	35.28533	4.52E-09		Age	6.66E-06	1	0	6.66E-06	0.032303	0.857441		Age	0.010621	1	0	0.010621	6.611907	0.010429	
Genotype	0.002657	1	0	0.002657	1.262483	0.261572		Genotype	0.000273	1	0	0.000273	1.323132	0.250602		Genotype	0.008314	1	0	0.008314	5.175456	0.023347	
Regions*Age	0.018542	27	0	0.000687	0.326243	0.999587		Regions*Age	0.006616	27	0	0.000245	1.18842	0.237258		Regions*Age	0.033675	27	0	0.001247	0.776393	0.784063	
Regions*Genotype	0.014838	27	0	0.00055	0.261082	0.999954		Regions*Genotype	0.003368	27	0	0.000125	0.604877	0.943286		Regions*Genotype	0.032215	27	0	0.001193	0.742731	0.824262	
Age*Genotype	0.003385	1	0	0.003385	1.607947	0.205208		Age*Genotype	0.000411	1	0	0.000411	1.993734	0.158598		Age*Genotype	0.001299	1	0	0.001299	0.808547	0.369	
Error	1.452432	690	0	0.002105				Error	0.099183	481	0	0.000206				Error	0.772687	481	0	0.001606			
Total	2.841573	774	0					Total	0.146366	565	0					Total	0.957038	565	0				

C57

Direction								**Speed**															
Source	Sum Sq.	d.f.	Singular?	Mean Sq.	F	Prob>F		Source	Sum Sq.	d.f.	Singular?	Mean Sq.	F	Prob>F									
Age	8587.643	1	0	8587.643	29.12228	1.53E-05		Age	15.82549	1	0	15.82549	0.738138	0.405822									
Error	7077.172	24	0	294.8822				Error	278.7166	13	0	21.43974											
Total	15664.81	25	0					Total	294.5421	14	0												
Amplitude								**Rise Time**								**Fall Time**							
Source	Sum Sq.	d.f.	Singular?	Mean Sq.	F	Prob>F		Source	Sum Sq.	d.f.	Singular?	Mean Sq.	F	Prob>F		Source	Sum Sq.	d.f.	Singular?	Mean Sq.	F	Prob>F	
Regions	1.018781	27	0	0.037733	12.43529	3.05E-36		Regions	0.023766	26	0	0.000914	3.2928	1.11E-06		Regions	0.052207	26	0	0.002008	1.085531	0.361056	
Age	0.080706	1	0	0.080706	26.59788	4.28E-07		Age	0.001165	1	0	0.001165	4.195724	0.041852		Age	0.054366	1	0	0.054366	29.39106	1.72E-07	
Regions*Age	0.040713	27	0	0.001508	0.496939	0.984525		Regions*Age	0.00699	26	0	0.000269	0.968418	0.512884		Regions*Age	0.077972	26	0	0.002999	1.621266	0.035129	
Error	1.022565	337	0	0.003034				Error	0.054687	197	0	0.000278				Error	0.364401	197	0	0.00185			
Total	2.263485	392	0					Total	0.091317	250	0					Total	0.552072	250	0				

Whisker Stimulus: To identify disease associated changes in barrel cortex, 1 ms stimulation was applied to contralateral C2 whisker using a piezoelectric device. Interestingly whisker evoked cortical signal flow had a preferred direction towards midline and higher-order multimodal areas, more specifically parietal associational area (ptA). Additionally, secondary activation was observed in supplementary somatosensory area and auditory areas (fig 2.12A). The auditory activation could also be due to slight click sound produced when the piezoelectric device moves. An increased auditory activation was observed in 5xFAD mice, which could be due to hypersensitivity to auditory stimulus. A significant effect of age was observed in 5xFAD group for changes in direction, speed, amplitude, and rise-time of activation, further a significant effect of genotype was observed for direction, amplitude of activation and rise-time. Significant interaction between age and genotype was observed for direction, amplitude, and fall-time (see Table 2.7 5xFAD for detail statistics). A significant difference in the direction of propagation was observed in 12-month-old $5xFAD^{+}$ mice, further an increase in peak amplitude of activation, rise-time and fall-time was observed in 12-month-old $5xFAD^{+}$ mice (fig 2.12). For App group significant effect of age was observed in direction of propagation and amplitude further a significant effect of genotype was observed for speed and amplitude, significant interaction between age and genotype was observed for amplitude and fall-time (see Table 2.7 App for detail statistics). A significant increase in amplitude of cortical activation was observed for 6-month-old $App^{+/+}$ mice, further there was significant decrease in fall-time for 12-month-old $App^{+/+}$ mice (fig 2.13). For C57 group a significant effect of age was observed in amplitude of cortical activation, there was a decrease in amplitude with age (fig 2.14) (see Table 2.7 C57 for detail statistics).

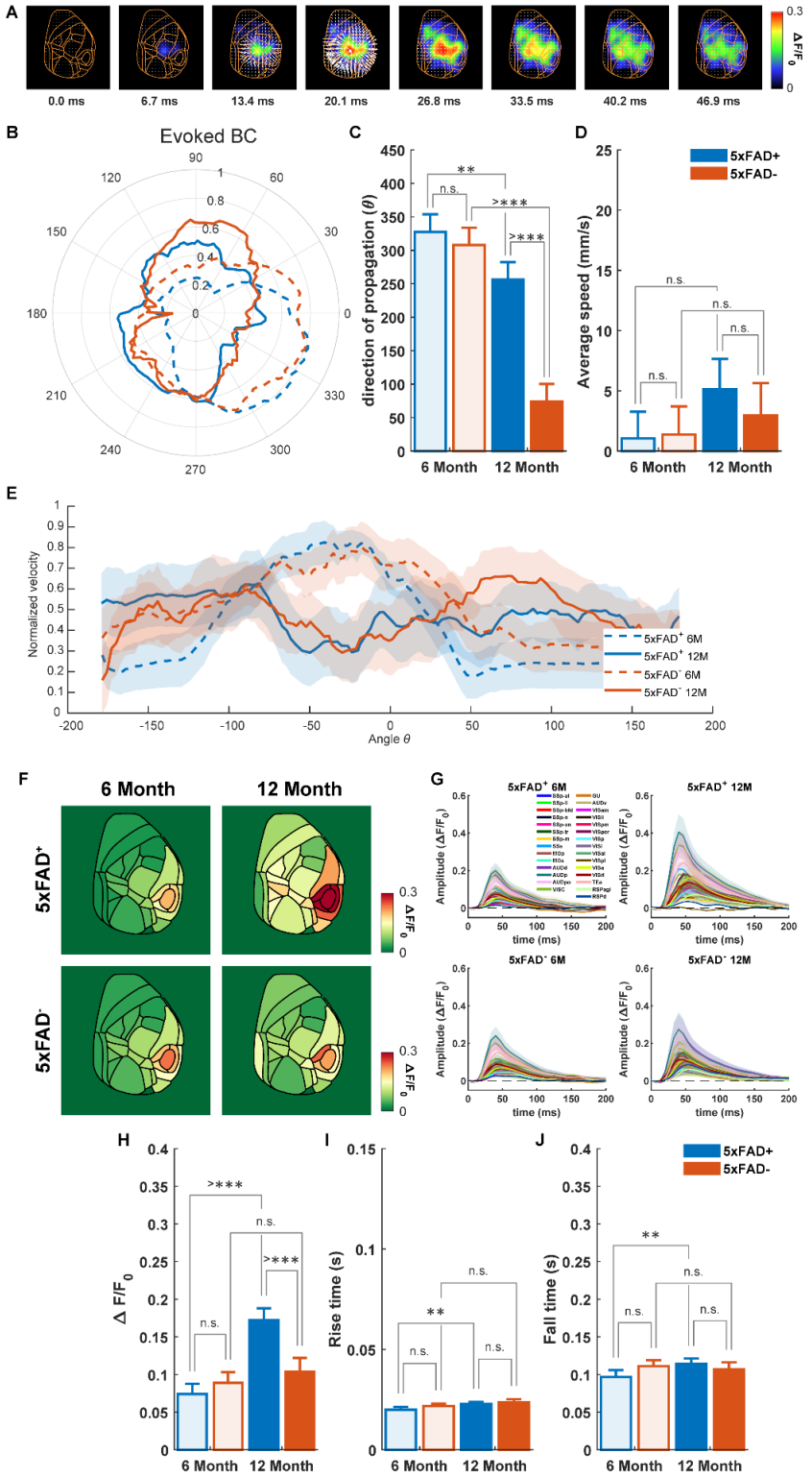

Figure 2.12: Whisker stimulus evoked cortical dynamics for 5xFAD mice.
(A) Montage of representative whisker stimulus (1 ms) evoked cortical activity with overlaid velocity vector fields determined using Combined local-global (CLG) method for optical flow analysis. (B) polar plot and (E) mean ± S.E.M. of normalized velocity with respect to the angle/direction of signal flow. (C-D) Direction and speed of whisker evoked cortical signal propagation changes with age. (F) A spatial representation of region-wise peak amplitude of evoked cortical activations. (G) time series representation of evoked cortical activations in multiple regions of interest (ROIs) shown in fig 2.1A. (H) Peak amplitude of cortical activation increases with age in 5xFAD^{+} mice suggesting hyperactivity associated with disease

progression. (I-J) There is a significant increase in rise-time and fall-time with age in 5xFAD^{+} mice. (6-month-old: 5xFAD^{+}, n = 8; 5xFAD^{-}, n = 8 and 12-month-old: 5xFAD^{+}, n = 7; 5xFAD^{-}, n = 6). * = $p < 0.05$; ** = $p < 0.01$; *** = $p < 0.001$; >*** = $p < 0.001$.

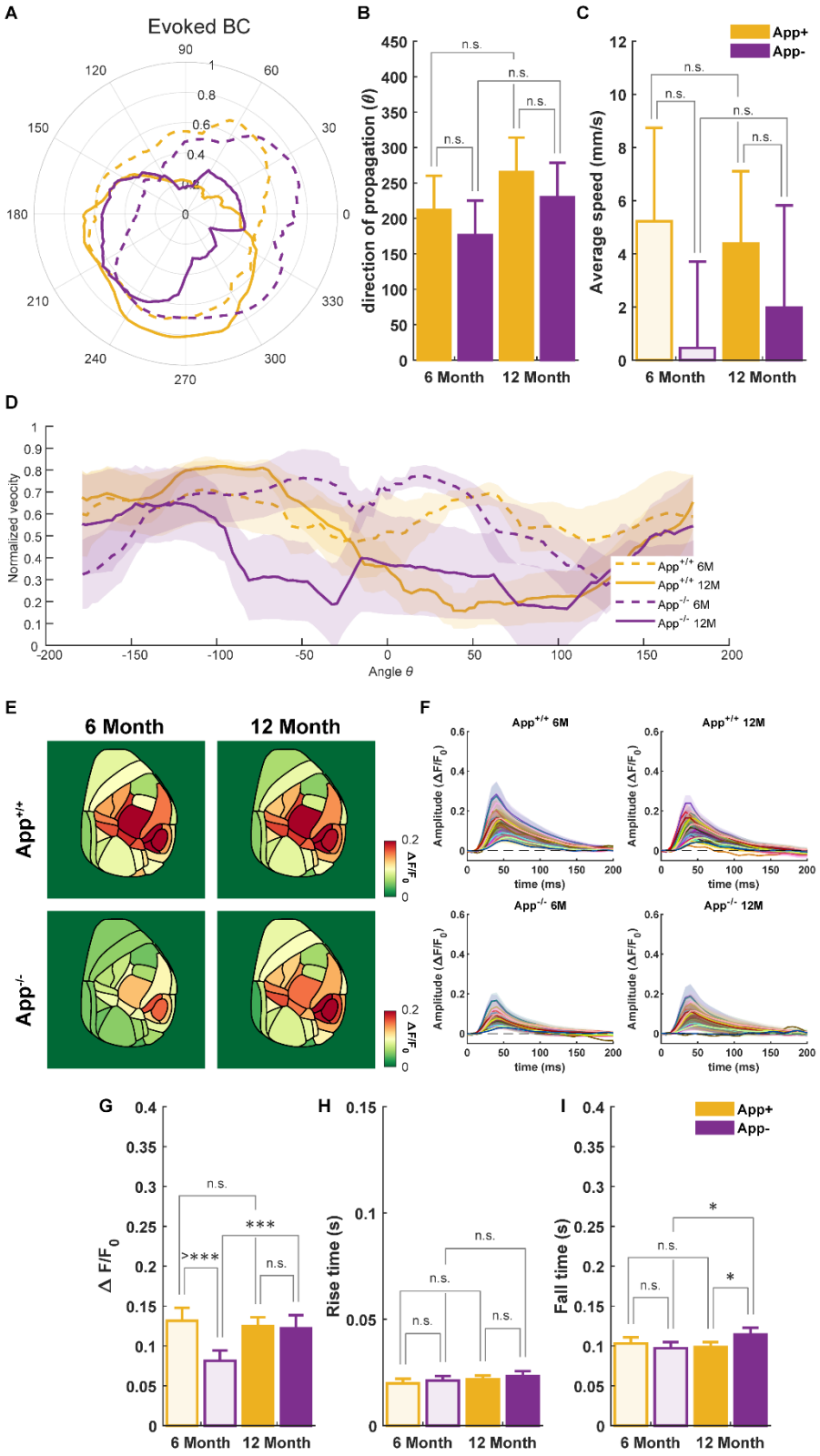

Figure 2.13: Whisker stimulus evoked cortical dynamics for *App*$^{NL-G-F}$ mice.
(A) polar plot and (D) mean ± S.E.M. of normalized velocity with respect to the angle/direction of signal flow. (B-C) No significant changes are observed in direction and speed of whisker evoked cortical signal propagation. (E) A spatial representation of region-wise peak amplitude

of evoked cortical activations. (F) time series representation of evoked cortical activations in multiple regions of interest (ROIs) shown in fig 2.1A. (G) Peak amplitude of cortical activation is significantly increased in 6-month-old $App^{+/+}$ mice compared to control. (H-I) 12-month-old $App^{+/+}$ mice had reduced fall-time suggesting short period of activation. (6-month-old: $App^{+/+}$, n = 7; $App^{-/-}$, n = 7 and $App^{+/+}$, n = 7; $App^{-/-}$, n = 6). * = $p < 0.05$; ** = $p < 0.01$; *** = $p < 0.001$; >*** = $p < 0.001$.

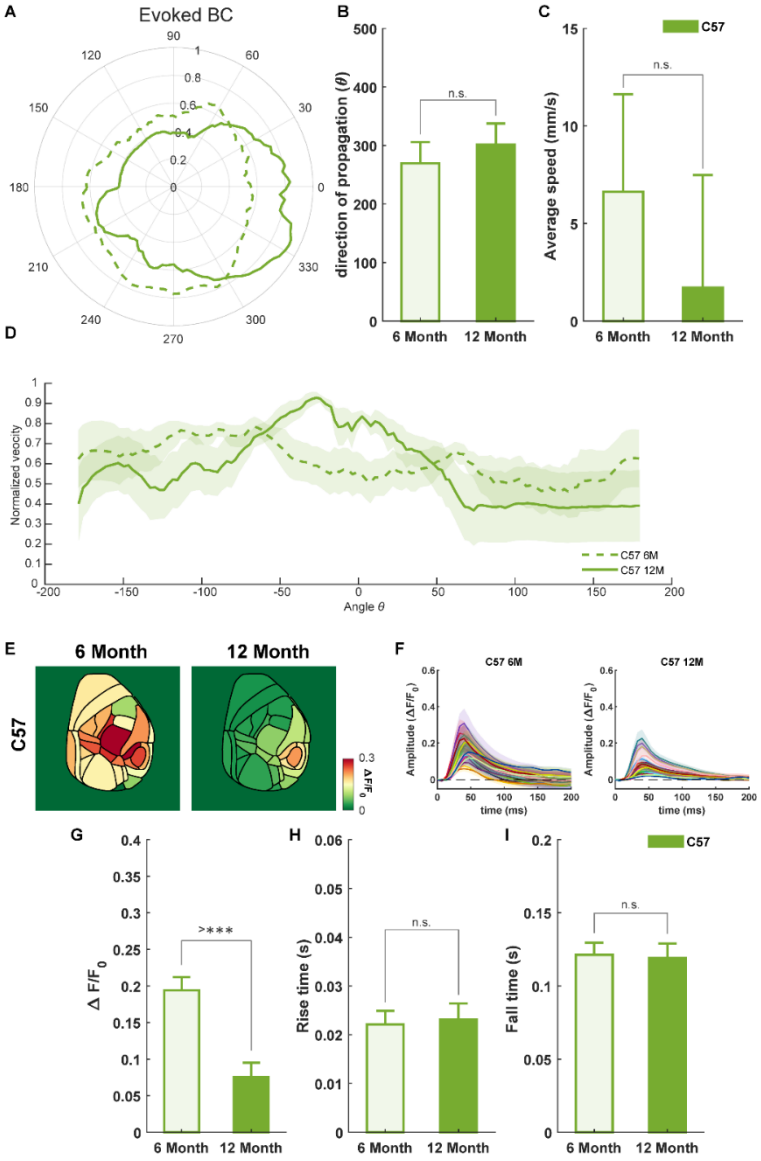

Figure 2.14: Whisker stimulus evoked cortical dynamics for C57 mice.
(A) polar plot and (D) mean ± S.E.M. of normalized velocity with respect to the angle/direction of signal flow. (B-C) There is no change in direction and speed of whisker evoked cortical signal propagation with age. (E) A spatial representation of region-wise peak amplitude of evoked cortical activations. (F) time series representation of evoked cortical activations in multiple regions of interest (ROIs) shown in fig 2.1A. (G) Peak amplitude of cortical activation decreases with age in C57 mice. (H-I) No change in rise-time or fall-time is observed in C57 mice. (6-month-old: C57BL/6J, n = 8 and 12-month-old: C57BL/6J, n = 5). * = $p < 0.05$; ** = $p < 0.01$; *** = $p < 0.001$; >*** = $p < 0.001$.

Table 2.7: ANOVA table for statistical comparison of direction of propagation, propagation speed, amplitude, rise time and fall time of whisker evoked cortical activations.

5xFAD

Direction								**Speed**															
Source	Sum Sq.	d.f.	Singular?	Mean Sq.	F	Prob>F		Source	Sum Sq.	d.f.	Singular?	Mean Sq.	F	Prob>F									
Age	302638.6	1	0	302638.6	135.4896	1.4E-15		Age	58.97561	1	0	58.97561	5.416863	0.027997									
Genotype	132522.2	1	0	132522.2	59.32945	6.22E-10		Genotype	6.612958	1	0	6.612958	0.607395	0.442807									
Age*Genotype	85707.23	1	0	85707.23	38.37064	1.26E-07		Age*Genotype	11.67818	1	0	11.67818	1.072631	0.309889									
Error	107216	48	0	2233.667				Error	283.0727	26	0	10.88741											
Total	628084	51	0					Total	362.5605	29	0												
Amplitude								**Rise Time**								**Fall Time**							
Source	Sum Sq.	d.f.	Singular?	Mean Sq.	F	Prob>F		Source	Sum Sq.	d.f.	Singular?	Mean Sq.	F	Prob>F		Source	Sum Sq.	d.f.	Singular?	Mean Sq.	F	Prob>F	
Regions	2.835255	27	0	0.105009	9.770873	1.26E-33		Regions	0.005373	27	0	0.000199	5.253916	1.13E-14		Regions	0.019727	27	0	0.000731	0.451718	0.992673	
Age	0.548048	1	0	0.548048	50.9945	2.34E-12		Age	0.000476	1	0	0.000476	12.56838	0.000437		Age	0.004045	1	0	0.004045	2.500594	0.114562	
Genotype	0.127803	1	0	0.127803	11.89176	0.000598		Genotype	0.000166	1	0	0.000166	4.386641	0.036825		Genotype	0.000965	1	0	0.000965	0.596344	0.440414	
Regions*Age	0.100909	27	0	0.003737	0.347754	0.999254		Regions*Age	0.001218	27	0	4.51E-05	1.190867	0.236125		Regions*Age	0.039047	27	0	0.001446	0.894107	0.621194	
Regions*Genotype	0.064023	27	0	0.002371	0.220637	0.999992		Regions*Genotype	0.001116	27	0	4.13E-05	1.091518	0.34555		Regions*Genotype	0.037428	27	0	0.001386	0.857044	0.674808	
Age*Genotype	0.325005	1	0	0.325005	30.24091	5.36E-08		Age*Genotype	1.97E-05	1	0	1.97E-05	0.519406	0.471499		Age*Genotype	0.013333	1	0	0.013333	8.243073	0.004299	
Error	7.480045	696	0	0.010747				Error	0.015793	417	0	3.79E-05				Error	0.674478	417	0	0.001617			
Total	11.67056	780	0					Total	0.025416	501	0					Total	0.790816	501	0				

App

Direction								**Speed**															
Source	Sum Sq.	d.f.	Singular?	Mean Sq.	F	Prob>F		Source	Sum Sq.	d.f.	Singular?	Mean Sq.	F	Prob>F									
Age	37401.95	1	0	37401.95	4.904785	0.031563		Age	0.738345	1	0	0.738345	0.039856	0.843444									
Genotype	16063.09	1	0	16063.09	2.106468	0.153182		Genotype	84.75504	1	0	84.75504	4.575107	0.042819									
Age*Genotype	0.28487	1	0	0.28487	3.74E-05	0.995149		Age*Genotype	9.102835	1	0	9.102835	0.491374	0.490056									
Error	366029	48	0	7625.605				Error	444.6062	24	0	18.52526											
Total	419494.3	51	0					Total	543.534	27	0												
Amplitude								**Rise Time**								**Fall Time**							
Source	Sum Sq.	d.f.	Singular?	Mean Sq.	F	Prob>F		Source	Sum Sq.	d.f.	Singular?	Mean Sq.	F	Prob>F		Source	Sum Sq.	d.f.	Singular?	Mean Sq.	F	Prob>F	
Regions	1.419675	27	0	0.052581	6.764528	1.24E-21		Regions	0.011052	27	0	0.000409	3.086954	5.75E-07		Regions	0.027946	27	0	0.001035	0.622365	0.932494	
Age	0.041955	1	0	0.041955	5.39749	0.020467		Age	0.000497	1	0	0.000497	3.74939	0.053417		Age	0.004771	1	0	0.004771	2.868936	0.090957	
Genotype	0.098502	1	0	0.098502	12.67231	0.000398		Genotype	0.00022	1	0	0.00022	1.658712	0.198402		Genotype	0.002889	1	0	0.002889	1.737419	0.188099	
Regions*Age	0.021803	27	0	0.000808	0.103887	1		Regions*Age	0.002557	27	0	9.47E-05	0.714296	0.855059		Regions*Age	0.024502	27	0	0.000907	0.54565	0.970987	
Regions*Genotype	0.060717	27	0	0.002249	0.289306	0.999869		Regions*Genotype	0.002901	27	0	0.000107	0.810239	0.740152		Regions*Genotype	0.019929	27	0	0.000738	0.443828	0.993719	
Age*Genotype	0.096318	1	0	0.096318	12.39138	0.000461		Age*Genotype	1.07E-07	1	0	1.07E-07	0.000803	0.977398		Age*Genotype	0.014148	1	0	0.014148	8.50733	0.003704	
Error	5.153487	663	0	0.007773				Error	0.063252	477	0	0.000133				Error	0.793296	477	0	0.001663			
Total	7.090515	747	0					Total	0.081434	561	0					Total	0.892772	561	0				

C57

Direction								**Speed**															
Source	Sum Sq.	d.f.	Singular?	Mean Sq.	F	Prob>F		Source	Sum Sq.	d.f.	Singular?	Mean Sq.	F	Prob>F									
Age	6569.516	1	0	6569.516	1.526069	0.22866		Age	82.66397	1	0	82.66397	1.652995	0.222809									
Error	103316.7	24	0	4304.863				Error	600.1032	12	0	50.0086											
Total	109886.2	25	0					Total	682.7672	13	0												
Amplitude								**Rise Time**								**Fall Time**							
Source	Sum Sq.	d.f.	Singular?	Mean Sq.	F	Prob>F		Source	Sum Sq.	d.f.	Singular?	Mean Sq.	F	Prob>F		Source	Sum Sq.	d.f.	Singular?	Mean Sq.	F	Prob>F	
Regions	0.847627	27	0	0.031394	2.037563	0.002214		Regions	0.00556	24	0	0.000232	1.056881	0.396838		Regions	0.049895	24	0	0.002079	1.035992	0.422411	
Age	1.222172	1	0	1.222172	79.3236	4.45E-17		Age	4.71E-05	1	0	4.71E-05	0.214811	0.643534		Age	0.000224	1	0	0.000224	0.111593	0.738693	
Regions*Age	0.331824	27	0	0.01229	0.797653	0.754975		Regions*Age	0.003799	24	0	0.000158	0.722282	0.825398		Regions*Age	0.053259	24	0	0.002219	1.105849	0.340124	
Error	4.807115	312	0	0.015407				Error	0.043178	197	0	0.000219				Error	0.395326	197	0	0.002007			
Total	7.407129	367	0					Total	0.052633	246	0					Total	0.520045	246	0				

Visual Stimulus: To identify disease associated changes in visual cortex, 1 ms green light visual stimulation was given to contralateral eye. Interestingly visual evoked cortical signal flow had a preferred direction towards higher-order multimodal areas, more specifically parietal associational area (ptA) and lateral visual areas (fig 2.15A). A significant effect of age was observed in 5xFAD group for changes in direction, amplitude, and fall-time of activation, further a significant effect of genotype was observed for amplitude of activation and fall-time. Significant interaction between age and genotype was observed for direction, amplitude, and rise-time (see Table 2.8 5xFAD for detail statistics). A significant difference in the direction of propagation was observed in 6- and 12-month-old $5xFAD^{+}$ mice, further an increase in peak amplitude of activation was observed in 12-month-old $5xFAD^{+}$ mice (fig 2.15). For App group significant effect of age was observed in direction of propagation, amplitude, rise-time, and fall-time, further a significant effect of genotype was observed for direction of propagation, amplitude, rise-time, and fall-time, significant interaction between age and genotype was observed for direction and fall-time (see Table 2.8 App for detail statistics). A significant increase in amplitude of cortical activation was observed for 12-month-old $App^{+/+}$ mice, further there was significant decrease in fall-time for 6- and 12-month-old $App^{+/+}$ mice and an increase in fall time of 12-month-old $App^{+/+}$ mice suggesting prolonged activations (fig 2.16). For C57 group a significant effect of age was observed in amplitude and fall-time of cortical activation, there was a decrease in amplitude and increase in fall-time with age (fig 2.17) (see Table 2.8 C57 for detail statistics).

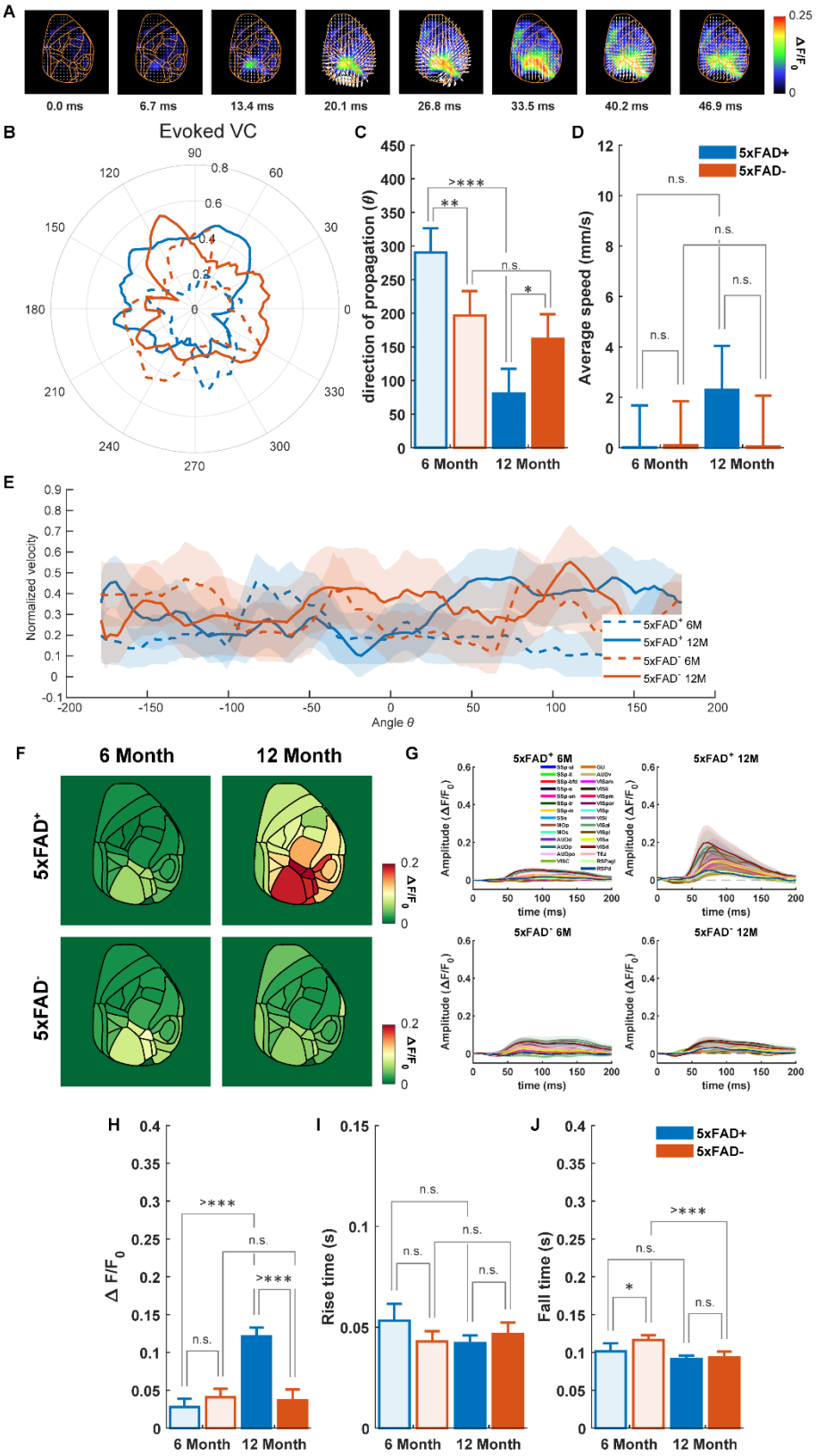

Figure 2.15: Visual stimulus evoked cortical dynamics for 5xFAD mice.
(A) Montage of representative visual stimulus (1 ms) evoked cortical activity with overlaid velocity vector fields determined using Combined local-global (CLG) method for optical flow analysis. (B) polar plot and (E) mean ± S.E.M. of normalized velocity with respect to the angle/direction of signal flow. (C-D) Direction of visual evoked cortical signal propagation changes with age and there is significant interaction between age and genotype. (F) A spatial representation of region-wise peak amplitude of evoked cortical activations. (G) time series

representation of evoked cortical activations in multiple regions of interest (ROIs) shown in fig 2.1A. (H) Peak amplitude of cortical activation increases with age in 5xFAD^{+} mice suggesting hyperactivity associated with disease progression. (I-J) fall-time is significantly reduced in 6-month-old 5xFAD^{-} mice suggesting short duration of activation. (6-month-old: 5xFAD^{+}, n = 9; 5xFAD^{-}, n = 8 and 12-month-old: 5xFAD^{+}, n = 7; 5xFAD^{-}, n = 6). * = $p < 0.05$; ** = $p < 0.01$; *** = $p < 0.001$; >*** = $p < 0.001$.

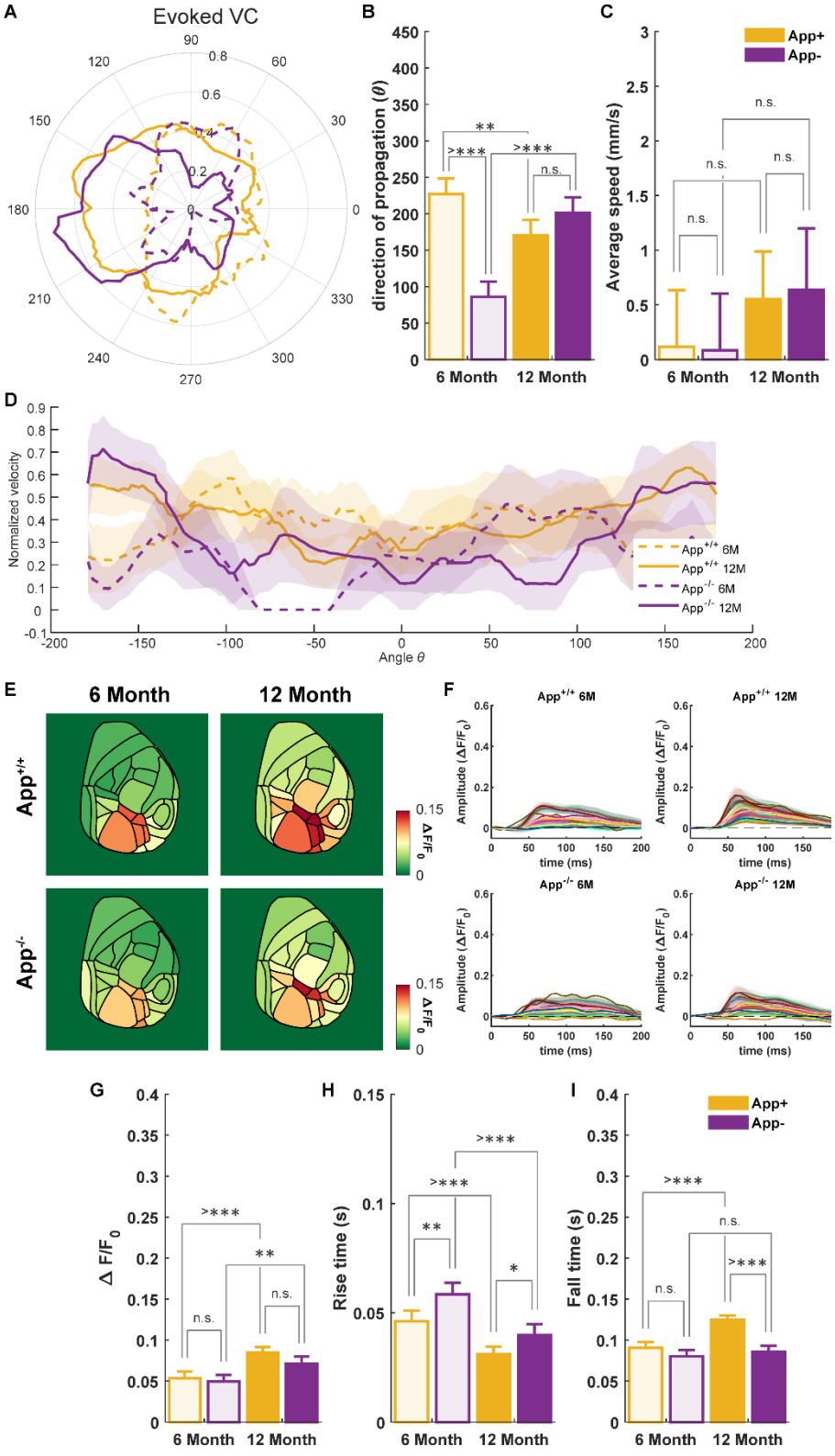

Figure 2.16: Visual stimulus evoked cortical dynamics for *App*$^{NL-G-F}$ mice.

(A) polar plot and (D) mean ± S.E.M. of normalized velocity with respect to the angle/direction of signal flow. (B-C) Direction of visual evoked cortical signal propagation changes with genotype and age, however, no effect on speed of propagation in observed. (E) A spatial representation of region-wise peak amplitude of evoked cortical activations. (F) time series representation of evoked cortical activations in multiple regions of interest (ROIs) shown in fig 2.1A. (G) Peak amplitude of cortical activation increases with age in $App^{+/+}$ mice suggesting hyperactivity associated with disease progression. (H-I) $App^{+/+}$ mice had reduced rise-time suggesting quick activation after stimulus onset, however, increased fall-time at 12 months suggest prolonged activation in $App^{+/+}$ mice. (6-month-old: $App^{+/+}$, n = 7; $App^{-/-}$, n = 7 and $App^{+/+}$, n = 9; $App^{-/-}$, n = 6). * = $p < 0.05$; ** = $p < 0.01$; *** = $p < 0.001$; >*** = $p < 0.001$.

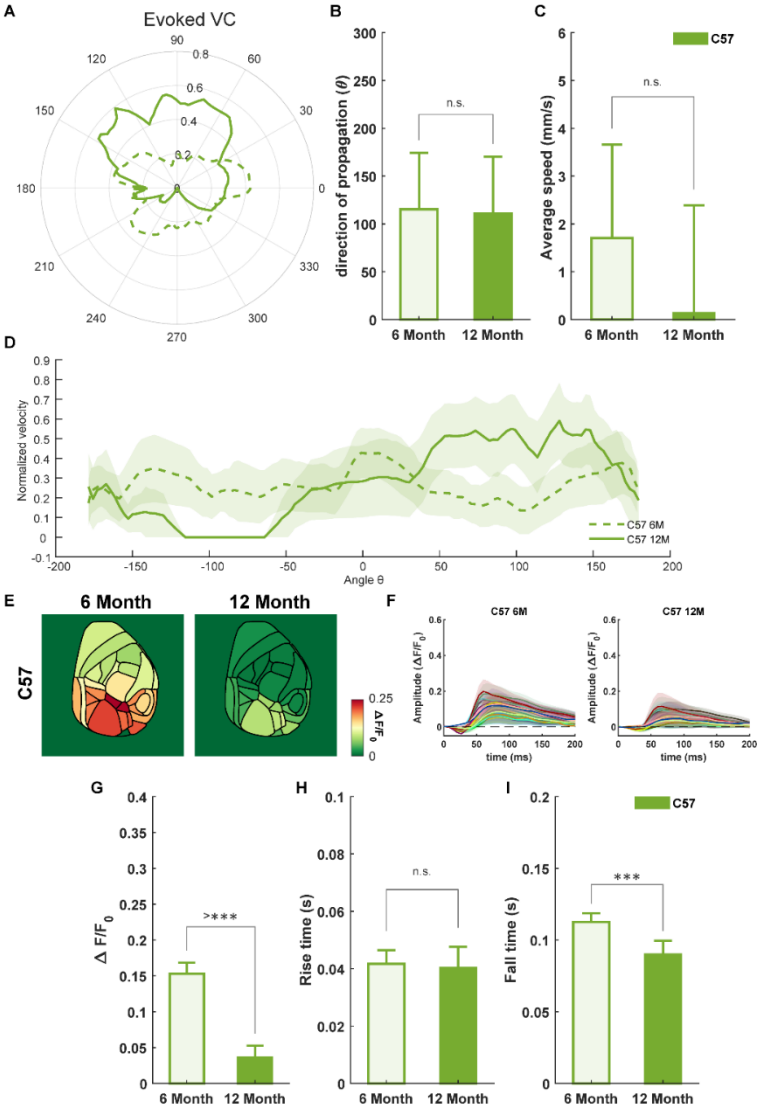

Figure 2.17: Visual stimulus evoked cortical dynamics for C57 mice.
(A) polar plot and (D) mean ± S.E.M. of normalized velocity with respect to the angle/direction of signal flow. (B-C) No change is observed in direction and speed of propagation for visual evoked cortical signal. (E) A spatial representation of region-wise peak amplitude of evoked cortical activations. (F) time series representation of evoked cortical activations in multiple regions of interest (ROIs) shown in fig 2.1A. (G) Peak amplitude of cortical activation decreases with age in C57 mice. (H-I) C57 mice had increased fall-time at 12 months age suggesting prolonged activation. (6-month-old: C57BL/6J, n = 7 and 12-month-old: C57BL/6J, n = 6). * = $p < 0.05$; ** = $p < 0.01$; *** = $p < 0.001$; >*** = $p < 0.001$.

Table 2.8: ANOVA table for statistical comparison of direction of propagation, propagation speed, amplitude, rise time and fall time of visual evoked cortical activations.

5xFAD

Direction								**Speed**															
Source	Sum Sq.	d.f.	Singular?	Mean Sq.	F	Prob>F		Source	Sum Sq.	d.f.	Singular?	Mean Sq.	F	Prob>F									
Age	193410.2	1	0	193410.2	45.18114	1.96E-08		Age	9.365211	1	0	9.365211	1.534544	0.226094									
Genotype	505.1799	1	0	505.1799	0.118011	0.732702		Genotype	8.933506	1	0	8.933506	1.463807	0.236812									
Age*Genotype	99212.93	1	0	99212.93	23.17641	1.51E-05		Age*Genotype	10.13674	1	0	10.13674	1.660963	0.208407									
Error	205477.1	48	0	4280.773				Error	164.779	27	0	6.102927											
Total	498605.4	51	0					Total	194.4953	30	0												
Amplitude								**Rise Time**								**Fall Time**							
Source	Sum Sq.	d.f.	Singular?	Mean Sq.	F	Prob>F		Source	Sum Sq.	d.f.	Singular?	Mean Sq.	F	Prob>F		Source	Sum Sq.	d.f.	Singular?	Mean Sq.	F	Prob>F	
Regions	0.516221	27	0	0.019119	2.850043	2.62E-06		Regions	0.023044	27	0	0.000853	1.949917	0.004116		Regions	0.042828	27	0	0.001586	2.164359	0.000999	
Age	0.350292	1	0	0.350292	52.21678	1.27E-12		Age	0.000602	1	0	0.000602	1.375766	0.241807		Age	0.011836	1	0	0.011836	16.15016	7.46E-05	
Genotype	0.237998	1	0	0.237998	35.47758	4.03E-09		Genotype	0.000399	1	0	0.000399	0.910663	0.34075		Genotype	0.00399	1	0	0.00399	5.443802	0.020322	
Regions*Age	0.044735	27	0	0.001657	0.246984	0.999974		Regions*Age	0.0088	27	0	0.000326	0.744619	0.819318		Regions*Age	0.04797	27	0	0.001777	2.424222	0.000167	
Regions*Genotype	0.039584	27	0	0.001466	0.21854	0.999993		Regions*Genotype	0.010721	27	0	0.000397	0.907137	0.601784		Regions*Genotype	0.014076	27	0	0.000521	0.711356	0.855423	
Age*Genotype	0.455934	1	0	0.455934	67.96449	7.86E-16		Age*Genotype	0.003497	1	0	0.003497	7.989415	0.005039		Age*Genotype	0.002553	1	0	0.002553	3.484124	0.062969	
Error	4.836769	721	0	0.006708				Error	0.124309	284	0	0.000438				Error	0.212536	290	0	0.000733			
Total	6.673241	805	0					Total	0.173817	368	0					Total	0.370472	374	0				

App

Direction								**Speed**															
Source	Sum Sq.	d.f.	Singular?	Mean Sq.	F	Prob>F		Source	Sum Sq.	d.f.	Singular?	Mean Sq.	F	Prob>F									
Age	11197.96	1	0	11197.96	7.758979	0.007629		Age	1.779141	1	0	1.779141	3.767696	0.063165									
Genotype	39593.34	1	0	39593.34	27.43391	3.57E-06		Genotype	0.005025	1	0	0.005025	0.010642	0.918626									
Age*Genotype	96380.77	1	0	96380.77	66.78148	1.21E-10		Age*Genotype	0.024381	1	0	0.024381	0.051631	0.822026									
Error	69274.85	48	0	1443.226				Error	12.27744	26	0	0.472209											
Total	216446.9	51	0					Total	14.0649	29	0												
Amplitude								**Rise Time**								**Fall Time**							
Source	Sum Sq.	d.f.	Singular?	Mean Sq.	F	Prob>F		Source	Sum Sq.	d.f.	Singular?	Mean Sq.	F	Prob>F		Source	Sum Sq.	d.f.	Singular?	Mean Sq.	F	Prob>F	
Regions	0.740069	27	0	0.02741	9.770777	8.73E-34		Regions	0.025033	27	0	0.000927	1.923664	0.004188		Regions	0.01879	27	0	0.000696	0.665799	0.89947	
Age	0.123011	1	0	0.123011	43.84964	6.96E-11		Age	0.023887	1	0	0.023887	49.56126	8.6E-12		Age	0.033437	1	0	0.033437	31.98942	2.98E-08	
Genotype	0.01381	1	0	0.01381	4.922972	0.026815		Genotype	0.009409	1	0	0.009409	19.52228	1.29E-05		Genotype	0.052398	1	0	0.052398	50.13024	6.65E-12	
Regions*Age	0.038256	27	0	0.001417	0.505078	0.983634		Regions*Age	0.009141	27	0	0.000339	0.70246	0.866108		Regions*Age	0.020966	27	0	0.000777	0.742911	0.823155	
Regions*Genotype	0.02873	27	0	0.001064	0.379302	0.99838		Regions*Genotype	0.011761	27	0	0.000436	0.903768	0.606996		Regions*Genotype	0.010847	27	0	0.000402	0.384336	0.998052	
Age*Genotype	0.004661	1	0	0.004661	1.661655	0.197796		Age*Genotype	0.000335	1	0	0.000335	0.696094	0.404605		Age*Genotype	0.021242	1	0	0.021242	20.32218	8.64E-06	
Error	2.008596	716	0	0.002805				Error	0.189897	394	0	0.000482				Error	0.411824	394	0	0.001045			
Total	3.06233	800	0					Total	0.272115	478	0					Total	0.628804	478	0				

C57

Direction								**Speed**															
Source	Sum Sq.	d.f.	Singular?	Mean Sq.	F	Prob>F		Source	Sum Sq.	d.f.	Singular?	Mean Sq.	F	Prob>F									
Age	110.7773	1	0	110.7773	0.00969	0.922401		Age	8.462979	1	0	8.462979	1.108289	0.313191									
Error	274364	24	0	11431.83				Error	91.63287	12	0	7.636073											
Total	274474.8	25	0					Total	100.0959	13	0												
Amplitude								**Rise Time**								**Fall Time**							
Source	Sum Sq.	d.f.	Singular?	Mean Sq.	F	Prob>F		Source	Sum Sq.	d.f.	Singular?	Mean Sq.	F	Prob>F		Source	Sum Sq.	d.f.	Singular?	Mean Sq.	F	Prob>F	
Regions	0.527228	27	0	0.019527	1.711038	0.017171		Regions	0.007899	20	0	0.000395	0.726289	0.793445		Regions	0.01761	20	0	0.000881	0.952368	0.52331	
Age	1.197047	1	0	1.197047	104.8906	2.06E-21		Age	5.87E-05	1	0	5.87E-05	0.107903	0.743057		Age	0.014464	1	0	0.014464	15.64413	0.000123	
Regions*Age	0.106235	27	0	0.003935	0.34477	0.999222		Regions*Age	0.006876	20	0	0.000344	0.632184	0.88259		Regions*Age	0.011104	20	0	0.000555	0.600529	0.906852	
Error	3.560649	312	0	0.011412				Error	0.07287	134	0	0.000544				Error	0.12389	134	0	0.000925			
Total	5.500083	367	0					Total	0.08774	175	0					Total	0.175884	175	0				

Effects of age and strain on cortical functional connectivity

Average pixel values over time in 29 regions of interest from resting state (task-independent) spontaneous VSDI data was used to calculate zero-lag Pearson correlation between regions to generate functional connectivity matrices. Previous studies have shown a modular community structure in the mouse isocortex (Rubinov et al., 2015; Knox et al., 2018; Harris et al., 2019). Figure 2.18A shows $\log_{10}-$transformed ipsilateral normalized connection densities between 29 cortical areas in C57BL/6J mice, generated by a data-driven model (figure adapted from (Knox et al., 2018; Harris et al., 2019)). Fig. 2.18B represents a functional connectivity map generated from resting state spontaneous widefield voltage sensitive dye imaging experiment in 6-month-old C57BL/6J mice. There is stark resemblance in the network architecture in both structural and functional connectivity matrices, the similarity between these two networks has also been shown by (Mohajerani et al., 2013).

For 5xFAD group significant effect of age and genotype was observed in overall functional connectivity, further there is significant interaction between age and genotype (see Table 2.9 5xFAD for detail statistics). Functional connectivity is reduced in diseased mice as compare to littermate control mice at 6- and 12- months of age (fig 2.20A). However, there was slight increase in functional connectivity with age in $5xFAD^{+}$ mice (fig 2.20B). ROI level statistics are shown as binary matrix with results presented after *fdr* correction; we found a major effect of genotype (fig 2.20C). For App group significant effect of age and genotype was observed in overall functional connectivity, further there is significant interaction between age and genotype (see Table 2.9 App for detail statistics). No change in functional connectivity at 6-months but there was significant reduction in functional connectivity of diseased mice w.r.t. littermate controls at 12- months of age (fig 2.20D-E). However, when compared to

C57 control *App*$^{+/+}$ mice show hyper connectivity (fig 2.21A). The difference in interpreting the results when comparing to wild-type (C57) and littermate controls suggests the importance of selecting controls in an experimental design. ROI level statistics are shown as binary matrix with results presented after *fdr* correction; we found a major effect of age and genotype (fig 2.20F). For C57 group we observed significant effect of age and an increase in functional connectivity at 12-months of age. Mean correlation matrices from all the groups are presented in fig 2.19.

Further we looked at intra- *versus* inter- network functional connectivity differences. Cortical areas of interest in the imaging window were grouped into six functional subgroups based on anatomy: somatomotor, somatosensory, lateral, retrosplenial + association, visual + association, and auditory areas; and average cortical functional connectivity from these subgroups was further compared across groups. (fig 2.22) Inter-network functional connectivity was lower as compared with intra-network functional connectivity for all groups. For inter-network functional connectivity 5xFAD group showed a strong effect of genotype, App group showed a strong effect of age and genotype, and no significant effect was observed in C57 group (see Table 2.11 for detail statistics).

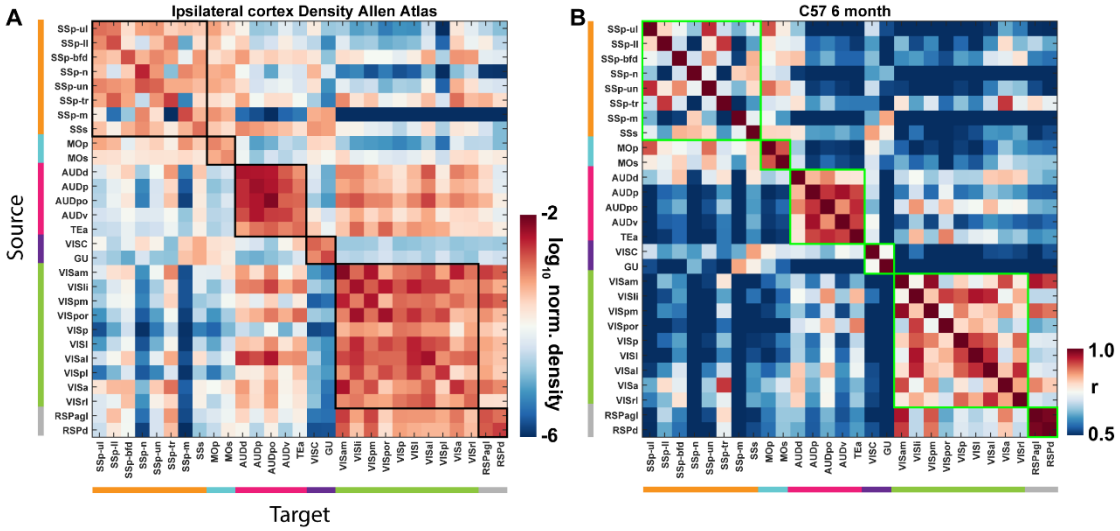

Figure 2.18: Structural and functional connectivity.

(A) Modular community structure in the mouse isocortex, $\log_{10}$ −transformed ipsilateral normalized connection densities between 29 cortical areas in C57BL/6J mice, generated by a data-driven model (figure adapted from (Knox et al., 2018; Harris et al., 2019), data are freely available on https://portal.brain-map.org/). (B) A functional connectivity map generated from resting state spontaneous widefield voltage sensitive dye imaging experiment in 6-month-old C57BL/6J mice. There is stark resemblance in the network architecture in both structural and functional connectivity matrices.

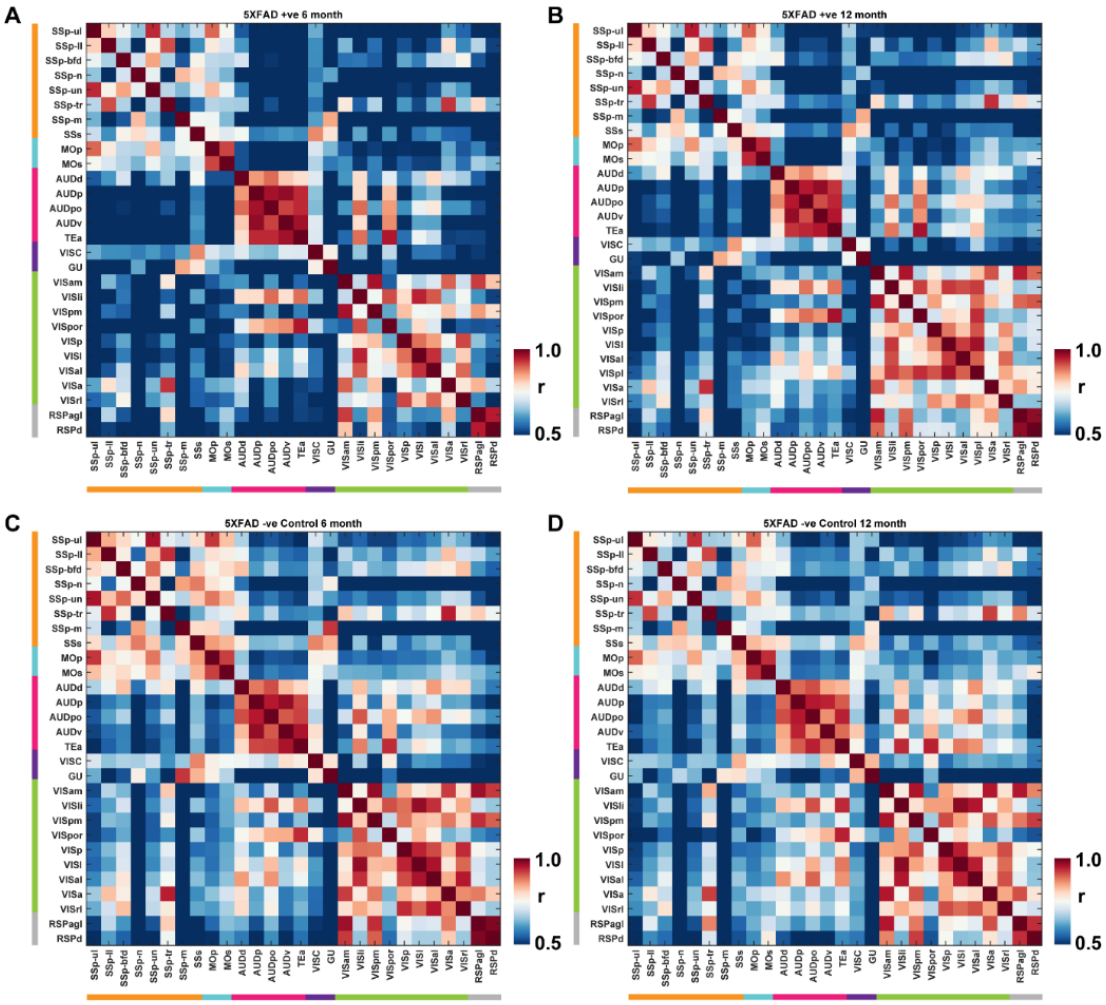

Contd...

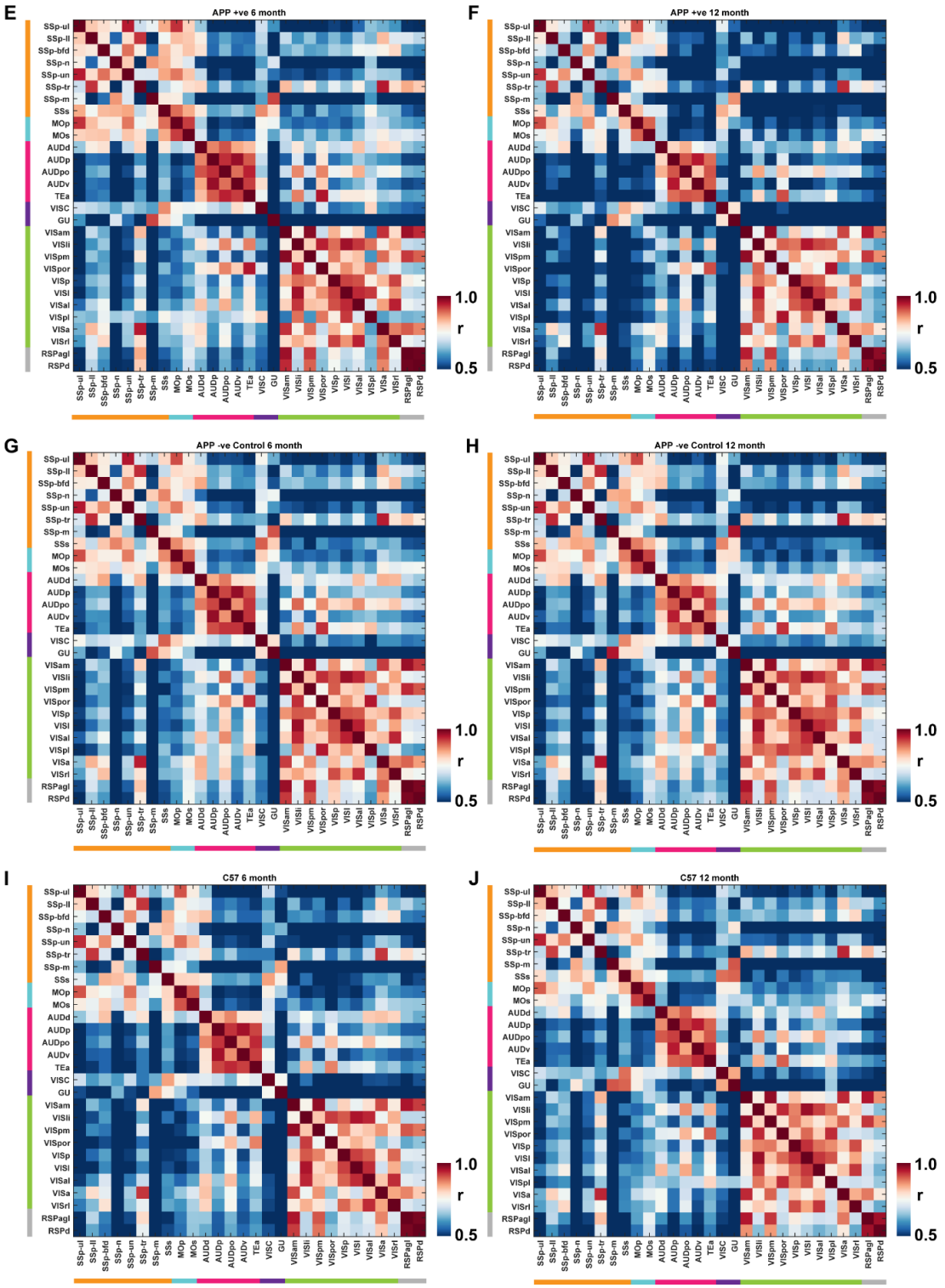

Figure 2.19: Mean cortical functional connectivity matrices.
(A-J) represents mean cortical functional connectivity matrices for AD and control groups at different age. (6-month-old: C57BL/6J, n = 9; App$^{+/+}$, n = 7; App$^{-/-}$, n = 7; 5xFAD^{+}, n = 9; 5xFAD^{-}, n = 8 and 12-month-old: C57BL/6J, n = 6; App$^{+/+}$, n = 10; App$^{-/-}$, n = 6; 5xFAD^{+}, n = 8; 5xFAD^{-}, n = 6).

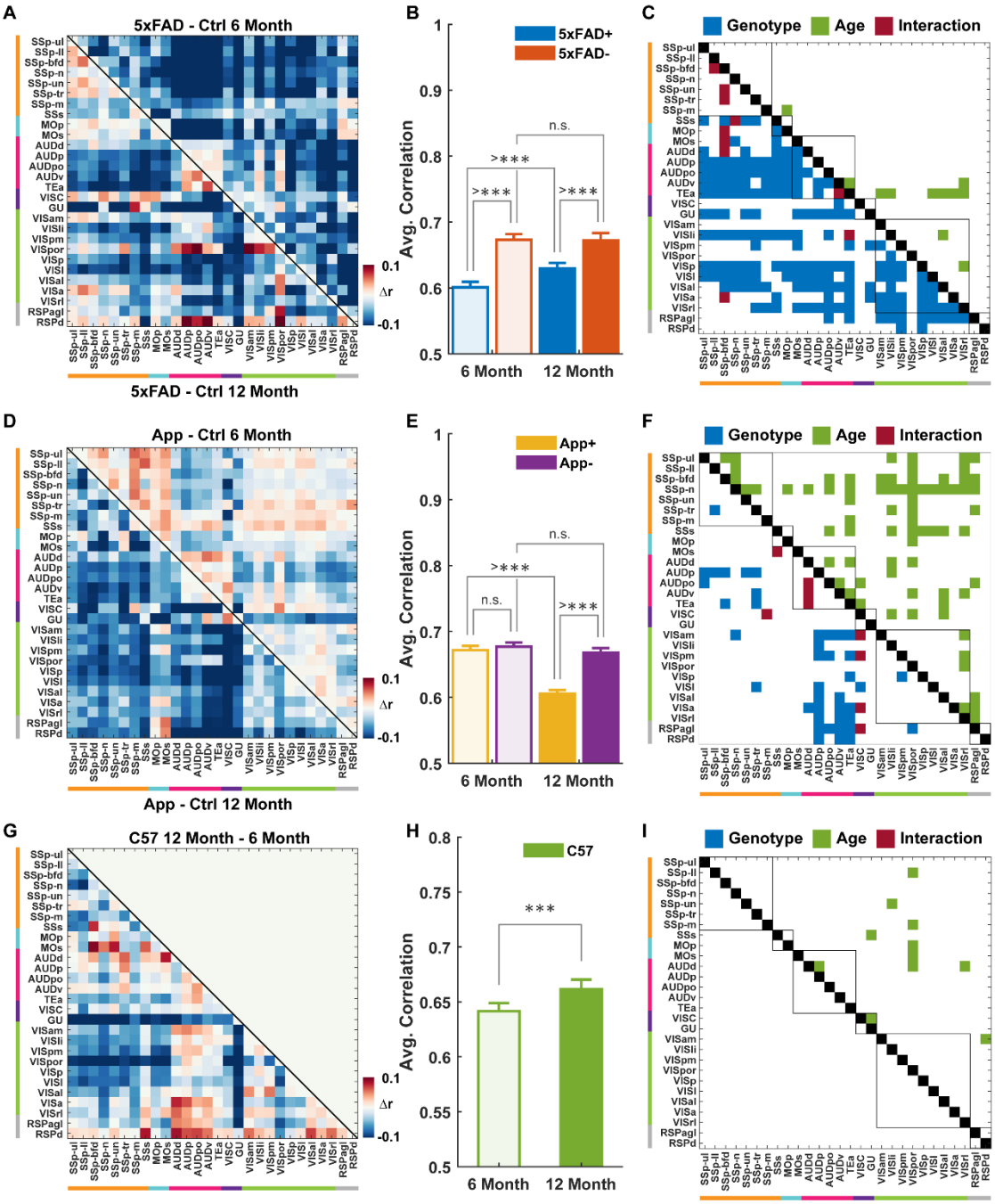

Figure 2.20: Cortical functional connectivity alterations in AD.
(A) Difference mean correlation of 5xFAD^{+} and 5xFAD^{-} control mice, upper triangular matrix and lower triangular matrix show difference between 6 and 12 month diseased and control mice respectively. (B) There is a decreased functional connectivity in 5xFAD^{+} w.r.t. control at 6 and 12 months. However, there is slight increase in functional connectivity of 5xFAD^{+} at 12 month w.r.t. 6 month disease mice. (C) Statistical analysis of cortical functional connectivity is shown as a binary matrix, indicating statistically significant effect (after FDR correction) of genotype (blue), age (green) and interaction (red) for each pair of regional connections. The results suggest a strong effect of genotype. (D) Difference mean correlation of App$^{+/+}$ and App$^{-/-}$, control mice, upper triangular matrix and lower triangular matrix show difference between 6 and 12 month diseased and control mice respectively. (E) There is a decreased functional connectivity in App$^{+/+}$ w.r.t. control only at 12 months. (F) Statistical analyses of cortical functional connectivity is shown as a binary matrix, indicating statistically significant effect (after FDR correction) of genotype (blue), age (green) and interaction (red) for each pair of regional connections. The results suggest a strong effect of age. (G) Difference mean correlation

of C57 6- and 12-month-old mice. (E) There is an increased functional connectivity in C57 12-month-old animals. (F) Statistical analysis of cortical functional connectivity is shown as a binary matrix, indicating statistically significant effect (after FDR correction) of age (green) for each pair of regional connections. The results suggest a strong effect of age. (6-month-old: C57BL/6J, n = 9; $App^{+/+}$, n = 7; $App^{-/-}$, n = 7; $5xFAD^{+}$, n = 9; $5xFAD^{-}$, n = 8 and 12-month-old: C57BL/6J, n = 6; $App^{+/+}$, n = 10; $App^{-/-}$, n = 6; $5xFAD^{+}$, n = 8; $5xFAD^{-}$, n = 6). * = $p < 0.05$; ** = $p < 0.01$; *** = $p < 0.001$; >*** = $p < 0.001$.

Table 2.9: ANOVA table for statistical comparison of cortical functional connectivity.

5xFAD						
Source	Sum Sq.	d.f.	Singular?	Mean Sq.	F	Prob>F
Regions	2.125781	27	0	0.078733	19.00385	0
Age	0.035712	1	0	0.035712	8.619994	0.003426
Genotype	0.635036	1	0	0.635036	153.28	3.55E-32
Regions*Age	0.055189	27	0	0.002044	0.493375	0.986278
Regions*Genotype	0.024358	27	0	0.000902	0.217749	0.999993
Age*Genotype	0.042717	1	0	0.042717	10.31063	0.001379
Error	3.119665	753	0	0.004143		
Total	6.19247	837	0			
App						
Source	Sum Sq.	d.f.	Singular?	Mean Sq.	F	Prob>F
Regions	2.752797	27	0	0.101955	56.5017	0
Age	0.247943	1	0	0.247943	137.4049	3.69E-29
Genotype	0.198258	1	0	0.198258	109.8705	5.11E-24
Regions*Age	0.026104	27	0	0.000967	0.535794	0.975032
Regions*Genotype	0.01764	27	0	0.000653	0.362067	0.998928
Age*Genotype	0.153284	1	0	0.153284	84.94688	3.33E-19
Error	1.295607	718	0	0.001804		
Total	4.957767	802	0			
C57						
Source	Sum Sq.	d.f.	Singular?	Mean Sq.	F	Prob>F
Regions	1.075815	27	0	0.039845	12.85082	1.19E-37
Age	0.037949	1	0	0.037949	12.23935	0.000529
Regions*Age	0.046377	27	0	0.001718	0.553985	0.967017
Error	1.0697	345	0	0.003101		
Total	2.319927	400	0			

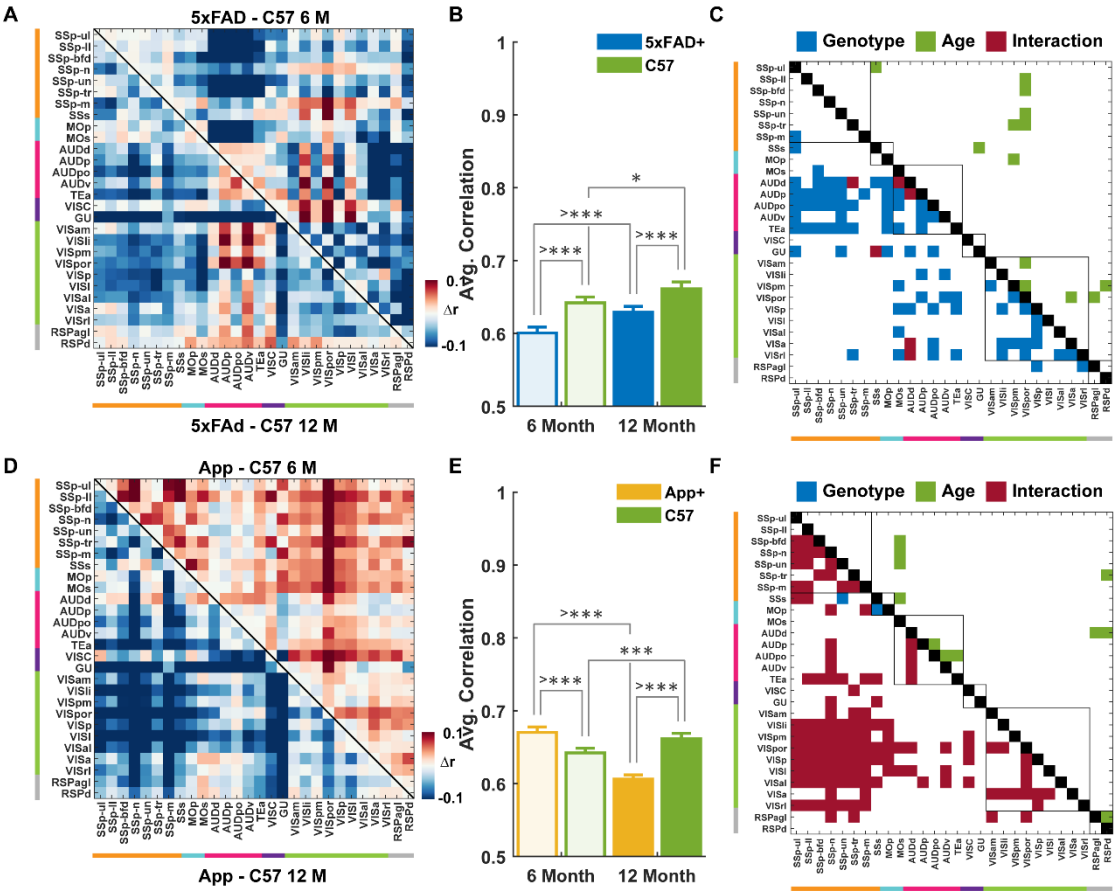

Figure 2.21: Changes in cortical functional connectivity in AD mice in comparison with C57 control.

(A) Difference mean correlation of 5xFAD^{+} w.r.t. C57 mice, upper triangular matrix and lower triangular matrix show difference between 6 and 12 month diseased and control mice respectively. (B) There is reduced functional connectivity in 5xFAD^{+} w.r.t. C57 mice at 6 and 12 months. However, there is slight increase in functional connectivity of both 5xFAD^{+} and C57 mice at 12 months. (C) Statistical analysis of cortical functional connectivity is shown as a binary matrix, indicating statistically significant effect (after FDR correction) of genotype (blue), age (green) and interaction (red) for each pair of regional connections. The results suggest a strong effect of genotype. (D) Difference mean correlation of App$^{+/+}$ mice w.r.t. C57 mice, upper triangular matrix and lower triangular matrix show difference between 6 and 12 month diseased and control mice respectively. At 6-month App$^{+/+}$ mice show hyper connectivity w.r.t. C57 control, however, if App$^{+/+}$ mice is compared to its littermate control (fig. 2.20 D-E) no such effect is observed. The difference in interpreting the results when comparing to wild-type (C57) and littermate controls suggests the importance of selecting controls in an experimental design. (E) There is an increase in functional connectivity in App$^{+/+}$ mice w.r.t. C57 mice only at 6 months. At 12 month there is reduction in functional connectivity of App$^{+/+}$ mice w.r.t. C57 mice. (F) Statistical analyses of cortical functional connectivity is shown as a binary matrix, indicating statistically significant effect (after FDR correction) of genotype (blue), age (green) and interaction (red) for each pair of regional connections. The results suggest a strong effect of interaction. (6-month-old: C57BL/6J, n = 9; App$^{+/+}$, n = 7; 5xFAD^{+}, n = 9 and 12-month-old: C57BL/6J, n = 6; App$^{+/+}$, n = 10; 5xFAD^{+}, n = 8). * = $p < 0.05$; ** = $p < 0.01$; *** = $p < 0.001$; >*** = $p < 0.001$.

Table 2.10: ANOVA table for statistical comparison of cortical functional connectivity w.r.t. C57

5xFAD_C57						
Source	Sum Sq.	d.f.	Singular?	Mean Sq.	F	Prob>F
Regions	2.345581	27	0	0.086873	23.38391	0
Age	0.117685	1	0	0.117685	31.6775	2.53E-08
Genotype	0.279016	1	0	0.279016	75.10339	2.51E-17
Regions*Age	0.024296	27	0	0.0009	0.242213	0.999979
Regions*Genotype	0.033045	27	0	0.001224	0.329435	0.999554
Age*Genotype	0.004557	1	0	0.004557	1.226654	0.268396
Error	2.934923	790	0	0.003715		
Total	5.787504	874	0			
App_C57						
Source	Sum Sq.	d.f.	Singular?	Mean Sq.	F	Prob>F
Regions	2.790302	27	0	0.103345	45.947	0
Age	0.100163	1	0	0.100163	44.53228	4.78E-11
Genotype	0.036263	1	0	0.036263	16.12233	6.52E-05
Regions*Age	0.02617	27	0	0.000969	0.430925	0.995248
Regions*Genotype	0.031653	27	0	0.001172	0.521215	0.979528
Age*Genotype	0.357728	1	0	0.357728	159.0462	2.78E-33
Error	1.731893	770	0	0.002249		
Total	5.178422	854	0			

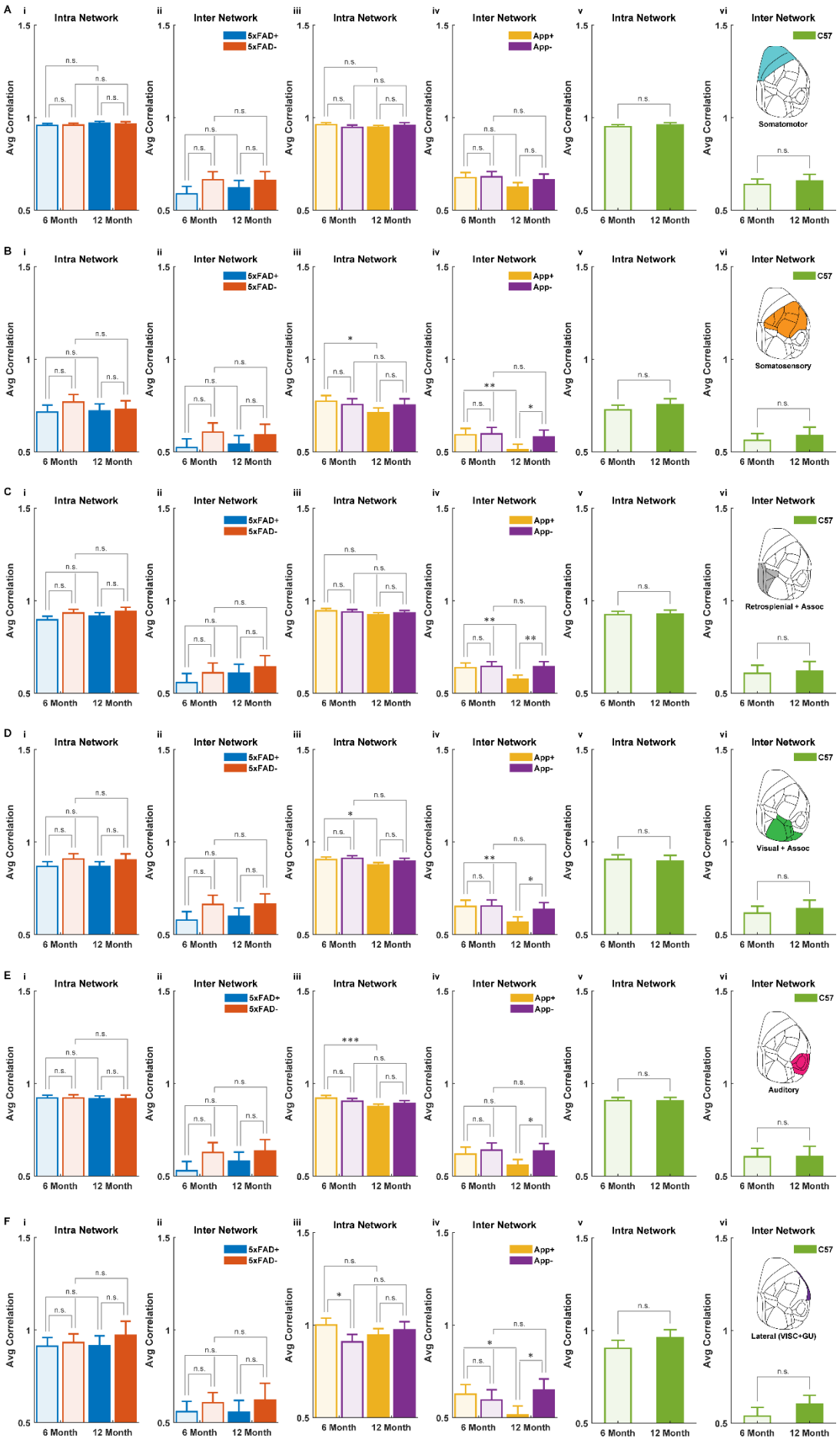
A
B
C
D
E
F
i
ii
iii
iv
v
vi
Intra Network
Inter Network
5xFAD+
5xFAD-
App+
App-
C57
Somatomotor
Somatosensory
Retrosplenial + Assoc
Visual + Assoc
Auditory
Lateral (VISC+GU)
Avg Correlation
6 Month
12 Month
n.s.
*
**
***

Figure 2.22: Intra- and Inter- Network correlation analysis.
(i,iii,v) represents intra- network average correlation comparison and (ii, iv, vi) represents inter-network average correlation comparison analysis. 29 cortical areas of interest in the imaging window based on the Allen common coordinate framework regions were then grouped into six functional subgroups: Somatomotor (Teal), Somatosensory (Orange), Lateral (Purple), Retrosplenial + Association (Gray), Visual + Association (Green), and Auditory areas (Pink); and average cortical functional connectivity from these subgroups was further compared across groups. (A-F) strong genotype effect and reduced inter-network correlation was observed for 5xFAD^{+} mice, further a strong effect of age and genotype suggest reduced inter-network correlation for 12-month-old App$^{+/+}$ mice, no significant effect of age was observed for C57 mice. (6-month-old: C57BL/6J, n = 9; App$^{+/+}$, n = 7; App$^{-/-}$, n = 7; 5xFAD^{+}, n = 9; 5xFAD^{-}, n = 8 and 12-month-old: C57BL/6J, n = 6; App$^{+/+}$, n = 10; App$^{-/-}$, n = 6; 5xFAD^{+}, n = 8; 5xFAD^{-}, n = 6). * = $p < 0.05$; ** = $p < 0.01$; *** = $p < 0.001$; >*** = $p < 0.001$.

Table 2.11: ANOVA table for statistical comparison of intra-, inter- network functional connectivity.
5xFAD

Avg. Intra_Network Correlation Somatosensory								**Avg. Inter_Network Correlation Somatosensory**						
Source	Sum Sq.	d.f.	Singular?	Mean Sq.	F	Prob>F		Source	Sum Sq.	d.f.	Singular?	Mean Sq.	F	Prob>F
Age	0.002222	1	0	0.002222	0.674689	0.418361		Age	1.5E-05	1	0	1.5E-05	0.003079	0.956141
Genotype	0.007566	1	0	0.007566	2.297948	0.140754		Genotype	0.034472	1	0	0.034472	7.081501	0.012749
Age*Genotype	0.004068	1	0	0.004068	1.235459	0.275801		Age*Genotype	0.002064	1	0	0.002064	0.423997	0.520258
Error	0.092195	28	0	0.003293				Error	0.136303	28	0	0.004868		
Total	0.106887	31	0					Total	0.174469	31	0			
Avg. Intra_Network Correlation Somatomotor								**Avg. Inter_Network Correlation Somatomotor**						
Source	Sum Sq.	d.f.	Singular?	Mean Sq.	F	Prob>F		Source	Sum Sq.	d.f.	Singular?	Mean Sq.	F	Prob>F
Age	0.000643	1	0	0.000643	2.960047	0.096381		Age	0.00133	1	0	0.00133	0.370517	0.54763
Genotype	1.06E-05	1	0	1.06E-05	0.048846	0.826688		Genotype	0.026482	1	0	0.026482	7.377293	0.011192
Age*Genotype	6.99E-05	1	0	6.99E-05	0.322145	0.574845		Age*Genotype	0.002802	1	0	0.002802	0.780562	0.384492
Error	0.006078	28	0	0.000217				Error	0.10051	28	0	0.00359		
Total	0.006882	31	0					Total	0.132432	31	0			
Avg. Intra_Network Correlation Auditory								**Avg. Inter_Network Correlation Auditory**						
Source	Sum Sq.	d.f.	Singular?	Mean Sq.	F	Prob>F		Source	Sum Sq.	d.f.	Singular?	Mean Sq.	F	Prob>F
Age	0.000147	1	0	0.000147	0.268577	0.60836		Age	0.006894	1	0	0.006894	1.208391	0.281013
Genotype	1.07E-05	1	0	1.07E-05	0.019516	0.889898		Genotype	0.046772	1	0	0.046772	8.197747	0.007857
Age*Genotype	1.9E-06	1	0	1.9E-06	0.00347	0.953444		Age*Genotype	0.003426	1	0	0.003426	0.600401	0.44492
Error	0.015369	28	0	0.000549				Error	0.159752	28	0	0.005705		
Total	0.015542	31	0					Total	0.218159	31	0			
Avg. Intra_Network Correlation Lateral(VISC+GU)								**Avg. Inter_Network Correlation Lateral(VISC+GU)**						
Source	Sum Sq.	d.f.	Singular?	Mean Sq.	F	Prob>F		Source	Sum Sq.	d.f.	Singular?	Mean Sq.	F	Prob>F
Age	0.002268	1	0	0.002268	0.524103	0.477085		Age	0.000184	1	0	0.000184	0.030057	0.864022
Genotype	0.00758	1	0	0.00758	1.751335	0.199937		Genotype	0.017039	1	0	0.017039	2.780548	0.110261
Age*Genotype	0.001882	1	0	0.001882	0.43481	0.516805		Age*Genotype	0.000401	1	0	0.000401	0.065379	0.800675
Error	0.090894	21	0	0.004328				Error	0.128688	21	0	0.006128		
Total	0.09943	24	0					Total	0.146492	24	0			
Avg. Intra_Network Correlation Visual + Assoc								**Avg. Inter_Network Correlation Visual + Assoc**						
Source	Sum Sq.	d.f.	Singular?	Mean Sq.	F	Prob>F		Source	Sum Sq.	d.f.	Singular?	Mean Sq.	F	Prob>F
Age	7.62E-05	1	0	7.62E-05	0.047556	0.828953		Age	0.000863	1	0	0.000863	0.180737	0.67399
Genotype	0.011502	1	0	0.011502	7.176736	0.012223		Genotype	0.044896	1	0	0.044896	9.401238	0.004766
Age*Genotype	3.76E-05	1	0	3.76E-05	0.023433	0.879434		Age*Genotype	0.000728	1	0	0.000728	0.152517	0.699097
Error	0.044873	28	0	0.001603				Error	0.133716	28	0	0.004776		
Total	0.056842	31	0					Total	0.180905	31	0			
Avg. Intra_Network Correlation Retrosplenial + Assoc								**Avg. Inter_Network Correlation Retrosplenial + Assoc**						
Source	Sum Sq.	d.f.	Singular?	Mean Sq.	F	Prob>F		Source	Sum Sq.	d.f.	Singular?	Mean Sq.	F	Prob>F
Age	0.001468	1	0	0.001468	1.874723	0.181819		Age	0.013027	1	0	0.013027	2.374233	0.134579
Genotype	0.007412	1	0	0.007412	9.464898	0.004645		Genotype	0.015364	1	0	0.015364	2.80006	0.105399
Age*Genotype	0.000296	1	0	0.000296	0.377508	0.5439		Age*Genotype	0.000639	1	0	0.000639	0.116472	0.735441
Error	0.021928	28	0	0.000783				Error	0.153636	28	0	0.005487		
Total	0.031144	31	0					Total	0.182344	31	0			

App

Avg. Intra_Network Correlation Somatosensory

Source	Sum Sq.	d.f.	Singular?	Mean Sq.	F	Prob>F
Age	0.007505	1	0	0.007505	4.509644	0.043381
Genotype	0.001015	1	0	0.001015	0.609577	0.441998
Age*Genotype	0.006162	1	0	0.006162	3.702682	0.065336
Error	0.043272	26	0	0.001664		
Total	0.061029	29	0			

Avg. Inter_Network Correlation Somatosensory

Source	Sum Sq.	d.f.	Singular?	Mean Sq.	F	Prob>F
Age	0.017316	1	0	0.017316	8.268103	0.007946
Genotype	0.009619	1	0	0.009619	4.592872	0.041635
Age*Genotype	0.007177	1	0	0.007177	3.426961	0.075532
Error	0.054452	26	0	0.002094		
Total	0.096435	29	0			

Avg. Intra_Network Correlation Somatomotor

Source	Sum Sq.	d.f.	Singular?	Mean Sq.	F	Prob>F
Age	1.35E-06	1	0	1.35E-06	0.005065	0.943809
Genotype	2.16E-05	1	0	2.16E-05	0.081173	0.777971
Age*Genotype	0.001075	1	0	0.001075	4.044288	0.054797
Error	0.00691	26	0	0.000266		
Total	0.008019	29	0			

Avg. Inter_Network Correlation Somatomotor

Source	Sum Sq.	d.f.	Singular?	Mean Sq.	F	Prob>F
Age	0.007865	1	0	0.007865	5.627431	0.025366
Genotype	0.003688	1	0	0.003688	2.638933	0.116336
Age*Genotype	0.002077	1	0	0.002077	1.486416	0.233719
Error	0.036336	26	0	0.001398		
Total	0.053021	29	0			

Avg. Intra_Network Correlation Auditory

Source	Sum Sq.	d.f.	Singular?	Mean Sq.	F	Prob>F
Age	0.005849	1	0	0.005849	15.1247	0.000624
Genotype	6.81E-07	1	0	6.81E-07	0.00176	0.966855
Age*Genotype	0.001868	1	0	0.001868	4.828871	0.037094
Error	0.010055	26	0	0.000387		
Total	0.018859	29	0			

Avg. Inter_Network Correlation Auditory

Source	Sum Sq.	d.f.	Singular?	Mean Sq.	F	Prob>F
Age	0.007611	1	0	0.007611	3.099599	0.090072
Genotype	0.017866	1	0	0.017866	7.275956	0.012104
Age*Genotype	0.005622	1	0	0.005622	2.289547	0.14231
Error	0.063841	26	0	0.002455		
Total	0.101289	29	0			

Avg. Intra_Network Correlation Lateral(VISC+GU)

Source	Sum Sq.	d.f.	Singular?	Mean Sq.	F	Prob>F
Age	0.000184	1	0	0.000184	0.07581	0.785627
Genotype	0.006515	1	0	0.006515	2.68536	0.115498
Age*Genotype	0.022285	1	0	0.022285	9.185005	0.006141
Error	0.053377	22	0	0.002426		
Total	0.082793	25	0			

Avg. Inter_Network Correlation Lateral(VISC+GU)

Source	Sum Sq.	d.f.	Singular?	Mean Sq.	F	Prob>F
Age	0.005317	1	0	0.005317	1.147886	0.295606
Genotype	0.016466	1	0	0.016466	3.554905	0.072645
Age*Genotype	0.042517	1	0	0.042517	9.179031	0.006156
Error	0.101903	22	0	0.004632		
Total	0.17315	25	0			

Avg. Intra_Network Correlation Visual + Assoc

Source	Sum Sq.	d.f.	Singular?	Mean Sq.	F	Prob>F
Age	0.003379	1	0	0.003379	9.890125	0.004129
Genotype	0.001257	1	0	0.001257	3.680648	0.06609
Age*Genotype	0.000374	1	0	0.000374	1.093359	0.305353
Error	0.008883	26	0	0.000342		
Total	0.014917	29	0			

Avg. Inter_Network Correlation Visual + Assoc

Source	Sum Sq.	d.f.	Singular?	Mean Sq.	F	Prob>F
Age	0.018886	1	0	0.018886	9.764109	0.004338
Genotype	0.009487	1	0	0.009487	4.904551	0.035757
Age*Genotype	0.008224	1	0	0.008224	4.251569	0.049341
Error	0.050291	26	0	0.001934		
Total	0.095339	29	0			

Avg. Intra_Network Correlation Retrosplenial + Assoc

Source	Sum Sq.	d.f.	Singular?	Mean Sq.	F	Prob>F
Age	0.001314	1	0	0.001314	4.192647	0.050827
Genotype	1.53E-05	1	0	1.53E-05	0.048685	0.827092
Age*Genotype	0.000468	1	0	0.000468	1.49523	0.232376
Error	0.008146	26	0	0.000313		
Total	0.01024	29	0			

Avg. Inter_Network Correlation Retrosplenial + Assoc

Source	Sum Sq.	d.f.	Singular?	Mean Sq.	F	Prob>F
Age	0.007272	1	0	0.007272	6.10716	0.020335
Genotype	0.009898	1	0	0.009898	8.312363	0.007801
Age*Genotype	0.006565	1	0	0.006565	5.513487	0.026754
Error	0.030961	26	0	0.001191		
Total	0.059992	29	0			

C57

Avg. Intra_Network Correlation Somatosensory

Source	Sum Sq.	d.f.	Singular?	Mean Sq.	F	Prob>F
Age	0.002941	1	0	0.002941	2.032734	0.177512
Error	0.018809	13	0	0.001447		
Total	0.02175	14	0			

Avg. Inter_Network Correlation Somatosensory

Source	Sum Sq.	d.f.	Singular?	Mean Sq.	F	Prob>F
Age	0.002566	1	0	0.002566	0.852452	0.372679
Error	0.039128	13	0	0.00301		
Total	0.041694	14	0			

Avg. Intra_Network Correlation Somatomotor

Source	Sum Sq.	d.f.	Singular?	Mean Sq.	F	Prob>F
Age	0.000321	1	0	0.000321	1.121783	0.308818
Error	0.003724	13	0	0.000286		
Total	0.004045	14	0			

Avg. Inter_Network Correlation Somatomotor

Source	Sum Sq.	d.f.	Singular?	Mean Sq.	F	Prob>F
Age	0.001195	1	0	0.001195	0.639129	0.43839
Error	0.024298	13	0	0.001869		
Total	0.025493	14	0			

Avg. Intra_Network Correlation Auditory

Source	Sum Sq.	d.f.	Singular?	Mean Sq.	F	Prob>F
Age	3.21E-05	1	0	3.21E-05	0.058584	0.812525
Error	0.007124	13	0	0.000548		
Total	0.007156	14	0			

Avg. Inter_Network Correlation Auditory

Source	Sum Sq.	d.f.	Singular?	Mean Sq.	F	Prob>F
Age	6.36E-06	1	0	6.36E-06	0.001388	0.970847
Error	0.059611	13	0	0.004585		
Total	0.059618	14	0			

Avg. Intra_Network Correlation Lateral(VISC+GU)

Source	Sum Sq.	d.f.	Singular?	Mean Sq.	F	Prob>F
Age	0.009721	1	0	0.009721	3.462242	0.092407
Error	0.028078	10	0	0.002808		
Total	0.037799	11	0			

Avg. Inter_Network Correlation Lateral(VISC+GU)

Source	Sum Sq.	d.f.	Singular?	Mean Sq.	F	Prob>F
Age	0.012476	1	0	0.012476	3.811951	0.079429
Error	0.032729	10	0	0.003273		
Total	0.045205	11	0			

Avg. Intra_Network Correlation Visual + Assoc

Source	Sum Sq.	d.f.	Singular?	Mean Sq.	F	Prob>F
Age	0.000269	1	0	0.000269	0.188622	0.671188
Error	0.018559	13	0	0.001428		
Total	0.018828	14	0			

Avg. Inter_Network Correlation Visual + Assoc

Source	Sum Sq.	d.f.	Singular?	Mean Sq.	F	Prob>F
Age	0.002216	1	0	0.002216	0.724644	0.410032
Error	0.039756	13	0	0.003058		
Total	0.041972	14	0			

Avg. Intra_Network Correlation Retrosplenial + Assc

Source	Sum Sq.	d.f.	Singular?	Mean Sq.	F	Prob>F
Age	1.94E-05	1	0	1.94E-05	0.027049	0.871894
Error	0.009342	13	0	0.000719		
Total	0.009361	14	0			

Avg. Inter_Network Correlation Retrosplenial + Assc

Source	Sum Sq.	d.f.	Singular?	Mean Sq.	F	Prob>F
Age	0.000418	1	0	0.000418	0.097012	0.760384
Error	0.056053	13	0	0.004312		
Total	0.056472	14	0			

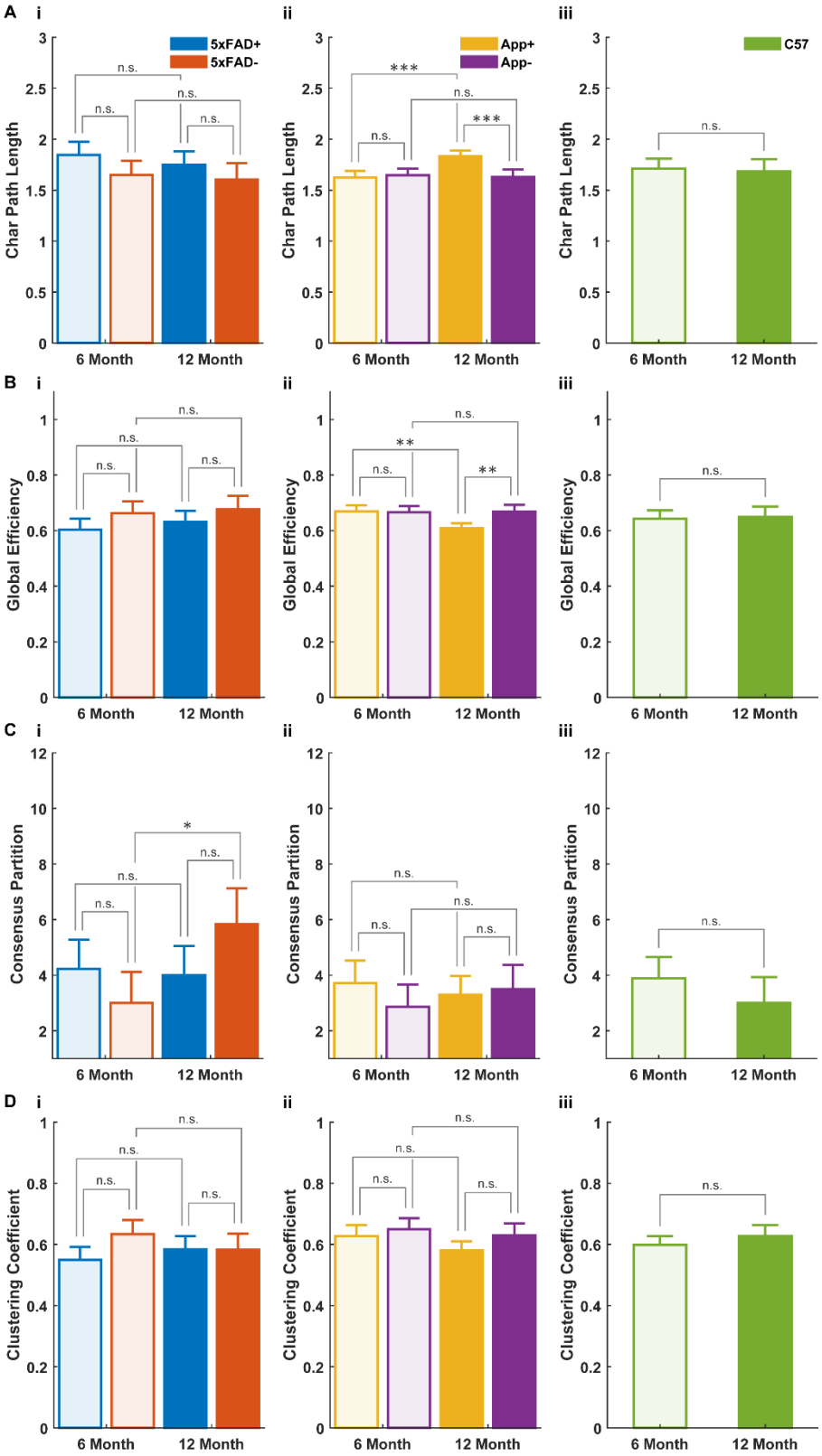

Figure 2.23: Comparison of network measures.

(A) Genotype effect and increase in characteristic path length is observed in 5xFAD^{+} group (i), similarly for App group there is genotype and age effect (ii), no effect is observed in C57 group (iii). (B) Global efficiency in inversely related to path length thus we observe inverse effect of that in (A). (C) there is an increase in consensus partition in 5xFAD group with age, but no genotype effect is observed (i), no change in observed in App (ii) or C57 group (iii). (D) No change was observed in clustering coefficient for 5xFAD, App and C57 group. (6-month-old:

C57BL/6J, n = 9; App$^{+/+}$, n = 7; App$^{-/-}$, n = 7; 5xFAD^{+}, n = 9; 5xFAD^{-}, n = 8 and 12-month-old: C57BL/6J, n = 6; App$^{+/+}$, n = 10; App$^{-/-}$, n = 6; 5xFAD^{+}, n = 8; 5xFAD^{-}, n = 6). * = $p < 0.05$; ** = $p < 0.01$; *** = $p < 0.001$; >*** = $p < 0.001$.

Table 2.12: ANOVA table for statistical comparison of network measures.

5xFAD_Char Path Length								**5xFAD_Global Efficiency**						
Source	Sum Sq.	d.f.	Singular?	Mean Sq.	F	Prob>F		Source	Sum Sq.	d.f.	Singular?	Mean Sq.	F	Prob>F
Age	0.038619	1	0	0.038619	1.011895	0.323064		Age	0.00331	1	0	0.00331	0.924291	0.34458
Genotype	0.22533	1	0	0.22533	5.90405	0.021771		Genotype	0.021333	1	0	0.021333	5.956452	0.021246
Age*Genotype	0.005125	1	0	0.005125	0.134278	0.716792		Age*Genotype	0.000393	1	0	0.000393	0.109672	0.742984
Error	1.068627	28	0	0.038165				Error	0.10028	28	0	0.003581		
Total	1.336537	31	0					Total	0.12516	31	0			
APP_Char Path Length								**APP_Global Efficiency**						
Source	Sum Sq.	d.f.	Singular?	Mean Sq.	F	Prob>F		Source	Sum Sq.	d.f.	Singular?	Mean Sq.	F	Prob>F
Age	0.066958	1	0	0.066958	8.428501	0.007435		Age	0.006154	1	0	0.006154	7.242621	0.01228
Genotype	0.059094	1	0	0.059094	7.438609	0.011284		Genotype	0.005922	1	0	0.005922	6.970354	0.013827
Age*Genotype	0.091578	1	0	0.091578	11.52767	0.002211		Age*Genotype	0.007247	1	0	0.007247	8.528803	0.007134
Error	0.206549	26	0	0.007944				Error	0.022091	26	0	0.00085		
Total	0.472719	29	0					Total	0.045775	29	0			
C57_Char Path Length								**C57_Global Efficiency**						
Source	Sum Sq.	d.f.	Singular?	Mean Sq.	F	Prob>F		Source	Sum Sq.	d.f.	Singular?	Mean Sq.	F	Prob>F
Age	0.002727	1	0	0.002727	0.127673	0.72659		Age	0.000178	1	0	0.000178	0.085941	0.77403
Error	0.277701	13	0	0.021362				Error	0.026959	13	0	0.002074		
Total	0.280428	14	0					Total	0.027138	14	0			
5xFAD_consensus partition								**5xFAD_Clustering Coefficient**						
Source	Sum Sq.	d.f.	Singular?	Mean Sq.	F	Prob>F		Source	Sum Sq.	d.f.	Singular?	Mean Sq.	F	Prob>F
Age	13.26727	1	0	13.26727	5.277587	0.029286		Age	0.000507	1	0	0.000507	0.119849	0.731786
Genotype	0.726727	1	0	0.726727	0.289085	0.595056		Genotype	0.013492	1	0	0.013492	3.187922	0.085021
Age*Genotype	18.16817	1	0	18.16817	7.227117	0.011955		Age*Genotype	0.014669	1	0	0.014669	3.466185	0.073163
Error	70.38889	28	0	2.513889				Error	0.118498	28	0	0.004232		
Total	98.21875	31	0					Total	0.149374	31	0			
APP_consensus partition								**APP_Clustering Coefficient**						
Source	Sum Sq.	d.f.	Singular?	Mean Sq.	F	Prob>F		Source	Sum Sq.	d.f.	Singular?	Mean Sq.	F	Prob>F
Age	0.094581	1	0	0.094581	0.082284	0.776499		Age	0.007984	1	0	0.007984	3.54577	0.070932
Genotype	0.781773	1	0	0.781773	0.680128	0.417045		Genotype	0.009313	1	0	0.009313	4.136249	0.052297
Age*Genotype	2.023153	1	0	2.023153	1.760104	0.196147		Age*Genotype	0.001411	1	0	0.001411	0.626599	0.435768
Error	29.88571	26	0	1.149451				Error	0.058542	26	0	0.002252		
Total	32.66667	29	0					Total	0.081139	29	0			
C57_consensus partition								**C57_Clustering Coefficient**						
Source	Sum Sq.	d.f.	Singular?	Mean Sq.	F	Prob>F		Source	Sum Sq.	d.f.	Singular?	Mean Sq.	F	Prob>F
Age	2.844444	1	0	2.844444	2.189474	0.162778		Age	0.003191	1	0	0.003191	1.691021	0.216048
Error	16.88889	13	0	1.299145				Error	0.024533	13	0	0.001887		
Total	19.73333	14	0					Total	0.027724	14	0			

Effect of age and strain on network measures

Weighted undirected network approach was used for our analysis where, network nodes were cortical ROIs and links were the magnitude of temporal correlation between ROIs obtained from spontaneous activity. The characteristic path length which is the average shortest path length in the network was measured for all the groups, for 5xFAD group there was significant effect of genotype, for App group there was significant of age, genotype and interaction, there was no significant effect of C57 (see Table 2.12 for detail statistics). The global efficiency which is the average inverse shortest path length in the network was measured for all the groups, for 5xFAD group there was significant effect of genotype, for App group there was significant of age, genotype and interaction, there was no significant effect of C57 (see Table 2.12 for

detail statistics). In 5xFAD group there was significant effect of age and interaction between age and genotype for consensus partition of functional network, no significant difference was observed in App or 5xFAD group (see Table 2.12 for detail statistics). Further, clustering coefficient was not significant in 5xFAD, App or C57 group (see Table 2.12 for detail statistics).

Discussion

In this chapter, using widefield *in vivo* VSD imaging of mouse cortex, I examined how sensory evoked and spontaneous cortical activity is altered in an age and strain dependent manner in two mouse models of AD. There is ample evidence of abnormal hyper- and hypo- activity in AD (Palop et al., 2007; Busche et al., 2012; Verret et al., 2012; Busche et al., 2015b; Busche et al., 2015a; Xu et al., 2015; Yamamoto et al., 2015; Nuriel et al., 2017; Busche et al., 2019; Marinković et al., 2019; Petrache et al., 2019; Zott et al., 2019), but these studies have focused on cellular hyper-hypo- excitation. Even though some studies have discussed mesoscale dysfunctions of sensory evoked activity (Maatuf et al., 2016) and spontaneous cortical activity (Bero et al., 2012; Busche et al., 2015a; Beker et al., 2016; Kastanenka et al., 2017), it is not yet clear from those results how different sensory evoked modalities and spontaneous cortical activity gets altered with age and AD strain. I found that in 12-month 5xFAD mice there was an increase in sensory-evoked cortical activation for five different sensory stimuli (contra-lateral stimulation): forelimb or hindlimb paw (1mA, 1 ms), whisker (1ms), auditory (1ms) and visual (1ms). Not only there was an increase in activation amplitude, the velocity of signal propagation across the cortex was also increased, together with alterations in direction of signal flow. Interestingly, sensory-evoked cortical signal flow had a preferred direction towards higher-order multimodal areas. This is consistent with the spatial gradients of cortical connectivity shown in

mouse functional and structural studies and is similar to the gradients found in humans and primates (Mesulam, 1998; Margulies et al., 2016; Coletta et al., 2020).

The hyper excitation observed with age in evoked cortical activation for both 5xFAD and *App*$^{NL\text{-}G\text{-}F}$ mice could be due to mechanisms affecting both excitatory and inhibitory neurons in AD. The mechanism underlying this hyperexcitability has not been fully elucidated, recent studies using transgenic animal models AD and AD-hiPSC-derived neurons/organoids suggests that altered channel properties (e.g. Nav1.6 , Nav1.1 voltage-gated sodium channel) and neurite length could be involved in hyperactivity (Verret et al., 2012; Šišková et al., 2014; Liu et al., 2015; Palop and Mucke, 2016; Wang et al., 2016b; Martinez-Losa et al., 2018; Ghatak et al., 2019). AD pathology may also contribute to loss of interneuron population and subsequent increase in hyperactivity (Schmid et al., 2016; Ghatak et al., 2019). Further, Aβ dimers or oligomers may contribute to hyperexcitability in AD by reducing GABAergic inhibition (Busche et al., 2008; Busche et al., 2015a), by suppression of glutamate reuptake (Selkoe, 2019; Zott et al., 2019), by excessive release of glutamate from astrocytes (Talantova et al., 2013) or by increasing release probability at excitatory synapses (Fogel et al., 2014; Wang et al., 2017b; Ghatak et al., 2019).

rs-fMRI studies in the past have shown functional network disruptions in AD patients. (Liu et al., 2008; Chhatwal and Sperling, 2012; Sugarman et al., 2012; Weiner et al., 2012; Dennis and Thompson, 2014; Li et al., 2015; Asaad and Lee, 2018; Zott et al., 2018). In animal models (both rat and mouse) of AD, resting state brain activity (rs-fMRI) and task or stimulus-related brain activity, has been studied using fMRI (Mueggler et al., 2003; Sanganahalli et al., 2013; Shah et al., 2013; Grandjean et al., 2014; Grandjean et al., 2016; Shah et al., 2016; Parent et al., 2017; Shah et al., 2018;

Latif-Hernandez et al., 2019). Interestingly, the studies in rs-fMRI have variable results. Some studies have shown early reduction in functional connectivity (Grandjean et al., 2014) and others show early age hyper-connectivity and late stage hypo-connectivity (Shah et al., 2016; Latif-Hernandez et al., 2019). This early- and late-stage functional connectivity dissociation has also been shown in APP/PS1 mice using functional connectivity optical intrinsic signal (fcOIS) imaging technique (Bero et al., 2012). In our study we found reduced functional connectivity at 6 and 12 months. At these time points, Aβ pathology increases in association with appearance of cognitive deficits (Jawhar et al., 2012; Mehla et al., 2019). This reduction in functional connectivity was more prominent with aged in $App^{NL\text{-}G\text{-}F}$ mice than in 5xFAD mice. Interestingly, Latif-Hernandez et al. have shown that there is early hyper- functional connectivity in 3 month old $App^{NL\text{-}G\text{-}F}$ and hypo-function connectivity in 11 month old $App^{NL\text{-}G\text{-}F}$ (Latif-Hernandez et al., 2019). It is important to note that in that study they used age matched App^{NL} mice as control, which is not a littermate control. This could lead to confounding interpretations. An example supporting this interpretation comes from my study as well. If FC of 6-month-old $App^{NL\text{-}G\text{-}F}$ mice are compared to C57BL/6J mice, I observe hyper-functional connectivity which changes to hypo- functional connectivity when compared at 12 months. If I compare FC of $App^{NL\text{-}G\text{-}F}$ mice with its age-matched littermate control then no significant difference is observed at 6 months but I observe reduced functional connectivity in $App^{NL\text{-}G\text{-}F}$ mice at 12 months of age. Overall, these results suggest that local subnetwork circuitry and long-range circuits are impaired in AD mice and these dysfunctions increase with increasing Aβ pathology.

Chapter 3 : Hippocampal-Cortical interactions in mouse models of Alzheimer's disease

Abstract

Synaptic loss and neurodegeneration associated with plaques and neurofibrillary tangles (NFTs) in Alzheimer's disease (AD) may lead to progressive learning and memory impairment. Hippocampal-cortical interactions are necessary for memory consolidation and subsequent successful memory retrieval and disruption of these networks by AD pathology leads to memory impairments. This study focuses on understanding how sharp wave ripples (SWRs) and SWRs associated hippocampal-cortical interactions change between 6- and 12- month of age in mice including a knock-in App^{NL-G-F} and a transgenic 5xFAD mouse model of AD. I found that the incidence of SWRs is significantly reduced in 12-month-old 5xFAD mice, in association with an increase in gamma and SWR band power. Cortical activation around the time of occurrence of SWRs had a maximum amplitude in retrosplenial cortex (RSC). At 6 month of age 5xFAD and App^{NL-G-F} animals had lower activations in RSC compared to littermate controls. An increased activation in RSC around SWRs was observed in 5xFAD at 12-month of age. In 12-month App^{NL-G-F} mice, a significant reduction in RSC activation was observed. Optical flow analysis revealed that the direction of cortical activity propagation around SWRs was reversed for 6- and 12-month 5xFAD animals, whereas the information flow initiated from more anterolateral regions of somatosensory areas (e.g. SSp-m, SSp-n, SSs) towards posteromedial subnetworks such as RSC, association, and visual areas. Further, for 6- and 12-month 5xFAD animals, RSC activity mostly followed SWRs, as opposed to other groups where RSC activity was leading SWRs. These results suggest that there is dysfunction of hippocampal-cortical interactions in AD in which SWRs and SWR-coupled cortical activation is

altered. Targeting these dysfunctions could provide a novel route to ameliorate AD-related pathology, restore/improve memory and cognitive functions.

Introduction

Alzheimer's disease (AD) is a neurodegenerative disease that is pathologically characterized by extracellular deposition of amyloid beta (Aβ) plaques and intracellular deposition of neurofibrillary tangles (NFT) caused by hyperphosphorylated tau protein and neuroinflammation. Clinically it is characterized by progressive loss of cognition (learning and memory), executive function and sensory processing (Hardy and Selkoe, 2002; Qiu et al., 2009; Selkoe and Hardy, 2016). The amyloid cascade hypothesis posits that the deposition of Aβ is the central event in AD pathology leading to tau deposition, and eventually neurodegeneration (Hardy and Selkoe, 2002; Edwards, 2019).

Atrophy of brain regions that are involved in memory processing, such as hippocampus and the neocortex are affected in the early stages of the disease pathology. According to Braak's staging of AD (Braak and Braak, 1991, 1998; Braak et al., 2006; Braak and Del Tredici, 2015) neurons in the entorhinal cortex (EC) that provide input to the hippocampus degenerate early in the course of the disease, followed by hippocampal neurons and then cortical neurons that communicate with hippocampal neurons (Braak and Braak, 1991; Gomez-Isla et al., 1996; Mattson and Magnus, 2006; Stranahan and Mattson, 2010). Aberrant hyperexcitation related to intrinsic firing has been observed in AD, and several studies suggest that impaired spontaneous excitation and inhibition and an increasing state of hyperexcitability originates from EC and then appears in HPC and other cortical areas as the disease progresses (Khan et al., 2014).

Recent studies report that gamma oscillations are impaired in the EC-HPC circuit of AD patients and AD animal models (Stam et al., 2002; Iaccarino et al., 2016;

Nakazono et al., 2017; Wang et al., 2017a; Nakazono et al., 2018; Etter et al., 2019; Chen et al., 2021). In addition, alterations in hippocampal network oscillations such as sharp wave ripples (SWRs) (Gillespie et al., 2016; Jones et al., 2019; Benthem et al., 2020), theta–gamma coupling (Goutagny et al., 2013; Goodman et al., 2018), and abnormal hyper- and hypo- activity (Busche et al., 2008; Busche et al., 2015b; Busche et al., 2019; Marinković et al., 2019) have also been reported in mouse models of AD. Further, grid cell or grid-cell–like representations and place cell dysfunctions have been reported in humans and mouse models of AD (Kunz et al., 2015; Fu et al., 2017; Jun et al., 2020). These disruptions in grid/place cell function might lead to impairments in path integration and spatial remapping causing spatial memory deficits (Allen et al., 2014; Gil et al., 2018; Bierbrauer et al., 2019). Unfortunately, the underlying mechanism by which these dysfunctions occur are unknown. Abnormal hyperactivity has been shown to be an early marker of AD pathology (Busche et al., 2008; Busche et al., 2015b; Xu et al., 2015; Yamamoto et al., 2015; Nuriel et al., 2017; Petrache et al., 2019). Further, increased neuronal activity has been shown to enhance tau propagation and pathology in mice (Wu et al., 2016). This early hyperexcitation could be caused by pro-inflammatory mediators, such as cytokines, reactive oxygen species and free radicals released from the activated astrocytes and glial cells, which themselves are morphologically altered in AD (Olabarria et al., 2010; Rodríguez et al., 2010). Seizure-like activity or hyper activity may be caused by excitation inhibition imbalance that at times is pathologically manifested by inhibitory interneuron deficits (Verret et al., 2012). In a recent study, persistent synaptic hyperexcitation and reduced inhibition are shown in CA1 neurons of 10-18 month old $App^{NL\text{-}F/NL\text{-}F}$ mice. Further, a reduction in the number of parvalbumin-containing (PV) interneurons in Lateral entorhinal cortex (LEC) occurs relative to other cortical areas (Petrache et al., 2019).

A main function of hippocampus and neocortex circuitry in learning and memory is to encode, store and retrieve the information. The disruption of these networks by AD pathology explains the loss of memory in AD patients. One way that this progressive learning and memory impairment happens is by synaptic loss and neurodegeneration caused by plaques and NFTs (Spires-Jones and Hyman, 2014; Edwards, 2019). Hippocampal network activity is likely a biomarker of AD pathology. Multiple signatures of altered hippocampal activity in AD exist depending on the measuring method (EEG, LFP, PET, fMRI etc.). One readout of interest is the electrophysiological signatures of sharp wave ripples (SWRs), which are high frequency oscillatory (100-250 Hz) signals hypothesised to be involved in memory consolidation and retrieval (Buzsáki, 2015). In experiments on spatial navigation, SWRs are associated with memory reactivation, or replay (Wilson and McNaughton, 1994; Skaggs and McNaughton, 1996; Lee and Wilson, 2002). Coordinated interplay between SWRs and cortical slow oscillations is implicated in learning and memory (Schabus et al., 2004; Ulrich, 2016). SWRs mediate hippocampal-cortical interactions during slow wave sleep and in the awake state (during consummation and immobility) and these cortical reactivations are reported to preceded and follow SWRs (Ji and Wilson, 2007; Wierzynski et al., 2009; Buhry et al., 2011; Wang and Ikemoto, 2016; Rothschild et al., 2017; Tang et al., 2017; Gardner et al., 2019). There is a causal role of SWR in learning and memory (Girardeau et al., 2009; Ego-Stengel and Wilson, 2010; Jadhav et al., 2012) and its disruption occurs in mouse models of AD (Ciupek et al., 2015; Gillespie et al., 2016; Iaccarino et al., 2016; Nicole et al., 2016; Jones et al., 2019; Jura et al., 2019; Benthem et al., 2020; Caccavano et al., 2020; Sanchez-Aguilera and Quintanilla, 2021).

The emerging picture is that there is disruption of SWRs in AD and hippocampal-cortical coupling around SWRs is also impaired. In this chapter using widefield cortical voltage sensitive dye imaging and local field potential (LFP) recording from CA1 region of the hippocampus I will address how SWRs and SWR-coupled cortical activity is impaired with age in a knock-in ($App^{NL\text{-}G\text{-}F}$) and a transgenic (5xFAD) mouse model of AD.

Materials and Methods

Surgery for craniotomy and VSDI

At 6 and 12 months of age, craniotomy for VSDI was performed as described previously (Mohajerani et al., 2010; Mohajerani et al., 2013; Kyweriga and Mohajerani, 2016). Mice were anesthetized with isoflurane (1.2–1.5%) for induction, followed by urethane for data collection (1.0-1.2 mg/kg, i.p). Mice were transferred on a metal plate that could be mounted onto the stage of the upright macroscope, and the skull was rotated laterally 30° and fastened to a steel plate. A tracheotomy was performed on mice to assist with breathing before starting the craniotomy. A 7×6 mm unilateral craniotomy (bregma 2.5 to −4.5 mm, lateral 0 to 6 mm) was made and the underlying dura was removed. Body temperature was maintained at 37 ± 0.2 °C degrees using a heating pad with a feedback thermistor.

For *in vivo* VSDI, RH1691 dye (Optical Imaging, New York, NY) was applied to the cortex for 30-45 min. For data collection, 12-bit images were captured with a CCD camera (1M60 Pantera, Dalsa, Waterloo, ON) and E8 frame grabber with XCAP 3.9 imaging software (EPIX, Inc., Buffalo Grove IL). The voltage sensitive dye was excited with a red LED (Luxeon K2, 627 nm center), and excitation filters 630 ± 15 nm (Mohajerani et al., 2010; Mohajerani et al., 2013; Chan et al., 2015; Karimi Abadchi et

al., 2020). Images were taken through a macroscope composed of front-to-front video lenses (8.6 × 8.6 mm field of view, 67 μm per pixel). The depth of field of the imaging setup used was ~1 mm (Lim et al., 2012). To stimulate the forelimbs and hindlimbs, thin acupuncture needles (0.14 mm) were inserted into the paws, and a 1 mA, 1-ms electrical pulse was delivered.

Local field potential (LFP) electrode

Teflon coated stainless steel wires (A-M Systems) with the thickness of 50 μm were used for the hippocampal LFP recordings. The HPC electrode was inserted at an angle of ~58 degrees from the vertical, ~2.5 mm lateral from the midline and tangent to the posterior side of the occipital suture and an approximate depth of 1.8 mm to record LFP activity from pyramidal layer of dorsal CA1.

VSD data pre-processing

VSDI of spontaneous cortical activity was recorded in the absence of visual, olfactory, tactile, or auditory stimulation during 15 min epochs with 10 ms (100 Hz) temporal resolution. Data was first denoised by applying singular-value decomposition and taking only the components with greatest associated singular values. The baseline of the optical signal (F_0) captured from each pixel in the imaging window was calculated using the *locdetrend* function in the Chronux toolbox was used to fit a piecewise linear curve to the pixel time series using the local regression method (Mitra and Bokil, 2008). The fluorescence changes were quantified as $(F-F_0)/F_0 \times 100\%$; F represents the fluorescence signal at any given time and F_0 represents the average of fluorescence over all frames. A band pass filter was applied (0.5–6 Hz) FIR filter on the $\Delta F/F_0$ signal as most of the optical signal power is concentrated in low frequencies (Mohajerani et al., 2013).

VSDI registration

Each mouse cortical imaging data was registered to 2D top view of Allen Mouse brain atlas (https://atlas.brain-map.org/) rotated laterally 30° to match the angle of the mouse head rotation in the VSD experiments. The registration was done based on regions identified by functional cortical mapping done with five different evoked sensory stimuli (contra-lateral stimulation): forelimb or hindlimb paw (1mA, 1 ms), whisker (1ms), auditory (1ms) and visual (1ms). Matlab's *fitgeotrans* function was used to register VSDI data to reference map. Briefly, *figeotrans* function implements a 2D geometric transformation in which points from one Euclidean space are mapped to points in another Euclidean space. For instance, a geometric transform T that implements nonreflective similarity transformation that may include a rotation, a scaling, and a translation, will map a point with Cartesian coordinates (x, y) to another point with Cartesian coordinates (u, v) with the following rule:

$$[u\ v] = [x\ y\ 1]T$$

where, T is a 3-by-3 matrix that depends on four parameters namely, scale factor S, rotation angle θ, translation in x dimension t_x and translation in y dimension t_y.

$$T = \begin{bmatrix} S\cos\theta & -S\sin\theta & 0 \\ S\sin\theta & S\cos\theta & 0 \\ t_x & t_y & 1 \end{bmatrix}$$

We defined 29 cortical areas of interest in the imaging window based on the Allen common coordinate framework, this ensured that all mice had similar regions of interest that were comparable across animals. We then grouped the cortical surface into six functional subgroups (fig 3.1A) according to the Allen CCF (Wang et al., 2020) and some recent studies using widefield optical imaging (Harris et al., 2019; Musall et al.,

2019; Gilad and Helmchen, 2020; Gallero-Salas et al., 2021). Somatomotor areas (Teal): primary motor area (MOp), secondary motor area (MOs). Somatosensory areas (Orange): primary somatosensory area upper limb (SSp-ul), primary somatosensory area lower limb (SSp-ll), primary somatosensory area barrel field (SSp-bfd), primary somatosensory area nose (SSp-n), primary somatosensory area unassigned (SSp-un), primary somatosensory area trunk (SSp-tr), primary somatosensory area mouth (SSp-m), and supplemental somatosensory area (SSs). Lateral areas (Purple): visceral area (VISC) and gustatory areas (GU). Retrosplenial area (Gray): retrosplenial area lateral agranular part (RSPagl) and retrosplenial area dorsal part (RSPd). Visual + Association areas (Green): anteromedial visual area (VISam), laterointermediate area (VISli), posteromedial visual area (VISpm), postrhinal area (VISpor), primary visual area (VISp), lateral visual area (VISl), anterolateral visual area (VISal), posterolateral visual area (VISpl), anterior area (VISa), and rostrolateral visual area (VISrl). Auditory areas (Pink): dorsal auditory area (AUDd), primary auditory area (AUDp), posterior auditory area (AUDpo), ventral auditory area (AUDv), and temporal association areas (TEa).

Sharp wave ripple (SWRs) detection

To detect ripples from the LFP data we used the methodology described in (Mölle et al., 2006). Raw LFP signal was first filtered in the range of 100-250 Hz using a 400-order band-pass FIR filter (Hamming window design) designed in MATLAB. The filtered signal was rectified and smoothed using a rectangular window with the length of 8 ms (RMS signal). The threshold for ripple detection was set to >3 SDs above the mean RMS signal. The beginning and end of a ripple were marked at points at which the RMS signal dropped below 0.75 SD, provided that these two points were separated by 25–75 ms. The center of ripples was defined as the timestamp of their largest troughs between the onset and offset times.

To identify bundled ripples in detected SWRs we used an approach defined in (Karimi Abadchi et al., 2020). First, signal power in the ripple-band frequency (150–250 Hz) was calculated using analytic Morlet wavelet, then following criteria was used to classify the ripple event as bundled ripple: (1) The power signal surpassed an adaptively determined power threshold for at least two successive times; (2) The minimum duration was met for each supra-threshold event; and (3) The temporal distance between two successive supra-threshold peaks was less than 200 ms.

Multiple-unit activity (MUA) was calculated from hippocampal LFP signals using an approach defined in (Karimi Abadchi et al., 2020). Briefly, HPC-LFP was filtered above 300 Hz, rectified, and smoothed with a rectangular window with length of ~3 ms.

Cortical Activity Around SWRs

To study hippocampal-cortical interactions, VSDI data were first filtered in the range of 0.5-6 Hz using a 100-order band-pass FIR filter (Hamming window design) designed in MATLAB. Further, the VSDI frame corresponding to the ripple center was identified, LFP and VSDI data in a 2-second window around the ripple center (i.e. 1 sec before and 1 sec after ripple center) were averaged across all detected ripples to study average cortical activations around HPC-ripples. This peri-SWR cortical activity was z-scored by using mean and standard deviation of cortical activity around timepoints following the same distribution of inter-SWR intervals.

Dividing SWRs and Cortical Activity in Q1 and Q4

To measure asymmetry or skewness of HPC-MUA or cortical activity we used asymmetry index (AI) which is the ratio of difference and sum of mean peri-SWR activity, (X-Y)/(X+Y), where X and Y is mean peri-SWR activity in time Δt and $-\Delta t$

respectively, for analysis we used Δt= 200 ms. Positive AI values represent signal skewed towards right of the SWR center, suggesting the signal to be lagging SWR. Similarly, negative AI values represent signal skewed towards left of the SWR center, suggesting the signal to be leading SWR.

Optical Flow Analysis

The direction of information flow is important to understand the information integration over multiple brain areas. Optical flow analysis provides a novel approach to identify the velocity and directionality of information flow in the brain. Multiple algorithms such as Horn-Schunck (HS), Lucas-Kanade (LK), Temporospatial (TS) and Combined local-global (CLG) have been used in previous studies to quantify information propagation across mouse cortex in widefield optical imaging data (Mohajerani et al., 2013; Afrashteh et al., 2017; Karimi Abadchi et al., 2020). Here we used the CLG (Bruhn et al., 2005; Jara et al., 2015) method to quantify optical flow of widefield VSDI data during evoked activations. The advantage of using CLG method over others is that it considers both local and global approaches, leading to dense flow fields that are robust against noise. We used the Matlab implementation of CLG method by Ce Liu (Liu, 2009) to quantify the direction of information flow in the cortex around sharp wave ripples (200 ms before and 200 ms after the SWR center).

Statistical Analysis

MATLAB 2019b was used for statistical analysis of SWRs and per-SWR cortical activity. A p value < 0.05 was considered statistically significant, adjusted p values reported. Two-Sample t-test was used to compare change in Q1 and Q4 of RSC or HPC-MUA activity. One-sample t-test was used to find if AI was above or below chance. One-, two- or three- way ANOVA followed by Bonferroni multiple comparison

was used to determine the effects of age, age + genotype, age + genotype + region. The adjusted critical p-value ($p < 0.05$) was considered significant.

Results

Disrupted SWRs in AD

SWR disruption has been shown previously in mouse models of AD, however, most of these studies have focused on simple metrics such as SWR rate/abundance (Ciupek et al., 2015; Gillespie et al., 2016; Iaccarino et al., 2016; Nicole et al., 2016; Jones et al., 2019; Jura et al., 2019; Benthem et al., 2020; Caccavano et al., 2020; Sanchez-Aguilera and Quintanilla, 2021). SWR abundance has been shown to be reduced in AD (Ciupek et al., 2015; Gillespie et al., 2016; Nicole et al., 2016). In our study we found a significant effect of age on SWR abundance in 5xFAD mice, there was significant reduction of SWR in 12-month-old 5xFAD$^+$ mice. No significant change in SWR abundance was observed for App and C57 group (see Table 3.1 for detail statistics). We extended our analysis from simple ripple abundance analysis to identify more specific patterns of disordered activity during events of SWRs. We evaluated if certain specific signal band are impacted during SWRs as shown by others (Gillespie et al., 2016; Iaccarino et al., 2016; Caccavano et al., 2020). Fig 3.1B presents welch's power spectral density estimate of per-SWR CA1-LFP. We focused our analysis on three frequency bands around SWRs *viz.* low-, high- gamma band power (30-55 Hz and 65-90 Hz) and ripple band power (100-250 Hz) (fig 3.1C-E) (see Table 3.1 for detail statistics). For 5xFAD group, significant effect of age was observed in low-, high- gamma and ripple band power, with increased low-gamma and ripple band power in 12-month-old 5xFAD$^+$ mice. For App group, significant effect of age was observed in ripple power. For C57 group there was significant decrease in high-gamma band power at 12-month.

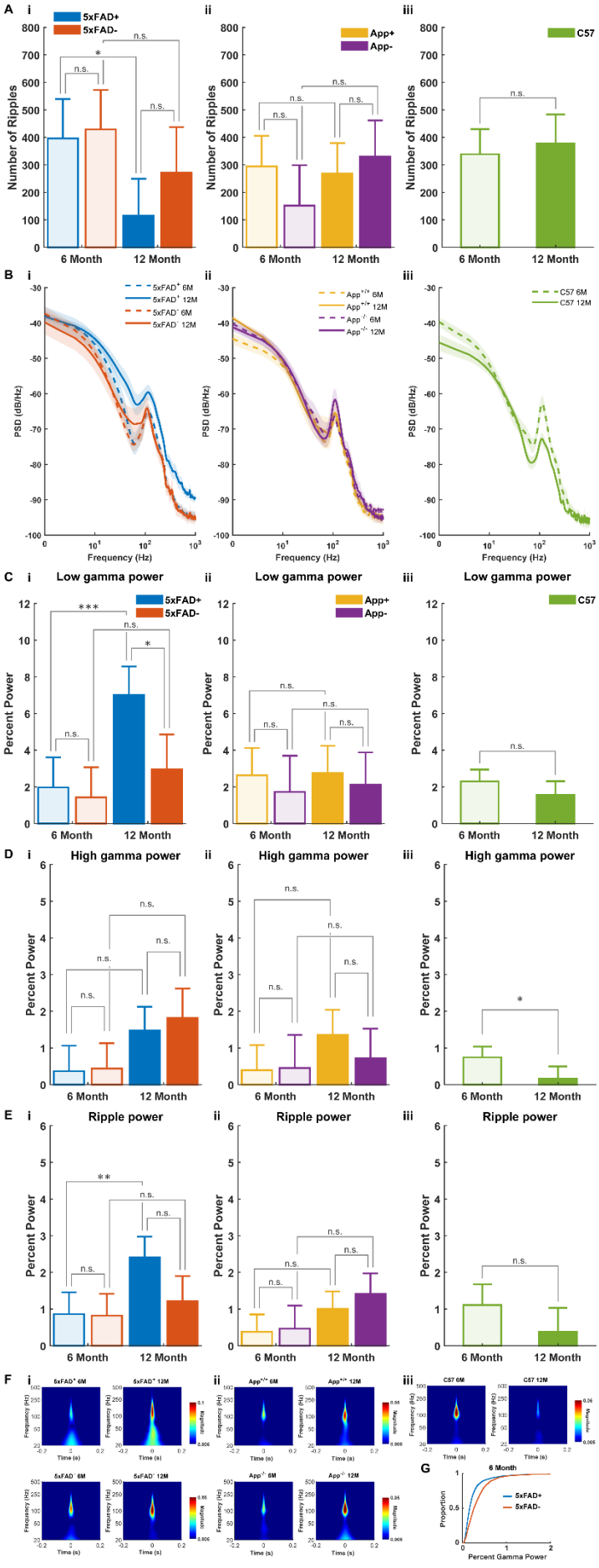
A
i
5xFAD+
5xFAD-
Number of Ripples
6 Month
12 Month
ii
App+
App-
iii
C57
B
PSD (dB/Hz)
Frequency (Hz)
C
Low gamma power
Percent Power
D
High gamma power
E
Ripple power
F
Time (s)
G
Proportion
Percent Gamma Power
n.s.

Figure 3.1: LFP power around sharp wave ripple.
(A) Ripple abundance is significantly reduced in 12-month-old 5xFAD^{+} mice. (B) Welch's power spectral density estimate of per-SWR LFP signal show an increase in SWR band power across all groups, the shaded is signal is SEM. (C-E) changes in low-, high- gamma band power (30-55 Hz and 65-90 Hz) and SWR band power (100-250 Hz) during SWR. A significant increase in signal power is observed in 5xFAD^{+} 12-month group. (F) time frequency representation of mean peri-SWR LFP using continuous wavelet transform (cwt) - analytical Morlet (Gabor) wavelet. There is an increase in ripple band power (100-250 Hz) and gamma band power (30-90 Hz) around zero time which is the center of the SWR. In general, an increase in these frequency bands is observed with age in all groups except C57 in which at 12 month there is reduction in ripple and gamma band power. (G) cumulative distribution function (*cdf*) of pooled high gamma band power during all SWRs for 6-month 5xFAD group showing significant reduction in gamma band power in 5xFAD^{+} mice as shown by (Iaccarino et al., 2016). (6-month-old: C57BL/6J, n = 7; App$^{+/+}$, n = 6; App$^{-/-}$, n = 5; 5xFAD^{+}, n = 8; 5xFAD^{-}, n = 8 and 12-month-old: C57BL/6J, n = 6; App$^{+/+}$, n = 7; App$^{-/-}$, n = 4; 5xFAD^{+}, n = 8; 5xFAD^{-}, n = 6). * = $p < 0.05$; ** = $p < 0.01$; *** = $p < 0.001$; >*** = $p < 0.001$.

Table 3.1: ANOVA table for statistical comparison of number of ripples, low gamma power, high gamma power and ripple power.

5xFAD Number of Ripples						
Source	Sum Sq.	d.f.	Singular?	Mean Sq.	F	Prob>F
Age	364947.7	1	0	364947.7	8.909813	0.005962
Genotype	69091.74	1	0	69091.74	1.686802	0.205006
Age*Genotype	29467.27	1	0	29467.27	0.719412	0.403794
Error	1105925	27	0	40960.19		
Total	1628347	30	0			
APP Number of Ripples						
Source	Sum Sq.	d.f.	Singular?	Mean Sq.	F	Prob>F
Age	31388.74	1	0	31388.74	1.454127	0.242669
Genotype	8878.587	1	0	8878.587	0.411313	0.528965
Age*Genotype	56862.91	1	0	56862.91	2.634254	0.121057
Error	410133.3	19	0	21585.96		
Total	488257.2	22	0			
C57 Number of Ripples						
Source	Sum Sq.	d.f.	Singular?	Mean Sq.	F	Prob>F
Age	5293.149	1	0	5293.149	0.315853	0.584456
Error	201099.2	12	0	16758.27		
Total	206392.4	13	0			

5xFAD Low Gamma Power						
Source	Sum Sq.	d.f.	Singular?	Mean Sq.	F	Prob>F
Age	82.1717	1	0	82.1717	15.25757	0.000567
Genotype	40.0334	1	0	40.0334	7.433368	0.011107
Age*Genotype	23.40866	1	0	23.40866	4.346501	0.046672
Error	145.4121	27	0	5.385634		
Total	311.6894	30	0			
APP Low Gamma Power						
Source	Sum Sq.	d.f.	Singular?	Mean Sq.	F	Prob>F
Age	0.344691	1	0	0.344691	0.088665	0.769112
Genotype	3.23222	1	0	3.23222	0.831429	0.373284
Age*Genotype	0.098514	1	0	0.098514	0.025341	0.8752
Error	73.86345	19	0	3.88755		
Total	77.32129	22	0			
C57 Low Gamma Power						
Source	Sum Sq.	d.f.	Singular?	Mean Sq.	F	Prob>F
Age	1.862677	1	0	1.862677	2.222999	0.16178
Error	10.05494	12	0	0.837912		
Total	11.91762	13	0			

5xFAD High Gamma Power						
Source	Sum Sq.	d.f.	Singular?	Mean Sq.	F	Prob>F
Age	11.69251	1	0	11.69251	12.20668	0.00166
Genotype	0.334972	1	0	0.334972	0.349702	0.559201
Age*Genotype	0.150124	1	0	0.150124	0.156726	0.6953
Error	25.86272	27	0	0.957879		
Total	37.604	30	0			
APP High Gamma Power						
Source	Sum Sq.	d.f.	Singular?	Mean Sq.	F	Prob>F
Age	2.060291	1	0	2.060291	2.529455	0.12824
Genotype	0.460024	1	0	0.460024	0.564779	0.461549
Age*Genotype	0.662888	1	0	0.662888	0.813839	0.378282
Error	15.47587	19	0	0.81452		
Total	19.30883	22	0			
C57 High Gamma Power						
Source	Sum Sq.	d.f.	Singular?	Mean Sq.	F	Prob>F
Age	1.183452	1	0	1.183452	6.919687	0.021954
Error	2.052322	12	0	0.171027		
Total	3.235774	13	0			

5xFAD Ripple Power						
Source	Sum Sq.	d.f.	Singular?	Mean Sq.	F	Prob>F
Age	7.176099	1	0	7.176099	10.11967	0.003669
Genotype	2.915392	1	0	2.915392	4.111259	0.052573
Age*Genotype	2.554031	1	0	2.554031	3.601671	0.068462
Error	19.14635	27	0	0.709124		
Total	33.59408	30	0			
APP Ripple Power						
Source	Sum Sq.	d.f.	Singular?	Mean Sq.	F	Prob>F
Age	3.35906	1	0	3.35906	8.54927	0.008708
Genotype	0.325326	1	0	0.325326	0.828	0.374251
Age*Genotype	0.136487	1	0	0.136487	0.347379	0.562544
Error	7.465216	19	0	0.392906		
Total	11.30946	22	0			
C57 Ripple Power						
Source	Sum Sq.	d.f.	Singular?	Mean Sq.	F	Prob>F
Age	1.833376	1	0	1.833376	2.870527	0.115987
Error	7.664278	12	0	0.63869		
Total	9.497654	13	0			

Fig 3.1F is time frequency representation of mean peri-SWR LFP using continuous wavelet transform (cwt) - analytical Morlet (Gabor) wavelet. These results of gamma-band power analysis for six month old 5xFAD mice are different from those reported earlier (Iaccarino et al., 2016), the reason for an opposite finding lies in their analytic approach in which they pooled gamma band power during all SWRs that accumulated to ~2000-3000 events across all animals, this was followed by a rank-sum

test. Interestingly, if we pool our data in same way as Iaccarino et al. we get similar results (6-month 5xFAD^{+} n = 3169 events, 8 animals; 5xFAD^{-} n = 3434 events, 8 animals; rank-sum test p = 1.4193 x 10^{-12}) (fig 3.1G).

Hippocampal cortical interactions during SWRs

In vivo wide field voltage sensitive dye (VSD) imaging of mouse neocortical dynamics and simultaneous recording of local field potential (LFP) from the dorsal region of CA1 was conducted in head-fixed mice under urethane anaesthesia (Fig. 3.1 A). A large unilateral craniotomy over right hemisphere was done which provided us access to more lateral regions like primary auditory cortex, LFPs were recorded from the ipsilateral hippocampus. Spontaneous alternations between REM-like and non-REM like episodes was observed in animals under urethane anaesthesia. Classical electrophysiological signatures of slow-wave sleep (SWS), such as up- and down-states, sleep spindles, delta waves and sharp wave ripples, are known to exist in animals under urethane anaesthesia (Wolansky et al., 2006; Clement et al., 2008; Pagliardini et al., 2013; Karimi Abadchi et al., 2020).

To detect events of SWRs, the LFP from CA1 region of the hippocampus was first filtered in the range of 100-250 Hz using a 400-order band-pass FIR filter (Hamming window design) designed in MATLAB. This filtered signal was then rectified and smoothed to create an RMS signal, a threshold of 3 standard deviations above the mean RMS signal was used to detect SWRs (fig 3.1B). VSDI data ($\Delta F/F_0$) was first registered to the reference atlas map and then band pass filtered in the range of 0.5-6 Hz. Cortical activation 1 sec before and after the center of the SWR events was extracted, aligned and averaged over all events to study spatio-patterns of cortical activity around SWRs (fig 3.1C). We found that cortical activation around SWRs

resembles a default mode network (DMN)-like module shown in rodent rs-fMRI studies (Liska et al., 2015; Gutierrez-Barragan et al., 2019; Coletta et al., 2020; Whitesell et al., 2021).

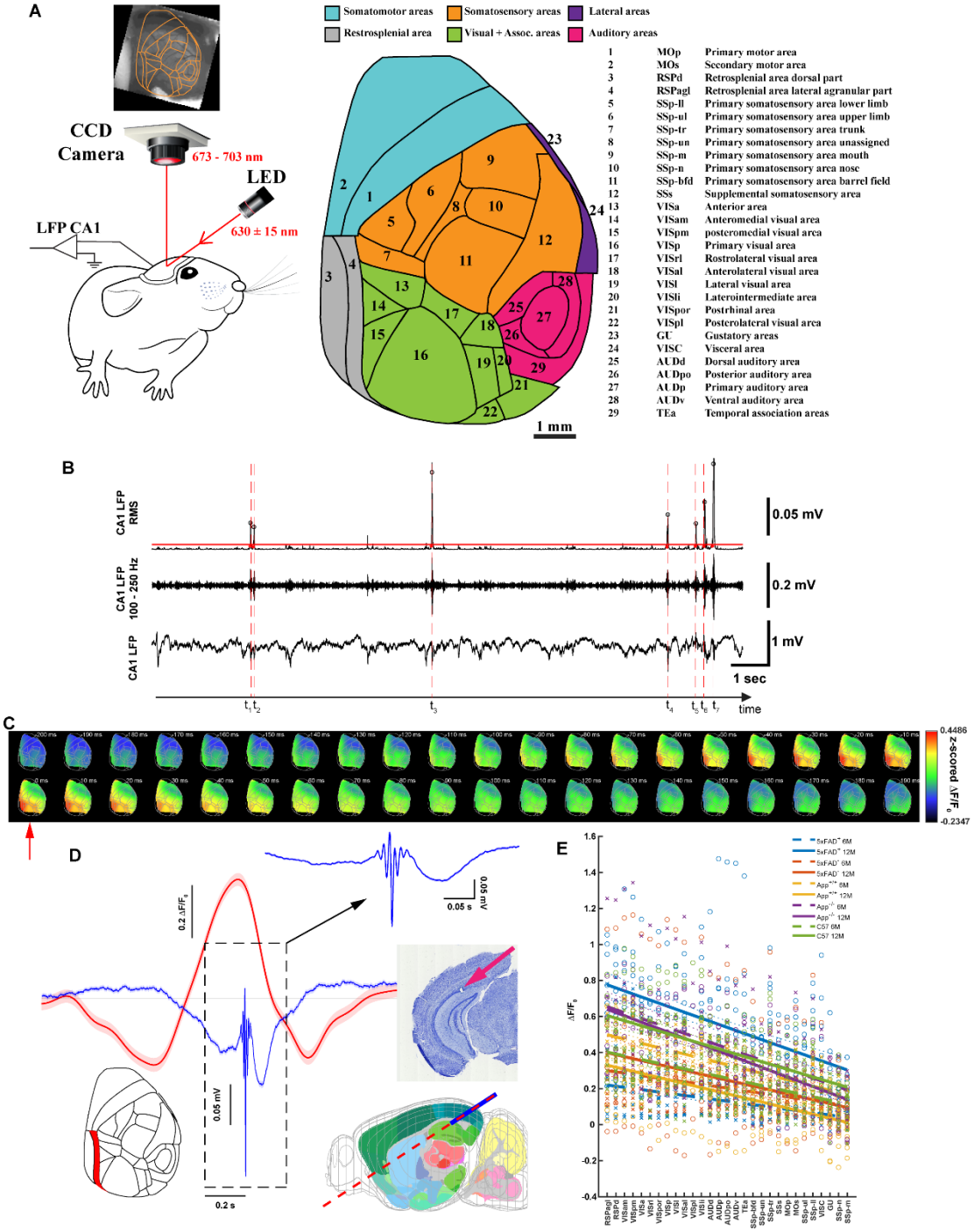

Figure 3.2: Experimental paradigm for SWR triggered cortical activation.

(A) cartoon representation of experimental paradigm. Animal is head-fixed under urethane anaesthesia with unilateral craniotomy, right hemisphere, 7×6 mm window; bregma: 2.5 to −4.5 mm, lateral: 0 to 6 mm. LFP electrode in ipsilateral dorsal CA1 inserted at an angle of ~58°

from the vertical, ~2.5 mm lateral from the midline and tangent to the posterior side of the occipital suture and an approximate depth of 1.8 mm. We defined 29 cortical areas of interest in the imaging window based on the Allen common coordinate framework, which were then grouped into six functional subgroups: Somatomotor (Teal), Somatosensory (Orange), Lateral (Purple), Retrosplenial (Gray), Visual + Association (Green), and Auditory areas (Pink). (B) To identify events of SWRs, LFP from CA1 region was filtered in the range of 100-250 Hz then rectified and smoothed to create a (RMS signal). The threshold for ripple detection was then applied to this RMS signal (>3 SDs above the mean RMS signal). It is worth noticing that events of SWR sometime occur as single events (e.g. t_3 t_4) and sometime in groups of 2 or 3 (e.g. t_1-t_2 , t_5-t_7) which we call here as bundled ripples (C) VSDI data was first filtered in the range of 0.5-6 Hz and frame corresponding to the ripple center was identified. VSDI data in a 2-second window around the ripple center (i.e. 1 sec before and 1 sec after ripple center) was averaged across all detected ripples. Here we present an example of peri-SWR cortical activation 200 ms before and after the SWR center (red arrow). Interestingly this peri-SWR cortical activation started from midline and retrosplenial areas and travelled laterally towards auditory cortex. (D) peri-SWR average cortical activity trace from RSC area lateral agranular part (RSPagl) highlighted in red on the cortical map, and corresponding average SWR (blue), the shaded signal is SEM. Inset is zoomed average SWR. Nissl-stained brain slice showing electrode location in dorsal CA1 region of hippocampus. (E) Peak cortical activation around SWR center sorted in decreasing order reveals that somatomotor, somatosensory, auditory, and lateral areas have reduced activation as compared to retrosplenial, association and visual areas. There is a significant linear relationship between decreasing amplitude and regions ($\Delta F/F_0 \sim 1 + Regions$); adjusted R-squared: 0.1739, 0.2278, 0.2107, 0.0785, 0.4354, 0.2345, 0.2249, 0.3803, 0.2409, 0.2678; *p*-value: 4.23×10^{-11}, 2.60828×10^{-14}, 2.39342×10^{-13}, 0.000180181, 2.44654×10^{-26}, 2.25536×10^{-13}, 1.50357×10^{-09}, 2.99947×10^{-16}, 1.02312×10^{-14}, 2.99571×10^{-13}; for $5xFAD^{+}$-6 month (n = 8), $5xFAD^{+}$-12 month (n = 8), $5xFAD^{-}$-6 month (n = 8), $5xFAD^{-}$-12 month (n = 6), $App^{+/+}$-6 month (n = 6), $App^{+/+}$-12 month (n = 7), $App^{-/-}$-6 month (n = 5), $App^{-/-}$-12 month (n = 4), C57BL/6J -6 month (n = 7) and C57BL/6J -12 month (n = 6) animals respectively.

Cortical activation around SWRs followed a unique spatio-temporal pattern in which the midline and posterior cortical areas show increase in activation ~200 ms before the center of SWR, cortical activity peaked around time 0 which is the center of SWR and decreased subsequently over next ~200 ms. However, cortical subnetworks had unique patterns of peak activations in which the somatomotor, somatosensory, auditory, and lateral areas have reduced activation as compared to retrosplenial, association and visual areas. Fig 3.1E show activity in cortical regions sorted in decreasing order of activation, where retrosplenial (RSC) cortex showed peak activations around SWR events.

Cortical activations around SWRs in AD

We investigated if there are changes associated with disease pathology on overall SWR-triggered cortical activation. Cortical frames in the time window of 1 sec

before and after the SWR center were z-score averaged and time series of regional activation was extracted from 29-regions of interest. For 5xfAD group we found that there was significant effect of age and genotype on cortical activation around SWR, further, interaction between age and genotype was significant (see Table 3.2 for detail statistics). At 6-months 5xFAD^{+} mice had reduced overall activation w.r.t. littermate controls, however at 12-month there was hyper activation w.r.t. age and littermate control (fig 3.3A). For App group there was significant effect of age and genotype on cortical activation around SWR, further, interaction between age and genotype was significant (see Table 3.2 for detail statistics). Cortical activation in *App*$^{+/+}$ group significantly reduced w.r.t. littermate controls at 6- and 12- months (fig 3.3A). For C57 group there was significant increase in cortical activation with age (fig 3.3A). These changes could be related to the AD pathology (synaptic deficits, axonal transportation, Aβ, inflammation etc.) which may be differentially affecting cortical dynamics in these two different mouse models. Beker et al. proposed that higher firing rate during Up state may lead to hyperexcitability in AD, and a reduction in the sustained firing rate may lead to failures in generating and maintaining the Up states (Beker et al., 2016). It has also been shown that failure of inhibitory neurons to generate action potentials in the hippocampus and subsequent hyperexcitation could be the underlying cellular mechanisms of AD pathophysiology (Hazra et al., 2013).

Full width half max (FWHM) is time duration for which peri-SWR cortical activation is greater than or equal to half of its maximum value. FWHM quantifies if the pulse width of cortical activation changes with disease or age. For 5xFAD group we found significant effect of age and genotype, there is reduction of FWHM in 5xFAD^{+} mice suggesting short temporal activation (fig 3.3B) (see Table 3.2 for detail statistics). For App group there is significant effect of genotype, there is increased FWHM for

App$^{+/+}$ group suggesting longer temporal activation (fig 3.3B). For C57 group there is significant increase in FWHM with age (fig. 3.3B). Fig 3.4A presents cortical activations in individual brain regions across all groups. At 6-month of age 5xFAD^{+} and *App*$^{+/+}$ animals had lower activations as compared to littermate controls, interestingly compared to C57BL/6J animals *App*$^{+/+}$ animals had increased activations around SWR at 6 months (fig 3.4B). This effect of comparison with littermate and C57 control was also observed in cortical-correlation analysis of *App*$^{+/+}$ mice at 6-months (fig 2.19 & fig 2.20). If we look at subnetwork level activations (fig 3.5) significant difference is observed in 12-month-old 5xFAD^{+} mice for all subnetworks, where there is hyper activation (see Table 3.3 for detail statistics). For App group there is significant effect of genotype on RSC + association, visual + association, and auditory network with reduced activation in *App*$^{+/+}$ mice (see Table 3.3 for detail statistics). No significant effect of age was observed on C57 subnetwork activations.

Further using optical flow and lagged correlation analyses we evaluated how the spatial propagation of cortical activity in 200 ms time window around SWR center is impacted with disease. Using Combined local-global (CLG) method for optical flow analysis we observed that cortical activation around SWRs follows a pattern of activation from posteromedial subnetworks such as RSC, association, and visual areas, towards lateral subnetworks such as auditory, and lateral areas. For most of the control cases the cortical signal flow followed this propagation pattern. For 5xFAD group there was significant effect of genotype and age on direction of propagation, further, there was interaction between age and genotype (see Table 3.4 for detail statistics). For 6- and 12-month 5xFAD^{+} animals the direction of peri-SWR cortical signal propagation was reversed where the information flow initiated from more anterolateral regions of somatosensory areas (e.g., SSp-m, SSp-n, SSs) towards posteromedial subnetworks

such as RSC, association, and visual areas (fig 3.6). For App group there was significant effect of genotype on direction of propagation, further, there was interaction between age and genotype (see Table 3.4 for detail statistics). for 6- and 12-month $App^{+/+}$ animals the direction of propagation was stronger towards anterolateral regions of somatosensory areas (e.g., SSp-m, SSp-n, SSs) (fig. 3.7). For C57 group there was significant effect of age on direction of propagation, further for 12- month C57 mice the direction of propagation was stronger towards temporal association areas (TEa) (fig. 3.8).

Using lagged correlation analysis of peri-SWR cortical activity (fig 3.9) we found that cortical activity around SWRs in posteromedial subnetworks such as RSC, association and visual areas leads the somatosensory and lateral networks. However, for 6- and 12- month $5xFAD^{+}$ mice, cortical activity around SWRs in anterolateral regions of somatosensory areas (e.g. SSp-m, SSp-n, SSs) and lateral areas (VIS, GU) leads posteromedial subnetworks such as retrosplenial, association and visual areas. These results are similar to that observed using optical flow analysis presented in fig 3.6.

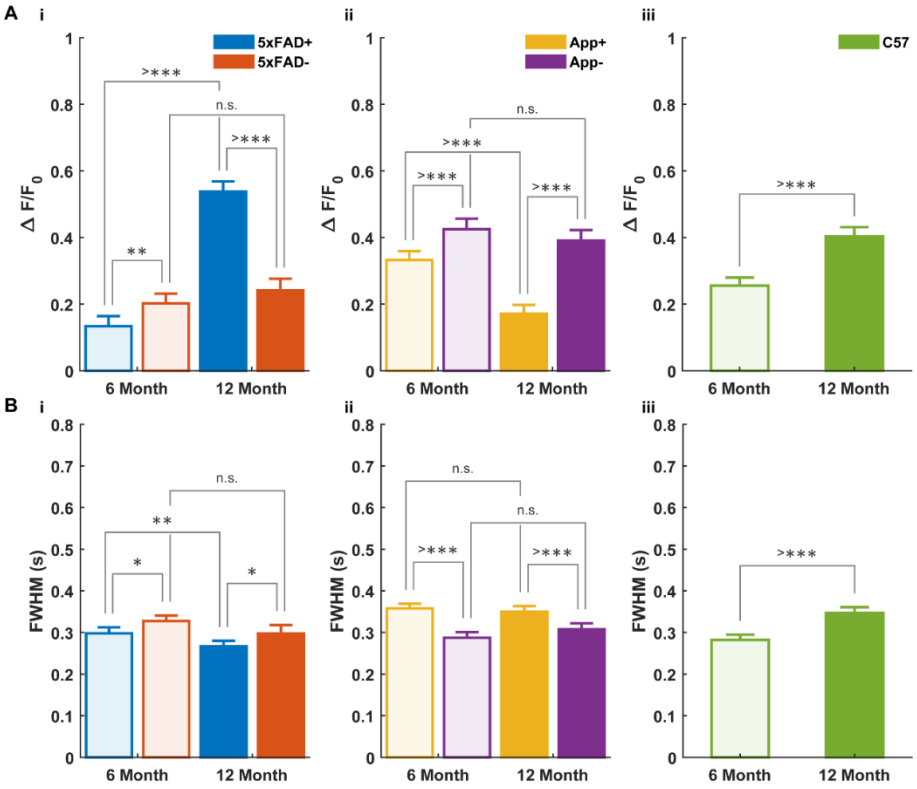

Figure 3.3: peri-SWR cortical activation amplitude and FWHM.
(A) Increased cortical activation around SWR is observed in 5xFAD^{+}-12-month mice, here is reduced cortical activation in *App*$^{+/+}$ mice at 6- and 12-month, and for C57 group there is increased activation with age. (B) FWHM is reduced in 5xFAD^{+} mice suggesting reduced temporal activation, for *App*$^{+/+}$ and 12-month C57 mice FWHM in increased suggesting increased temporal activation. (6-month-old: C57BL/6J, n = 7; App$^{+/+}$, n = 6; App$^{-/-}$, n = 5; 5xFAD^{+}, n = 8; 5xFAD^{-}, n = 8 and 12-month-old: C57BL/6J, n = 6; App$^{+/+}$, n = 7; App$^{-/-}$, n = 4; 5xFAD^{+}, n = 8; 5xFAD^{-}, n = 6). * = $p < 0.05$; ** = $p < 0.01$; *** = $p < 0.001$; >*** = $p <$ 0.001.

Table 3.2: ANOVA table for statistical comparison of peri-SWR cortical activation amplitude and FWHM.

5xFAD Amplitude						
Source	Sum Sq.	d.f.	Singular?	Mean Sq.	F	Prob>F
Regions	7.828183	28	0	0.279578	6.210586	2.89E-20
Age	8.733209	1	0	8.733209	194.0008	2.27E-39
Genotype	2.311035	1	0	2.311035	51.33767	1.87E-12
Regions*Age	1.30117	28	0	0.04647	1.032299	0.420189
Regions*Genotype	0.377861	28	0	0.013495	0.299781	0.999859
Age*Genotype	6.792334	1	0	6.792334	150.8859	1.02E-31
Error	33.62722	747	0	0.045016		
Total	64.43884	834	0			
APP Amplitude						
Source	Sum Sq.	d.f.	Singular?	Mean Sq.	F	Prob>F
Regions	11.56058	28	0	0.412878	12.07056	5.29E-42
Age	1.54368	1	0	1.54368	45.12978	4.34E-11
Genotype	3.926771	1	0	3.926771	114.7999	1.32E-24
Regions*Age	0.295443	28	0	0.010552	0.308476	0.999807
Regions*Genotype	0.410374	28	0	0.014656	0.428477	0.996002
Age*Genotype	0.661529	1	0	0.661529	19.33992	1.3E-05
Error	20.24957	592	0	0.034205		
Total	38.71501	679	0			
C57 Amplitude						
Source	Sum Sq.	d.f.	Singular?	Mean Sq.	F	Prob>F
Regions	4.889209	27	0	0.181082	5.756654	9.06E-16
Age	2.048524	1	0	2.048524	65.1233	1.34E-14
Regions*Age	0.267176	27	0	0.009895	0.314578	0.99967
Error	10.3176	328	0	0.031456		
Total	17.38118	383	0			

5xFAD FWHM						
Source	Sum Sq.	d.f.	Singular?	Mean Sq.	F	Prob>F
Regions	0.244723	28	0	0.00874	1.037003	0.414034
Age	0.118782	1	0	0.118782	14.09329	0.000189
Genotype	0.12299	1	0	0.12299	14.59266	0.000146
Regions*Age	0.11472	28	0	0.004097	0.486121	0.988943
Regions*Genotype	0.107973	28	0	0.003856	0.457531	0.993171
Age*Genotype	0.000109	1	0	0.000109	0.012906	0.909586
Error	5.495209	652	0	0.008428		
Total	6.372325	739	0			
APP FWHM						
Source	Sum Sq.	d.f.	Singular?	Mean Sq.	F	Prob>F
Regions	0.249839	28	0	0.008923	1.479319	0.05558
Age	0.005264	1	0	0.005264	0.87273	0.350636
Genotype	0.442141	1	0	0.442141	73.30268	1.27E-16
Regions*Age	0.071899	28	0	0.002568	0.425719	0.996162
Regions*Genotype	0.072368	28	0	0.002585	0.428496	0.995945
Age*Genotype	0.028828	1	0	0.028828	4.779369	0.029249
Error	3.124428	518	0	0.006032		
Total	4.106276	605	0			
C57 FWHM						
Source	Sum Sq.	d.f.	Singular?	Mean Sq.	F	Prob>F
Regions	0.245605	27	0	0.009096	1.208597	0.222478
Age	0.373329	1	0	0.373329	49.6021	1.19E-11
Regions*Age	0.058674	27	0	0.002173	0.28873	0.999854
Error	2.370842	315	0	0.007526		
Total	3.075566	370	0			

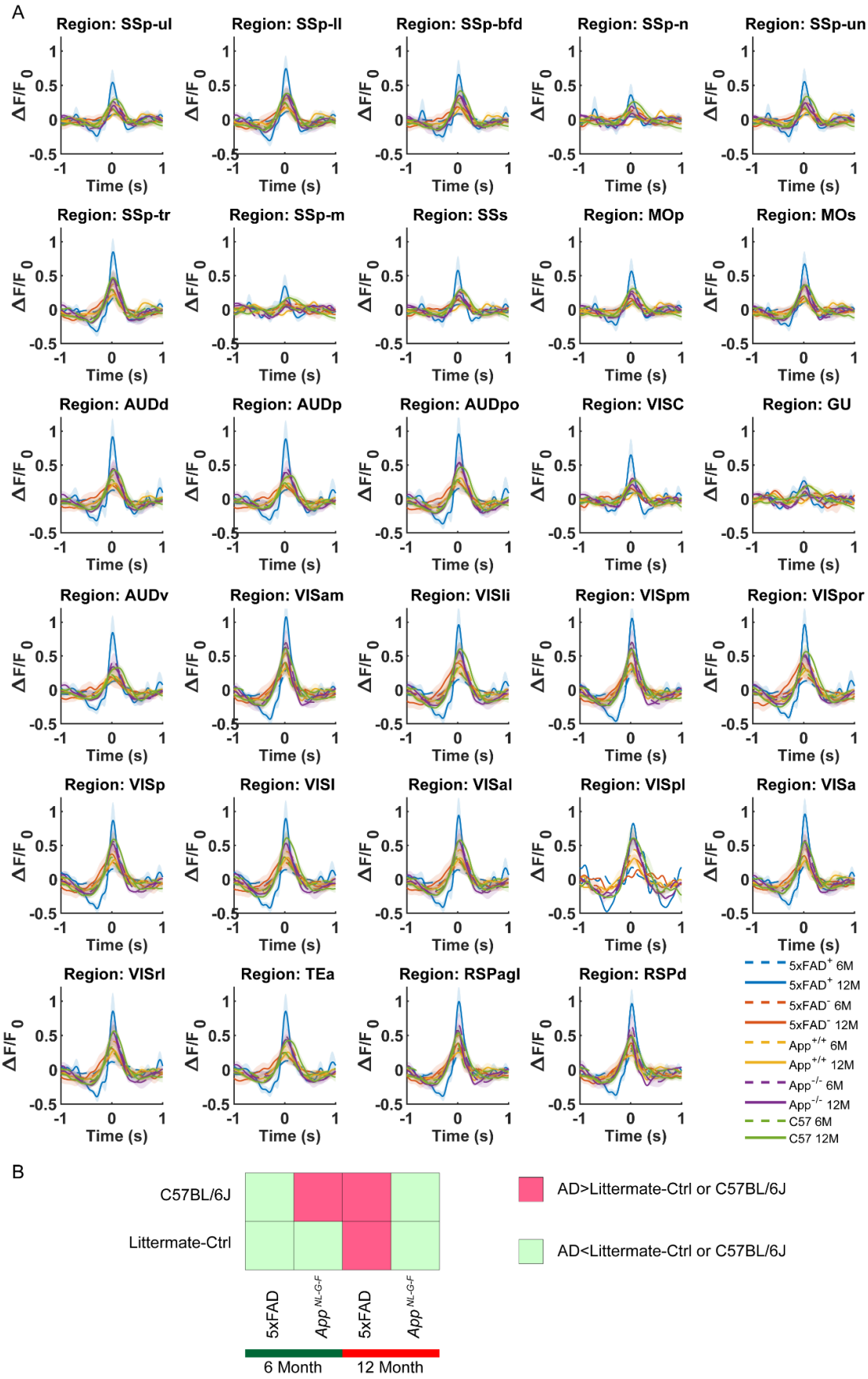

Figure 3.4: Region based cortical activations around SWR.
(A) Analysis of regional cortical activity around SWRs reveals that for most neocortical regions transiently deactivated followed by a strong activation around SWR center in most regions.

Cortical activations in lateral areas are significantly reduced in some somatomotor, somatosensory, auditory, and lateral areas (e.g. SSp-m, SSp-n, GU, VISC) as compared to retrosplenial, association and visual areas. Aberrant cortical activations were observed in AD animals as compared to littermate controls and C57BL/6J animals. (B) Increased cortical activations around SWR were observed in 5xFAD^{+} at 12-months of age however in 12-month *App*$^{+/+}$ animals' significant reduction in activations was observed. At 6 month of age 5xFAD^{+} and *App*$^{+/+}$ animals had lower activations as compared to littermate controls, interestingly compared to C57BL/6J animals *App*$^{+/+}$ animals had increased activations around SWR at 6 months. This effect of comparison with littermate and C57 control was also observed in cortical-correlation analysis at 6 months (fig 2.19 & fig 2.20). primary motor area (MOp), secondary motor area (MOs). Somatosensory areas (Orange): primary somatosensory area upper limb (SSp-ul), primary somatosensory area lower limb (SSp-ll), primary somatosensory area barrel field (SSp-bfd), primary somatosensory area nose (SSp-n), primary somatosensory area unassigned (SSp-un), primary somatosensory area trunk (SSp-tr), primary somatosensory area mouth (SSp-m), and supplemental somatosensory area (SSs), visceral area (VISC), gustatory areas (GU, retrosplenial area lateral agranular part (RSPagl) and retrosplenial area dorsal part (RSPd). Visual + Association areas (Green): anteromedial visual area (VISam), laterointermediate area (VISli), posteromedial visual area (VISpm), postrhinal area (VISpor), primary visual area (VISp), lateral visual area (VISl), anterolateral visual area (VISal), posterolateral visual area (VISpl), anterior area (VISa), and rostrolateral visual area (VISrl). Auditory areas (Pink): dorsal auditory area (AUDd), primary auditory area (AUDp), posterior auditory area (AUDpo), ventral auditory area (AUDv), and temporal association areas (TEa). (6-month-old: C57BL/6J, n = 7; App$^{+/+}$, n = 6; App$^{-/-}$, n = 5; 5xFAD^{+}, n = 8; 5xFAD^{-}, n = 8 and 12-month-old: C57BL/6J, n = 6; App$^{+/+}$, n = 7; App$^{-/-}$, n = 4; 5xFAD^{+}, n = 8; 5xFAD^{-}, n = 6).

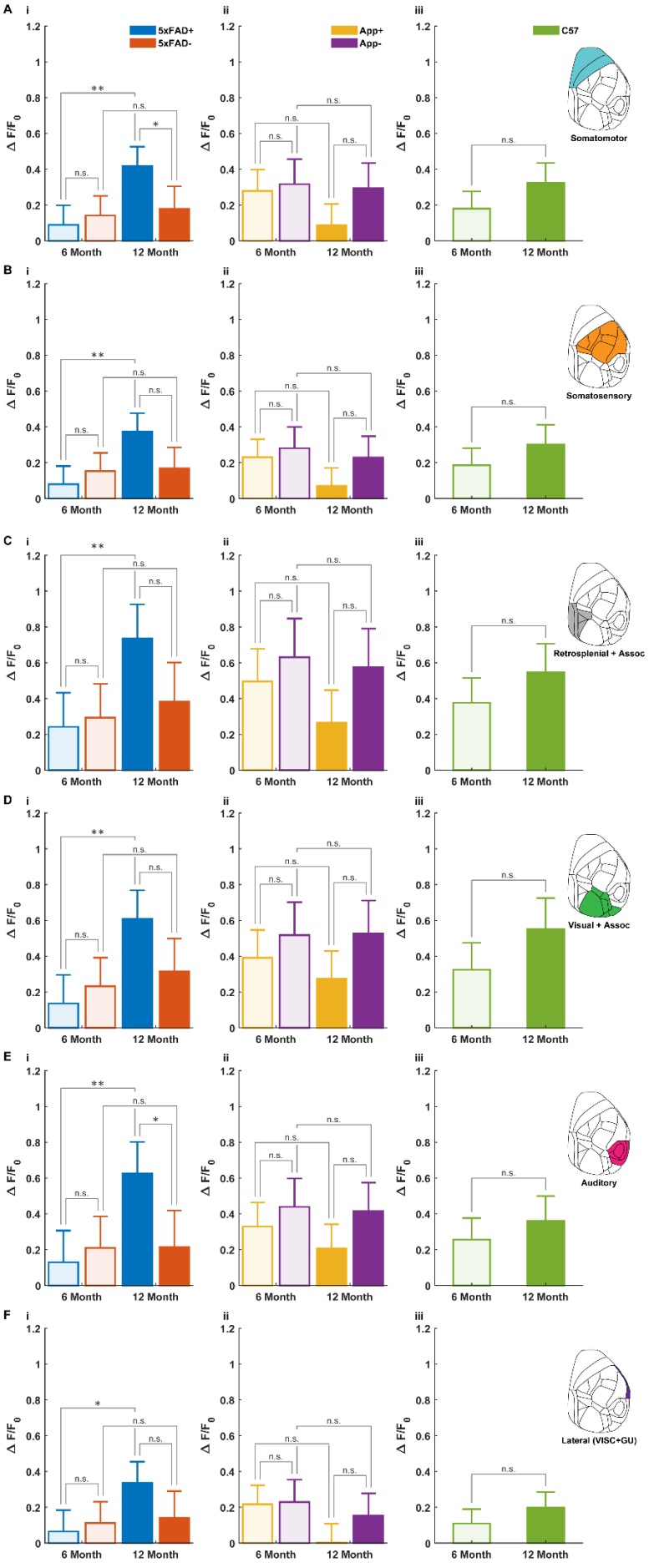
A
B
C
D
E
F
i
ii
iii
5xFAD+
5xFAD-
App+
App-
C57
Somatomotor
Somatosensory
Retrosplenial + Assoc
Visual + Assoc
Auditory
Lateral (VISC+GU)
Δ F/F0
6 Month
12 Month
n.s.
*
**

Figure 3.5: Average peri-SWR cortical subnetworks activations.
(A-F) 29 cortical areas of interest in the imaging window based on the Allen common coordinate framework regions were then grouped into six functional subgroups: Somatomotor (Teal), Somatosensory (Orange), Lateral (Purple), Retrosplenial + Association (Gray), Visual + Association (Green), and Auditory areas (Pink); and average cortical functional connectivity from these subgroups was further compared across groups. Average cortical activity around SWR was calculated in these subnetworks. Significant difference is observed in average cortical activity of 12-month-old 5xFAD^{+} mice for all subnetworks, where there is hyper activation. For App group there is significant effect of genotype on RSC + association, visual + association, and auditory network with reduced activation in *App*$^{+/+}$ mice (C-E). No significant effect of age was observed on C57 subnetwork activations (A-F). (6-month-old: C57BL/6J, n = 7; App$^{+/+}$, n = 6; App$^{-/-}$, n = 5; 5xFAD^{+}, n = 8; 5xFAD^{-}, n = 8 and 12-month-old: C57BL/6J, n = 6; App$^{+/+}$, n = 7; App$^{-/-}$, n = 4; 5xFAD^{+}, n = 8; 5xFAD^{-}, n = 6). * = $p < 0.05$; ** = $p < 0.01$; *** = $p < 0.001$; >*** = $p < 0.001$.

Table 3.3: ANOVA table for statistical comparison of average per-SWR cortical subnetwork activations.

Ripple Triggred Amplitude Somatomotor

5xFAD

Source	Sum Sq.	d.f.	Singular?	Mean Sq.	F	Prob>F
Age	0.245844	1	0	0.245844	10.39007	0.0034
Genotype	0.063879	1	0	0.063879	2.699729	0.112406
Age*Genotype	0.155189	1	0	0.155189	6.558735	0.016588
Error	0.615197	26	0	0.023661		
Total	1.117208	29	0			

APP

Source	Sum Sq.	d.f.	Singular?	Mean Sq.	F	Prob>F
Age	0.066691872	1	0	0.066692	2.701773	0.115865
Genotype	0.086901745	1	0	0.086902	3.520501	0.075285
Age*Genotype	0.041908013	1	0	0.041908	1.697747	0.207386
Error	0.493689608	20	0	0.024684		
Total	0.710419933	23	0			

C57

Source	Sum Sq.	d.f.	Singular?	Mean Sq.	F	Prob>F
Age	0.069967	1	0	0.069967	3.706702	0.07822
Error	0.22651	12	0	0.018876		
Total	0.296477	13	0			

Ripple Triggred Amplitude Somatosensory

5xFAD

Source	Sum Sq.	d.f.	Singular?	Mean Sq.	F	Prob>F
Age	0.177308	1	0	0.177308	8.592315	0.00695
Genotype	0.03255	1	0	0.03255	1.577382	0.220307
Age*Genotype	0.144162	1	0	0.144162	6.986063	0.013732
Error	0.536528	26	0	0.020636		
Total	0.918654	29	0			

APP

Source	Sum Sq.	d.f.	Singular?	Mean Sq.	F	Prob>F
Age	0.065750988	1	0	0.065751	3.709498	0.068438
Genotype	0.063842057	1	0	0.063842	3.601801	0.072247
Age*Genotype	0.017141908	1	0	0.017142	0.967101	0.337152
Error	0.354500742	20	0	0.017725		
Total	0.515114556	23	0			

C57

Source	Sum Sq.	d.f.	Singular?	Mean Sq.	F	Prob>F
Age	0.046213	1	0	0.046213	2.530213	0.13767
Error	0.219175	12	0	0.018265		
Total	0.265388	13	0			

Ripple Triggred Amplitude Retrosplenial + Association

5xFAD

Source	Sum Sq.	d.f.	Singular?	Mean Sq.	F	Prob>F
Age	0.627357	1	0	0.627357	8.704589	0.006637
Genotype	0.169524	1	0	0.169524	2.352151	0.13719
Age*Genotype	0.301977	1	0	0.301977	4.189933	0.050897
Error	1.873871	26	0	0.072072		
Total	3.062233	29	0			

APP

Source	Sum Sq.	d.f.	Singular?	Mean Sq.	F	Prob>F
Age	0.120248524	1	0	0.120249	2.066275	0.166051
Genotype	0.288662848	1	0	0.288663	4.960202	0.037585
Age*Genotype	0.044803424	1	0	0.044803	0.769874	0.390675
Error	1.163915772	20	0	0.058196		
Total	1.647512019	23	0			

C57

Source	Sum Sq.	d.f.	Singular?	Mean Sq.	F	Prob>F
Age	0.09903	1	0	0.09903	2.581996	0.134063
Error	0.460247	12	0	0.038354		
Total	0.559277	13	0			

Ripple Triggred Amplitude Visual + Association

5xFAD

Source	Sum Sq.	d.f.	Singular?	Mean Sq.	F	Prob>F
Age	0.565977	1	0	0.565977	11.0945	0.0026
Genotype	0.072197	1	0	0.072197	1.415231	0.244941
Age*Genotype	0.280915	1	0	0.280915	5.506596	0.026841
Error	1.32637	26	0	0.051014		
Total	2.321895	29	0			

APP

Source	Sum Sq.	d.f.	Singular?	Mean Sq.	F	Prob>F
Age	0.01704017	1	0	0.01704	0.404771	0.53185
Genotype	0.210408	1	0	0.210408	4.998019	0.036938
Age*Genotype	0.023472469	1	0	0.023472	0.557564	0.463932
Error	0.841965561	20	0	0.042098		
Total	1.100900632	23	0			

C57

Source	Sum Sq.	d.f.	Singular?	Mean Sq.	F	Prob>F
Age	0.176541	1	0	0.176541	3.923401	0.071009
Error	0.539964	12	0	0.044997		
Total	0.716505	13	0			

Ripple Triggred Amplitude Auditory

5xFAD

Source	Sum Sq.	d.f.	Singular?	Mean Sq.	F	Prob>F
Age	0.465098	1	0	0.465098	7.474527	0.011111
Genotype	0.202395	1	0	0.202395	3.252661	0.082909
Age*Genotype	0.443486	1	0	0.443486	7.127212	0.012911
Error	1.617834	26	0	0.062224		
Total	2.8078	29	0			

APP

Source	Sum Sq.	d.f.	Singular?	Mean Sq.	F	Prob>F
Age	0.030691626	1	0	0.030692	0.968876	0.336719
Genotype	0.146914574	1	0	0.146915	4.637812	0.043655
Age*Genotype	0.013977768	1	0	0.013978	0.441251	0.514105
Error	0.633551178	20	0	0.031678		
Total	0.833512782	23	0			

C57

Source	Sum Sq.	d.f.	Singular?	Mean Sq.	F	Prob>F
Age	0.03742	1	0	0.03742	1.299487	0.27655
Error	0.345549	12	0	0.028796		
Total	0.382968	13	0			

Ripple Triggred Amplitude Lateral (VISC+GU)

5xFAD

Source	Sum Sq.	d.f.	Singular?	Mean Sq.	F	Prob>F
Age	0.15487	1	0	0.15487	5.506731	0.027171
Genotype	0.038564	1	0	0.038564	1.371215	0.252644
Age*Genotype	0.101805	1	0	0.101805	3.619892	0.068672
Error	0.703093	25	0	0.028124		
Total	1.040849	28	0			

APP

Source	Sum Sq.	d.f.	Singular?	Mean Sq.	F	Prob>F
Age	0.123060604	1	0	0.123061	6.299515	0.02079
Genotype	0.038564539	1	0	0.038565	1.974132	0.175353
Age*Genotype	0.02778074	1	0	0.027781	1.422106	0.247014
Error	0.390698663	20	0	0.019535		
Total	0.604461079	23	0			

C57

Source	Sum Sq.	d.f.	Singular?	Mean Sq.	F	Prob>F
Age	0.025715	1	0	0.025715	2.271268	0.159961
Error	0.124539	11	0	0.011322		
Total	0.150254	12	0			

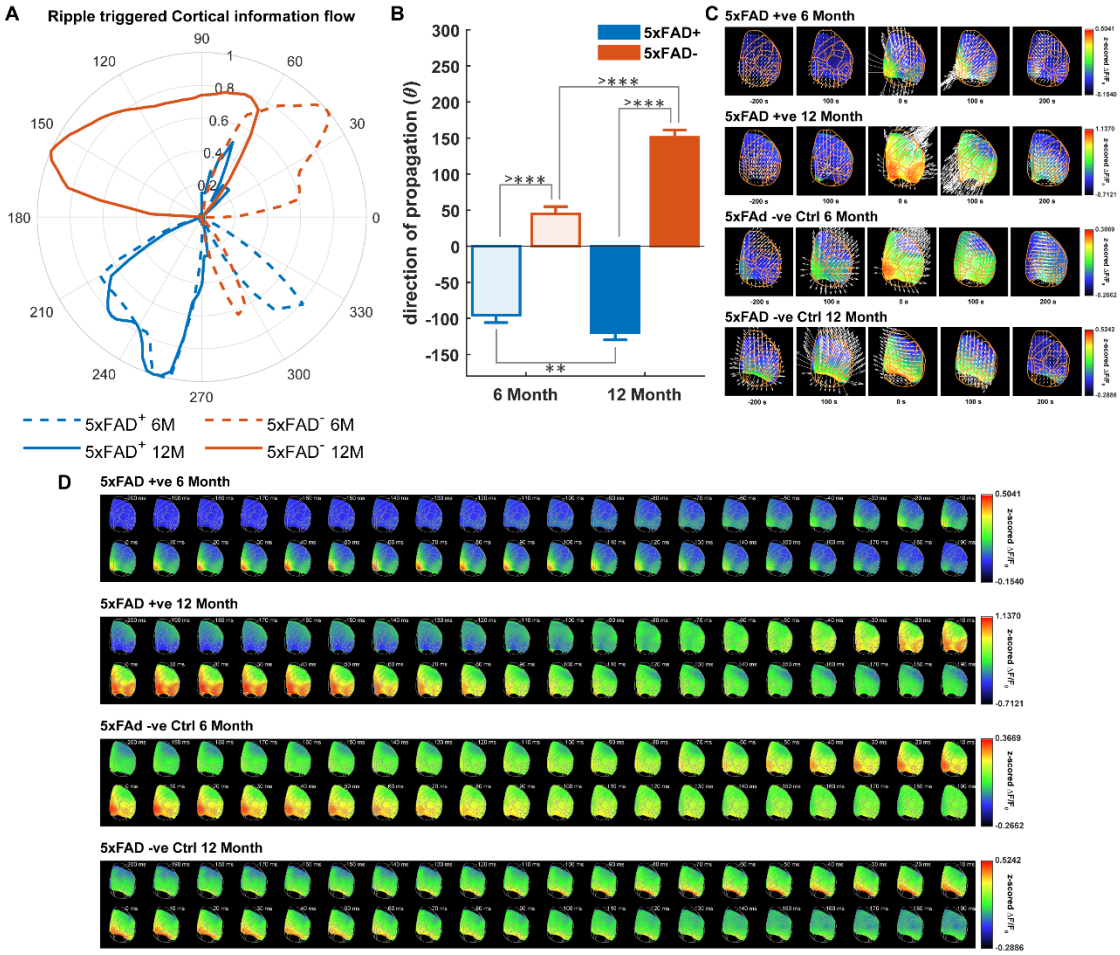

Figure 3.6: Spatio-temporal pattern of cortical signal flow around SWR for 5xFAD mice. (A) Polar plot of normalized average speed with respect to the angle/direction of peri-SWR cortical signal flow. (B) Direction of peri-SWR cortical signal propagation changes with genotype and age, further, there is interaction between age and genotype. (C) Montage of peri-SWR cortical activity with overlaid velocity vector fields determined using Combined local-global (CLG) method for optical flow analysis. We observed that cortical activation around SWRs follows a pattern of activation from posteromedial subnetworks such as RSC, association, and visual areas, towards lateral subnetworks such as auditory, and lateral areas. For most the control case the cortical signal flow followed this propagation pattern. However, for 6- and 12-month 5xFAD$^+$ animals the direction of propagation was reversed where the information flow initiated from more anterolateral regions of somatosensory areas (e.g., SSp-m, SSp-n, SSs) towards posteromedial subnetworks such as RSC, association, and visual areas. (D) Montage of average peri-SWR cortical activation in ± 200ms time window from ripple center, for 6- and 12- month 5xFAD$^+$ and 5xFAD$^+$ mice. * = $p < 0.05$; ** = $p < 0.01$; *** = $p < 0.001$; >*** = $p < 0.001$.

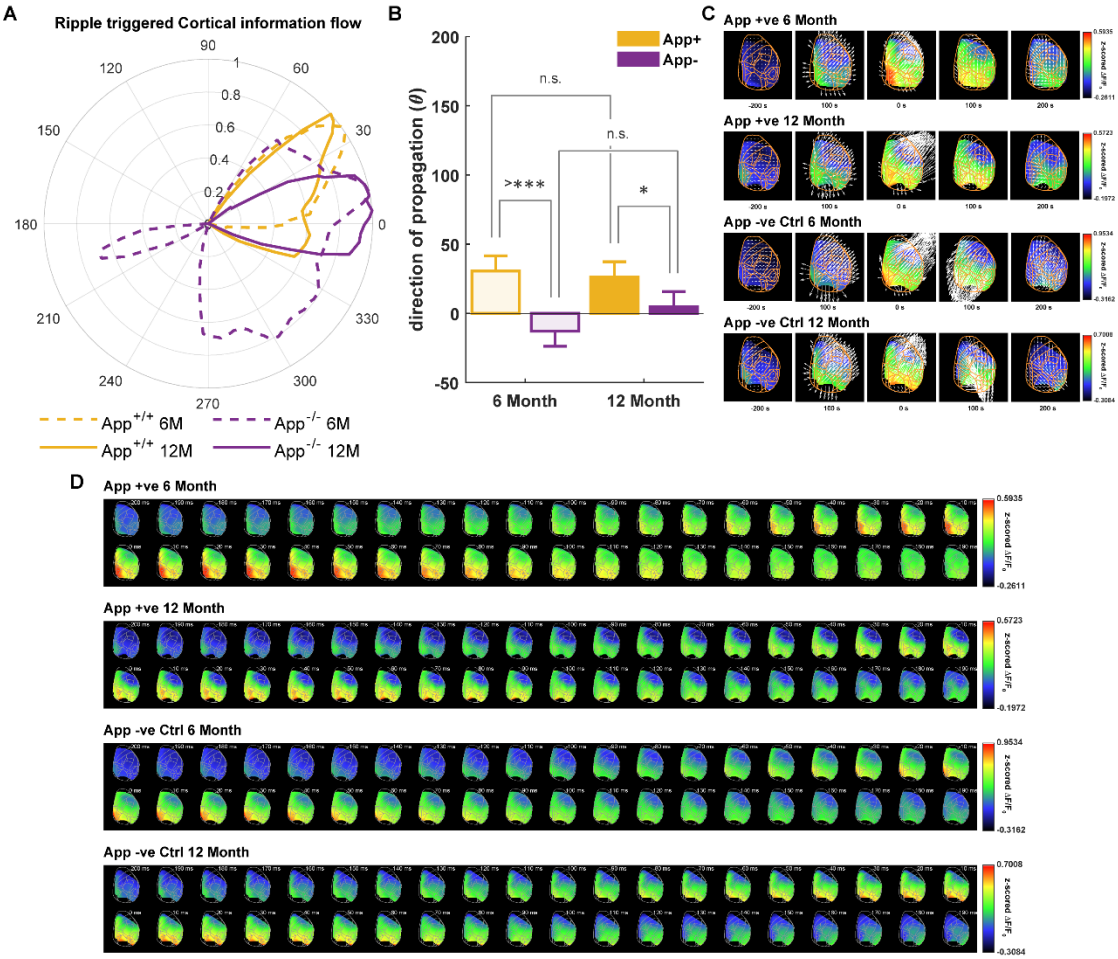

Figure 3.7: Spatio-temporal pattern of cortical signal flow around SWR for *App*$^{NL\text{-}G\text{-}F}$ mice.

(A) Polar plot of normalized average speed with respect to the angle/direction of peri-SWR cortical signal flow. (B) Direction of peri-SWR cortical signal propagation changes with genotype, further, there is interaction between age and genotype. (C) Montage of peri-SWR cortical activity with overlaid velocity vector fields determined using Combined local-global (CLG) method for optical flow analysis. We observed that cortical activation around SWRs follows a pattern of activation from posteromedial subnetworks such as RSC, association, and visual areas, towards lateral subnetworks such as auditory, and lateral areas. For most the control case the cortical signal flow followed this propagation pattern. However, for 6- and 12-month *App*$^{+/+}$ animals the direction of propagation was stronger towards anterolateral regions of somatosensory areas (e.g., SSp-m, SSp-n, SSs). (D) Montage of average peri-SWR cortical activation in ± 200ms time window from ripple center, for 6- and 12- month *App*$^{+/+}$ and *App*$^{-/-}$ mice. * = $p < 0.05$; ** = $p < 0.01$; *** = $p < 0.001$; >*** = $p < 0.001$.

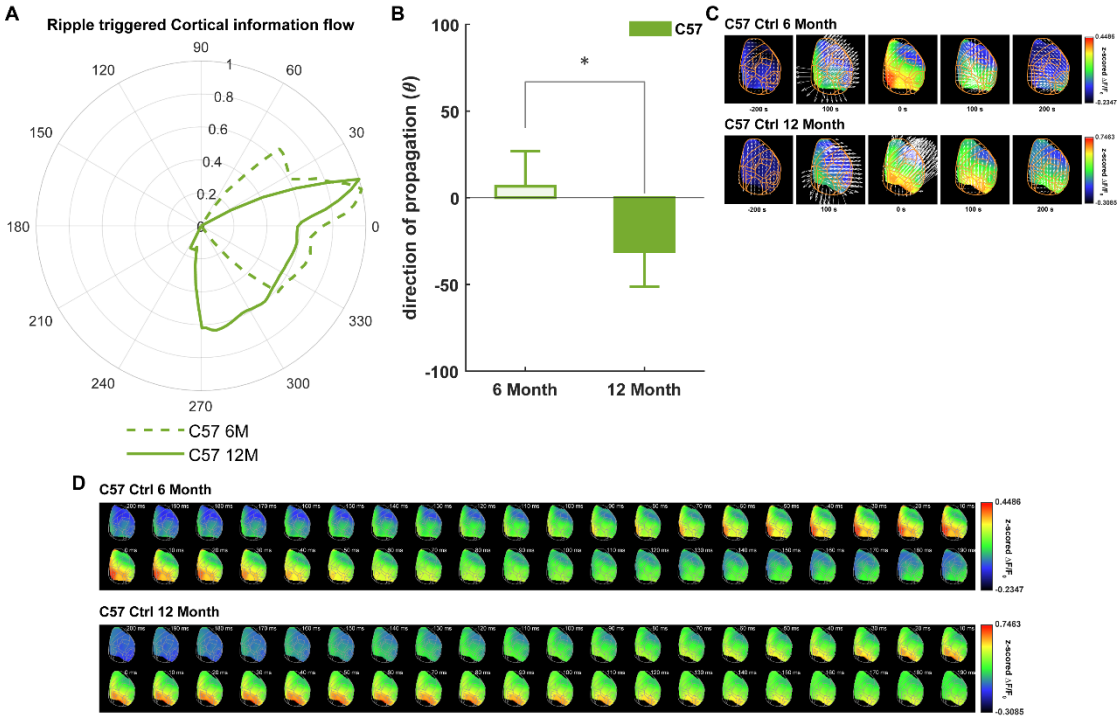

Figure 3.8: Spatio-temporal pattern of cortical signal flow around SWR for C57 mice. (A) Polar plot of normalized average speed with respect to the angle/direction of peri-SWR cortical signal flow. (B) Direction of peri-SWR cortical signal propagation changes with age. (C) Montage of peri-SWR cortical activity with overlaid velocity vector fields determined using Combined local-global (CLG) method for optical flow analysis. We observed that cortical activation around SWRs follows a pattern of activation from posteromedial subnetworks such as RSC, association, and visual areas, towards lateral subnetworks such as auditory, and lateral areas. For 6- and 12- month C57 mice the cortical signal flow followed this propagation pattern. However, for 12- month C57 mice the direction of propagation was stronger towards temporal association areas (TEa). (D) Montage of average peri-SWR cortical activation in ± 200ms time window from ripple center, for 6- and 12- month C57BL/6J mice. * = $p < 0.05$; ** = $p < 0.01$; *** = $p < 0.001$; >*** = $p < 0.001$.

Table 3.4: ANOVA table for statistical comparison of per-SWR cortical signal flow.

5xFAD						
Source	Sum Sq.	d.f.	Singular?	Mean Sq.	F	Prob>F
Age	21840.64	1	0	21840.64	65.46863	1.6E-10
Genotype	549664.7	1	0	549664.7	1647.653	8.14E-39
Age*Genotype	54876.88	1	0	54876.88	164.4967	4.03E-17
Error	16013.03	48	0	333.6047		
Total	642395.2	51	0			
APP						
Source	Sum Sq.	d.f.	Singular?	Mean Sq.	F	Prob>F
Age	577.9442	1	0	577.9442	1.475766	0.23038
Genotype	13770.21	1	0	13770.21	35.1619	3.21E-07
Age*Genotype	1538.233	1	0	1538.233	3.92784	0.053235
Error	18797.91	48	0	391.6231		
Total	34684.3	51	0			
C57						
Source	Sum Sq.	d.f.	Singular?	Mean Sq.	F	Prob>F
Age	9157.736	1	0	9157.736	6.843296	0.015147
Error	32116.93	24	0	1338.206		
Total	41274.67	25	0			

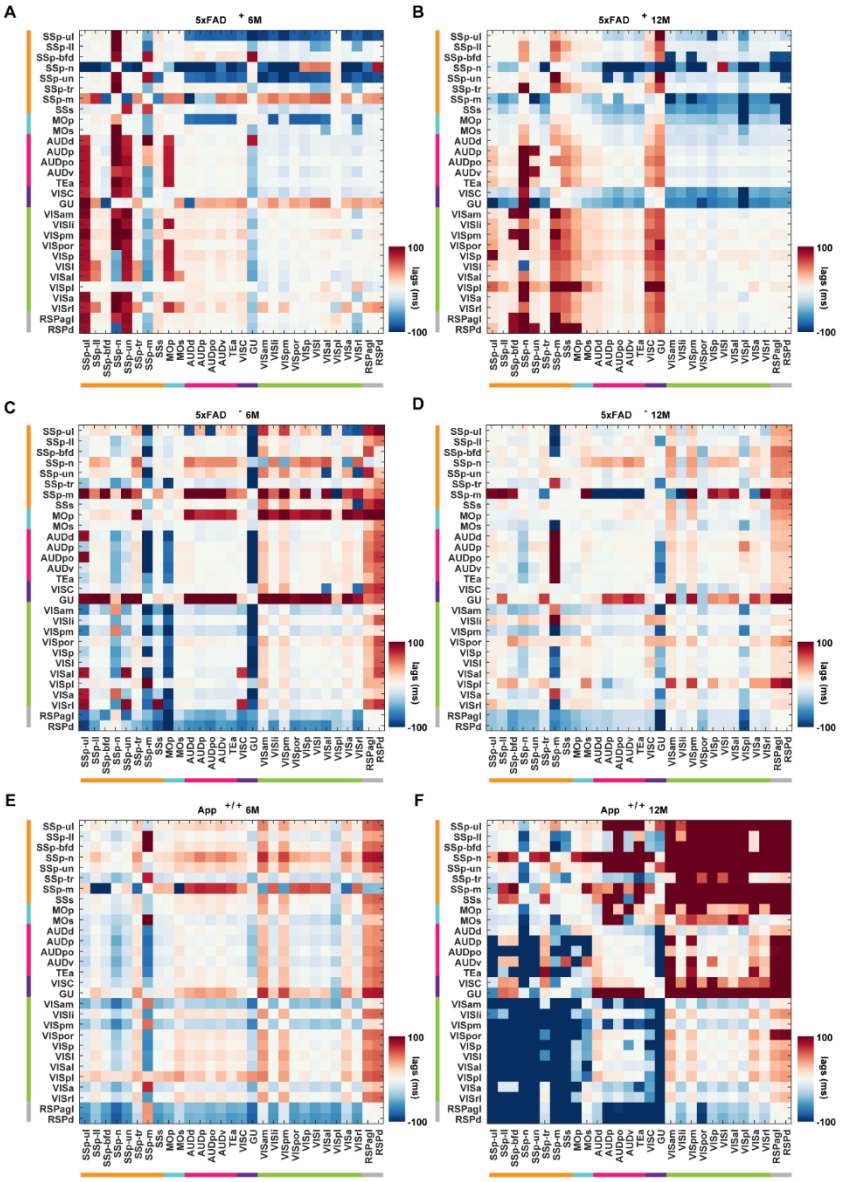

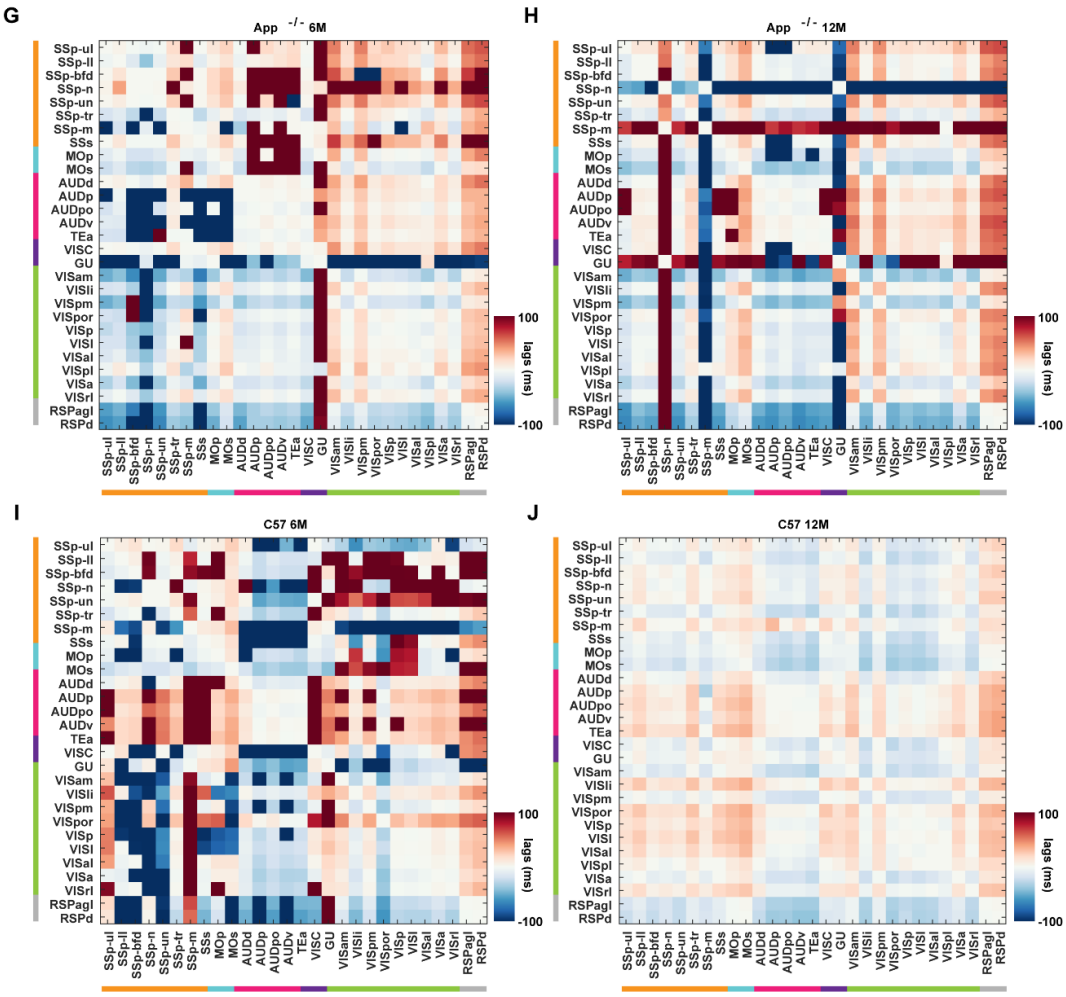

Figure 3.9: Correlation lags of cortical activations around SWR.
(A-J) Time lags of maximum correlation of cortical activity around SWRs. In all the groups (C-J) except 6- and 12- month 5xFAD (A-B), cortical activity around SWRs in posteromedial subnetworks such as retrosplenial, association and visual areas leads the somatosensory and lateral networks. However, for 6- and 12- month 5xFAD (A-B), cortical activity around SWRs in anterolateral regions of somatosensory areas (e.g. SSp-m, SSp-n, SSs) and lateral areas (VIS, GU) leads posteromedial subnetworks such as retrosplenial, association and visual areas. This finding is similar to that observed using optical flow analysis in fig 3.6 where the information flow is reversed in 6- and 12- month 5xFAD animals. (6-month-old: C57BL/6J, n = 7; $App^{+/+}$, n = 6; $App^{-/-}$, n = 5; $5xFAD^{+}$, n = 8; $5xFAD^{-}$, n = 8 and 12-month-old: C57BL/6J, n = 6; $App^{+/+}$, n = 7; $App^{-/-}$, n = 4; $5xFAD^{+}$, n = 8; $5xFAD^{-}$, n = 6).

Temporal properties of RSC and HPC-MUA activity around SWRs

Hippocampal-neocortical interaction is necessary for memory consolidation, and it is hypothesized that during the events of SWRs hippocampus interacts with cortex in a coordinated manner for the long-term storage of memory (Joo and Frank, 2018; Sutherland et al., 2020). While hippocampal-cortical interaction is important for memory consolidation there is conflicting evidence on whether cortex or hippocampus

drives this interaction. Bidirectional information flow between hippocampus and cortex has also been shown during SWRs (Maingret et al., 2016; Rothschild et al., 2017; Helfrich et al., 2019). Thus, we investigated if neocortical activity around SWRs precedes or lags SWRs, or there is a neocortical-hippocampal-neocortical loop of interaction, and how is it related to the disease pathology. We focused on RSC for cortical activations and used asymmetry index (AI) as the measure to identify lead/lag of cortex w.r.t. SWRs (see Table 3.5 for detail statistics). AI was defined as (X - Y) / (X + X), where X and Y are the mean values within time $\pm\Delta t$, (200 ms) (see fig. 3.10A), the first and fourth quartiles of AI distribution was used for further analysis to identify SWRs preceding/following RSC or HPC-MUA. As shown in a recent study from our lab (Karimi Abadchi et al., 2020) we found that for control case RSC activity lead SWRs, however, for 12- month 5xFAD^{+} mice SWRs lead RSC activity, compared to the chance level of 50% (fig. 3.10D). Interestingly we observed that for 6- and 12-month 5xFAD^{+} mice ~200 ms before the SWR center there was first increase in activation of anterolateral regions of somatosensory areas (e.g. SSp-m, SSp-n, SSs) (fig 3.6) as opposed to early activation of posteromedial RSC subnetwork in control case. Now assuming neocortical-hippocampal-neocortical loop of information processing around SWRs, early activation of anterolateral regions in 12- month 5xFAD mice could have driven this delay in RSC activation around SWRs, which may not be advantageous for memory consolidation. HPC-MUA activity was also slightly leading hippocampal-SWRs and was significantly higher than chance for 12-month App$^{+/+}$ group (3.10E). RSC and HPC-MUA was highly coordinated as shown by proportion of same sign asymmetry index (AI) events, suggesting that the lead or lag of RSC w.r.t. SWR could be predicted from HPC-MUA (3.10F).

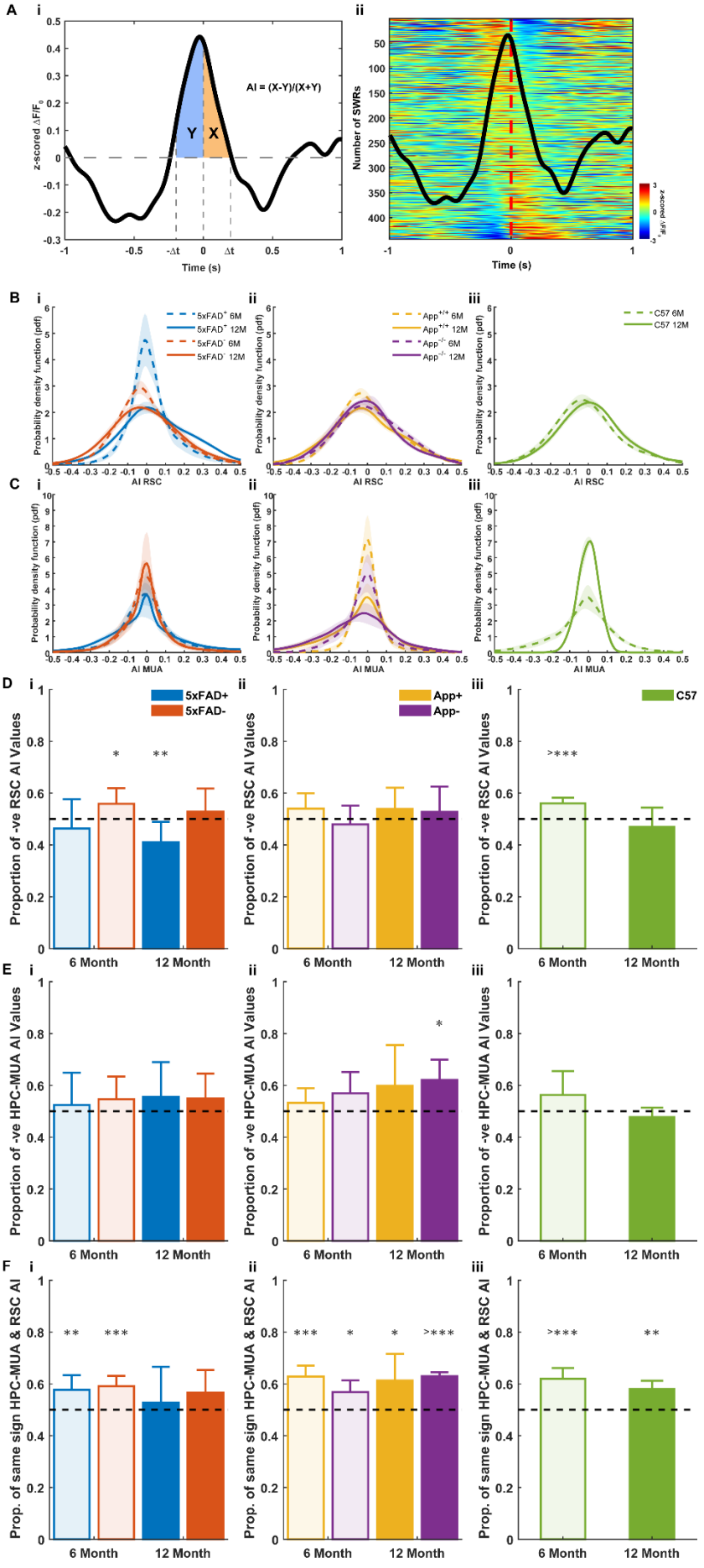
A
i
ii
AI = (X-Y)/(X+Y)
Y
X
z-scored ΔF/F0
Time (s)
Number of SWRs
z-scored ΔF/F
B
C
Probability density function (pdf)
AI RSC
AI MUA
5xFAD+ 6M
5xFAD+ 12M
5xFAD- 6M
5xFAD- 12M
App+/+ 6M
App+/+ 12M
App-/- 6M
App-/- 12M
C57 6M
C57 12M
D
E
F
Proportion of -ve RSC AI Values
Proportion of -ve HPC-MUA AI Values
Prop. of same sign HPC-MUA & RSC AI
5xFAD+
5xFAD-
App+
App-
C57
6 Month
12 Month

Figure 3.10: Distribution of RSC activity and HPC-MUA around SWRs.
(A) (i) Asymmetry Index (AI) is defined as the ratio of difference and sum of mean peri-SWR activity, (X-Y)/(X+Y), where X and Y is mean peri-SWR activity in time Δt and $-\Delta t$ respectively, for analysis we used Δt= 200 ms. (ii) SWRs sorted according to asymmetry index for a representative animal. (B-C) The cortical activity in RSC and HPC-MUA around SWRs is expressed in terms of AI asymmetry index which is a measure to quantify if the activity leads or lags the SWR. It is observed that there is a whole range of activations latencies w.r.t. SWRs, in which some time the RSC and HPC-MUA activity leads or lags the SWRs. (D) Proportion of leading RSC events as identified by negative asymmetry index (AI). For most groups RSC tends to activate prior to hippocampal-SWR, except 6- and 12-month 5xFAD^{+} animals for which RSC activity mostly followed hippocampal-SWR, dashed black line represents chance (50%). (E) HPC-MUA was also slightly leading hippocampal-SWRs and was significantly higher than chance for 12-month App$^{+/+}$ group. (F) RSC and HPC-MUA was highly coordinated as shown by proportion of same sign asymmetry index (AI) events, suggesting that the lead or lag of RSC w.r.t. SWR could be predicted from HPC-MUA. (6-month-old: C57BL/6J, n = 7; App$^{+/+}$, n = 6; App$^{-/-}$, n = 5; 5xFAD^{+}, n = 8; 5xFAD^{-}, n = 8 and 12-month-old: C57BL/6J, n = 6; App$^{+/+}$, n = 7; App$^{-/-}$, n = 4; 5xFAD^{+}, n = 8; 5xFAD^{-}, n = 6). * = $p < 0.05$; ** = $p < 0.01$; *** = $p < 0.001$; >*** = $p < 0.001$.

Table 3.5: Statistical comparison of AI, p-values of one sample t-test.

Proportion of negative RSC AI											
5xFAD					**App**					**C57**	
0.384551	0.028545	0.00904	0.477194		0.117407	0.558529	0.253583	0.564019		9.04E-05	0.364204
Proportion of negative HPC-MUA AI											
5xFAD					**App**					**C57**	
0.594657	0.1757	0.239937	0.251664		0.176022	0.128919	0.147412	0.026224		0.096503	0.191792
Proportion of Same Sign HPC-MUA & RSC AI											
5xFAD					**App**					**C57**	
0.006473	0.000376	0.565117	0.124789		0.000186	0.027665	0.027494	3.72E-05		7.36E-05	0.001828

RSC and HPC-MUA activity in Q1 and Q4

We first identified RSC and HPC-MUA events in first and fourth quartiles of respective AI distribution. We found that cortical activity in RSC Q1 was mostly leading SWRs and in RSC Q4 was mostly lagging SWRs, further HPC-MUA followed RSC Q1 and RSC Q4 as shown by negative and positive mean AI values respectively (fig 3.11C). this trend was consistent for most of the groups but was not significant for 12-month 5xFAD^{+} mice (see Table 3.6 for detail statistics). Similarly, RSC followed HPC-MUA Q1 and HPC-MUA Q4 as shown by negative and positive mean AI values respectively (fig 3.12C) (see Table 3.6 for detail statistics). However, for 12-month 5xFAD^{+} mice although the mean RSC AI in HPC-MUA Q1 and Q4 was significantly

different, RSC AI in HPC-MUA Q1 have mean positive AI value. This is not surprising as RSC AI values are significantly skewed towards positive values as shown in fig 3.10D.

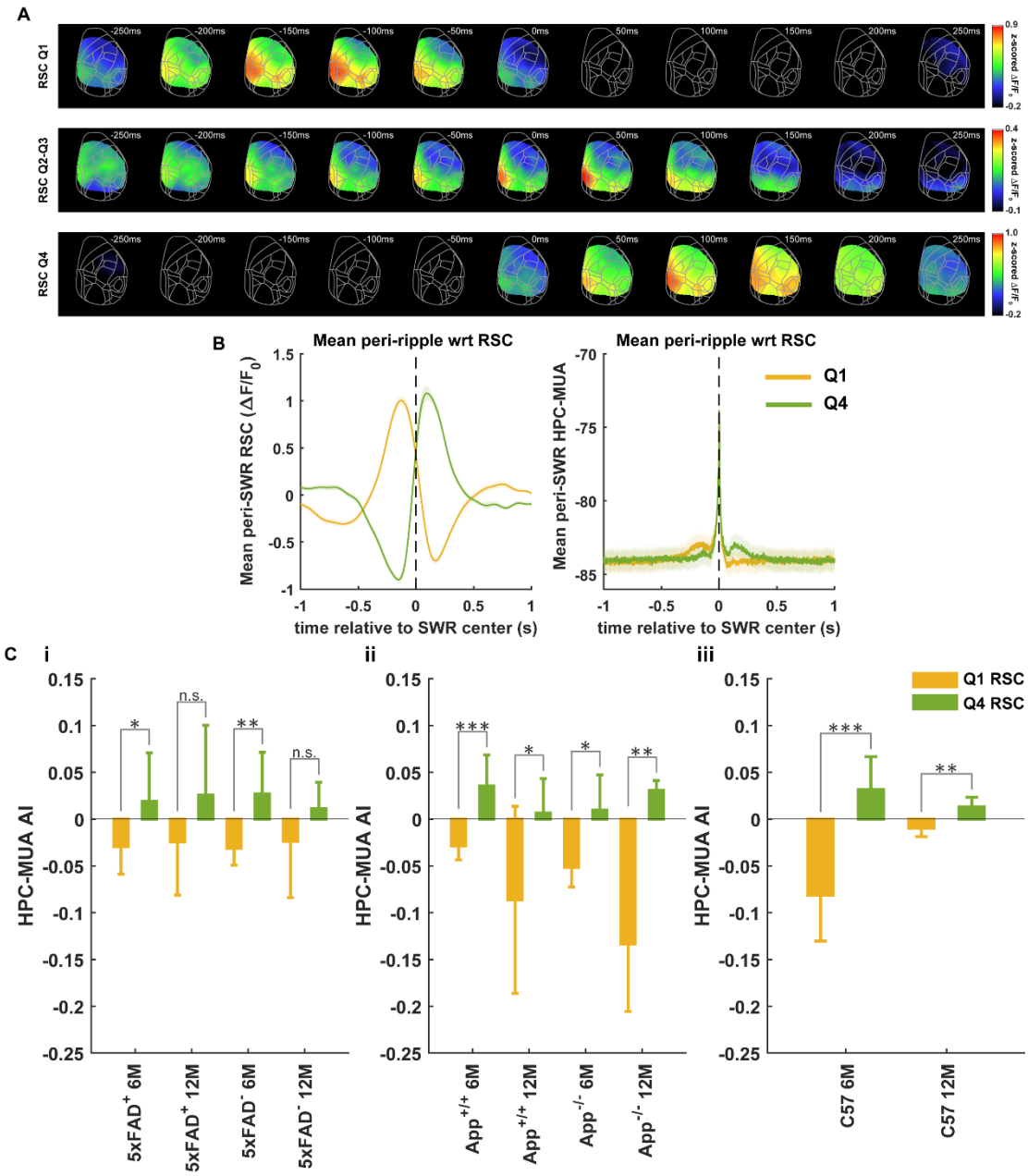

Figure 3.11: HPC-MUA activity in Q1 and Q4 of RSC activity around SWRs.
(A) Montage of average peri-SWR cortical activation present temporal shifts associated with RSC Q1, Q2-3, and Q4 in a representative animal. (B) Mean peri-SWR activity of representative 6-month C57Bl/6J mice. RSC – Q1 (negative AI) activity peaks before SWR center and RSC-Q4 (positive AI) peak activation is after SWR center, similarly HPC-MUA during RSC-Q1 and Q4 the is negatively and positively skewed. (C) HPC-MUA activity in the first quarter Q1 of RSC AI distribution is mostly leading and during fourth quarter Q4 of RSC AI is usually following or lagging the SWRs, suggesting correlated HPC-MUA and RSC activity. (6-month-old: C57BL/6J, n = 7; $App^{+/+}$, n = 6; $App^{-/-}$, n = 5; $5xFAD^{+}$, n = 8; $5xFAD^{-}$, n = 8 and 12-month-

old: C57BL/6J, n = 6; App$^{+/+}$, n = 7; App$^{-/-}$, n = 4; 5xFAD^{+}, n = 8; 5xFAD^{-}, n = 6). * = $p < 0.05$; ** = $p < 0.01$; *** = $p < 0.001$; >*** = $p < 0.001$.

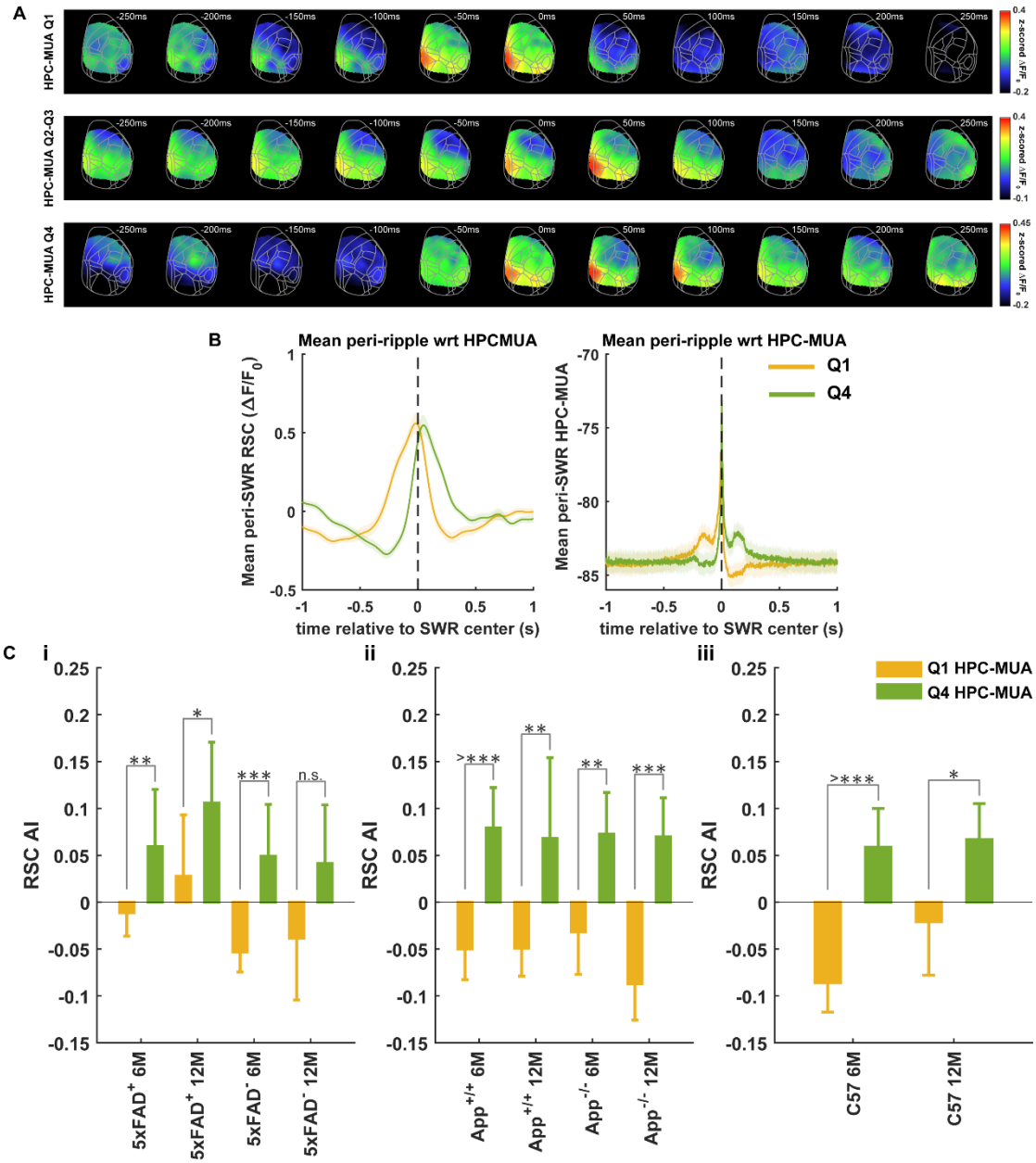

Figure 3.12: RSC activity in Q1 and Q4 of HPC-MUA activity around SWRs.
(A) Montage of average peri-SWR cortical activation present temporal shifts associated with HPC-MUA Q1, Q2-3, and Q4 in a representative animal. (B) Mean peri-SWR activity of representative 6-month C57Bl/6J mice. Both HPC-MUA and RSC activity are negatively (negative AI) and positively (positive AI) skewed around SWR for HPC-MUA Q1 and Q4. (C) RSC activity in the first quarter Q1 of HPC-MUA AI distribution is mostly leading and during fourth quarter Q4 of HPC-MUA AI is usually following or lagging the SWRs, suggesting correlated HPC-MUA and RSC activity. (6-month-old: C57BL/6J, n = 7; App$^{+/+}$, n = 6; App$^{-/-}$, n = 5; 5xFAD^{+}, n = 8; 5xFAD^{-}, n = 8 and 12-month-old: C57BL/6J, n = 6; App$^{+/+}$, n = 7; App$^{-/-}$, n = 4; 5xFAD^{+}, n = 8; 5xFAD^{-}, n = 6). * = $p < 0.05$; ** = $p < 0.01$; *** = $p < 0.001$; >*** = $p < 0.001$.

Table 3.6: Statistical comparison of AI in Q1 and Q4 of RSC and HPC-MUA activity around SWRs, p-values of two sample t-test.

HPC-MUA AI RSC Q1 & Q4											
5xFAD					**APP**					**C57**	
0.039296	0.130729	0.004124	0.229759		0.000532	0.040308	0.013058	0.001009		0.000116	0.002168
RSC AI HPC-MUA Q1 & Q4											
5xFAD					**APP**					**C57**	
0.008956	0.022073	0.00026	0.057533		3.76E-05	0.005282	0.006262	0.000271		1.72E-06	0.011032

Single vs bundled SWRs

Long-duration SWRs or SWRs that occur in close temporal proximity of each other (bundled SWRs) are hypothesised to be more involved in situations demanding memory, for example traversing through a larger space (Davidson et al., 2009; Wu and Foster, 2014; Fernández-Ruiz et al., 2019). Further, Fernández-Ruiz et al. have shown that memory during maze learning was increased by prolongation of spontaneously occurring ripples, but not randomly induced ripples. Suggesting that just abundance of SWRs might not be a correct measure of learning and memory. In our data we found spontaneous occurrences of single and bundled ripples, of all the SWRs we found that ~75% are single/isolated SWRs and remaining are bundled/long-duration SWRs (fig 3.13B). Further, we found that not only there was reduction of SWRs in 12-month 5xFAD^{+} mice (fig 3.1A), the proportion of bundled ripples was also slightly reduced although not significant. A comprehensive analysis of single vs. bundled SWRs during sleep and urethane anaesthesia has been presented in a recent study from our lab (Karimi Abadchi et al., 2020). We also investigated properties of single and bundled SWRs in our data (fig 3.14), we found that proportion of single and bundled SWRs was similar in Q1 and Q4 of RSC-AI except for 6-month C57 group which had reduced bundled SWRs in RSC Q1. Further, for HPC-MUA Q1 no significant difference was observed in proportion of single and bundled ripples except for 12- month 5xFAD^{+} group for which the proportion of bundled ripples increased in Q1. For HPC-MUA Q4 there was significant increase in bundled SWRs of 12- month App$^{+/+}$ and 6- month C57 group (see Table 3.7 for detail statistics).

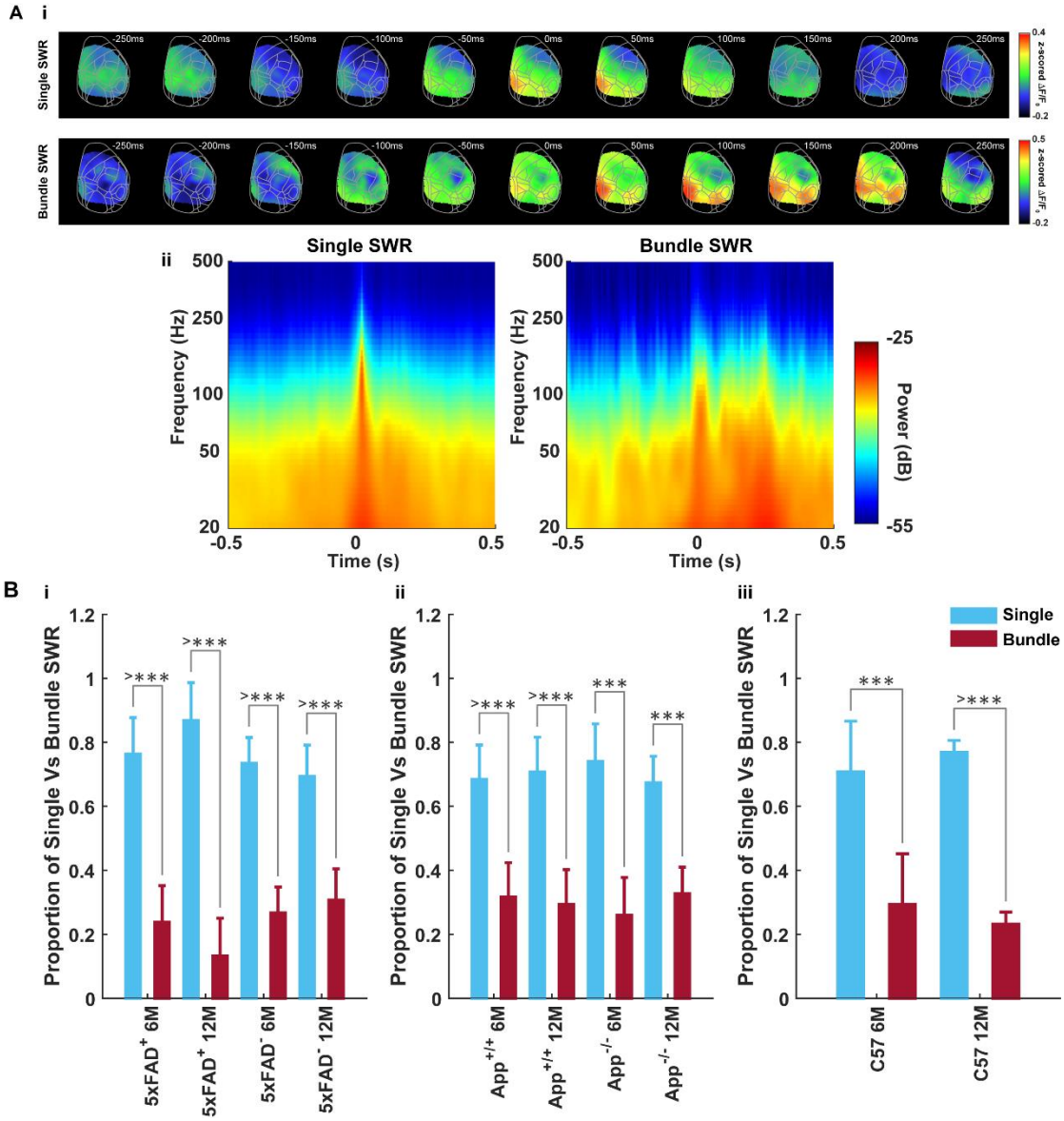

Figure 3.13: Proportions of single and bundled SWRs.

(A) Montage of average peri-SWR cortical activation associated with single and bundle SWR in a representative animal. (ii) time frequency representation of mean peri-SWR LFP using continuous wavelet transform (cwt) - analytical Morlet (Gabor) wavelet, for single and bundle SWR in a representative animal. (B) Proportion of single SWRs is significantly higher in all groups as compared to the bundled SWRs. (6-month-old: C57BL/6J, n = 7; $App^{+/+}$, n = 6; $App^{-/-}$, n = 5; $5xFAD^{+}$, n = 8; $5xFAD^{-}$, n = 8 and 12-month-old: C57BL/6J, n = 6; $App^{+/+}$, n = 7; $App^{-/-}$, n = 4; $5xFAD^{+}$, n = 8; $5xFAD^{-}$, n = 6). * = $p < 0.05$; ** = $p < 0.01$; *** = $p < 0.001$; >*** = $p < 0.001$.

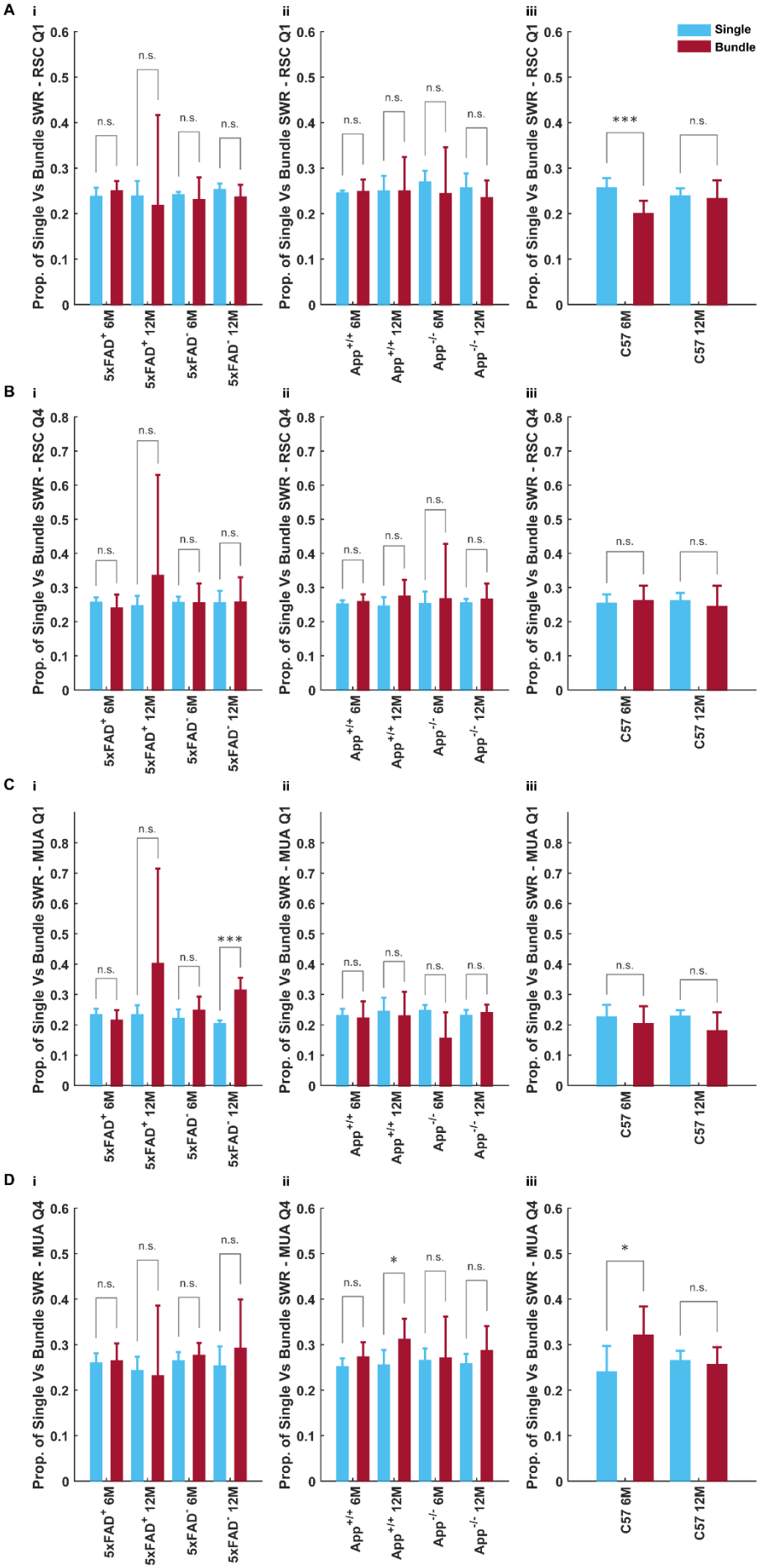
A
B
C
D
i
ii
iii
Single
Bundle
Prop. of Single Vs Bundle SWR - RSC Q1
Prop. of Single Vs Bundle SWR - RSC Q4
Prop. of Single Vs Bundle SWR - MUA Q1
Prop. of Single Vs Bundle SWR - MUA Q4
n.s.
*
***
5xFAD+ 6M
5xFAD+ 12M
5xFAD- 6M
5xFAD- 12M
App+/+ 6M
App+/+ 12M
App-/- 6M
App-/- 12M
C57 6M
C57 12M

Figure 3.14: Proportions of single and bundled SWRs during Q1 and Q4 of RSC and HPC-MUA asymmetry index.
(A-B) proportion of single and bundled SWRs was similar in Q1 and Q4 of RSC-AI except for 6-month C57 group which had reduced bundled SWRs in RSC-AI Q1. (C-D) for HPC-MUA AI Q1 no significant difference was observed in proportion of single and bundled ripples except for 12- month 5xFAD^{+} group for which the proportion of bundled ripples increased in Q1, for HPC-MUA Q4 there was significant increase in bundled SWRs for 12- month App$^{+/+}$ and 6-month C57 group. (6-month-old: C57BL/6J, n = 7; App$^{+/+}$, n = 6; App$^{-/-}$, n = 5; 5xFAD^{+}, n = 8; 5xFAD^{-}, n = 8 and 12-month-old: C57BL/6J, n = 6; App$^{+/+}$, n = 7; App$^{-/-}$, n = 4; 5xFAD^{+}, n = 8; 5xFAD^{-}, n = 6). * = $p < 0.05$; ** = $p < 0.01$; *** = $p < 0.001$; >*** = $p < 0.001$.

Table 3.7: Statistical comparison of single vs bundle SWRs, p-values of two sample t-test.

Single Vs Bundle SWR ALL											
5xFAD					**APP**					**C57**	
2.57E-07	4.99E-10	1.62E-08	4.4E-05		3.39E-05	1.22E-05	0.000193	0.000167		0.000128	2.47E-10
Single Vs Bundle SWR - RSC Q1											
5xFAD					**APP**					**C57**	
0.28668	0.768499	0.565563	0.236388		0.744965	0.997987	0.601889	0.376755		0.000742	0.752403
Single Vs Bundle SWR - RSC Q4											
5xFAD					**APP**					**C57**	
0.290366	0.38272	0.977667	0.953328		0.505071	0.187102	0.853079	0.623895		0.66868	0.559974
Single Vs Bundle SWR - MUA Q1											
5xFAD					**APP**					**C57**	
0.218223	0.12829	0.196258	0.000117		0.726428	0.686063	0.051556	0.563464		0.406378	0.101544
Single Vs Bundle SWR - MUA Q4											
5xFAD					**APP**					**C57**	
0.794765	0.832289	0.341352	0.434381		0.176414	0.023323	0.909838	0.301269		0.019165	0.651

Discussion

Sharp wave ripples (SWRs) are highly synchronous neural activity patterns in the hippocampus and are associated with cognition (Buzsáki, 2015; Joo and Frank, 2018). Coordinated interplay between HPC-SWRs and cortical slow oscillations is strongly implicated in learning and memory (Schabus et al., 2004; Ulrich, 2016). During SWRs there is modulation of neural activity in distributed brain regions (Schwindel and McNaughton, 2011) and SWRs mediate hippocampal-cortical interactions during slow wave sleep and in the awake state (during consummation and immobility) (Ji and Wilson, 2007; Wierzynski et al., 2009; Buhry et al., 2011; Logothetis et al., 2012; Ramirez-Villegas et al., 2015; Roumis and Frank, 2015; Staresina et al., 2015; Kaplan et al., 2016; Walker and Robertson, 2016; Tang et al., 2017; Gardner et al., 2019; Tang and Jadhav, 2019; Karimi Abadchi et al., 2020). A causal link of SWR to learning and

memory also occurs in mouse models of AD (Ciupek et al., 2015; Gillespie et al., 2016; Iaccarino et al., 2016; Nicole et al., 2016; Jones et al., 2019; Jura et al., 2019; Benthem et al., 2020; Caccavano et al., 2020; Jura et al., 2020; Sanchez-Aguilera and Quintanilla, 2021).

The results presented in this chapter reveal that neocortical activity around SWRs has a unique spatiotemporal pattern that varies with disease condition. The cortical network that gets activated around SWRs follows the cytoarchitectural organization of the retrosplenial (RSC) and parietal cortices (PC) of rodents (Kolb and Walkey, 1987; Clark et al., 2018). Using rs-fMRI in mice, Liska et al. (Liska et al., 2015) have identified two main anticorrelated cortical modules in mice, the default mode network (DMN) and lateral cortical network (LCN). DMN extended along prefrontal midline structures, including bilateral posterior parietal and temporal association regions, this network has also been described in rats and multi-centre mouse rs-fMRI data (Lu et al., 2012; Stafford et al., 2014; Grandjean et al., 2020). LCN include frontal association, anterior somatosensory, motor, and insular cortices. This network is also described for rats (Schwarz et al., 2013) as topologically reminiscent of the task-positive network in humans. In a recent study combining rs-fMRI and viral tracing, Whitesell et al. provided an anatomical description and cell type correlates of DMN (Whitesell et al., 2021). Harris et al. have shown hierarchical organization of cortical connectivity using laminar-based rules, in which primary sensory modules were at the bottom of the hierarchy (somatomotor, visual, and auditory) and prefrontal and medial modules were at the top (Harris et al., 2019). Further, two unique spatial gradients of cortical connectivity are shown in functional and structural studies in the mouse that are similar to the gradients found in humans and primates. The dominant cortical gradient is involved in sensory-fugal transition between unimodal motor–sensory regions (LCN)

and higher-order multimodal areas (DMN). The other gradient extends across unimodal visual and auditory cortices up to primary motor–sensory regions, providing a regional differentiation between sensorimotor modalities (Mesulam, 1998; Margulies et al., 2016; Coletta et al., 2020).

The cortical activation around SWRs in my experiments match the DMN-like module as shown in rodents (Liska et al., 2015; Gutierrez-Barragan et al., 2019; Coletta et al., 2020; Whitesell et al., 2021). Additional cortical regions such as visual and barrel cortex have also been reported to be active during SWRs (Walker and Robertson, 2016; Karimi Abadchi et al., 2020). This could be explained by the anatomical and functional correlations that suggest that layer 2/3 DMN neurons project mostly in the DMN and layer 5 neurons project in and out of DMN (Harris et al., 2019; Coletta et al., 2020; Whitesell et al., 2021).

SWRs have been shown to be disrupted in normal ageing and in animal models of AD, epilepsy, schizophrenia (Suh et al., 2013; Altimus et al., 2015; Gillespie et al., 2016; Wiegand et al., 2016; Witton et al., 2016; Valero et al., 2017; Jones et al., 2019). I found that there is a reduction of SWRs in 12-month 5xFAD animals, a finding consistent with previous studies in APOE ε4-KI mice (Gillespie et al., 2016; Jones et al., 2019) and other mouse models of AD (Ciupek et al., 2015; Nicole et al., 2016). Further, gamma oscillations are impaired in the EC-HPC circuit of AD patients and AD animal models (Stam et al., 2002; Iaccarino et al., 2016; Nakazono et al., 2017; Wang et al., 2017a; Nakazono et al., 2018; Etter et al., 2019; Chen et al., 2021). Most of these studies suggest reduction in gamma band power, however, I found an opposite trend, an increase in gamma and SWR band power with age, although with slight reduction of these frequency band power in 6-month $App^{NL\text{-}G\text{-}F}$ and 5xFAD mice compared to

littermate controls. An increase in gamma band power is shown in a recent *in vitro* study of 3-month-old 5xFAD mouse model of AD (Caccavano et al., 2020). An increased SWR band power is also observed in mouse models of schizophrenia (Suh et al., 2013; Altimus et al., 2015).

Cortical activation around SWRs has been shown to have a maximum amplitude in RSC (Karimi Abadchi et al., 2020). My results show an increased activation around SWRs in 5xFAD at 12 months of age and a significant reduction in activation in 12-month $App^{NL\text{-}G\text{-}F}$ animals. At 6 month of age 5xFAD and $App^{NL\text{-}G\text{-}F}$ animals had lower activation as compared to littermate controls. Using optical flow analysis, I observed that the direction of cortical activity around SWRs was directed from posteromedial subnetworks, such as RSC, association and visual areas, towards lateral subnetworks, including auditory areas. However, for 6- and 12-month 5xFAD animals the direction of propagation was reversed, with the information flow initiated from more anterolateral regions of somatosensory areas (e.g. SSp-m, SSp-n, SSs) towards posteromedial subnetworks such as retrosplenial, association and visual areas (fig 3.6-8). The results from optical flow analysis were supported by time lags of cortical correlations during SWRs which revealed that for 6- and 12- month 5xFAD, cortical activity around SWRs in anterolateral regions of somatosensory areas (e.g. SSp-m, SSp-n, SSs) and lateral areas (VIS, GU) leads posteromedial subnetworks such as retrosplenial, association and visual areas (fig 3.9). These findings were supported by the observation that for 6- and 12-month $5xFAD^{+}$ animals, RSC activity mostly followed hippocampal-SWR (fig 3.10D) as opposed to other groups where RSC activity was leading SWRs. Using different methodology and recording from mostly midline areas in the cortex, Jura et al. have shown that in the ripple frequency band during SWR occurrence, there is strong coupling between cortex and hippocampus. This coupling

from posterior cingulate cortex (PCC) and RSC to CA1 in the wildtype mice is replaced by the coupling from anterior cingulate cortex (ACC) and prefrontal cortex (PFC) to CA1 in APP/PS1 mice. This shift in direction of coupling (posterior to anterior) could be due to more advanced Aβ pathology in PCC (Jura et al., 2020). Interestingly, in my experiments, 5xFAD mice have more advanced AD pathology in RSC and the direction of cortical information flow around SWRs is also impacted in a somewhat posterior to anterior manner. Overall, these results suggest that SWRs and SWR-coupled cortical activation are altered in an age and strain dependent manner in mouse models of AD. Targeting these network level dysfunctions could result in restoration of memory, improvement in cognitive functions, or amelioration of Alzheimer's disease related pathology.

Chapter 4 : Gradual cerebral hypoperfusion in *App*$^{NL-G-F}$ mice triggers cortical network dysfunction

Abstract

Alzheimer's disease (AD) is characterized neuropathologically by amyloid-β (Aβ) plaques and neurofibrillary tangles. Vascular pathology caused by chronic cerebral hypoperfusion (HP) is hypothesised to exacerbate AD pathology and has emerged as an increasing cause of age-related cognitive impairment. In this study I examine the effects of gradual cerebral HP on cognitive dysfunction, Aβ and microgliosis pathology, and cortical network dynamics in HP and sham C57BL/6J and *App*$^{NL-G-F}$ mice. We performed unilateral common carotid artery gradual occlusion (UCAgO) in two-month-old mice using an ameroid constrictor. At five months of age, the mice were tested using the Morris water task, novel object recognition, and balance beam. Following cognitive testing, *in vivo* mesoscale wide-field voltage imaging was used to assess cortical connectivity. Brains were collected for pathology characterization using immunohistochemistry. I found that UCAgO reduced CBF in the occluded hemisphere (OH) but only produced subtle memory deficits in the *App*$^{NL-G-F}$ mice. At 6 months of age dissociative effects of HP were observed in resting state functional connectivity analysis, where HP lead to hypo-connectivity in *App*$^{NL-G-F}$ mice and hyper-connectivity in C57BL/6J mice. Reduced cortical hindlimb (HL) and forelimb (FL) evoked activation was observed due to HP in both the strains. Furthermore, I found that the UCAgO bilaterally increased cortical and hippocampal microgliosis and Aβ deposition in the *App*$^{NL-G-F}$ mice. The results suggest that cortical network alterations in AD due to gradual cerebral HP is mediated in part by microgliosis and potentially by other glial cells as well.

Introduction

Alzheimer's disease (AD) is a neurodegenerative disorder associated with extracellular amyloid beta (Aβ) deposition within the brain parenchyma and the aggregation of the microtubule protein tau in neurofibrillary tangles in neurons (Hardy and Selkoe, 2002; Forner et al., 2017; Heneka et al., 2018). The amyloid cascade hypothesis has dominated AD research in the past few decades. Recent studies suggest that the vascular system is also a major contributor to disease progression. Vascular dysfunction and reduced cerebral blood flow (CBF) may occur prior to the accumulation and aggregation of Aβ plaques and hyperphosphorylated tau tangles (Meyer et al., 2000; de la Torre, 2002b, a). Autopsy findings in patients with dementia reveal that AD with cerebrovascular disease (mixed dementia), is more common than the 'pure' conditions of AD and vascular cognitive impairment (VCI) (Snowdon et al., 1997; Esiri et al., 1999; Gold et al., 2007; Schneider et al., 2007; Launer et al., 2008; Schneider et al., 2009; Gorelick et al., 2011; Mazza et al., 2011; Kalaria et al., 2012; Toledo et al., 2013; Attems and Jellinger, 2014; Hattori et al., 2016; Dichgans and Leys, 2017; Feng et al., 2018; Girouard and Munter, 2018; Hartmann et al., 2018; Smith, 2018).

Large/small cerebral vasculature damage and vascular risk factors (e.g., hypertension, diabetes mellitus, atherosclerosis, smoking, hypercholesterolemia, homocysteinemia obesity) could cause cerebral hypoperfusion (HP) (McDonald, 2002; McDonald et al., 2010; Attems and Jellinger, 2014; Gardener et al., 2015; Daulatzai, 2017; van Veluw et al., 2017; Hartmann et al., 2018; Iadecola et al., 2019). The effect of chronic cerebral hypoperfusion on cognitive dysfunction and neurodegenerative

processes is unknown. Understanding the functional and pathogenic synergy between neurons, glia, and vascular cells, could providing a mechanistic insight into how alterations in cerebral blood vessels exacerbate neuronal dysfunction and underlying cognitive impairment (Iadecola, 2010; Quaegebeur et al., 2011; Zlokovic, 2011). Preclinical animal models provide us an opportunity to study the contribution of vascular alterations to AD pathology and could be an important step in the development of new treatments for the prevention of AD.

Increased levels of Aβ oligomer creation/accumulation (Feng et al., 2018), pro-inflammatory cytokines (Yoshizaki et al., 2008), reduced levels of ACh synthesis (Mehla et al., 2018a) and alteration of amyloid precursor protein (APP) cleavage metabolism (Bennett et al., 2000) is observed in animal models of chronic cerebral HP. Further, chronic cerebral HP has negative effects on various cognitive functions, including learning and memory (Bennett et al., 1998; Kitagawa et al., 2005; Miki et al., 2009; Wang et al., 2016a; Zhai et al., 2016; Feng et al., 2018)

To my knowledge, no single study has evaluated the effect of unilateral common carotid gradual artery occlusion (UCAgO) on resting state cortical functional connectivity, microgliosis, amyloid pathology, and cognition in mouse model of AD. A single APP knock-in mouse model of AD ($App^{NL\text{-}G\text{-}F}$) is used here (Saito et al., 2014). An advantage of this mouse model over other transgenic AD models is that it lacks APP overexpression and toxicity and shows appreciable plaque expression and cognitive decline at six months, with clear cognitive impairment at twelve months of age (Saito et al., 2014; Saito et al., 2016; Sasaguri et al., 2017; Mehla et al., 2019). Another important aspect of our experimental design is the use of an ameroid constrictor (AC) for gradual reduction of CBF, which replicates “chronic” cerebral hypoperfusion

apparent in VCI. I then assessed memory and cognitive functions using the Morris water task (MWT) and novel object recognition (NOR) task (Mehla et al., 2019). Later, using *in vivo* mesoscale wide-field voltage imaging (Mohajerani et al., 2010; Mohajerani et al., 2011; Mohajerani et al., 2013; Lim et al., 2014; Chan et al., 2015), I identified resting state functional connectivity and evoked activity pattern changes associated with HP in the mouse cortex.

I found that UCAgO significantly reduced CBF in the occluded hemisphere (OH) and increased microgliosis and Aβ plaque aggregation in both occluded and non-occluded hemispheres (OH and NoH). These pathological changes lead to mild memory impairments and dissociative effects on cortical functional connectivity in C57 *versus* $App^{NL\text{-}G\text{-}F}$ (hyper- *versus* hypo- cortical connectivity).

Materials and Methods

All experimental procedures were approved by the institutional animal care committee and performed in accordance with the standards set out by the Canadian Council for Animal Care. Naïve male and female pairs of C57BL/6J (n = 19) and $App^{NL\text{-}G\text{-}F}$ (n = 27) mice bred in a pathogen free facility were used. UCAgO surgery was completed at two months of age, cerebral blood flow was measured for one month following surgery, behavioural testing occurred from 4-5 months, VSDI was completed following behavioural testing, and immunohistochemistry was completed at the end of all testing (fig 4.1A). UCAgO procedure and CBF measurements were described previously (Mehla, Lacoursiere, et al., 2018). Behavioural testing has been described previously (Mehla et al., 2018b; Mehla et al., 2018a; Mehla et al., 2019).

For *in vivo* VSD imaging mice were anesthetized with isoflurane (1.2–1.5%) for induction, followed by urethane for data collection (1.0-1.2 mg/kg, i.p). RH1691 dye

(Optical Imaging, New York, NY) was applied to the cortex for 30-45 min. The voltage sensitive dye was excited with a red LED (Luxeon K2, 627 nm center), and excitation filters 630 ± 15 nm. Images were taken through a macroscope composed of front-to-front video lenses (8.6 × 8.6 mm field of view, 67 μm per pixel). The depth of field of the imaging setup used was ~1 mm. To stimulate the forelimbs and hindlimbs, a 1 mA, 1-ms electrical pulse was delivered. The baseline of the optical signal (F_0) were captured and the fluorescence changes were quantified as $(F-F_0)/F_0 \times 100\%$; F represents the fluorescence signal at any given time and F_0 represents the average of fluorescence over all frames.

Aβ plaque was stained with 82E1 immunohistochemical markers. Microglial cells were stained with an ionized calcium-binding adapter molecule 1 (Iba1). A Nanozoomer serial slide scanner (NanoZoomer Digital Pathology 2.0-RS, HAMAMATSU, JAPAN) and Laser Scanning confocal microscope were used for imaging. Quantification of pathology was done using iLastik (Version 1.3.0-OSX) (Berg et al., 2019) and ImageJ software.

GraphPad Prism 7 for Mac OS X, v.7.0D (GraphPad Software, La Jolla California USA, www.graphpad.com) was used for statistical analysis of behavioral and pathology quantification. A p value < 0.05 was considered statistically significant, adjusted p values reported. For spontaneous VSDI data a generalized linear mixed-effects (GLME) model in MATLAB 2018b was used to predict correlation values with a fixed effect for group, including random effects for inter-regional correlations. Significance was set at $\alpha \leq 0.05$. Further, bootstrapping (resampling with replacement, 1000 samples) was used to determine 95% confidence intervals (CI) of condition mean differences (McGirr et al., 2017). Data was presented as mean ± SEM.

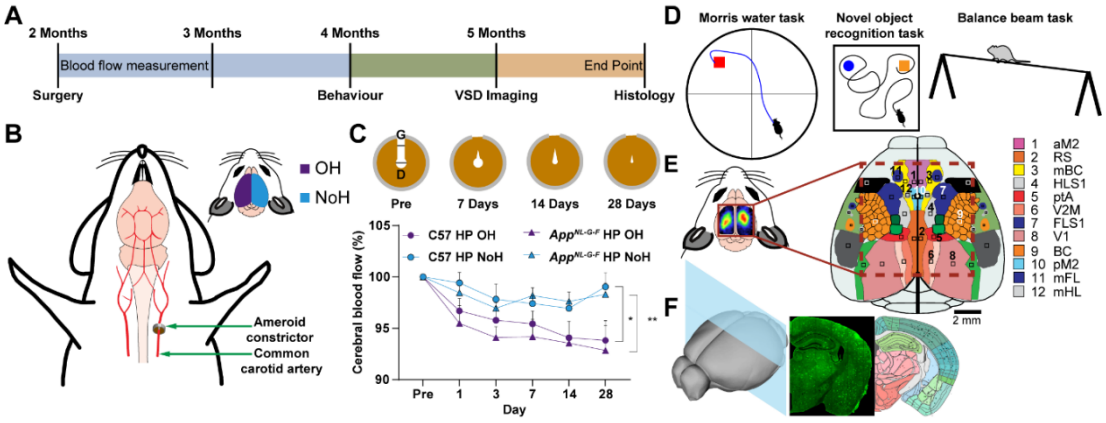

Figure 4.1: Experimental timeline.

(A) Two months old mice were randomly divided into sham or HP groups. The C57 (n = 13) and $App^{NL\text{-}G\text{-}F}$ (n = 11) groups consisted of mice that underwent sham surgery. The C57 HP (n = 6) and $App^{NL\text{-}G\text{-}F}$ HP (n = 16) groups were mice that underwent left common carotid artery occlusion (UCAgO). Cerebral blood flow (CBF) was measured pre surgery and post UCAgO surgery at intervals of 1, 3, 7, 14 and 28 days. Behavioral testing started two months after surgery, once behavioral testing was finished, wide-field cortical voltage imaging (VSDI) was done. At the experimental end point, mice were perfused, and tissue was collected for immunohistochemistry. (B) Mice were anesthetized with 1.5% isoflurane and a midline cervical incision exposed the common carotid artery (CCA), which was separated from the sheaths. The artery was lifted and placed in the internal lumen of the ameroid constrictor located just below the carotid bifurcation on the left side. The sham surgery followed the same protocol but without implanting an ameroid constrictor. The midline incision was sutured, and the mice were transferred to a recovery room. The inset represents the left hemisphere as the occluded hemisphere (OH) in purple and right hemisphere as the non-occluded hemisphere (NoH) in blue. (C) Relative CBF was measured pre-surgery and on day 1, 3, 7, 14, & 28 post-surgery using laser speckle flowmetry, which has a linear relationship with absolute CBF values and obtains high spatial resolution 2D imaging. Following UCAgO surgery, the gap (G) and the internal diameter (D) of the ameroid constrictor shrank progressively and disappeared (top panel is the cartoon representation of this process). The blood flow in the occluded hemisphere (OH) decreased gradually but significantly from the first day to the 28th day (F(3.116, 37.39) = 7.916, p = 0.0003) as the ameroid constrictor began to swell and the diameter reduced. Further, by 28th day CBF in occluded hemisphere (OH) was significantly reduced compared to the Non-occluded hemisphere (NoH) (F(3,12) = 5.246, p < 0.05) and this effect was found in both the C57 (p < 0.05) and $App^{NL\text{-}G\text{-}F}$ mice (p < 0.005) mice. (D) Behavioural characterization was done at 4 months, mice were handled for at least three days before starting the behavioral tasks. Spatial learning and memory were assessed using the Morris Water Task (MWT), Novel Object Recognition (NOR) was used to assess object learning and memory, and the Balance Beam (BB) test was performed to assess the sensory motor function. (E) Cartoon of cortical areas imaged using wide-field voltage imaging. Bilateral imaging of membrane depolarization using voltage imaging (VSDI) of spontaneous and evoked cortical dynamics. Twenty-four (24), 5 × 5-pixel regions of interest (ROIs) were selected (12 from each hemisphere). Primary hindlimb and forelimb sensory areas (HLS1 and FLS1), parietal associational area (ptA), retrosplenial cortex (RS) medial secondary visual cortex (V2M), primary visual cortex (V1), lateral secondary visual cortex (V2L), barrel cortex (BCS1), hindlimb motor cortex (mHL) and forelimb motor cortex (mFL), as estimated using stereotaxic coordinates (Paxinos & Franklin, 2004). (F) At the experimental end point, mice were perfused, and tissue was collected for immunohistochemistry (IHC). To quantify Aβ plaque, the brain sections were stained with

82E1 immunohistochemical markers. Microgliosis was measured by staining microglial cells with an ionized calcium-binding adapter molecule 1 (Iba1) marker. Quantification of pathology in the HPC and cortex was done using iLastik and ImageJ software.

Animals and experimental timeline

Naïve male and female pairs of C57BL/6J (C57) and APP-KI mice carrying Arctic, Swedish, and Beyreuther/Iberian mutations ($App^{NL\text{-}G\text{-}F/NL\text{-}G\text{-}F}$) (25-30 g) bred in a pathogen free facility were used. The APP-KI mice were gifted by RIKEN Center for Brain Science, Japan. Mice were housed 4-5 mice per cage with *ad libitum* access to standard rodent chow and water and maintained on a 12-hour light/dark cycle. Colony room temperature was maintained at 21^{o} C ± 1^{o}. All experimentation was completed during the light cycle at the same time each day. All experimental procedures were approved by the institutional animal care committee and performed in accordance with the standards set out by the Canadian Council for Animal Care.

At two months of age, mice were randomly divided into sham or HP groups. The C57 (n = 13) and $App^{NL\text{-}G\text{-}F}$ (n = 11) groups consisted of mice that underwent sham surgery. The C57 HP (n = 6) and $App^{NL\text{-}G\text{-}F}$ HP (n = 16) groups were mice that underwent UCAgO. Behavioral testing started two months after surgery. Once behavioral testing was finished, VSDI was done. At the experimental end point, mice were perfused, and tissue was collected for immunohistochemistry (Fig. 4.1).

UCAgO surgery and Laser Speckle flowmetry

The surgical procedure performed was described in a previous study (Mehla et al., 2018a). Briefly, mice were anesthetized with 1.5% isoflurane and a midline cervical incision exposed the common carotid artery (CCA), and the CCA was separated from the sheaths. The artery was lifted and placed in the internal lumen of the ameroid constrictor (AC, Research Instruments NW, 30094 Ingram Rd, Lebanon, OR 97355,

USA; inner diameter, 0.5 mm; outer diameter, 3.25 mm, length, 1.28 mm) located just below the carotid bifurcation on the left side (Fig. 4.1B). The sham surgery followed the same protocol but without implanting an ameroid constrictor. The midline incision was sutured, and the mice were transferred to a recovery room.

Relative CBF was measured pre-surgery and on day 1, 3, 7, 14, & 28 post-surgery using laser speckle flowmetry, which has a linear relationship with absolute CBF values and obtains high spatial resolution 2D imaging as described in previous studies (Ayata et al., 2004; Mohajerani et al., 2011; Winship et al., 2014). The recordings were performed through a glass cover slip cranial window under anesthesia with 1.0 - 1.2% isoflurane (Mostany and Portera-Cailliau, 2008; Kyweriga et al., 2017). The mean CBF measurement was from identically sized ROI (located 2 mm lateral and 1 mm posterior from bregma) using ImageJ as described previously (Mohajerani et al., 2011; Winship et al., 2014). The reflectance optical signals reflect the CBF of the surface micro vessels in the cortex (Winship, 2014). CBF values are expressed as a percentage of the pre-surgery value. The subjects (n = 4) used for CBF were different from those used for behavioral assessment and histology in both sham and HP groups. The mean CBF measurement was from identically sized regions of interest (ROI) using ImageJ as described previously (Mohajerani et al., 2011).

Behavioral testing

Mice were handled for at least three days before starting the behavioral tasks. Spatial learning and memory were assessed using the Morris Water Task (MWT), Novel Object Recognition (NOR) was used to assess object learning and memory, and the Balance Beam (BB) test was performed to assess the sensory motor function.

MWT

Mice were trained on the MWT, as described previously in order to investigate spatial navigation learning and memory (Mehla et al., 2018b; Mehla et al., 2019). The acquisition phase consisted of four trials (60 sec maximum) per day for eight days. The trial was stopped once the mouse found the platform or 60 seconds elapsed, whichever occurred first. Mice were guided to the platform if they failed to find the platform. An intertrial interval of five minutes was used. Latency, pathlength, and swim speed were measured during the acquisition phase. On the ninth day, a single 60 sec no-platform probe trial was done. Mice were placed at a novel starting location opposing the target quadrant and allowed to swim freely for 60 sec before the trial ended. The percent of time spent in the target and non-target quadrants was measured during the no-platform probe trial.

NOR

The NOR was conducted to investigate object memory in mice as described previously (Mehla et al., 2018a). Mice were habituated to the testing box (White plastic, 52 x 51 x 30 cm; standard mouse bedding bottom) for five minutes for four days before testing. On the training day mice explored two identical objects for ten minutes. On the testing day, 24 hours later, a novel object replaced a familiar object, and mice explored for five minutes. Each trial started with a clean box and objects were cleaned with 70% isopropyl alcohol. Mice started each trial opposing the objects location. The investigation ratio (IR), the total time investigating object A divided by the sum of the time investigating Object A and Object B, was used to control for the individual differences investigating objects between mice. The IR was analyzed from recorded videos by an investigator, blinded to the groups.

Balance Beam

The BB is used to assess sensorimotor function (Mehla et al., 2018a). Mice were trained to traverse a 100 cm long, 1 cm diameter steel beam. Mice were trained incrementally starting from 10 cm, then 50 cm, and finally 100 cm. The training was complete once the mouse fully traversed the beam three times. Testing was done 24 hours later. The average time of three trials to traverse the beam was recorded. Falling would end the trial.

Surgery for craniotomy and VSDI

At five months of age, craniotomy for VSDI was performed as described previously (Mohajerani et al., 2010; Mohajerani et al., 2013; Kyweriga and Mohajerani, 2016). Mice were anesthetized with isoflurane (1.2–1.5%) for induction, followed by urethane for data collection (1.0-1.2 mg/kg, i.p). Mice were transferred on a metal plate that could be mounted onto the stage of the upright macroscope, and the skull was fastened to a steel plate. A tracheotomy was performed on mice to assist with breathing before starting the craniotomy. A 7×8 mm bilateral craniotomy (bregma 2.5 to −4.5 mm, lateral 0 to 4 mm) was made and the underlying dura was removed. Body temperature was maintained at 37 ± 0.2 °C degrees using a heating pad with a feedback thermistor.

For *in vivo* VSDI, RH1691 dye (Optical Imaging, New York, NY) was applied to the cortex for 30-45 min. For data collection, 12-bit images were captured with a CCD camera (1M60 Pantera, Dalsa, Waterloo, ON) and E8 frame grabber with XCAP 3.9 imaging software (EPIX, Inc., Buffalo Grove IL). The voltage sensitive dye was excited with a red LED (Luxeon K2, 627 nm center), and excitation filters 630 ± 15 nm (Mohajerani et al., 2010; Mohajerani et al., 2013; Chan et al., 2015). Images were taken through a macroscope composed of front-to-front video lenses (8.6 × 8.6 mm field of

view, 67 μm per pixel). The depth of field of the imaging setup used was ~1 mm (Lim et al., 2012). To stimulate the forelimbs and hindlimbs, thin acupuncture needles (0.14 mm) were inserted into the paws, and a 1 mA, 1-ms electrical pulse was delivered.

VSD data pre-processing

VSDI of spontaneous cortical activity was recorded in the absence of visual, olfactory, tactile, or auditory stimulation during 15 min epochs with 10 ms (100 Hz) temporal resolution. Data was first denoised by applying singular-value decomposition and taking only the components with greatest associated singular values. The baseline of the optical signal (F_0) captured from each pixel in the imaging window was calculated using the *locdetrend* function in the Choronux toolbox was used to fit a piecewise linear curve to the pixel time series using the local regression method (Mitra and Bokil, 2008). The fluorescence changes were quantified as $(F-F_0)/F_0 \times 100\%$; F represents the fluorescence signal at any given time and F_0 represents the average of fluorescence over all frames. A band pass filter was applied (0.5–6 Hz) FIR filter on the $\Delta F/F_0$ signal as most of the optical signal power is concentrated in low frequencies (Mohajerani et al., 2013).

VSD responses to sensory-evoked stimulation were calculated as the normalized difference to the average baseline recorded before stimulation ($\Delta F/F0 \times 100$) using custom-written code in Matlab (Mathworks) or ImageJ (National Institutes of Health). Averages of sensory stimulation were calculated from 20 trials of stimulation with an inter-stimulus interval of 10 s.

Spontaneous Data analysis

For region-based correlation analyses, 24, 5 × 5-pixel ROIs were selected (12 from each hemisphere) from resting state (task-independent) spontaneous VSDI data in C57, C57 HP, $App^{NL\text{-}G\text{-}F}$, and $App^{NL\text{-}G\text{-}F}$ HP mice (n = 4, 4, 7, and 8 respectively). Sensory stimulation was used to determine the coordinates for the primary hindlimb and forelimb sensory areas (HLS1 and FLS1). From these primary sensory coordinates, the relative locations of additional associational areas, medial secondary visual cortex (ptA, RS, V2M), primary visual cortex (V1), lateral secondary visual cortex (V2L), barrel cortex (BCS1), hindlimb motor cortex (mHL) and forelimb motor cortex (mFL), were estimated using stereotaxic coordinates (Paxinos & Franklin, 2004). The regional functional connectivity strength matrix was generated using the zero-lag Pearson correlation of ROI time courses.

Evoked data analysis

Alteration in evoked population responses were compared based on the following five parameters: rise time, fall time, inter-hemispheric delay, peak $\Delta F/F_0$, and laterality index. The rise-time was defined as the time taken for the signal to rise from 10% to 90% of the peak evoked activation in occluded and non-occluded hemispheres. Fall-time was defined as the time taken by the signal to fall from 90% to 10% of the peak evoked activation in occluded and non-occluded hemispheres. Inter-hemispheric delay is the time difference of peak evoked activation in occluded and non-occluded hemispheres. Peak amplitude is the peak evoked change in fluorescence ($\Delta F/F_0$)in occluded and non-occluded hemispheres. The laterality index is defined as the ratio of difference is peak activations and the sum of peak activations (peak OH – peak NoH) / (peak OH + peak NoH).

Network analysis

Custom written MATLAB scripts in addition to modified version of Bioinformatics (Lim et al., 2015) and Brain Connectivity Toolbox (Rubinov and Sporns, 2010) were used to create a network diagram from the correlation matrices. Node size is proportional to the strength of the connections per node and edges represents connections that were greater (green) or less (red) than 10% of the control connections (Fig. 4.2).

Immunohistochemistry

Mice were transcardially perfused with 1X phosphate buffer solution (PBS) followed by 4% paraformaldehyde (PFA). The brains were post-fixed in 4% PFA for 24 hours, followed by cryoprotection in a 30% sucrose solution with 0.02% sodium azide for at least three days before sectioning. Frozen brains were sectioned (40 µm) on a sliding microtome. The sections were stored in 1X PBS and 0.02% sodium azide at 4^{o}C until processed.

To quantify Aβ plaque, the brain sections were stained with 82E1 immunohistochemical markers. Microgliosis was measured by staining microglial cells with an ionized calcium-binding adapter molecule 1 (Iba1) marker and the number of activated microglia (Iba1+) was quantified in the HPC and cortex of (see supplementary information: key reagents table for antibodies used). Sections were co-stained with DAPI (0.01 mg/ml; 140 ul/slides with cover slip).

Pathology Imaging and Quantification

A Nanozoomer serial slide scanner (NanoZoomer Digital Pathology 2.0-RS, HAMAMATSU, JAPAN) and Laser Scanning confocal microscope were used for

imaging. Quantification of pathology was done using iLastik (Version 1.3.0-OSX) (Berg et al., 2019) and ImageJ software. To quantify pathology, single channel images were used. Thresholding the channel of interest was done to apply consistency among all images to ensure training and prediction accuracy in iLastik. As iLastik uses several parameters for automated counting, predictions were not based solely on intensity of signal alone. Images were exported at 2.5x magnification and the regions of interests were isolated and copied into a 3000 x 3000-pixel window in ImageJ. The scale for each image was set by using the scale bar on the initial image which gave the number of pixels per millimeter; this value was used to determine the size of the plaque in millimeters. Images were uploaded to iLastik and the program was trained to automatically identify specific pathological markers. The process was done for Aβ plaque and activated microglia, See supplementary material for prediction of counts vs raw data comparison.

Statistical Analysis

GraphPad Prism 7 for Mac OS X, v.7.0D (GraphPad Software, La Jolla California USA, www.graphpad.com) was used for statistical analysis of behavioral and pathology quantification. A p value < 0.05 was considered statistically significant, adjusted p values reported. A two-way repeated measures ANOVA followed by Sidak's multiple comparison was used to determine significance between CBF across days and between the occluded hemisphere and non-occluded hemispheres (Fig. 4.1D). Effects of STRAIN, HP, and DAY were assessed with 3-way ANOVA and Tukey's multiple comparison significance in behavioural experiments; sphericity was corrected with the Giesser-Greenhouse correction (Fig. 4.7). For spontaneous VSDI data a Generalized linear mixed-effects (GLME) model in MATLAB 2018b was used to predict correlation values with a fixed effect for group, including random effects for inter-regional

correlations. Significance was set at $\alpha \leq 0.05$. Further, bootstrapping (resampling with replacement, 1000 samples) was used to determine 95% confidence intervals (CI) of condition mean differences (McGirr et al., 2017) (Fig. 4.2). An ordinary one-way ANOVA was used to analyze the groups and between ipsilateral and contralateral sides and between groups for Aβ and microgliosis pathology. The effect size was calculated with Cohen's d for the effects of HP in the *App*$^{NL-G-F}$ mice (Fig. 4.6). Results presented as mean ± standard error of the mean (SEM).

Results

UCAgO causes significant reduction in cerebral blood flow of the occluded hemisphere in both App^{NL-G-F} *and C57 mice.*

We assessed CBF before UCAgO and at intervals of 1, 3, 7, 14 and 28 days following UCAgO surgery to determine if the implanted ameroid constrictor would reduce CBF in the C57 and *App*$^{NL-G-F}$ mice. We found that following UCAgO surgery, the blood flow in the occluded hemisphere (OH) decreased gradually but significantly from the first day to the 28th day [$F(3.116, 37.39) = 7.916$, $p = 0.0003$] as the ameroid constrictor began to swell and the diameter reduced. By the 28th day CBF in occluded hemisphere (OH) was significantly reduced compared to the Non-occluded hemisphere (NoH) [$F(3,12) = 5.246$, $p < 0.05$] and this effect was found in both the C57 ($p < 0.05$) and *App*$^{NL-G-F}$ mice ($p < 0.005$) mice (Fig 4.1D). We conclude that the UCAgO was successful in gradually reducing blood flow over time to the ipsilateral side of the brain (OH) of the occluded artery, while blood flow to the contralateral side of occlusion (NoH) was not impacted. Furthermore, the UCAgO surgery reduced CBF equally in the C57 and *App*$^{NL-G-F}$ mice.

Gradual cerebral HP disrupts cortical networks

After determining that UCAgO successfully reduced blood flow to the OH, we wanted to identify changes in cortical functional connectivity associated with hypoperfusion and AD. Following behavioural testing and when the mice were 6 months of age, we imaged bilateral and ongoing spontaneous cortical activity to examine the functional connectivity of the cortex as previously described (Mohajerani et al., 2013; Kyweriga and Mohajerani, 2016; Balbi et al., 2019) and calculated functional connectivity matrices based on correlation analysis.

The mice were anesthetised with urethane and a 7×8 mm bilateral craniotomy (bregma 2.5 to −4.5 mm, lateral 0 to 4 mm) was performed on the sham (C57, $n = 4$ and $App^{NL\text{-}G\text{-}F}$, $n = 7$) and HP (C57, $n = 4$ and $App^{NL\text{-}G\text{-}F}$, $n = 8$) mice as described previously (Mohajerani et al., 2010; Mohajerani et al., 2013; Kyweriga and Mohajerani, 2016) and spontaneous Voltage-sensitive dye (VSD) imaging of cortical responses were recorded.

Following recording, region-based cortical correlation analysis was performed on resting state VSDI data. Twelve, 5 × 5-pixel regions of interest (ROIs) were selected from each hemisphere for a total of 24 cortical responses. Sensory stimulation was used to determine the coordinates for the primary sensory areas (HLS1 and FLS1). From these primary sensory coordinates, the relative locations of additional associational areas, medial secondary visual cortex (ptA, RS, V2M), primary visual cortex (V1), lateral secondary visual cortex (V2L), barrel cortex (BCS1), hindlimb motor cortex (mHL) and forelimb motor cortex (mFL), were estimated using stereotaxic coordinates (Paxinos and Franklin, 2004). The regional functional connectivity strength matrix was generated using the zero-lag Pearson correlation of ROI time courses.

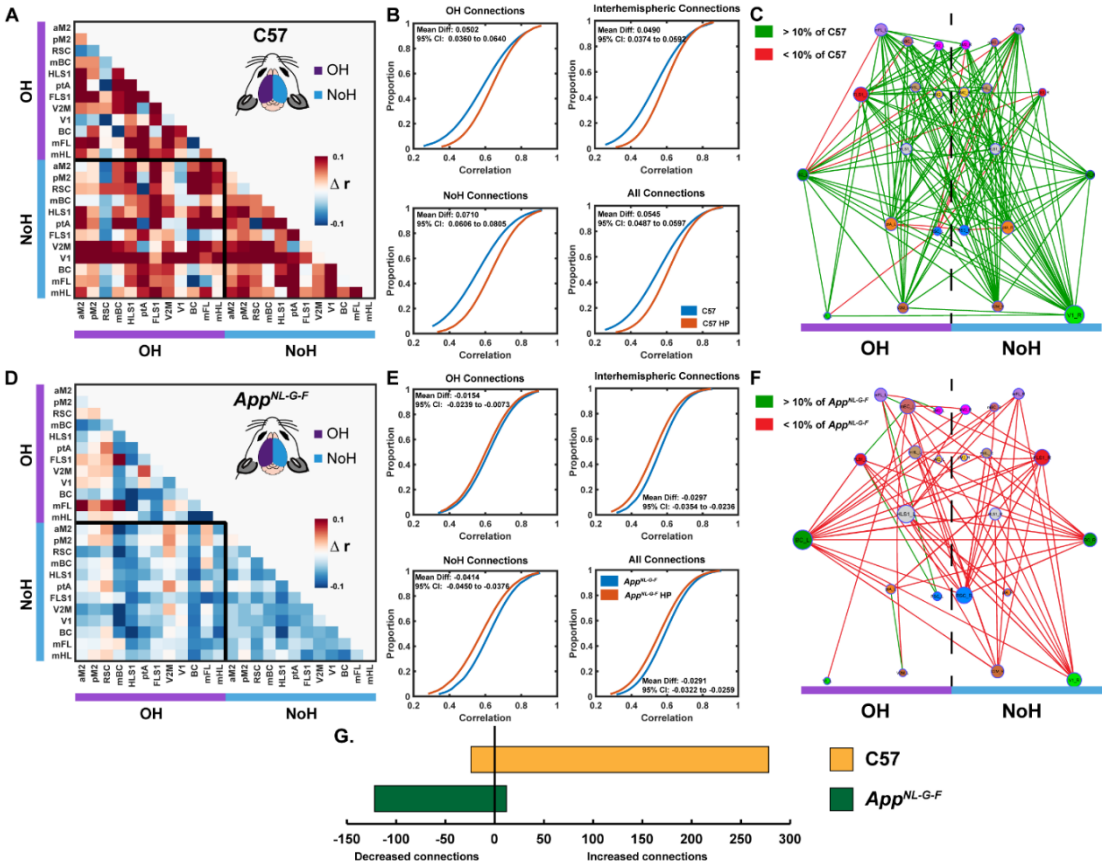

Figure 4.2: Unilateral cerebral hypoperfusion associated changes in cortical functional connectivity of C57 and *App*$^{NL\text{-}G\text{-}F}$ mice.

(A) Difference of mean correlation matrix for C57 HP - C57 animals (n = 4 and n= 4) representing increased cortical connectivity due to HP in C57 animals. (B) Cumulative distribution functions (*cdf*) of correlation values suggest increased cortical connectivity in C57 HP group as compared to C57 group. These changes in cortical connectivity strength were accessed using Generalized linear mixed-effects (GLME) models (n = 4; C57 and n = 4; C57 HP). Intrahemispheric (OH) connections: 66 connections/animal; GLME HP-effect $t(526) = 6.9296$, $p < 0.001$; intrahemispheric (NoH) connections: 66 connections/animal; GLME HP-effect $t(526) = 17.133$, $p < 0.001$); interhemispheric connections: 144 connections/animal; GLME HP-effect $t(1150) = 12.328$, $p < 0.001$ and all connections: 276 connections/animal; GLME HP-effect $t(2206) = 19.39$, $p < 0.001$. (C) Network graph of changes in cortical connections (HP-effect) shows that HP in C57 animals leads to hyperconnectivity in cortical network (red lines represents more than 10% reduction and green lines represents more than 10% increase in connection strength in C57 HP group compared to C57 group. (D) Difference of mean correlation matrix for *App*$^{NL\text{-}G\text{-}F}$ HP - *App*$^{NL\text{-}G\text{-}F}$ animals (n = 8 and n= 7) representing reduced cortical connectivity due to HP in Alzheimer's disease mouse model. (E) Cumulative distribution functions (*cdf*) of correlation values suggest reduced cortical connectivity in *App*$^{NL\text{-}G\text{-}F}$ HP group as compared to *App*$^{NL\text{-}G\text{-}F}$ group. These changes in cortical connectivity strength were accessed using Generalized linear mixed-effects (GLME) models (n = 7; *App*$^{NL\text{-}G\text{-}F}$ and n = 8; *App*$^{NL\text{-}G\text{-}F}$ HP). Intrahemispheric (OH) connections: 66 connections/animal; GLME HP-effect $t(988) = 1.382$, n.s.; intrahemispheric (NoH) connections: 66 connections/animal; GLME HP-effect $t(988) = 6.1703$, $p < 0.001$; interhemispheric connections: 144 connections/animal; GLME HP-effect $t(2158) = 5.2929$, $p < 0.001$ and all connections: 276 connections/animal; GLME HP-effect $t(4138) = 7.2909$, $p < 0.001$. (F) Network graph of changes in cortical connections (HP-effect) shows that HP in *App*$^{NL\text{-}G\text{-}F}$ animals leads to reduction of network connectivity (red lines represents more than 10% reduction and green lines represents more than

10% increase in connection strength in App^{NL-G-F} HP group compared to App^{NL-G-F} group). (G) Number of connections greater/less than 10% of the control correlation, explains the dissociative effects of hypoperfusion on cortical functional connectivity.

Gradual cerebral HP in the C57 mice lead to a hyperconnectivity in the cortical network (Fig. 4.2C).The *cdf* of correlation values suggest that there was a significant increase of cortical functional connectivity in the C57 HP mice (n = 4) as compared to the C57 mice (n = 4). When looking at all connections, there is a significant increase in functional connectivity in the C57 HP mice compared to the C57 sham mice [$t(2206) = 19.39$, $p < 0.001$; GLME HP-effect, all connections/mouse = 276]. The same pattern of increase in functional connectivity was also found across hemispheres [$t(1150) = 12.328$, $p < 0.001$; GLME HP-effect, interhemispheric connections/mouse = 144], and within both the OH hemisphere [$t(526) = 6.9296$, $p < 0.001$; GLME HP-effect, intrahemispheric (OH) connections/mouse = 66] and NoH [$t(526) = 17.133$, $p < 0.001$; GLME HP-effect, intrahemispheric (NoH) connections/mouse = 66].

However, we found the opposite pattern of connectivity in the App^{NL-G-F} mice where gradual cerebral HP in App^{NL-G-F} mice lead to a hypoconnectivity in the cortical network (Fig 4.2F). The *cdf* of correlation values suggest reduced cortical functional connectivity in the App^{NL-G-F} HP mice (n = 8) as compared to the App^{NL-G-F} group ($n = 7$). When looking at all connections, the App^{NL-G-F} sham mice showed significantly stronger connections compared to the App^{NL-G-F} HP mice [$t(4138) = 7.2909$, $p < 0.001$; GLME HP-effect, all connections/mouse = 276]. When looking across hemispheres the same pattern was observed [$t(2158) = 5.2929$, $p < 0.001$; GLME HP-effect, interhemispheric connections/mouse = 144]. Within hemispheres, we found no significant difference in the OH [$t(988) = 1.382$, $p = 0.167$; GLME HP-effect, intrahemispheric (OH) connections/mouse = 66] but we did in the NoH [$t(988) =$

6.1703, $p < 0.001$; GLME HP-effect, intrahemispheric (NoH) connections/mouse = 66]. See Fig. 4.3. for full mean and SEM matrices of cortical correlation.

We found that hypoperfusion had a dissociative effect on cortical functional connectivity in both C57 and *App*$^{NL\text{-}G\text{-}F}$ mice. While hypoperfusion increased functional connectivity (*hyper connectivity*; Fig. 4.2A) in the C57 mice, it reduced cortical functional connectivity (*hypo connectivity*; Fig. 4.2D) in the *App*$^{NL\text{-}G\text{-}F}$ mice. These differential effects of cerebral HP on functional connectivity strength were consistently observed in inter-, intra- and overall connections of both the C57 and *App*$^{NL\text{-}G\text{-}F}$ mice.

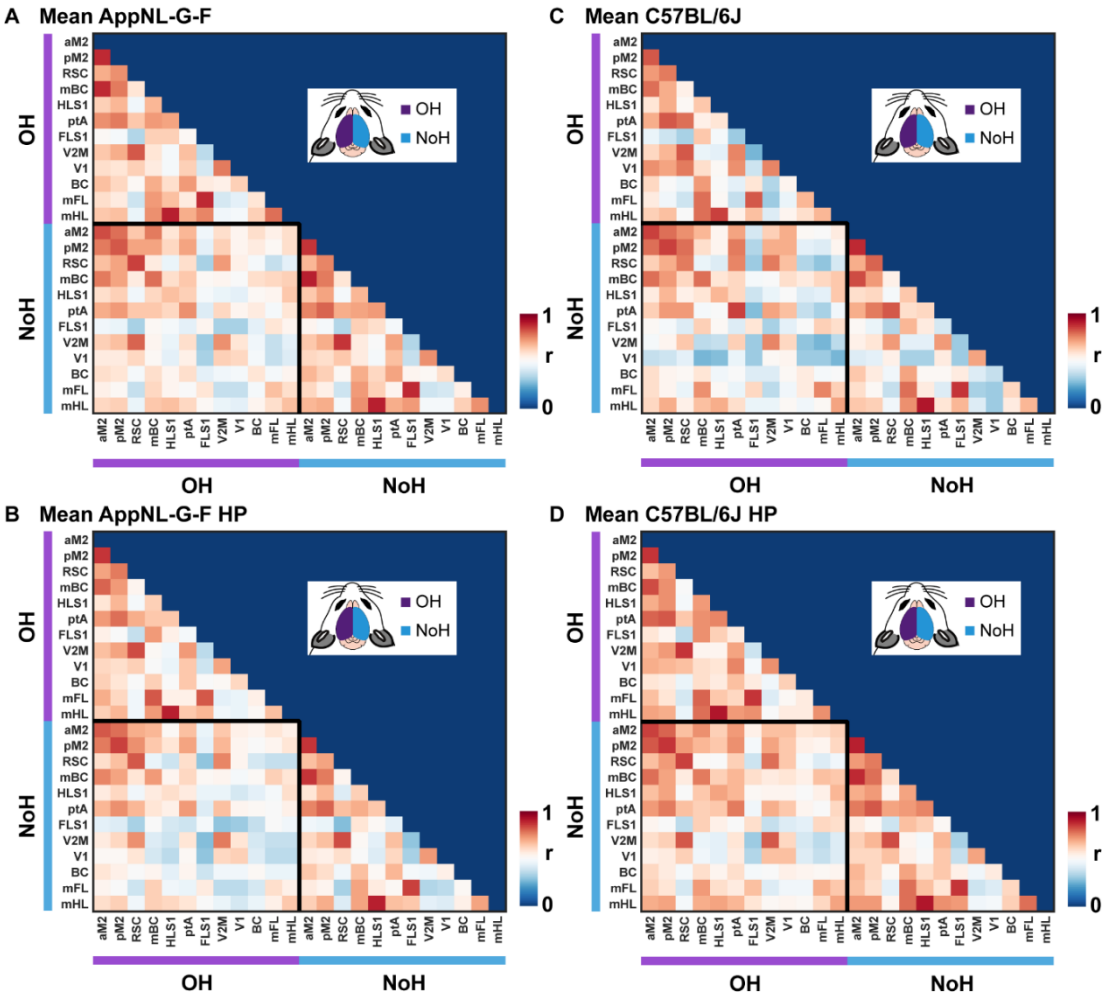

Figure 4.3: Cortical correlation matrix.
Mean of cortical correlation matrix of **(A)** *App*$^{NL\text{-}G\text{-}F}$ mice (n = 7), **(B)** *App*$^{NL\text{-}G\text{-}F}$ HP mice (n = 8), **(C)** C57 mice (n = 4), and **(D)** C57 HP mice (n = 4).

Evoked somatosensory cortical activity

In addition to bilateral resting state spontaneous cortical activity, fore- and hindlimb stimulation-evoked VSD signals were recorded in both cortical hemispheres of sham and HP mice. We hypothesized that in addition to spontaneous activity alterations with hypoperfusion, sensory cortical evoked responses will also be affected. Patterns of sensory signal processing are shown to be altered in mouse models of AD and after targeted mini-strokes (Sigler et al., 2009; Mohajerani et al., 2011; Maatuf et al., 2016). In our experiments sensory stimulation of forelimb (FL) and hindlimb (HL) somatosensory cortex was conducted to map relevant brain regions and to study the bilateral changes associated with hypoperfusion. Alteration in population responses were compared based on the following five parameters: rise time, fall time, inter-hemispheric delay, peak change in fluorescence ($\Delta F/F_0$) and laterality index. The rise-time was defined as the time taken for the signal to rise from 10% to 90% of the peak evoked activation in occluded and non-occluded hemispheres. Fall-time was defined as the time taken by the signal to fall from 90% to 10% of the peak evoked activation in occluded and non-occluded hemispheres. Inter-hemispheric delay is the time difference of peak evoked activation in occluded and non-occluded hemispheres. Peak amplitude is the peak evoked change in fluorescence ($\Delta F/F_0$) in occluded and non-occluded hemispheres. The laterality index is defined as the ratio of difference is peak activations and the sum of peak activations (peak OH – peak NoH) / (peak OH + peak NoH).

As previously described for the non-stroke conditions (Ferezou et al., 2007; Mohajerani et al., 2011) we also found that sensory stimulation of FL or HL leads to first activation in contralateral hemisphere and the signal later (~20 ms delay) propagates to hemisphere ipsilateral to stimulated limb. In addition, the secondary

response in the ipsilateral hemisphere is lower in magnitude as compared contralateral hemisphere.

For FL left stimulation we found that in C57 HP and $App^{NL\text{-}G\text{-}F}$ HP mice there is a significant reduction in the fall time of the sensory evoked signal ($p < 0.05$), in addition the peak amplitude of activation is also reduced ($p < 0.05$). Suggesting that disease and HP causes reduction in *ipsi*- and *contra*- lateral FL left evoked cortical population responses both in magnitude and time of activation (Fig. 4.4B). For FL right stimulation we found that inter-hemispheric delay was significantly higher ($p < 0.05$) for the C57 group as compared to C57 HP group suggesting that in hypoperfusion group the activation in OH and NoH was faster or more synchronized. This finding is of particular interest as in our earlier results of spontaneous cortical activity in C57 group we found hyper-cortical connectivity due to hypoperfusion. Further, there are significant changes in rise-time, fall time and peak amplitude as shown in *p*-value maps in Fig. 4.4E.

HL left stimulation revealed reduction in fall time due to hypoperfusion ($p < 0.05$) in both C57 and $App^{NL\text{-}G\text{-}F}$ groups (Fig. 4.5B), but no significant change was observed in peak amplitude as was observed earlier for FL left stimulation. Further, for HL right stimulation we observed significant hemisphere selective changes in fall time and peak amplitude for C57 and $App^{NL\text{-}G\text{-}F}$ groups (Fig. 4.5E). Interestingly, we found that inter-hemispheric delay was significantly higher ($p < 0.05$) for the C57 group as compared to C57 HP, this finding is in accordance with our earlier observation of faster or more synchronized brain activity both in FL right evoked and spontaneous activity of C57 HP group.

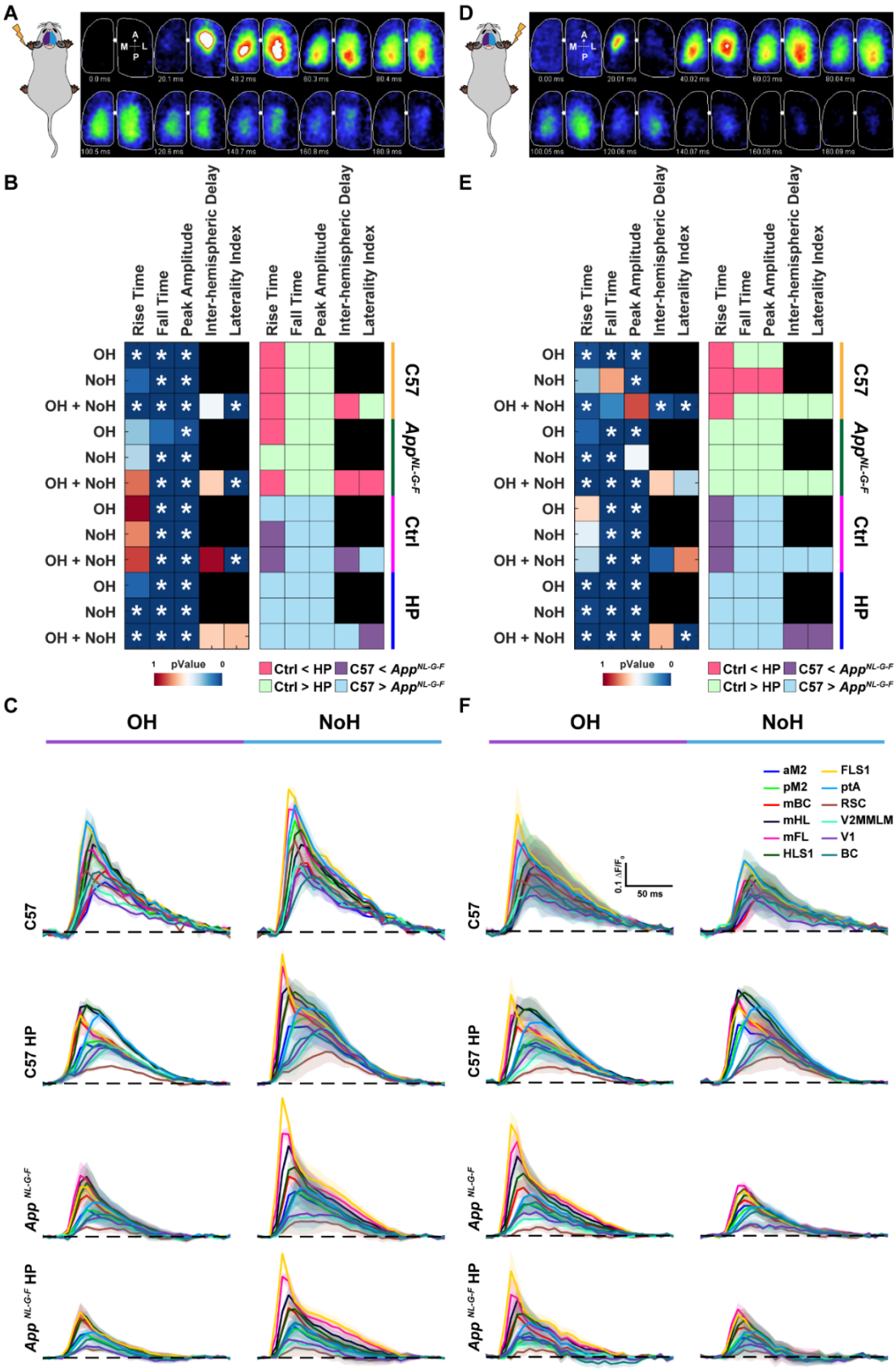

Figure 4.4: Left/Right forelimb (FL) evoked cortical activations.
(A, D) representative patterns of bilateral cortical activation following 1 mA, 1 ms pulse stimulation to left and right FL. The VSDI montages represents 10 frames of evoked cortical

responses at interval of 20 ms after stimulus onset (0.00 ms). The first image in the montage indicates the anterior (A), posterior (P), medial (M) and lateral (L) directions. (B,E) Comparison of rise time (10% to 90% of peak) , fall time (90% to 10% of peak), peak amplitude, inter-hemispheric delay (abs(peak time OH – peak time NoH)) and laterality index ((peak OH – peak NoH)/ (peak OH + peak NoH) across all groups. These changes in these five parameters were accessed using Generalized linear mixed-effects (GLME) models. Mustard bar represents comparison of C57 HP and C57, green bar represents comparison of $App^{NL\text{-}G\text{-}F}$ and $App^{NL\text{-}G\text{-}F}$ HP, magenta bar represents comparison of C57 and $App^{NL\text{-}G\text{-}F}$, dark blue bar represents comparison of C57 HP and $App^{NL\text{-}G\text{-}F}$ HP groups. (C,F) Mean and S.E.M. of evoked cortical activations in twenty-four (24), 5 × 5-pixel regions of interest (ROIs) were selected (12 from each hemisphere). Primary hindlimb and forelimb sensory areas (HLS1 and FLS1), parietal associational area (ptA), retrosplenial cortex (RS) medial secondary visual cortex (V2M), primary visual cortex (V1), lateral secondary visual cortex (V2L), barrel cortex (BCS1), hindlimb motor cortex (mHL) and forelimb motor cortex (mFL), as estimated using stereotaxic coordinates (Paxinos & Franklin, 2004). $App^{NL\text{-}G\text{-}F}$ animals (n = 7 Ctrl; n = 8 HP) and C57BL6/J HP animals (n = 4 Ctrl; n = 4 HP). All values are expressed as mean ± SEM. * $p < 0.05$

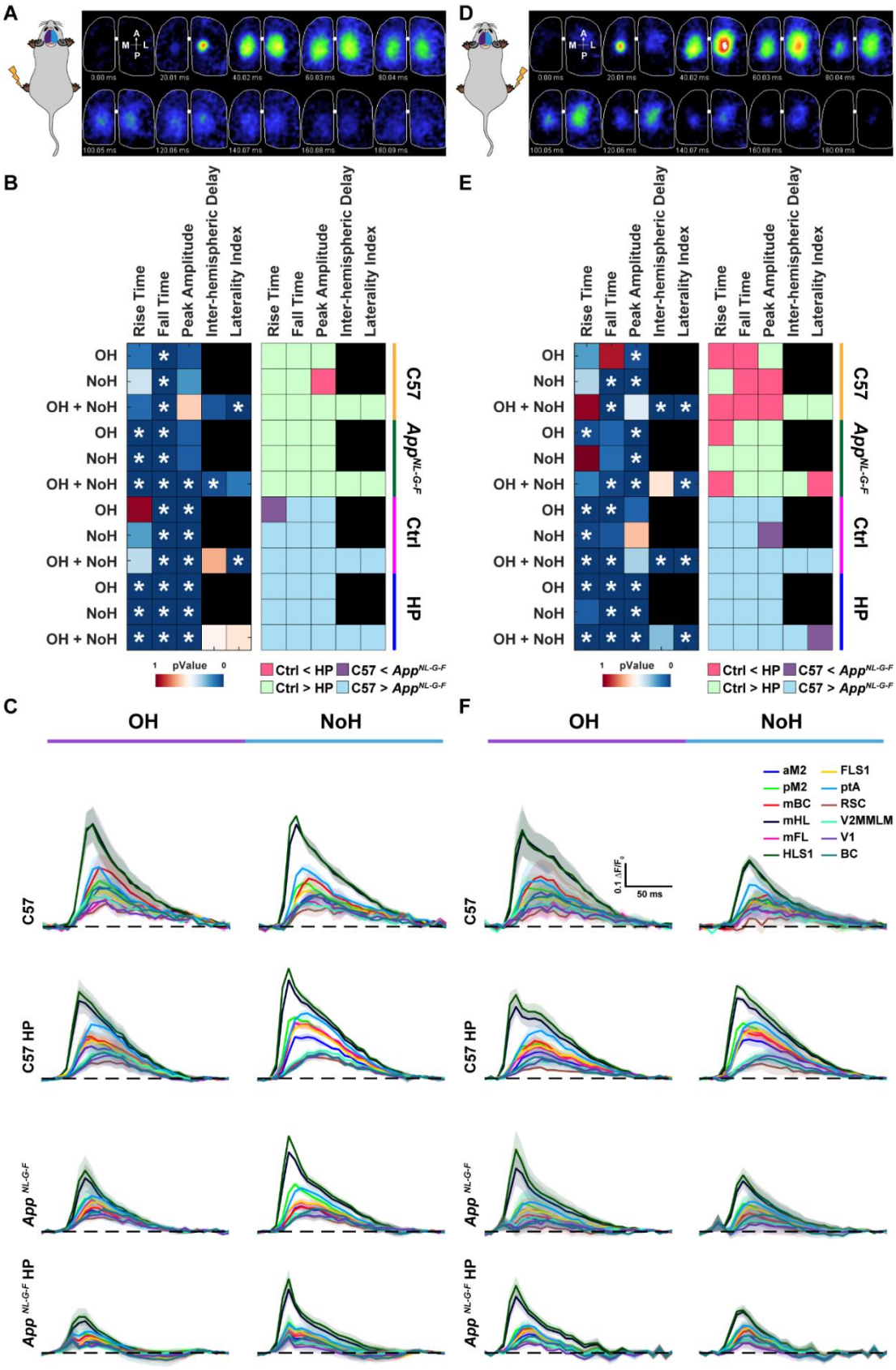

Figure 4.5: Left/Right hind limb (HL) evoked cortical activations.

(A, D) representative patterns of bilateral cortical activation following 1 mA, 1 ms pulse stimulation to left and right HL. The VSDI montages represents 10 frames of evoked cortical

responses at interval of 20 ms after stimulus onset (0.00 ms). The first image in the montage indicates the anterior (A), posterior (P), medial (M) and lateral (L) directions. (B,E) Comparison of rise time (10% to 90% of peak) , fall time (90% to 10% of peak), peak amplitude, inter-hemispheric delay (abs(peak time OH – peak time NoH)) and laterality index ((peak OH – peak NoH)/ (peak OH + peak NoH) across all groups. These changes in these five parameters were accessed using Generalized linear mixed-effects (GLME) models. Mustard bar represents comparison of C57 HP and C57, green bar represents comparison of App^{NL-G-F} and App^{NL-G-F} HP, magenta bar represents comparison of C57 and App^{NL-G-F}, dark blue bar represents comparison of C57 HP and App^{NL-G-F} HP groups. (C,F) Mean and S.E.M. of evoked cortical activations in twenty-four (24), 5 × 5-pixel regions of interest (ROIs) were selected (12 from each hemisphere). Primary hindlimb and forelimb sensory areas (HLS1 and FLS1), parietal associational area (ptA), retrosplenial cortex (RS) medial secondary visual cortex (V2M), primary visual cortex (V1), lateral secondary visual cortex (V2L), barrel cortex (BCS1), hindlimb motor cortex (mHL) and forelimb motor cortex (mFL), as estimated using stereotaxic coordinates (Paxinos & Franklin, 2004). App^{NL-G-F} animals (n = 7 Ctrl; n = 8 HP) and C57BL6/J HP animals (n = 4 Ctrl; n = 4 HP). All values are expressed as mean ± SEM. * $p < 0.05$.

Gradual cerebral HP increased microgliosis and Aβ plaque throughout the brain.

Aβ plaque

We wanted to know whether the gradual cerebral HP method used in this study would increase Aβ plaque deposition differently in the OH and NoH of the cortex and HPC to determine if this was correlated with behaviour or cortical dynamics. We found that despite differences in cerebral blood flow in the OH and NoH at 28 days following constrictor implantation, the Aβ pathology was found not to be significantly different across hemispheres in the cortex [$F(1,14) = 0.0002$, $p = 0.964$] or HPC [$F(1,14) = 0.016$, $p = 0.901$] of the App^{NL-G-F} mice or App^{NL-G-F} HP mice; no plaque was found in the C57 mice. We did however, find an effect of hypoperfusion on Aβ plaque count in both the cortex [$F(1,14) = 98.10$, $p < 0.0001$] and HPC [$F(1,14) = 36.24$, $p < 0.0001$]. We therefore combined the data to compare group differences. When doing so, the App^{NL-G-F} HP mice had significantly more Aβ plaque in the cortex ($p < 0.0001$) and HPC ($p < 0.01$) compared to the App^{NL-G-F} control mice (Fig. 4.6).

Microgliosis

We also wanted to know if gradual cerebral HP would influence microglial activation in the cortex and HPC. We therefore counted Iba1+ cells in the cortex and HPC in the OH and NoH hemispheres. We found microgliosis was not different across hemispheres in the cortex [$F(1,26) = 0.005$, $p = 0.941$] or HPC [$F(1,26) = 0.113$, $p = 0.739$]. We therefore combined the OH and NoH data to examine differences between strain and HP. In the cortex, we found that HP increased microgliosis in the $App^{NL\text{-}G\text{-}F}$ mice but not in the C57 mice; however, sham $App^{NL\text{-}G\text{-}F}$ mice did not have significantly greater microgliosis compared to the C57 sham and C57 HP mice. HP had a significant effect on microgliosis [$F(1,30) = 23.20$, $p < 0.0001$]; however, we also found a significant strain effect [$F(1,30) = 13.67$, $p = 0.0009$] and interaction of HP and strain [$F(1,30) = 11.60$, $p = 0.0019$]. Microgliosis was found to be significantly greater in the $App^{NL\text{-}G\text{-}F}$ HP mice compared to the $App^{NL\text{-}G\text{-}F}$ sham mice ($p < 0.0001$) and the sham and HP C57 mice ($p < 0.0001$). However, the $App^{NL\text{-}G\text{-}F}$ sham mice did not show increased microgliosis compared to the C57 sham or HP mice ($p > 0.05$). Lastly, HP did not have a significant effect on the C57 mice ($p > 0.05$).

In the HPC, HP appeared to cause an equal increase of microgliosis in both the $App^{NL\text{-}G\text{-}F}$ and C57 mice. A significant effect of HP was found [$F(1,30) = 37.42$, $p < 0.0001$]; however, we found no effect of strain [$F(1,30) = 2.314$, $p = 0.139$] and no interaction [$F(1,30) = 1.914$, $p = 0.177$]. The C57 HP mice had significantly greater microgliosis compared to the sham C57 ($p < 0.05$). The $App^{NL\text{-}G\text{-}F}$ HP mice also showed a significant increase in microgliosis compared to the C57 HP mice ($p < 0.0001$) and sham $App^{NL\text{-}G\text{-}F}$ mice ($p < 0.0001$). Lastly, the C57 HP mice had significantly more microgliosis in the HPC compared to the $App^{NL\text{-}G\text{-}F}$ sham mice ($p < 0.05$).

The pathology analysis performed conclude that HP can increase Aβ and microgliosis pathology in the *App*$^{NL-G-F}$ mouse model. The effect of HP on microgliosis appeared greatest in the cortex of the *App*$^{NL-G-F}$ mice however, HP also caused an increase in microgliosis of the C57 HPC.

Aβ plaque and Microgliosis Ratio

To further understand the relationship between fibrillar Aβ deposition and microgliosis, we compared the ratio of microglia expression to Aβ plaque (Fig. 4.6). When comparing the ratio of plaque to microglia expression, we see a similar pattern in the HPC and the rest of the cortex. In the *App*$^{NL-G-F}$ mice, the OH and NoH show similar levels of plaque and microglia expression. The *App*$^{NL-G-F}$ HP mice show significantly more microglia in both OH and NoH compared to the *App*$^{NL-G-F}$ mice, but no significant difference was found between the OH and NoH.

The plaque levels are higher compared to the microglia in the *App*$^{NL-G-F}$ mice in both the HPC and cortex. However, in the *App*$^{NL-G-F}$ HP mice, the pattern is reversed with higher counts of microglia compared to plaques. Furthermore, we examined the ratio of the average microglia to plaque count in the HPC, the ratio in the *App*$^{NL-G-F}$ mice was 0.37 in the OH and 0.44 in the NoH. In the *App*$^{NL-G-F}$ HP mice, the ratio was 1.57 in the OH and 1.21 in the NoH. In the HPC and comparing the NoH and OH of the *App*$^{NL-G-F}$ and *App*$^{NL-G-F}$ HP mice, the *App*$^{NL-G-F}$ HP mice show a change in microglia to plaque that is 4.2 times greater in the OH and 2.75 times greater in the NoH.

In the cortex, the ratio in the *App*$^{NL-G-F}$ mice was 0.15 in the OH and 0.16 in the NoH. In the *App*$^{NL-G-F}$ HP mice, the ratio was 1.12 in the OH and 1.11 in the NoH. When comparing the NoH and OH of the *App*$^{NL-G-F}$ and *App*$^{NL-G-F}$ HP mice, the *App*$^{NL-G-F}$ HP

mice show a change in microglia to plaque that is 7.43 times greater in the OH and 6.73 times greater in the NoH.

These results suggest that the gradual cerebral HP greatly increases the microglia response relative to the number of plaque while it also increases the overall microglia response. The effects could be mediating the changes in inter-regional and intra-hemispheric cortical connectivity patterns, suggesting that the large change in microgliosis might be a key driver for the alteration in cortical dynamics.

Gradual cerebral HP did not impair spatial learning, fine sensory motor abilities, object memory.

Morris Water Task

To assess HPC memory we used the Morris water task to test spatial navigation using our previously used protocol (Mehla et al., 2019). Mice were trained to find a submerged platform over 8 days. Through training, the mice were able to significantly reduce their latency to find the target. The C57 showed a greater reduction in latency compared to the $App^{NL\text{-}G\text{-}F}$ mice. No effect of HP was found on latency.

We found no effect of HP on latency [$F(1,42) = 2.040$, $p = 0.161$] but did find a significant effect of training [$F(5.807, 243.9) = 24.28$, $p < 0.0001$] and strain [$F(1,42) = 78.77$, $p < 0.0001$]. Mice were then consolidated based on strain. The response to training of the C57 and $App^{NL\text{-}G\text{-}F}$ mice was significantly different [$F(7,308) = 2.582$, $p < 0.05$] and multiple comparisons revealed that at every day except the first, the C57 mice had a significantly shorter latency compared to the $App^{NL\text{-}G\text{-}F}$ mice (Day 1, $p < 0.05$; Day 8, $p < 0.0001$). By the 8^{th} day, both C57 and $App^{NL\text{-}G\text{-}F}$ mice showed

significant reduction in latency to find the target platform compared to the first day of training ($p < 0.0001$; Fig. 4.7A).

To determine if the reduction in latency was not due to increased swim speed across training, swim speed was analyzed. Swim speed was found to significantly increase from the first to last day of training. The C57 mice had the fastest swim speed compared to all other groups. The C57 HP and $App^{NL\text{-}G\text{-}F}$ Sham mice showed similar swim speed, but the $App^{NL\text{-}G\text{-}F}$ HP mice were found to significantly slower than all other mice in this experiment. We conclude that HP caused a reduction in average swim speed; however, by the final day of training all mice showed similar swim speeds.

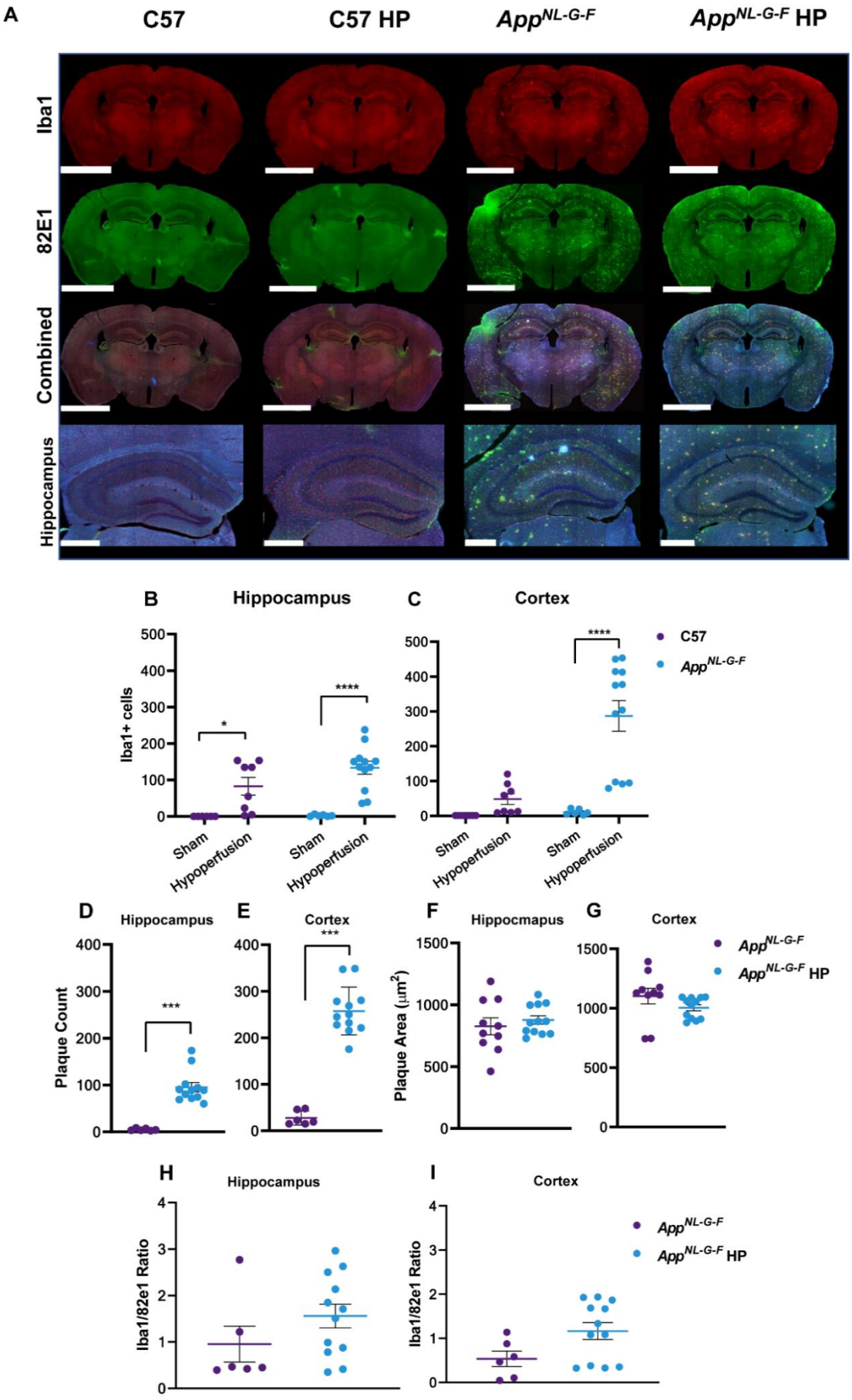
A
C57
C57 HP
App^NL-G-F
App^NL-G-F HP
Iba1
82E1
Combined
Hippocampus
B
Hippocampus
C
Cortex
Iba1+ cells
Sham
Hypoperfusion
C57
App^NL-G-F
D
Hippocampus
E
Cortex
Plaque Count
F
Hippocmapus
G
Cortex
Plaque Area (μm²)
App^NL-G-F HP
H
Hippocampus
I
Cortex
Iba1/82e1 Ratio

Figure 4.6: Gradual cerebral HP was found to significantly exacerbate microgliosis and Aβ pathology in the *App*$^{NL-G-F}$ mice.

(**A)** Photomicrographs of immunohistochemistry staining of microgliosis (Iba1), Aβ plaque (82E1), combined (82E1 + Iba1 + DAPI), and combined magnified images of HPC. Scale bar for Iba1, 82E1, and combined is 2.5 μm; for HPC, 500 μm. (**B and C)** Activated microglia count in HPC (**B**) and cortex **(C)** was significantly increased in the cortex of *App*$^{NL-G-F}$ HP mice (n = 6) compared to the *App*$^{NL-G-F}$ mice (n = 5; $p < 0.005$). Furthermore, the cortex of the *App*$^{NL-G-F}$ HP mice showed significantly greater microglia count compared to the C57 HP mice (n = 5; $p < 0.05$) and C57 mice (n = 3; $p < 0.005$). The HPC in the *App*$^{NL-G-F}$ HP mice showed increased microglial count compared to the *App*$^{NL-G-F}$ mice ($p < 0.005$). (**D-G)** Aβ plaque count in both the HPC (**D)** and cortex (**E)** was significantly greater in the *App*$^{NL-G-F}$ HP mice compared to the *App*$^{NL-G-F}$ sham mice. Aβ plaque area in HPC (**F)** and cortex (**G)** in the *App*$^{NL-G-F}$ HP mice was found to be similar to that of the *App*$^{NL-G-F}$ Sham mice. (**H and I)** We compared the ratio of microglial count to Aβ plaque count in the *App*$^{NL-G-F}$ HP and *App*$^{NL-G-F}$ mice HPC (**H)** and cortex **(I)** and found that the *App*$^{NL-G-F}$ mice showed 0.5 microglia for every plaque in the cortex and 1 in the HPC. The *App*$^{NL-G-F}$ HP mice showed 1.2 microglia/plaque in the cortex and 1.6 in the HPC. Scale bar for whole section is 2.5 mm; for HPC, 500 μm. Data are presented as mean ± SEM. * $p < 0.05$; ** $p < 0.005$; *** $p < 0.001$; **** $p < 0.0001$.

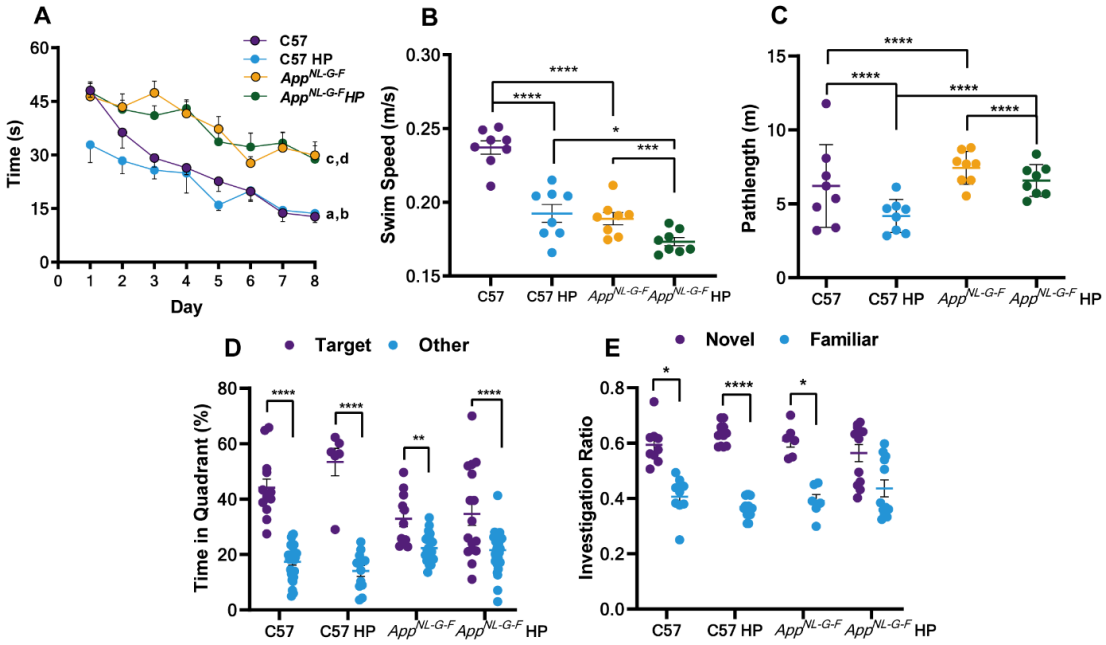

Figure 4.7: Gradual cerebral HP did not impair spatial memory or fine sensory motor abilities or object recognition.

(**A-E**) Spatial learning and memory performance in the MWT (**A**) we found that all mice significantly shortened their latency to find the hidden platform target from day 1 to day 8; **a.** C57, $p < 0.0001$; **b.** C57 HP, $p < 0.01$; **c.** *App*$^{NL-G-F}$, $p < 0.05$; **d.** *App*$^{NL-G-F}$ HP, $p < 0.001$. The C57 mice had significantly shorter latency overall compared to the *App*$^{NL-G-F}$ mice ($p < 0.0001$) (**B)** The C57 mice swim speed was significantly faster than the C57 HP, *App*$^{NL-G-F}$, and *App*$^{NL-G-F}$ HP ($p < 0.0001$) mice. The *App*$^{NL-G-F}$ HP were found to have an average swim speed significantly slower than both the C57 HP ($p < 0.0005$) and *App*$^{NL-G-F}$ ($p < 0.005$) mice. (**C**) A path length analysis showed a similar learning pattern to the latency when comparing day 1 and day 8; **e.** C57, $p < 0.0001$; **f.** C57 HP, $p < 0.05$; **g.** *App*$^{NL-G-F}$ $p < 0.05$; **h.** *App*$^{NL-G-F}$ HP, $p < 0.0001$. The C57 mice had a significantly shorter average path length compared to the *App*$^{NL-G-F}$ ($p < 0.05$). On the final day of acquisition, the *App*$^{NL-G-F}$ and *App*$^{NL-G-F}$ HP mice had similar

path length measurements, both being longer than the C57 ($p < 0.05$) and C57 HP mice ($p < 0.05$). (**D**) The no-platform probe trial showed all mice spent a significantly greater percentage of time in the target quadrant compared to the non-target quadrants. The C57 mice spent a significantly higher percentage of time in the target quadrant compared to the App^{NL-G-F} ($p < 0.05$) and App^{NL-G-F} HP ($p < 0.05$) mice. The C57 HP mice also spent a significantly higher percentage of time in the target quadrant compared to the App^{NL-G-F} ($p = 0.0001$) and App^{NL-G-F} HP ($p = 0.0002$) mice. No difference was found in target preference percent between the C57 and C57 HP mice, nor between the App^{NL-G-F} and App^{NL-G-F} HP mice. (**E**) The NOR task showed the mice spent significantly more time investigating the novel object compared to the familiar object. All values are expressed as mean ± SEM. * $p < 0.05$; ** $p < 0.005$; *** $p < 0.001$; **** $p < 0.0001$.

Training had a significant effect on swim speed [$F(4.625, 194.2) = 8.723$, $p < 0.0001$] with all the mice increasing their swim speed across training. Furthermore, we found a significant effect of both strain [$F(1,42) = 13.80$, $p = 0.0006$] and HP [$F(1,42) = 11.04$, $p = 0.0019$] on swim speed but no interactions were found (Fig. 4.7B). The mice that underwent HP had significantly slower average swim speeds compared to their strain controls ($p < 0.005$; Fig 4.7B). Furthermore, the C57 and C57 HP mice had significantly faster swim speed than the App^{NL-G-F} and App^{NL-G-F} HP mice ($p < 0.05$; Fig. 4.7B). The C57 mice swam significantly faster than all groups of mice, and the App^{NL-G-F} HP mice swam the slowest. However, by the 8th day, no significant differences in swim speed were found between groups.

Due to the differences in swim speed between groups, the average path length was also assessed as this dependent measure is less likely to be influenced by swim speed (Fig. 4.7C). Overall, the C57 mice compared to the App^{NL-G-F} mice but it was found that in both strains, HP resulted in a significantly shorter pathlength. While the mice that underwent HP had a slower swim speed, they had a shorter pathlength which would explain why latency to find the platform was similar between strain (Fig 4.7A-C).

Training had a significant effect on the path length [$F(5.799, 243.6) = 17.98$, $p < 0.0001$), but we also found that the strain [$F(1, 42) = 39.11$, $p < 0.0001$] and HP

[$F(1,42) = 24.86$, $p < 0.0001$] significantly affected pathlength. Furthermore, significant interactions of day and strain [$F(7,294) = 2.938$, $p = 0.0055$], strain and HP [$F(1,42) = 4.127$, $p = 0.0486$], and day and strain and HP [$F(7,294) = 2.120$, $p = 0.0415$] were found. On day 1, the C57 mice had a significantly longer path length compared to the C57 HP ($p < 0.05$), $App^{NL\text{-}G\text{-}F}$, and $App^{NL\text{-}G\text{-}F}$ HP ($p < 0.05$) mice. Furthermore, the C57 HP mice had a significantly shorter path length on the first day compared to the $App^{NL\text{-}G\text{-}F}$ mice ($p < 0.005$). The C57 mice were the only group to significantly reduce their path length from day 1 to day 8 ($p < 0.0001$) but by the 8th day, all groups showed similar path length.

No-Platform Probe Trial

Finally, to determine if the mice were able to learn the platform location, a no-platform probe trail was done and the percent time in the target quadrant was compared to the percent time spent in the other, non-target quadrants (Fig 4.7D). Despite the differences in measures during the acquisition phase, the mice on average spent more time in the target quadrant compared to other quadrants [$F(1,83) = 110.0$, $p < 0.0001$]. On average, the C57 mice did spend significantly more time in the target quadrant compared to the $App^{NL\text{-}G\text{-}F}$ mice [$F(1,83) = 6.66$, $p < 0.05$], but HP did not have an effect on this measure [$F(1,83) = 0.512$, $p = 0.476$]. Multiple comparisons showed that the C57 and C57 HP mice spent significantly greater time in the target quadrant compared to the other quadrants ($p < 0.0001$). The $App^{NL\text{-}G\text{-}F}$ HP mice also showed a significant preference for the target quadrant ($p < 0.01$) and the $App^{NL\text{-}G\text{-}F}$ sham mice also showed a significant preference for the target quadrant ($p < 0.05$).

We found that gradual cerebral HP did not show a significant effect on spatial learning and memory but the differences found between the C57 and $App^{NL\text{-}G\text{-}F}$ mice in

the acquisition phase may be in large part due to motor impairment and not necessarily memory impairment. However, in the no-platform probe trial, we found that the C57 mice performed significanlty better than the $App^{NL\text{-}G\text{-}F}$ mice.

Novel Object Recognition

The novel object recognition was completed to test object memory. As mice prefer novelty, it is predicted they will spend more time investigating the novel object compared to the already familiar object. Overall, we found that the mice investigated the novel object significantly more than the familiar object [$F(1,35) = 63.30$, $p < 0.0001$]. We found that the strain of mice also had a significant effect as well [$F(1,35) = 39.44$, $p < 0.0001$]. All the mice were found to spend a significantly greater amount of time investigating the novel object (Fig 4.7E).

Balance Beam

The balance beam test was used to assess sensorimotor function (Mehla et al., 2018a). All groups crossed the beam with comparable times, and no significant difference between latency to cross was found between any group, showing no impairment in fine sensorimotor function (data not shown).

Discussion

In this study I address three mechanistic points related to vascular impairment and its effects on AD. First, I asked if using UCAgO significantly reduced cerebral blood flow. Second, I asked whether the reduction in blood flow altered two markers of AD pathology, Aβ plaque deposition and microgliosis. Third, I asked whether the reduction in blood flow and subsequent pathological changes altered cortical connectivity and cognition as observed through VSD imaging and behavioural testing.

I found that UCAgO significantly reduced blood flow to the ipsilateral side of the occlusion in both C57 and *App*$^{NL\text{-}G\text{-}F}$ mice. The gradual cerebral HP was associated with increased Aβ plaque deposition and microgliosis in the HPC and cortex of the *App*$^{NL\text{-}G\text{-}F}$ mice. I did not find inter-hemispheric Aβ pathology differences suggesting that gradual cerebral HP increased Aβ deposition uniformly across hemispheres. In the C57 mice, gradual cerebral HP was associated with a significant increase in microgliosis in the HPC but not the cortex. I did not find a significant difference in the cognitive function of the *App*$^{NL\text{-}G\text{-}F}$ HP mice and the *App*$^{NL\text{-}G\text{-}F}$ mice. Previous studies using similar methods (Hattori et al., 2015) have found similar pathology changes but no differences in behaviour. These results suggest that the UCAgO is a mild HP method more similar to human pathology and cardiovascular risk factors than other versions of inducing gradual cerebral HP. Finally, I found that gradual cerebral HP resulted in hypo-cortical connectivity in the *App*$^{NL\text{-}G\text{-}F}$ mice whereas in the C57 mice hyper-cortical connectivity was found.

A major hallmark of AD is the predictable Aβ pathology and this pathology been found to increase following gradual cerebral hypoperfusion (Yoshizaki et al., 2008). The increased levels of Aβ deposition may affect cognitive function by inducing abnormal patterns of neuronal activity and compensatory responses at the level of neuronal circuits and networks (Palop et al., 2006). Hyperconnectivity is a fundamental response to neurological disruption and may represent a compensatory strategy against the progression of cognitive impairment (Carmichael et al., 2005; Di Filippo et al., 2008; Sigler et al., 2009; Mohajerani et al., 2011; Hillary et al., 2015; Siegel et al., 2016; Delli Pizzi et al., 2019). The components of this compensatory mechanism are unknown but during damage and disease progression, hyper-synchronous activity increases initially but decreases as the disease progresses, shifting to hypo-synchronous activity

(Hillary and Grafman, 2017; Shah et al., 2018; Bing et al., 2019). The compensatory mechanisms might be responsible for the decreased bilateral functional connectivity in various brain regions (Liao et al., 2014). Increased inflammation could be leading to hyper-synchronous activity, but extensive inflammation in combination with plaque deposition could be driving the change to the hypo-synchronous activity that appears to be occurring during natural disease progression in the App^{NL-G-F} mouse model (Latif-Hernandez et al., 2019). The combination of Aβ pathology and cerebrovascular impairment could accelerate the switch between hyper to hypo-synchronous activity. I was able to detect subtle changes in cortical activity before the onset of behavioural deficits, showing that the advanced imaging techniques used are more sensitive to detect changes in cortical function compared to other techniques (Latif-Hernandez et al., 2019).

The mechanism underlying the hyper- and hypo-synchronization is still unknown but has been suggested to be a change in neuronal excitation/inhibition (Shah et al., 2018; Latif-Hernandez et al., 2019). The underlying pathology causing this change is not known. Some data suggest that the hypersynchronous activity is present in early diseases stages, such as during the pre-plaque stage of Aβ (Shah et al., 2016). This idea is supported by an animal study showing hippocampal memory impairment and glial cell changes occur before obvious plaque deposition (Beauquis et al., 2014). The increased microglial response found in my study could explain why no difference in behavioral outcome was found between the App^{NL-G-F} and App^{NL-G-F} HP mice but changes in cortical networks occurred (Szalay et al., 2016). By increasing the burden on microglia and other glial cells, the brain can compensate for reduced blood flow and potentially other pathology (Venkat et al., 2016).

These results suggest a window may exist following the initial glial cell mediated alteration in excitation/inhibition activity where behavioural impairments are not observed. If this window is initially mediated by glial cell alterations, i.e. inflammation, therapeutic interventions could target the glial cell alterations and atrophy and potentially revert the activity to baseline, preventing further decline. If this window is triggered by reduced cerebral blood flow, increasing cerebral perfusion or eliminating factors causing the reduction in cerebral blood flow may be able to delay or prevent the switch between hyper to hypo-synchronous activity (Kalaria et al., 2012). As these changes are subtle, standard assessments of cognition are unlikely to determine any changes at the start of the activity changes. Intervention may be delayed to the point where the switch from hypersynchronous activity has already switched to hypo-synchronous activity.

Several studies do contradict the hypothesis that microglia activation could be a means to compensate for Aβ burden and hypoperfusion. The removal of microglia using colony stimulating factor 1 receptor (CSF1R) antagonist PLX3397 prior to bilateral CCAO ameliorated deficits in novel object recognition (Kakae et al., 2019). Removing microglia in 5xFAD mice early in life reduced Aβ plaque and fibrillar Aβ, and prevented emotional and contextual cognitive impairment (Sosna et al., 2018). Systemic administration of CSF1 reduced neuroinflammation and neurodegeneration caused by kainic acid (Luo et al., 2013). Some reports suggest that in certain AD mouse models, alterations in glial cell morphology occur before obvious sign of plaque deposition (Beauquis et al., 2014) whereas other data suggests that the fibrillar Aβ initiates proteome changes in glial cells (Monasor et al., 2019). Glial cells may in fact be learning through proteome changes to react to the presence of Aβ.

This study adds weight to the current literature on HP and AD, as I were able to assess disease pathology and cognition and identify patterns of functional network connectivity using a technique sensitive enough to detect network changes. These findings are similar to those observed in human studies using resting-state fMRI (Bing et al., 2019), where areas showing HP had abnormal functional connectivity with other brain regions. Specifically, left inferior temporal gyrus showed decreased perfusion and decreased functional connectivity with other regions in AD patients, while the right medial superior frontal gyrus showed decreased perfusion and increased FC with other regions in MCI patients. These results suggest that abnormal functional connectivity due to HP may be an additional factor contributing to cognitive impairment. In my experiment, no cognitive deficit was observed due to HP, even though HP had dissociative effects on functional connectivity featuring hypo-connectivity in the App^{NL-G-F} mice and hyper-connectivity in the C57 mice. Future experiments validating the potential mechanisms for the progression of AD and the role of vascular factors on cognitive decline are still necessary. Furthermore, increasing the duration of the experiment would have allowed me to examine cortical activity changes and ask whether the compensatory mechanism is found to fail at the end stages of AD, which could open up new lines of treatment.

Conclusion

I caused gradual cerebral HP through UCAgO in the C57 and App^{NL-G-F} knock-in mouse model and found no significant behavioral impairment due to HP, but mesoscale level imaging of cortical activity revealed an impairment. The disruption at the mesoscale level could exacerbate AD-like pathology, leading to behavioral impairment. Due to UCAgO method used in this study, the NoH could be compensating for the reduced blood flow to the OH. The compensation may prevent global

impairment at a behavioural level. I predict that if the duration of gradual cerebral HP is increased, behavioral and cortical impairment in the $App^{NL\text{-}G\text{-}F}$ mice would be observed. Unfortunately, it is not clear as to the order at which the microglial and Aβ pathological change occurred in my study. However, a vicious cycle of pathology is most likely occurring. In conclusion, this gradual and mild form of cerebral HP mimics the AD risk factors such as hypercholesteremia, obesity, and atherosclerosis as these occur over a lifetime, gradually reducing blood flow to the brain, and do not have immediate onset.

Chapter 5 : Overall Conclusion

In this thesis using a knock-in (App^{NL-G-F}) and a transgenic (5xFAD) mouse model of AD, I have addressed three important questions; (1) how cortico-cortical interactions, (2) hippocampal-cortical interactions,and (3) cortico-cortical interactions due to chronic cerebral hypoperfusion are altered in Alzheimer's disease pathology.

- In chapter 2, using widefield *in vivo* voltage sensitive dye imaging of mouse cortex I examined how sensory evoked and spontaneous cortical activity is altered in age and strain dependent manner in mouse models of AD. Earlier studies have focused on cellular hyper- hypo- excitation, although, mesoscale dysfunctions of sensory evoked activity (Maatuf et al., 2016) and spontaneous cortical activity (Bero et al., 2012; Busche et al., 2015a; Kastanenka et al., 2017) have been studied. It is not clear how different sensory evoked modalities and spontaneous cortical activity gets altered with age and AD strain. I found an increase in sensory evoked cortical activation, velocity of signal propagation and alteration in direction of signal flow across the cortex in 12-month 5xFAD, for five different sensory stimuli (contra-lateral stimulation: forelimb or hindlimb paw (1mA, 1 ms), whisker (1ms), auditory (1ms) and visual (1ms)). There is variation in results for functional connectivity changes associated with AD pathology in rodent models, where some studies show early reduction in functional connectivity (Grandjean et al., 2014; Kastanenka et al., 2017) and others show early age hyper-connectivity and late stage hypo-connectivity (Bero et al., 2012; Shah et al., 2016; Latif-Hernandez et al., 2019). My study found reduced functional connectivity at 6 and 12 months in App^{NL-G-F} and 5xFAD mice. Earlier studies from our lab and others have shown significant Aβ pathology and cognitive deficits at these timepoints (Jawhar et al., 2012; Mehla et

al., 2019). Further, *App*$^{NL\text{-}G\text{-}F}$ mice showed a reduction in FC with age, as compared to 5xFAD mice. This study also highlighted the importance of using littermate controls, as comparing results to any other control groups may lead to different interpretations. This becomes evident when comparing FC of 6-month-old *App*$^{NL\text{-}G\text{-}F}$ mice to C57BL/6J mice, as hyper- FC which with age changes to hypo- FC with age. If FC of *App*$^{NL\text{-}G\text{-}F}$ mice are compared with age matched littermate controls, there is no significant difference at 6 months but reduced FC at 12 months. Interestingly, Latif-Hernandez et al. have shown hyper- to hypo- FC when they compared FC of 3 and 11 month old *App*$^{NL\text{-}G\text{-}F}$ with age matched *App*^{NL} mice as control (Latif-Hernandez et al., 2019). Overall, my results suggest that local subnetwork circuitry and long-range circuits are impaired in AD and these dysfunctions increase with increasing Aβ pathology.

- In chapter 3, using simultaneous local field potential (LFP) recording from CA1 region of hippocampus and widefield *in vivo* voltage sensitive dye imaging of mouse cortex, I focused on understanding how hippocampal-cortical interactions during sharp wave ripples (SWRs) are altered with disease pathology in *App*$^{NL\text{-}G\text{-}F}$ and 5xFAD mice. Sharp wave ripples (SWRs) are highly synchronous neural activity patterns in the hippocampus and are associated with many cognitive functions (Buzsáki, 2015; Joo and Frank, 2018). SWRs have been shown to be disrupted in normal ageing and in models of AD, epilepsy, schizophrenia. I found that there is reduction of SWRs in 12-month 5xFAD animals, a finding consistent with previous studies in apoE4-KI mice (Gillespie et al., 2016; Jones et al., 2019) and other mouse models of AD (Ciupek et al., 2015; Nicole et al., 2016). Previous studies have shown a reduction in gamma and SWR band power. I found an opposite trend, in general there was an increase in gamma and SWR band power with age,

although there is slight reduction of these frequency band power in 6-month *App*$^{NL-G-F}$ and 5xFAD mice compared to littermate controls. Increase in gamma band power has been shown in a recent *in vitro* study of 3-month-old 5xFAD mouse model of AD (Caccavano et al., 2020). Increased SWR band power has also been observed in mouse models relevant to schizophrenia (Suh et al., 2013; Altimus et al., 2015).

We found that neocortical activity around SWRs has a unique spatiotemporal pattern that varies with disease condition. Cortical activation around SWRs in my experiments match the DMN like module (Liska et al., 2015; Gutierrez-Barragan et al., 2019; Coletta et al., 2020; Whitesell et al., 2021). Further, around SWRs, there was a strong activation in cortical network that follows the cytoarchitectural organization of the retrosplenial (RSC) and parietal (PC) cortices in rodents (Kolb and Walkey, 1987; Clark et al., 2018). It appeared as if this activity was riding over the DMN activation. Overall, increased activation around SWRs was observed in 5xFAD mice at 12-months of age however in 12-month *App*$^{NL-G-F}$ mice significant reduction in activations was observed. At 6 month of age 5xFAD and *App*$^{NL-G-F}$ animals had lower activation as compared to littermate controls. Optical flow analysis and lagged correlation analysis revealed a change in direction of cortical activity propagation around SWRs in 12-month-old 5xFAD mice. Further, for 6- and 12-month 5xFAD animals RSC activity mostly followed hippocampal-SWR, as opposed to other groups where RSC activity was mostly leading SWRs. Overall, these results suggest that SWRs and SWR-coupled cortical activation are altered in an age and strain dependent manner in mouse models of AD and could be detrimental for memory and cognitive functions.

- In chapter 4, I studied the impact of chronic cerebral hypoperfusion (HP) on AD pathology, cognitive dysfunctions, and cortical network dynamics. Using an ameroid constrictor, unilateral (left) common carotid artery gradual occlusion (UCAgO) surgery was performed on two-month-old C57BL/6J and $App^{NL\text{-}G\text{-}F}$ mice. I found that UCAgO significantly reduced blood flow to the ipsilateral side of the occlusion in both C57 and $App^{NL\text{-}G\text{-}F}$ mice. Further, I found that HP led to increased amyloid-beta (Aβ) pathology in $App^{NL\text{-}G\text{-}F}$ mice, but no interhemispheric differences in Aβ pathology were observed. At five months of age, mice were tested on a battery of behavioral tasks (Morris water task, novel object recognition, and balance beam), No significant behavioral impairment due to HP was observed. However, using *in vivo* mesoscale wide-field voltage imaging, I found that gradual cerebral HP resulted in hypo-cortical connectivity in the $App^{NL\text{-}G\text{-}F}$ mice and hyper-cortical connectivity C57BL/6J mice. Early hyper-connectivity may represent a compensatory strategy against the progression of cognitive impairment (Hillary and Grafman, 2017; Shah et al., 2018; Bing et al., 2019). The underlying pathology causing this change is not known. Protective effect of microglia against brain injury induced by cerebral ischaemiahas been reported (Szalay et al., 2016). Increased microglial response found in my study could explain why no difference in behavioral outcome was found between the $App^{NL\text{-}G\text{-}F}$ and $App^{NL\text{-}G\text{-}F}$ HP mice whereas changes in cortical networks occurred. Overall, these results suggest that the UCAgO is a mild HP method that mimics the AD risk factors such as hypercholesteremia, obesity, and atherosclerosis as these occur over a lifetime, gradually reducing blood flow to the brain, and do not have immediate onset.

Overall, these results suggest that abnormal processing of amyloid precursor protein causes Aβ plaque formation (fig 1.1) which increases with age. Aβ plaque deposition

leads to dysfunctions in cortico-cortical and hippocampal-cortical interactions. Further, vasculature risk factors such as cerebral hypoperfusion reduces (fig 1.1) the cerebral blood flow which may cause hypoxia leading to over production of Aβ eventually leading to dysfunctions in cortico-cortical interactions.

References

(1994) Canadian study of health and aging: study methods and prevalence of dementia. CMAJ 150:899-913.

(2012) In: LiverTox: Clinical and Research Information on Drug-Induced Liver Injury. Bethesda (MD): National Institute of Diabetes and Digestive and Kidney Diseases.

(2020) 2020 Alzheimer's disease facts and figures. Alzheimer's & Dementia 16:391-460.

Adlimoghaddam A, Roy B, Albensi BC (2018) Future Trends and the Economic Burden of Dementia in Manitoba: Comparison with the Rest of Canada and the World. Neuroepidemiology 51:71-81.

Afrashteh N, Inayat S, Mohsenvand M, Mohajerani MH (2017) Optical-flow analysis toolbox for characterization of spatiotemporal dynamics in mesoscale optical imaging of brain activity. Neuroimage 153:58-74.

Allen K, Gil M, Resnik E, Toader O, Seeburg P, Monyer H (2014) Impaired path integration and grid cell spatial periodicity in mice lacking GluA1-containing AMPA receptors. The Journal of neuroscience : the official journal of the Society for Neuroscience 34:6245-6259.

Alonso AC, Li B, Grundke-Iqbal I, Iqbal K (2008) Mechanism of tau-induced neurodegeneration in Alzheimer disease and related tauopathies. Curr Alzheimer Res 5:375-384.

Altimus C, Harrold J, Jaaro-Peled H, Sawa A, Foster DJ (2015) Disordered ripples are a common feature of genetically distinct mouse models relevant to schizophrenia. Molecular neuropsychiatry 1:52-59.

Alzheimer A, Stelzmann RA, Schnitzlein HN, Murtagh FR (1995) An English translation of Alzheimer's 1907 paper, "Uber eine eigenartige Erkankung der Hirnrinde". Clin Anat 8:429-431.

Amat-Ur-Rasool H, Ahmed M, Hasnain S, Carter WG (2021) Anti-Cholinesterase Combination Drug Therapy as a Potential Treatment for Alzheimer's Disease. Brain Sci 11.

Andrews-Hanna JR, Snyder AZ, Vincent JL, Lustig C, Head D, Raichle Marcus E, Buckner RL (2007) Disruption of Large-Scale Brain Systems in Advanced Aging. Neuron 56:924-935.

Arai H, Kobayashi K, Ichimiya Y, Kosaka K, Iizuka R (1984) A preliminary study of free amino acids in the postmortem temporal cortex from Alzheimer-type dementia patients. Neurobiol Aging 5:319-321.

Asaad M, Lee JH (2018) A guide to using functional magnetic resonance imaging to study Alzheimer's disease in animal models. Dis Model Mech 11:dmm031724.

Attems J, Jellinger KA (2014) The overlap between vascular disease and Alzheimer’s disease - lessons from pathology. BMC Medicine 12.

Ayata C, Dunn AK, Gursoy-Özdemir Y, Huang Z, Boas DA, Moskowitz MA (2004) Laser speckle flowmetry for the study of cerebrovascular physiology in normal and ischemic mouse cortex. Journal of Cerebal Blood Flow Metabolics 24:744-755.

Balbi M, Vanni MP, Vega MJ, Silasi G, Sekino Y, Boyd JD, LeDue JM, Murphy TH (2019) Longitudinal monitoring of mesoscopic cortical activity in a mouse model of microinfarcts reveals dissociations with behavioral and motor function. Journal of Cerebral Blood Flow & Metabolism 39:1486-1500.

Bartus RT, Dean RL, 3rd, Beer B, Lippa AS (1982) The cholinergic hypothesis of geriatric memory dysfunction. Science 217:408-414.

Beauquis J, Vinuesa A, Pomilio C, Pavía P, Galván V, Saravia F (2014) Neuronal and glial alterations, increased anxiety, and cognitive impairment before hippocampal amyloid deposition in PDAPP mice, model of Alzheimer's disease. Hippocampus 24:257-269.

Bekdash RA (2021) The Cholinergic System, the Adrenergic System and the Neuropathology of Alzheimer's Disease. Int J Mol Sci 22.

Beker S, Goldin M, Menkes-Caspi N, Kellner V, Chechik G, Stern EA (2016) Amyloid-β disrupts ongoing spontaneous activity in sensory cortex. Brain Structure and Function 221:1173-1188.

Bekris LM, Yu CE, Bird TD, Tsuang DW (2010) Genetics of Alzheimer disease. J Geriatr Psychiatry Neurol 23:213-227.

Bennett SAL, Pappas BA, Stevens WD, Davidson CM, Fortin T, Chen J (2000) Cleavage of amyloid precursor protein elicited by chronic cerebral hypoperfusion. Neurobiology of Aging 21:207-214.

Bennett SAL, Tenniswood M, Chen JH, Davdison CM, Keyes MT, Fortin T, Pappas BA (1998) Chronic cerebral hypoperfusion elicits neuronal apoptosis and behavioral impairment. Neuroreport 9:161-166.

Benthem SD, Skelin I, Moseley SC, Stimmell AC, Dixon JR, Melilli AS, Molina L, McNaughton BL, Wilber AA (2020) Impaired Hippocampal-Cortical Interactions during Sleep in a Mouse Model of Alzheimer’s Disease. Current Biology 30:2588-2601.e2585.

Berg S, Kutra D, Kroeger T, Straehle CN, Kausler BX, Haubold C, Schiegg M, Ales J, Beier T, Rudy M, Eren K, Cervantes JI, Xu B, Beuttenmueller F, Wolny A,

Zhang C, Koethe U, Hamprecht FA, Kreshuk A (2019) ilastik: interactive machine learning for (bio)image analysis. Nature Methods.

Bero AW, Bauer AQ, Stewart FR, White BR, Cirrito JR, Raichle ME, Culver JP, Holtzman DM (2012) Bidirectional relationship between functional connectivity and amyloid-β deposition in mouse brain. The Journal of neuroscience : the official journal of the Society for Neuroscience 32:4334-4340.

Bezprozvanny I, Mattson MP (2008) Neuronal calcium mishandling and the pathogenesis of Alzheimer's disease. Trends Neurosci 31:454-463.

Bierbrauer A, Kunz L, Gomes CA, Luhmann M, Deuker L, Getzmann S, Wascher E, Gajewski PD, Hengstler JG, Fernandez-Alvarez M, Atienza M, Cammisuli DM, Bonatti F, Pruneti C, Percesepe A, Bellaali Y, Hanseeuw B, Strange BA, Cantero JL, Axmacher N (2019) Unmasking selective path integration deficits in Alzheimer's disease risk carriers. medRxiv:19009662.

Bing Z, Rui H, Zhao Q, Ling N, Xin Z, Hui Z, Renyuan L, Jiaming L, Sichu W, Yun X, Bin Z, Suiren W, Yu S (2019) Abnormal brain functional connectivity coupled with hypoperfusion measured by Resting-State fMRI: An additional contributing factor for cognitive impairment in patients with Alzheimer's disease. Psychiatry Research: Neuroimaging 289:18-25.

Bird TD, Stranahan S, Sumi SM, Raskind M (1983) Alzheimer's disease: choline acetyltransferase activity in brain tissue from clinical and pathological subgroups. Ann Neurol 14:284-293.

Blessed G, Tomlinson BE, Roth M (1968) The association between quantitative measures of dementia and of senile change in the cerebral grey matter of elderly subjects. Br J Psychiatry 114:797-811.

Braak H, Braak E (1991) Neuropathological stageing of Alzheimer-related changes. Acta neuropathologica 82:239-259.

Braak H, Braak E (1998) Evolution of neuronal changes in the course of Alzheimer's disease. Journal of neural transmission Supplementum 53:127-140.

Braak H, Del Tredici K (2015) The preclinical phase of the pathological process underlying sporadic Alzheimer's disease. Brain : a journal of neurology 138:2814-2833.

Braak H, Alafuzoff I, Arzberger T, Kretzschmar H, Del Tredici K (2006) Staging of Alzheimer disease-associated neurofibrillary pathology using paraffin sections and immunocytochemistry. Acta neuropathologica 112:389-404.

Brown R, Lam AD, Gonzalez-Sulser A, Ying A, Jones M, Chou RC-C, Tzioras M, Jordan CY, Jedrasiak-Cape I, Hemonnot A-L, Abou Jaoude M, Cole AJ, Cash SS, Saito T, Saido T, Ribchester RR, Hashemi K, Oren I (2018) Circadian and Brain State Modulation of Network Hyperexcitability in Alzheimer’s Disease. eneuro 5:ENEURO.0426-0417.2018.

Bruhn A, Weickert J, Schnörr C (2005) Lucas/Kanade Meets Horn/Schunck: Combining Local and Global Optic Flow Methods. International Journal of Computer Vision 61:211-231.

Buckner RL, Sepulcre J, Talukdar T, Krienen FM, Liu H, Hedden T, Andrews-Hanna JR, Sperling RA, Johnson KA (2009) Cortical Hubs Revealed by Intrinsic Functional Connectivity: Mapping, Assessment of Stability, and Relation to Alzheimer's Disease. The Journal of Neuroscience 29:1860.

Buhry L, Azizi AH, Cheng S (2011) Reactivation, Replay, and Preplay: How It Might All Fit Together. Neural plasticity 2011:203462.

Busche MA, Chen X, Henning HA, Reichwald J, Staufenbiel M, Sakmann B, Konnerth A (2012) Critical role of soluble amyloid-β for early hippocampal hyperactivity in a mouse model of Alzheimer's disease. Proceedings of the National Academy of Sciences 109:8740.

Busche MA, Kekuš M, Adelsberger H, Noda T, Förstl H, Nelken I, Konnerth A (2015a) Rescue of long-range circuit dysfunction in Alzheimer's disease models. Nature neuroscience 18:1623-1630.

Busche MA, Grienberger C, Keskin AD, Song B, Neumann U, Staufenbiel M, Förstl H, Konnerth A (2015b) Decreased amyloid-β and increased neuronal hyperactivity by immunotherapy in Alzheimer's models. Nature neuroscience 18:1725-1727.

Busche MA, Eichhoff G, Adelsberger H, Abramowski D, Wiederhold KH, Haass C, Staufenbiel M, Konnerth A, Garaschuk O (2008) Clusters of hyperactive neurons near amyloid plaques in a mouse model of Alzheimer's disease. Science 321:1686-1689.

Busche MA, Wegmann S, Dujardin S, Commins C, Schiantarelli J, Klickstein N, Kamath TV, Carlson GA, Nelken I, Hyman BT (2019) Tau impairs neural circuits, dominating amyloid-β effects, in Alzheimer models in vivo. Nature neuroscience 22:57-64.

Buzsáki G (2015) Hippocampal sharp wave-ripple: A cognitive biomarker for episodic memory and planning. Hippocampus 25:1073-1188.

Caccavano A, Bozzelli PL, Forcelli PA, Pak DTS, Wu JY, Conant K, Vicini S (2020) Inhibitory Parvalbumin Basket Cell Activity is Selectively Reduced during Hippocampal Sharp Wave Ripples in a Mouse Model of Familial Alzheimer's

Disease. The Journal of neuroscience : the official journal of the Society for Neuroscience 40:5116-5136.

Callaway EM (2016) Inhibitory Cell Types, Circuits and Receptive Fields in Mouse Visual Cortex. In: Micro-, Meso- and Macro-Connectomics of the Brain (Kennedy H, Van Essen DC, Christen Y, eds), pp 11-18. Cham (CH).

Carmichael ST, Achibeque I, Luke L, Nolan T, Momiy J, Li S (2005) Growth-associated gene expression after stroke: evidence for a growth-promoting region in peri-infarct cortex. Experimental neurology 193:291-311.

Chan AW, Mohajerani MH, LeDue JM, Wang YT, Murphy TH (2015) Mesoscale infraslow spontaneous membrane potential fluctuations recapitulate high-frequency activity cortical motifs. Nature Communication 6.

Chang F, Patel T, Schulz ME (2015) The "Rising Tide" of dementia in Canada: What does it mean for pharmacists and the people they care for? Can Pharm J (Ott) 148:193-199.

Chapman PF, White GL, Jones MW, Cooper-Blacketer D, Marshall VJ, Irizarry M, Younkin L, Good MA, Bliss TV, Hyman BT, Younkin SG, Hsiao KK (1999) Impaired synaptic plasticity and learning in aged amyloid precursor protein transgenic mice. Nature neuroscience 2:271-276.

Chen M, Chen Y, Huo Q, Wang L, Tan S, Misrani A, Jiang J, Chen J, Chen S, Zhang J, Tabassum S, Wang J, Chen X, Long C, Yang L (2021) Enhancing GABAergic signaling ameliorates aberrant gamma oscillations of olfactory bulb in AD mouse models. Molecular Neurodegeneration 16:14.

Chhatwal JP, Sperling RA (2012) Functional MRI of mnemonic networks across the spectrum of normal aging, mild cognitive impairment, and Alzheimer's disease. J Alzheimers Dis 31 Suppl 3:S155-167.

Ciupek SM, Cheng J, Ali YO, Lu HC, Ji D (2015) Progressive functional impairments of hippocampal neurons in a tauopathy mouse model. The Journal of neuroscience : the official journal of the Society for Neuroscience 35:8118-8131.

Clark BJ, Simmons CM, Berkowitz LE, Wilber AA (2018) The retrosplenial-parietal network and reference frame coordination for spatial navigation. Behavioral neuroscience 132:416-429.

Clement EA, Richard A, Thwaites M, Ailon J, Peters S, Dickson CT (2008) Cyclic and sleep-like spontaneous alternations of brain state under urethane anaesthesia. PloS one 3:e2004.

Coletta L, Pagani M, Whitesell JD, Harris JA, Bernhardt B, Gozzi A (2020) Network structure of the mouse brain connectome with voxel resolution. Science Advances 6:eabb7187.

Cummings J, Lee G, Ritter A, Sabbagh M, Zhong K (2020) Alzheimer's disease drug development pipeline: 2020. Alzheimer's & Dementia: Translational Research & Clinical Interventions 6:e12050.

Daulatzai MA (2017) Cerebral hypoperfusion and glucose hypometabolism: key pathophysiological modulators promote neurodegeneration, cognitive impairment, and Alzheimer's disease. Journal of neuroscience research 95:943-972.

Davidson TJ, Kloosterman F, Wilson MA (2009) Hippocampal replay of extended experience. Neuron 63:497-507.

Davies P, Maloney AJ (1976) Selective loss of central cholinergic neurons in Alzheimer's disease. Lancet 2:1403.

de la Torre JC (2002a) Alzheimer's disease: how does it start? Journal of Alzheimer's Disease 4:497-512.

de la Torre JC (2002b) Alzheimer disease as a vascular disorder: nosological evidence. Stroke 33:1152-1162.

Delli Pizzi S, Punzi M, Sensi SL (2019) Functional signature of conversion of patients with mild cognitive impairment. Neurobiology of Aging 74:21-37.

Demuro A, Mina E, Kayed R, Milton SC, Parker I, Glabe CG (2005) Calcium dysregulation and membrane disruption as a ubiquitous neurotoxic mechanism of soluble amyloid oligomers. J Biol Chem 280:17294-17300.

Dennis EL, Thompson PM (2014) Functional brain connectivity using fMRI in aging and Alzheimer's disease. Neuropsychology review 24:49-62.

Di Filippo M, Tozzi A, Costa C, Belcastro V, Tantucci M, Picconi B, Calabresi P (2008) Plasticity and repair in the post-ischemic brain. Neuropharmacology 55:353-362.

Dichgans M, Leys D (2017) Vascular Cognitive Impairment. Circulation Research 120:573-591.

Dorszewska J, Prendecki M, Oczkowska A, Dezor M, Kozubski W (2016) Molecular Basis of Familial and Sporadic Alzheimer's Disease. Curr Alzheimer Res 13:952-963.

Edwards FA (2019) A Unifying Hypothesis for Alzheimer’s Disease: From Plaques to Neurodegeneration. Trends in Neurosciences 42:310-322.

Ego-Stengel V, Wilson MA (2010) Disruption of ripple-associated hippocampal activity during rest impairs spatial learning in the rat. Hippocampus 20:1-10.

Ellison DW, Beal MF, Mazurek MF, Bird ED, Martin JB (1986) A postmortem study of amino acid neurotransmitters in Alzheimer's disease. Ann Neurol 20:616-621.

Esiri MM, Nagy Z, Smith MZ, Barnetson L, Smith AD (1999) Cerebrovascular disease and threshold for dementia in the early stages of Alzheimer's disease. Lancet 354:919-920.

Etter G, van der Veldt S, Manseau F, Zarrinkoub I, Trillaud-Doppia E, Williams S (2019) Optogenetic gamma stimulation rescues memory impairments in an Alzheimer's disease mouse model. Nature communications 10:5322.

Feng T, Yamashita T, Zhai Y, Shang J, Nakano Y, Morihara R, Fukui Y, Hishikawa N, Ohta Y, Abe K (2018) Chronic cerebral hypoperfusion accelerates Alzheimer's disease pathology with the change of mitochondrial fission and fusion proteins expression in a novel mouse model. Brain Research 1696:63-70.

Ferezou I, Haiss F, Gentet LJ, Aronoff R, Weber B, Petersen CCH (2007) Spatiotemporal Dynamics of Cortical Sensorimotor Integration in Behaving Mice. Neuron 56:907-923.

Fernández-Ruiz A, Oliva A, Fermino de Oliveira E, Rocha-Almeida F, Tingley D, Buzsáki G (2019) Long-duration hippocampal sharp wave ripples improve memory. Science 364:1082-1086.

Ferreira-Vieira TH, Guimaraes IM, Silva FR, Ribeiro FM (2016) Alzheimer's disease: Targeting the Cholinergic System. Current neuropharmacology 14:101-115.

Fogel H, Frere S, Segev O, Bharill S, Shapira I, Gazit N, O'Malley T, Slomowitz E, Berdichevsky Y, Walsh Dominic M, Isacoff Ehud Y, Hirsch Joel A, Slutsky I (2014) APP Homodimers Transduce an Amyloid-β-Mediated Increase in Release Probability at Excitatory Synapses. Cell Reports 7:1560-1576.

Forner S, Baglietto-Vargas D, Martini AC, Trujillo-Estrada L, LaFerla FM (2017) Synaptic Impairment in Alzheimer's Disease: A Dysregulated Symphony. Trends in Neurosciences 40:347-357.

Francis PT (2003) Glutamatergic systems in Alzheimer's disease. Int J Geriatr Psychiatry 18:S15-21.

Francis PT (2005) The interplay of neurotransmitters in Alzheimer's disease. CNS Spectr 10:6-9.

Fu AL, Li Q, Dong ZH, Huang SJ, Wang YX, Sun MJ (2004) Alternative therapy of Alzheimer's disease via supplementation with choline acetyltransferase. Neurosci Lett 368:258-262.

Fu H, Rodriguez GA, Herman M, Emrani S, Nahmani E, Barrett G, Figueroa HY, Goldberg E, Hussaini SA, Duff KE (2017) Tau Pathology Induces Excitatory Neuron Loss, Grid Cell Dysfunction, and Spatial Memory Deficits Reminiscent of Early Alzheimer's Disease. Neuron 93:533-541.e535.

Furukawa K, Barger SW, Blalock EM, Mattson MP (1996) Activation of K+ channels and suppression of neuronal activity by secreted beta-amyloid-precursor protein. Nature 379:74-78.

Gallero-Salas Y, Han S, Sych Y, Voigt FF, Laurenczy B, Gilad A, Helmchen F (2021) Sensory and Behavioral Components of Neocortical Signal Flow in Discrimination Tasks with Short-Term Memory. Neuron 109:135-148.e136.

Gardener H, Wright CB, Rundek T, Sacco RL (2015) Brain health and shared risk factors for dementia and stroke. Nature Reviews Neurology 11:651.

Gardner RJ, Lu L, Wernle T, Moser M-B, Moser EI (2019) Correlation structure of grid cells is preserved during sleep. Nature neuroscience 22:598-608.

Ghatak S, Dolatabadi N, Trudler D, Zhang X, Wu Y, Mohata M, Ambasudhan R, Talantova M, Lipton SA (2019) Mechanisms of hyperexcitability in Alzheimer's disease hiPSC-derived neurons and cerebral organoids vs isogenic controls. eLife 8:e50333.

Gil M, Ancau M, Schlesiger MI, Neitz A, Allen K, De Marco RJ, Monyer H (2018) Impaired path integration in mice with disrupted grid cell firing. Nature neuroscience 21:81-91.

Gilad A, Helmchen F (2020) Spatiotemporal refinement of signal flow through association cortex during learning. Nature communications 11:1744.

Gilbert J, Shu S, Yang X, Lu Y, Zhu LQ, Man HY (2016) beta-Amyloid triggers aberrant over-scaling of homeostatic synaptic plasticity. Acta Neuropathol Commun 4:131.

Gillespie Anna K, Jones Emily A, Lin Y-H, Karlsson Mattias P, Kay K, Yoon Seo Y, Tong Leslie M, Nova P, Carr Jessie S, Frank Loren M, Huang Y (2016) Apolipoprotein E4 Causes Age-Dependent Disruption of Slow Gamma Oscillations during Hippocampal Sharp-Wave Ripples. Neuron 90:740-751.

Girardeau G, Benchenane K, Wiener SI, Buzsáki G, Zugaro MB (2009) Selective suppression of hippocampal ripples impairs spatial memory. Nature neuroscience 12:1222-1223.

Girouard H, Munter LM (2018) The many faces of vascular cognitive impairment. Journal of Neurochemistry 144:509-512.

Glenner GG, Wong CW (1984) Alzheimer's disease: initial report of the purification and characterization of a novel cerebrovascular amyloid protein. Biochem Biophys Res Commun 120:885-890.

Gold G, Giannakopoulos P, Herrmann FR, Bouras C, Kövari E (2007) Identification of Alzheimer and vascular lesion thresholds for mixed dementia. Brain : a journal of neurology 130:2830-2836.

Gomez-Isla T, Price JL, McKeel DW, Jr., Morris JC, Growdon JH, Hyman BT (1996) Profound loss of layer II entorhinal cortex neurons occurs in very mild Alzheimer's disease. The Journal of neuroscience : the official journal of the Society for Neuroscience 16:4491-4500.

Goodman MS, Kumar S, Zomorrodi R, Ghazala Z, Cheam ASM, Barr MS, Daskalakis ZJ, Blumberger DM, Fischer C, Flint A, Mah L, Herrmann N, Bowie CR, Mulsant BH, Rajji TK (2018) Theta-Gamma Coupling and Working Memory in Alzheimer's Dementia and Mild Cognitive Impairment. Front Aging Neurosci 10:101-101.

Gorelick PB et al. (2011) Vascular contributions to cognitive impairment and dementia: a statement for healthcare professionals from the american heart association/american stroke association. Stroke 42:2672-2713.

Goutagny R, Gu N, Cavanagh C, Jackson J, Chabot JG, Quirion R, Krantic S, Williams S (2013) Alterations in hippocampal network oscillations and theta-gamma coupling arise before Abeta overproduction in a mouse model of Alzheimer's disease. The European journal of neuroscience 37:1896-1902.

Govindpani K, Calvo-Flores Guzman B, Vinnakota C, Waldvogel HJ, Faull RL, Kwakowsky A (2017) Towards a Better Understanding of GABAergic Remodeling in Alzheimer's Disease. Int J Mol Sci 18.

Grandjean J, Derungs R, Kulic L, Welt T, Henkelman M, Nitsch RM, Rudin M (2016) Complex interplay between brain function and structure during cerebral

amyloidosis in APP transgenic mouse strains revealed by multi-parametric MRI comparison. NeuroImage 134:1-11.

Grandjean J, Schroeter A, He P, Tanadini M, Keist R, Krstic D, Konietzko U, Klohs J, Nitsch RM, Rudin M (2014) Early alterations in functional connectivity and white matter structure in a transgenic mouse model of cerebral amyloidosis. The Journal of neuroscience : the official journal of the Society for Neuroscience 34:13780-13789.

Grandjean J et al. (2020) Common functional networks in the mouse brain revealed by multi-centre resting-state fMRI analysis. NeuroImage 205:116278.

Gray CW, Patel AJ (1995) Neurodegeneration mediated by glutamate and beta-amyloid peptide: a comparison and possible interaction. Brain Res 691:169-179.

Greicius MD, Srivastava G, Reiss AL, Menon V (2004) Default-mode network activity distinguishes Alzheimer's disease from healthy aging: evidence from functional MRI. Proc Natl Acad Sci U S A 101:4637-4642.

Grienberger C, Rochefort NL, Adelsberger H, Henning HA, Hill DN, Reichwald J, Staufenbiel M, Konnerth A (2012) Staged decline of neuronal function in vivo in an animal model of Alzheimer's disease. Nature communications 3:774.

Grossberg GT (2003) Cholinesterase inhibitors for the treatment of Alzheimer's disease:: getting on and staying on. Curr Ther Res Clin Exp 64:216-235.

Grothe M, Heinsen H, Teipel SJ (2012) Atrophy of the cholinergic Basal forebrain over the adult age range and in early stages of Alzheimer's disease. Biol Psychiatry 71:805-813.

Grothe M, Zaborszky L, Atienza M, Gil-Neciga E, Rodriguez-Romero R, Teipel SJ, Amunts K, Suarez-Gonzalez A, Cantero JL (2010) Reduction of basal forebrain

cholinergic system parallels cognitive impairment in patients at high risk of developing Alzheimer's disease. Cereb Cortex 20:1685-1695.

Grothe MJ, Schuster C, Bauer F, Heinsen H, Prudlo J, Teipel SJ (2014) Atrophy of the cholinergic basal forebrain in dementia with Lewy bodies and Alzheimer's disease dementia. J Neurol 261:1939-1948.

Gutierrez-Barragan D, Basson MA, Panzeri S, Gozzi A (2019) Infraslow State Fluctuations Govern Spontaneous fMRI Network Dynamics. Current Biology 29:2295-2306.e2295.

Haake A, Nguyen K, Friedman L, Chakkamparambil B, Grossberg GT (2020) An update on the utility and safety of cholinesterase inhibitors for the treatment of Alzheimer's disease. Expert Opin Drug Saf 19:147-157.

Haam J, Yakel JL (2017) Cholinergic modulation of the hippocampal region and memory function. J Neurochem 142 Suppl 2:111-121.

Hanseeuw BJ et al. (2019) Association of Amyloid and Tau With Cognition in Preclinical Alzheimer Disease: A Longitudinal Study. JAMA Neurol.

Hardy J, Allsop D (1991) Amyloid deposition as the central event in the aetiology of Alzheimer's disease. Trends Pharmacol Sci 12:383-388.

Hardy J, Selkoe DJ (2002) The amyloid hypothesis of Alzheimer's disease: progress and problems on the road to therapeutics. Science 297:353-356.

Hardy JA, Higgins GA (1992) Alzheimer's disease: the amyloid cascade hypothesis. Science 256:184-185.

Harris JA et al. (2019) Hierarchical organization of cortical and thalamic connectivity. Nature 575:195-202.

Hartmann DA, Hyacinth HI, Liao FF, Shih AY (2018) Does pathology of small venules contribute to cerebral microinfarcts and dementia? Journal of Neurochemistry 144:517-526.

Hasselmo ME (2006) The role of acetylcholine in learning and memory. Curr Opin Neurobiol 16:710-715.

Hattori Y, Enmi JI, Iguchi S, Saito S, Yamamoto Y, Tsuji M, Nagatsuka K, Kalaria RN, Lida H, Ihara M (2016) Gradual Carotid Artery Stenosis in Mice Closely Replicates Hypoperfusive Vascular Dementia in Humans. Journal of The American Heart Association 5:e002757.

Hattori Y, Enmi JI, Kitamura A, Yamamoto Y, Saito S, Takahashi Y, Iguchi S, Tsuji M, Yamahara K, Nagatsuka K, Lida H, Ihara M (2015) A Novel Mouse Model of Subcortical Infarcts with Dementia. The Journal of Neuroscience 35:3915-3928.

Hazra A, Gu F, Aulakh A, Berridge C, Eriksen JL, Ziburkus J (2013) Inhibitory neuron and hippocampal circuit dysfunction in an aged mouse model of Alzheimer's disease. PloS one 8:e64318.

Hector A, Brouillette J (2021) Hyperactivity Induced by Soluble Amyloid-β Oligomers in the Early Stages of Alzheimer's Disease. Frontiers in Molecular Neuroscience 13.

Helfrich RF, Lendner JD, Mander BA, Guillen H, Paff M, Mnatsakanyan L, Vadera S, Walker MP, Lin JJ, Knight RT (2019) Bidirectional prefrontal-hippocampal dynamics organize information transfer during sleep in humans. Nature communications 10:3572.

Heneka MT et al. (2018) Neuroinflammation in Alzheimer's disease. Lancet Neurology 14:388-405.

Hijazi S, Heistek TS, Scheltens P, Neumann U, Shimshek DR, Mansvelder HD, Smit AB, van Kesteren RE (2020) Early restoration of parvalbumin interneuron activity prevents memory loss and network hyperexcitability in a mouse model of Alzheimer's disease. Mol Psychiatry 25:3380-3398.

Hillary FG, Grafman JH (2017) Injured Brains and Adaptive Networks: The Benefits and Costs of Hyperconnectivity. TRENDS in Cognitive Sciences 21:385-401.

Hillary FG, Roman CA, Venkatesan U, Rajtmajer SM, Bajo R, Castellanos ND (2015) Hyperconnectivity is a fundamental response to neurological disruption. Neuropsychology 29:59-75.

Iaccarino HF, Singer AC, Martorell AJ, Rudenko A, Gao F, Gillingham TZ, Mathys H, Seo J, Kritskiy O, Abdurrob F, Adaikkan C, Canter RG, Rueda R, Brown EN, Boyden ES, Tsai LH (2016) Gamma frequency entrainment attenuates amyloid load and modifies microglia. Nature 540:230-235.

Iadecola C (2010) The overlap between neurodegenerative and vascular factors in the pathogenesis of dementia. Acta neuropathologica 120:287-296.

Iadecola C (2013) The pathobiology of vascular dementia. Neuron 80:844-866.

Iadecola C, Duering M, Hachinski V, Joutel A, Pendlebury ST, Schneider JA, Dichgans M (2019) Vascular Cognitive Impairment and Dementia: JACC Scientific Expert Panel. Journal of the American College of Cardiology 73:3326-3344.

Iqbal K, Liu F, Gong CX, Grundke-Iqbal I (2010) Tau in Alzheimer disease and related tauopathies. Curr Alzheimer Res 7:656-664.

Jadhav SP, Kemere C, German PW, Frank LM (2012) Awake hippocampal sharp-wave ripples support spatial memory. Science 336:1454-1458.

Jara J, Cerda M, Delpiano J, Härtel S (2015) An Implementation of Combined Local-Global Optical Flow. Image Process Line 5:139-158.

Jawhar S, Trawicka A, Jenneckens C, Bayer TA, Wirths O (2012) Motor deficits, neuron loss, and reduced anxiety coinciding with axonal degeneration and intraneuronal Aβ aggregation in the 5XFAD mouse model of Alzheimer's disease. Neurobiology of Aging 33:196.e129-196.e140.

Ji D, Wilson MA (2007) Coordinated memory replay in the visual cortex and hippocampus during sleep. Nature neuroscience 10:100-107.

Johnson RB, Johnson SR (1975) The self-instructional materials project: progress and prospects. J Biocommun 2:17-21.

Jones EA, Gillespie AK, Yoon SY, Frank LM, Huang Y (2019) Early Hippocampal Sharp-Wave Ripple Deficits Predict Later Learning and Memory Impairments in an Alzheimer's Disease Mouse Model. Cell Reports 29:2123-2133.e2124.

Joo HR, Frank LM (2018) The hippocampal sharp wave–ripple in memory retrieval for immediate use and consolidation. Nature Reviews Neuroscience 19:744-757.

Jun H, Bramian A, Soma S, Saito T, Saido TC, Igarashi KM (2020) Disrupted Place Cell Remapping and Impaired Grid Cells in a Knockin Model of Alzheimer's Disease. Neuron.

Jura B, Macrez N, Meyrand P, Bem T (2019) Deficit in hippocampal ripples does not preclude spatial memory formation in APP/PS1 mice. Scientific Reports 9:20129.

Jura B, Młoźniak D, Goszczyńska H, Blinowska K, Biendon N, Macrez N, Meyrand P, Bem T (2020) Reconfiguration of the cortical-hippocampal interaction may compensate for Sharp-Wave Ripple deficits in APP/PS1 mice and support spatial memory formation. PloS one 15:e0243767.

Kakae M, Tobori S, Morishima M, Nagayasu K, Shirakawa H, Kaneko S (2019) Depletion of microglia ameliorates white matter injury and cognitive

impairment in a mouse chronic cerebral hypoperfusion model. Biochemical and Biophysical Research Communications 514:1040-1044.

Kalaria RN, Akinyemi R, Ihara M (2012) Does vascular pathology contribute to Alzheimer changes? Journal of the Neurological Sciences 322:141-147.

Kamat PK, Rai S, Swarnkar S, Shukla R, Ali S, Najmi AK, Nath C (2013) Okadaic acid-induced Tau phosphorylation in rat brain: role of NMDA receptor. Neuroscience 238:97-113.

Kamenetz F, Tomita T, Hsieh H, Seabrook G, Borchelt D, Iwatsubo T, Sisodia S, Malinow R (2003) APP processing and synaptic function. Neuron 37:925-937.

Kaplan R, Adhikari Mohit H, Hindriks R, Mantini D, Murayama Y, Logothetis Nikos K, Deco G (2016) Hippocampal Sharp-Wave Ripples Influence Selective Activation of the Default Mode Network. Current Biology 26:686-691.

Karantzoulis S, Galvin JE (2011) Distinguishing Alzheimer's disease from other major forms of dementia. Expert Rev Neurother 11:1579-1591.

Karimi Abadchi J, Nazari-Ahangarkolaee M, Gattas S, Bermudez-Contreras E, Luczak A, McNaughton BL, Mohajerani MH (2020) Spatiotemporal patterns of neocortical activity around hippocampal sharp-wave ripples. eLife 9:e51972.

Kastanenka KV, Hou SS, Shakerdge N, Logan R, Feng D, Wegmann S, Chopra V, Hawkes JM, Chen X, Bacskai BJ (2017) Optogenetic Restoration of Disrupted Slow Oscillations Halts Amyloid Deposition and Restores Calcium Homeostasis in an Animal Model of Alzheimer's Disease. PloS one 12:e0170275-e0170275.

Khan UA, Liu L, Provenzano FA, Berman DE, Profaci CP, Sloan R, Mayeux R, Duff KE, Small SA (2014) Molecular drivers and cortical spread of lateral entorhinal

cortex dysfunction in preclinical Alzheimer's disease. Nature neuroscience 17:304-311.

Kinney JW, Bemiller SM, Murtishaw AS, Leisgang AM, Salazar AM, Lamb BT (2018) Inflammation as a central mechanism in Alzheimer's disease. Alzheimers Dement (N Y) 4:575-590.

Kirvell SL, Esiri M, Francis PT (2006) Down-regulation of vesicular glutamate transporters precedes cell loss and pathology in Alzheimer's disease. J Neurochem 98:939-950.

Kitagawa K, Yagita Y, Sasaki T, Sugiura S, Omura-Matsuoka E, Mabuchi T, Matsushita K, Hori M (2005) Chronic mild reduction of cerebral perfusion pressure induces ischemic tolerance in focal cerebral ischemia. Stroke 36:2270-2274.

Knox JE, Harris KD, Graddis N, Whitesell JD, Zeng H, Harris JA, Shea-Brown E, Mihalas S (2018) High-resolution data-driven model of the mouse connectome. Netw Neurosci 3:217-236.

Koelewijn L, Lancaster TM, Linden D, Dima DC, Routley BC, Magazzini L, Barawi K, Brindley L, Adams R, Tansey KE, Bompas A, Tales A, Bayer A, Singh K (2019) Oscillatory hyperactivity and hyperconnectivity in young APOE-ε4 carriers and hypoconnectivity in Alzheimer's disease. Elife 8.

Kolb B, Walkey J (1987) Behavioural and anatomical studies of the posterior parietal cortex in the rat. Behav Brain Res 23:127-145.

Kopke E, Tung YC, Shaikh S, Alonso AC, Iqbal K, Grundke-Iqbal I (1993) Microtubule-associated protein tau. Abnormal phosphorylation of a non-paired helical filament pool in Alzheimer disease. J Biol Chem 268:24374-24384.

Kunz L, Schroder TN, Lee H, Montag C, Lachmann B, Sariyska R, Reuter M, Stirnberg R, Stocker T, Messing-Floeter PC, Fell J, Doeller CF, Axmacher N (2015) Reduced grid-cell-like representations in adults at genetic risk for Alzheimer's disease. Science 350:430-433.

Kyweriga M, Mohajerani MH (2016) Optogenetic approaches for mesoscopic brain mapping. Methods in Molecular Biology 1408:251-265.

Kyweriga M, Sun J, Wang S, Kline R, Mohajerani MH (2017) A large lateral craniotomy procedure for mesoscale wide-field optical imaging of brain. JoVE (Journal of visualized experiments) 123:pp.e52642-e52642.

Lai AY, McLaurin J (2010) Mechanisms of amyloid-Beta Peptide uptake by neurons: the role of lipid rafts and lipid raft-associated proteins. Int J Alzheimers Dis 2011:548380.

Latif-Hernandez A, Shah D, Craessaerts K, Saido T, Saito T, De Stropper B, Van der Linden A, D'Hooge R (2019) Subtle behavioral changes and increased prefrontal-hippocampal network T synchronicity in APPNL−G−F mice before prominent plaque deposition. Behavioural Brain Research 364:431-441.

Launer LJ, Petrovitch H, Ross GW, Markesbery W, White LR (2008) AD brain pathology: vascular origins? Results from the HAAS autopsy study. Neurobiology of Aging 29:1587-1590.

Lee AK, Wilson MA (2002) Memory of sequential experience in the hippocampus during slow wave sleep. Neuron 36:1183-1194.

Lee MS, Kao SC, Lemere CA, Xia W, Tseng HC, Zhou Y, Neve R, Ahlijanian MK, Tsai LH (2003) APP processing is regulated by cytoplasmic phosphorylation. J Cell Biol 163:83-95.

Leissring MA, Murphy MP, Mead TR, Akbari Y, Sugarman MC, Jannatipour M, Anliker B, Muller U, Saftig P, De Strooper B, Wolfe MS, Golde TE, LaFerla FM (2002) A physiologic signaling role for the gamma -secretase-derived intracellular fragment of APP. Proc Natl Acad Sci U S A 99:4697-4702.

Li HJ, Hou XH, Liu HH, Yue CL, He Y, Zuo XN (2015) Toward systems neuroscience in mild cognitive impairment and Alzheimer's disease: a meta-analysis of 75 fMRI studies. Human brain mapping 36:1217-1232.

Liao F, Hori Y, Hundry E, Bauer AQ, Jiang H, Mahan TE, Lefton KB, Zhang TJ, Dearborn JT, Kim J, Culver JP, Betensky R, Wozniak DF, Hyman BT, Holtzman DM (2014) Anti-ApoE antibody given after plaque onset decreases Aβ accumulation and improves brain function in a mouse model of Aβ amyloidosis. Journal of Neuroscience 34:7281-7292.

Lim DH, LeDue JM, Murphy TH (2015) Network analysis of mesoscale optical recordings to assess regional, functional connectivity. Neurophotonics 2:041405.

Lim DH, LeDue JM, Mohajerani MH, Murphy TH (2014) Optogenetic Mapping after Stroke Reveals Network-Wide Scaling of Functional Connections and Heterogeneous Recovery of the Peri-Infarct. The Journal of Neuroscience 34:16455-16466.

Lim DH, Mohajerani MH, LeDue J, Boyd J, Chen S, Murphy TH (2012) In vivo Large-Scale Cortical Mapping Using Channelrhodopsin-2 Stimulation in Transgenic Mice Reveals Asymmetric and Reciprocal Relationships between Cortical Areas. frontiers in Neural Circuits 6.

Liska A, Galbusera A, Schwarz AJ, Gozzi A (2015) Functional connectivity hubs of the mouse brain. Neuroimage 115:281-291.

Liu C (2009) Beyond pixels: exploring new representations and applications for motion analysis. In: Massachusetts Institute of Technology.

Liu C, Tan FCK, Xiao Z-C, Dawe GS (2015) Amyloid precursor protein enhances Nav1.6 sodium channel cell surface expression. The Journal of biological chemistry 290:12048-12057.

Liu CC, Liu CC, Kanekiyo T, Xu H, Bu G (2013) Apolipoprotein E and Alzheimer disease: risk, mechanisms and therapy. Nat Rev Neurol 9:106-118.

Liu J, Chang L, Song Y, Li H, Wu Y (2019a) The Role of NMDA Receptors in Alzheimer's Disease. Front Neurosci 13:43.

Liu PP, Xie Y, Meng XY, Kang JS (2019b) History and progress of hypotheses and clinical trials for Alzheimer's disease. Signal Transduct Target Ther 4:29.

Liu Y, Wang K, Yu C, He Y, Zhou Y, Liang M, Wang L, Jiang T (2008) Regional homogeneity, functional connectivity and imaging markers of Alzheimer's disease: a review of resting-state fMRI studies. Neuropsychologia 46:1648-1656.

Logothetis NK, Eschenko O, Murayama Y, Augath M, Steudel T, Evrard HC, Besserve M, Oeltermann A (2012) Hippocampal-cortical interaction during periods of subcortical silence. Nature 491:547-553.

Lowe SL, Francis PT, Procter AW, Palmer AM, Davison AN, Bowen DM (1988) Gamma-aminobutyric acid concentration in brain tissue at two stages of Alzheimer's disease. Brain : a journal of neurology 111 (Pt 4):785-799.

Lu H, Zou Q, Gu H, Raichle ME, Stein EA, Yang Y (2012) Rat brains also have a default mode network. Proceedings of the National Academy of Sciences 109:3979.

Luo J, Elwood F, Britschgi M, Villeda S, Zhang H, Ding Z, Zhu L, Alabsi H, Getachew R, Narasimhan R, Wabl R, Fainberg N, James ML, Wong G, Relton J, Gambhir SS, Pollard JW, Wyss-Coray T (2013) Colony-stimulating factor 1 receptor (CSF1R) signaling in injured neurons facilitates protection and survival. Journal of Experimental Medicine 210:157-172.

Maatuf Y, Stern EA, Slovin H (2016) Abnormal Population Responses in the Somatosensory Cortex of Alzheimer's Disease Model Mice. Scientific Reports 6.

Maingret N, Girardeau G, Todorova R, Goutierre M, Zugaro M (2016) Hippocampo-cortical coupling mediates memory consolidation during sleep. Nature neuroscience 19:959-964.

Margulies DS, Ghosh SS, Goulas A, Falkiewicz M, Huntenburg JM, Langs G, Bezgin G, Eickhoff SB, Castellanos FX, Petrides M, Jefferies E, Smallwood J (2016) Situating the default-mode network along a principal gradient of macroscale cortical organization. Proceedings of the National Academy of Sciences 113:12574.

Marinković P, Blumenstock S, Goltstein PM, Korzhova V, Peters F, Knebl A, Herms J (2019) In vivo imaging reveals reduced activity of neuronal circuits in a mouse tauopathy model. Brain : a journal of neurology 142:1051-1062.

Martinez-Losa M, Tracy TE, Ma K, Verret L, Clemente-Perez A, Khan AS, Cobos I, Ho K, Gan L, Mucke L, Alvarez-Dolado M, Palop JJ (2018) Nav1.1-Overexpressing Interneuron Transplants Restore Brain Rhythms and Cognition in a Mouse Model of Alzheimer's Disease. Neuron 98:75-89.e75.

Mattson MP, Magnus T (2006) Ageing and neuronal vulnerability. Nature reviews Neuroscience 7:278-294.

Mattson MP, Cheng B, Davis D, Bryant K, Lieberburg I, Rydel RE (1992) beta-Amyloid peptides destabilize calcium homeostasis and render human cortical neurons vulnerable to excitotoxicity. The Journal of neuroscience : the official journal of the Society for Neuroscience 12:376-389.

Mazza M, Marano G, Traversi G, Bria P, Mazza S (2011) Primary Cerebral Blood Flow Deficiency and Alzheimer's Disease: Shadows and Lights. Journal of Alzheimer's Disease 23:375-389.

McDonald RJ (2002) Multiple Combinations of Co-Factors Produce Variants of Age-Related Cognitive Decline: A Theory. Canadian Journal of Experimental Psychology 56:221-339.

McDonald RJ, Craig LA, Hong NS (2010) The etiology of age-related dementia is more complicated than we think. Behavioural brain research 214:3-11.

McGirr A, LeDue J, Chan AW, Xie Y, Murphy TH (2017) Cortical functional hyperconnectivity in a mouse model of depression and selective network effects of ketamine. Brain : a journal of neurology 140:2210-2225.

Mehla J, Lacoursiere S, Stuart E, McDonald RJ, Mohajerani MH (2018a) Gradual Cerebral Hypoperfusion Impairs Fear Conditioning and Object Recognition Learning and Memory in Mice: Potential Roles of Neurodegeneration and Cholinergic Dysfunction. Journal of Alzheimer's Disease 61:283-293.

Mehla J, Deibel SH, Faraji J, Saito T, Saido TC, Mohajerani MH, McDonald RJ (2018b) Looking beyond the standard version of the Morris water task in the assessment of mouse models of cognitive deficits. Hippocampus 29:3-14.

Mehla J, Lacoursiere SG, Lapointe V, McNaughton BL, Sutherland RJ, McDonald RJ, Mohajerani MH (2019) Age-dependent behavioral and biochemical

characterization of single APP knock-in mouse (APPNL-G-F/NL-G-F) model of Alzheimer’s disease. Neurobiology of Aging 75:25-37.

Menon PK, Koistinen NA, Iverfeldt K, Strom AL (2019) Phosphorylation of the amyloid precursor protein (APP) at Ser-675 promotes APP processing involving meprin beta. J Biol Chem 294:17768-17776.

Mesulam MM (1998) From sensation to cognition. Brain : a journal of neurology 121:1013-1052.

Mevel K, Chételat G, Eustache F, Desgranges B (2011) The default mode network in healthy aging and Alzheimer's disease. International journal of Alzheimer's disease 2011:535816-535816.

Meyer SJ, Rauch G, Rauch RA, Haque A (2000) Risk factors for cerebral hypoperfusion, mild cognitive impairment, and dementia. Neurobiology of Aging 21:161-169.

Miguel-Hidalgo JJ, Alvarez XA, Cacabelos R, Quack G (2002) Neuroprotection by memantine against neurodegeneration induced by beta-amyloid(1-40). Brain Res 958:210-221.

Miki K, Ishibashi S, Sun L, Xu H, Osashi W, Kuroiwa T, Mizusawa H (2009) Intensity of chronic cerebral hypoperfusion determines white/gray matter injury and cognitive/motor dysfunction in mice. Journal of Neuroscience Research 87:1270-1281.

Minati L, Edginton T, Grazia Bruzzone M, Giaccone G (2009) Reviews: Current Concepts in Alzheimer's Disease: A Multidisciplinary Review. American Journal of Alzheimer's Disease & Other Dementiasr 24:95-121.

Mitra P, Bokil H (2008) Observed Brain Dynamic. New York.

Mohajerani MH, Aminoltejari K, Murphy TH (2011) Targeted mini-strokes produce changes in interhemispheric sensory signal processing that are indicative of disinhibition within minutes. Proceedings of the National Academy of Sciences 108:E183-191.

Mohajerani MH, McVea DA, Fingas M, Murphy TH (2010) Mirrored bilateral slow-wave cortical activity within local circuits revealed by fast bihemispheric voltage-sensitive dye imaging in anesthetized and awake mice. Journal of Neuroscience 30:3745-3751.

Mohajerani MH, Chan AW, Mohsenvand M, LeDue J, Liu R, McVea DA, Boyd JD, Wang YT, Reimers M, Murphy TH (2013) Spontaneous cortical activity alternates between motifs defined by regional axonal projections. Nature neuroscience 16:1426-1435.

Mölle M, Yeshenko O, Marshall L, Sara SJ, Born J (2006) Hippocampal sharp wave-ripples linked to slow oscillations in rat slow-wave sleep. Journal of neurophysiology 96:62-70.

Monasor LS, Müller SA, Colombo A, König J, Roth S, Liesz A, Berghofer A, Saito T, Saido TC, Herms J, Willem M, Haass C, Lichtenthaler SF, Tahirovic S (2019) Fibrillar Aβ triggers microglial proteome alterations and dysfunction in Alzheimer mouse models. bioRxiv.

Mostany R, Portera-Cailliau C (2008) A Craniotomy Surgery Procedure for Chronic Brain Imaging. Journal of Visualized Experiments.

Mueggler T, Baumann D, Rausch M, Staufenbiel M, Rudin M (2003) Age-dependent impairment of somatosensory response in the amyloid precursor protein 23 transgenic mouse model of Alzheimer's disease. The Journal of neuroscience : the official journal of the Society for Neuroscience 23:8231-8236.

Musall S, Kaufman MT, Juavinett AL, Gluf S, Churchland AK (2019) Single-trial neural dynamics are dominated by richly varied movements. Nature neuroscience 22:1677-1686.

Musiek ES, Holtzman DM (2015) Three dimensions of the amyloid hypothesis: time, space and 'wingmen'. Nature neuroscience 18:800-806.

Nakazono T, Jun H, Blurton-Jones M, Green KN, Igarashi KM (2018) Gamma oscillations in the entorhinal-hippocampal circuit underlying memory and dementia. Neuroscience research 129:40-46.

Nakazono T, Lam TN, Patel AY, Kitazawa M, Saito T, Saido TC, Igarashi KM (2017) Impaired In Vivo Gamma Oscillations in the Medial Entorhinal Cortex of Knock-in Alzheimer Model. Frontiers in systems neuroscience 11:48.

Nelson PT et al. (2012) Correlation of Alzheimer disease neuropathologic changes with cognitive status: a review of the literature. Journal of neuropathology and experimental neurology 71:362-381.

Nhan HS, Chiang K, Koo EH (2015) The multifaceted nature of amyloid precursor protein and its proteolytic fragments: friends and foes. Acta neuropathologica 129:1-19.

Nicole O, Hadzibegovic S, Gajda J, Bontempi B, Bem T, Meyrand P (2016) Soluble amyloid beta oligomers block the learning-induced increase in hippocampal sharp wave-ripple rate and impair spatial memory formation. Scientific Reports 6:22728.

Nuriel T, Angulo SL, Khan U, Ashok A, Chen Q, Figueroa HY, Emrani S, Liu L, Herman M, Barrett G, Savage V, Buitrago L, Cepeda-Prado E, Fung C, Goldberg E, Gross SS, Hussaini SA, Moreno H, Small SA, Duff KE (2017)

Neuronal hyperactivity due to loss of inhibitory tone in APOE4 mice lacking Alzheimer's disease-like pathology. Nature communications 8:1464.

O'Brien RJ, Wong PC (2011) Amyloid precursor protein processing and Alzheimer's disease. Annu Rev Neurosci 34:185-204.

Oakley H, Cole SL, Logan S, Maus E, Shao P, Craft J, Guillozet-Bongaarts A, Ohno M, Disterhoft J, Van Eldik L, Berry R, Vassar R (2006) Intraneuronal beta-amyloid aggregates, neurodegeneration, and neuron loss in transgenic mice with five familial Alzheimer's disease mutations: potential factors in amyloid plaque formation. The Journal of neuroscience : the official journal of the Society for Neuroscience 26:10129-10140.

Olabarria M, Noristani HN, Verkhratsky A, Rodríguez JJ (2010) Concomitant astroglial atrophy and astrogliosis in a triple transgenic animal model of Alzheimer's disease. Glia 58:831-838.

Pagliardini S, Funk GD, Dickson CT (2013) Breathing and brain state: urethane anesthesia as a model for natural sleep. Respiratory physiology & neurobiology 188:324-332.

Palop JJ, Mucke L (2010) Amyloid-beta-induced neuronal dysfunction in Alzheimer's disease: from synapses toward neural networks. Nature neuroscience 13:812-818.

Palop JJ, Mucke L (2016) Network abnormalities and interneuron dysfunction in Alzheimer disease. Nature Reviews Neuroscience 17:777-792.

Palop JJ, Chin J, Mucke L (2006) A network dysfunction perspective on neurodegenerative diseases. Nature 443:768-773.

Palop JJ, Chin J, Roberson ED, Wang J, Thwin MT, Bien-Ly N, Yoo J, Ho KO, Yu G-Q, Kreitzer A, Finkbeiner S, Noebels JL, Mucke L (2007) Aberrant Excitatory

Neuronal Activity and Compensatory Remodeling of Inhibitory Hippocampal Circuits in Mouse Models of Alzheimer's Disease. Neuron 55:697-711.

Parent MJ, Zimmer ER, Shin M, Kang MS, Fonov VS, Mathieu A, Aliaga A, Kostikov A, Do Carmo S, Dea D, Poirier J, Soucy JP, Gauthier S, Cuello AC, Rosa-Neto P (2017) Multimodal Imaging in Rat Model Recapitulates Alzheimer's Disease Biomarkers Abnormalities. The Journal of neuroscience : the official journal of the Society for Neuroscience 37:12263-12271.

Paxinos KBJ, Franklin G (2004) The Mouse Brain in Stereotaxic Coordinates.

Pelkey KA, Chittajallu R, Craig MT, Tricoire L, Wester JC, McBain CJ (2017) Hippocampal GABAergic Inhibitory Interneurons. Physiol Rev 97:1619-1747.

Petrache AL, Rajulawalla A, Shi A, Wetzel A, Saito T, Saido TC, Harvey K, Ali AB (2019) Aberrant Excitatory-Inhibitory Synaptic Mechanisms in Entorhinal Cortex Microcircuits During the Pathogenesis of Alzheimer's Disease. Cereb Cortex 29:1834-1850.

Qiu C, Kivipelto M, von Strauss E (2009) Epidemiology of Alzheimer's disease: occurrence, determinants, and strategies toward intervention. Dialogues Clin Neurosci 11:111-128.

Quaegebeur A, Lange C, Carmeliet P (2011) The neurovascular link in health and disease: molecular mechanisms and therapeutic implications. Neuron 71:406-424.

Ramirez-Villegas JF, Logothetis NK, Besserve M (2015) Diversity of sharp-wave–ripple LFP signatures reveals differentiated brain-wide dynamical events. Proceedings of the National Academy of Sciences 112:E6379.

Rayaprolu S, Higginbotham L, Bagchi P, Watson CM, Zhang T, Levey AI, Rangaraju S, Seyfried NT (2021) Systems-based proteomics to resolve the biology of

Alzheimer's disease beyond amyloid and tau. Neuropsychopharmacology 46:98-115.

Refolo LM, Snyder H, Liggins C, Ryan L, Silverberg N, Petanceska S, Carrillo MC (2012) Common Alzheimer's Disease Research Ontology: National Institute on Aging and Alzheimer's Association collaborative project. Alzheimers Dement 8:372-375.

Revett TJ, Baker GB, Jhamandas J, Kar S (2013) Glutamate system, amyloid ss peptides and tau protein: functional interrelationships and relevance to Alzheimer disease pathology. J Psychiatry Neurosci 38:6-23.

Rice HC, Marcassa G, Chrysidou I, Horre K, Young-Pearse TL, Muller UC, Saito T, Saido TC, Vassar R, de Wit J, De Strooper B (2020) Contribution of GABAergic interneurons to amyloid-beta plaque pathology in an APP knock-in mouse model. Mol Neurodegener 15:3.

Rodríguez JJ, Witton J, Olabarria M, Noristani HN, Verkhratsky A (2010) Increase in the density of resting microglia precedes neuritic plaque formation and microglial activation in a transgenic model of Alzheimer's disease. Cell Death Dis 1:e1-e1.

Rothschild G, Eban E, Frank LM (2017) A cortical–hippocampal–cortical loop of information processing during memory consolidation. Nature neuroscience 20:251-259.

Roumis DK, Frank LM (2015) Hippocampal sharp-wave ripples in waking and sleeping states. Current Opinion in Neurobiology 35:6-12.

Roux L, Buzsaki G (2015) Tasks for inhibitory interneurons in intact brain circuits. Neuropharmacology 88:10-23.

Rubinov M, Sporns O (2010) Complex network measures of brain connectivity: uses and interpretations. Neuroimage 52:1059-1069.

Rubinov M, Ypma RJF, Watson C, Bullmore ET (2015) Wiring cost and topological participation of the mouse brain connectome. Proceedings of the National Academy of Sciences 112:10032.

Rueckert D, Sonoda LI, Hayes C, Hill DL, Leach MO, Hawkes DJ (1999) Nonrigid registration using free-form deformations: application to breast MR images. IEEE transactions on medical imaging 18:712-721.

Saito T, Matsuba Y, Yamazaki N, Hashimoto S, Saido TC (2016) Calpain Activation in Alzheimer's Model Mice Is an Artifact of APP and Presenilin Overexpression. Journal of Neuroscience 36:9933-9936.

Saito T, Matsuba Y, Mihira N, Takano J, Nilsson P, Itohara S, Iwata N, Saido TC (2014) Single App knock-in mouse models of Alzheimer's disease. Nature neuroscience 17:661-663.

Sanchez-Aguilera A, Quintanilla JP (2021) Sharp Wave Ripples in Alzheimer's Disease: In Search of Mechanisms. The Journal of neuroscience : the official journal of the Society for Neuroscience 41:1366-1370.

Sanganahalli BG, Herman P, Behar KL, Blumenfeld H, Rothman DL, Hyder F (2013) Functional MRI and neural responses in a rat model of Alzheimer's disease. NeuroImage 79:404-411.

Sasaguri H, Nilsson P, Hashimoto S, Nagata K, Saito T, De Strooper B, Hardy J, Vassar R, Winblad B, Saido TC (2017) APP mouse models for Alzheimer's disease preclinical studies. EMBO J 36:2473-2487.

Schabus M, Gruber G, Parapatics S, Sauter C, Klösch G, Anderer P, Klimesch W, Saletu B, Zeitlhofer J (2004) Sleep spindles and their significance for declarative memory consolidation. Sleep 27:1479-1485.

Schedin-Weiss S, Winblad B, Tjernberg LO (2014) The role of protein glycosylation in Alzheimer disease. FEBS J 281:46-62.

Schmid Lena C, Mittag M, Poll S, Steffen J, Wagner J, Geis H-R, Schwarz I, Schmidt B, Schwarz Martin K, Remy S, Fuhrmann M (2016) Dysfunction of Somatostatin-Positive Interneurons Associated with Memory Deficits in an Alzheimer's Disease Model. Neuron 92:114-125.

Schneider JA, Arvanitakis Z, Bang W, Bennett DA (2007) Mixed brain pathologies account for most dementia cases in community-dwelling older persons. Neurology 69:2197-2204.

Schneider JA, Arvanitakis Z, Leurgans SE, Bennett DA (2009) The neuropathology of probable Alzheimer disease and mild cognitive impairment. Annals of Neurology 66:200-208.

Schultz AP, Chhatwal JP, Hedden T, Mormino EC, Hanseeuw BJ, Sepulcre J, Huijbers W, LaPoint M, Buckley RF, Johnson KA, Sperling RA (2017) Phases of Hyperconnectivity and Hypoconnectivity in the Default Mode and Salience Networks Track with Amyloid and Tau in Clinically Normal Individuals. The Journal of neuroscience : the official journal of the Society for Neuroscience 37:4323-4331.

Schwarz AJ, Gass N, Sartorius A, Risterucci C, Spedding M, Schenker E, Meyer-Lindenberg A, Weber-Fahr W (2013) Anti-correlated cortical networks of intrinsic connectivity in the rat brain. Brain Connect 3:503-511.

Schwindel CD, McNaughton BL (2011) Chapter 11 - Hippocampal–cortical interactions and the dynamics of memory trace reactivation. In: Progress in Brain Research (Van Someren EJW, Van Der Werf YD, Roelfsema PR, Mansvelder HD, Lopes Da Silva FH, eds), pp 163-177: Elsevier.

Seab JP, Jagust WJ, Wong ST, Roos MS, Reed BR, Budinger TF (1988) Quantitative NMR measurements of hippocampal atrophy in Alzheimer's disease. Magnetic resonance in medicine 8:200-208.

Selkoe DJ (2019) Early network dysfunction in Alzheimer's disease. Science 365:540.

Selkoe DJ, Hardy J (2016) The amyloid hypothesis of Alzheimer's disease at 25 years. EMBO molecular medicine 8:595-608.

Sery O, Povova J, Misek I, Pesak L, Janout V (2013) Molecular mechanisms of neuropathological changes in Alzheimer's disease: a review. Folia Neuropathol 51:1-9.

Shah D, Latif-Hernandez A, De Strooper B, Saito T, Saido T, Verhoye M, D'Hooge R, Van der Linden A (2018) Spatial reversal learning defect coincides with hypersynchronous telencephalic BOLD functional connectivity in APPNL-F/NL-F knock-in mice. Scientific Reports 8.

Shah D, Jonckers E, Praet J, Vanhoutte G, Delgado YPR, Bigot C, D'Souza DV, Verhoye M, Van der Linden A (2013) Resting state FMRI reveals diminished functional connectivity in a mouse model of amyloidosis. PloS one 8:e84241.

Shah D, Praet J, Latif-Hernandez A, Hofling C, Anckaerts C, Bard F, Morawski M, Detrez JR, Prinsen E, Villa A, De Vos WH, Maggi A, D'Hooge R, Balschun D, Rossner S, Verhoye M, Van der Linden A (2016) Early pathologic amyloid induces hypersynchrony of BOLD resting-state networks in transgenic mice and

provides an early therapeutic window before amyloid plaque deposition. Alzheimer's & Dementia 12:964-976.

Sheline YI, Raichle ME, Snyder AZ, Morris JC, Head D, Wang S, Mintun MA (2010) Amyloid plaques disrupt resting state default mode network connectivity in cognitively normal elderly. Biol Psychiatry 67:584-587.

Siegel JS, Ramsey LE, Snyder AZ, Metcalf NV, Chacko RV, Weinberger K, Baldassarre A, Hacker CD, Shulman GL, Corbetta M (2016) Disruptions of network connectivity predict impairment in multiple behavioral domains after stroke. Proceedings of the National Academy of Sciences 113:E4367-4376.

Sigler A, Mohajerani MH, Murphy TH (2009) Imaging rapid redistribution of sensory-evoked depolarization through existing cortical pathways after targeted stroke in mice. Proceedings of the National Academy of Sciences 106:11759-11764.

Silva MA, Kiametis AS, Treptow W (2020) Donepezil Inhibits Acetylcholinesterase via Multiple Binding Modes at Room Temperature. J Chem Inf Model 60:3463-3471.

Simic G, Babic M, Borovecki F, Hof PR (2014) Early failure of the default-mode network and the pathogenesis of Alzheimer's disease. CNS neuroscience & therapeutics 20:692-698.

Šišková Z, Justus D, Kaneko H, Friedrichs D, Henneberg N, Beutel T, Pitsch J, Schoch S, Becker A, von der Kammer H, Remy S (2014) Dendritic Structural Degeneration Is Functionally Linked to Cellular Hyperexcitability in a Mouse Model of Alzheimer’s Disease. Neuron 84:1023-1033.

Skaggs WE, McNaughton BL (1996) Replay of neuronal firing sequences in rat hippocampus during sleep following spatial experience. Science 271:1870-1873.

Smith EE (2018) Cerebral amyloid angiopathy as a cause of neurodegeneration. Journal of Neurochemistry 144:651-658.

Snowdon DA, Greiner LH, Mortimer JA, Riley KP, Greiner PA, Markesbery WR (1997) Brain infarction and the clinical expression of Alzheimer disease. The Nun Study. Journal of American Medical Association 277:813-817.

Sosna J, Philipp S, Ill RA, Reyes-Ruiz JM, Baglietto-Vargas D, LeFerla FM, Glabe CG (2018) Early long-term administration of the CSF1R inhibitor PLX3397 ablates microglia and reduces accumulation of intraneuronal amyloid, neuritic plaque deposition and pre-fibrillar oligomers in 5XFAD mouse model of Alzheimer's disease. Molecular Neurodegeneration 13:11.

Spires-Jones TL, Hyman BT (2014) The intersection of amyloid beta and tau at synapses in Alzheimer's disease. Neuron 82:756-771.

Stafford JM, Jarrett BR, Miranda-Dominguez O, Mills BD, Cain N, Mihalas S, Lahvis GP, Lattal KM, Mitchell SH, David SV, Fryer JD, Nigg JT, Fair DA (2014) Large-scale topology and the default mode network in the mouse connectome. Proceedings of the National Academy of Sciences 111:18745.

Stam CJ, van Cappellen van Walsum AM, Pijnenburg YA, Berendse HW, de Munck JC, Scheltens P, van Dijk BW (2002) Generalized synchronization of MEG recordings in Alzheimer's Disease: evidence for involvement of the gamma band. Journal of clinical neurophysiology : official publication of the American Electroencephalographic Society 19:562-574.

Staresina BP, Bergmann TO, Bonnefond M, van der Meij R, Jensen O, Deuker L, Elger CE, Axmacher N, Fell J (2015) Hierarchical nesting of slow oscillations, spindles and ripples in the human hippocampus during sleep. Nature neuroscience 18:1679-1686.

Stranahan AM, Mattson MP (2010) Selective vulnerability of neurons in layer II of the entorhinal cortex during aging and Alzheimer's disease. Neural plasticity 2010:108190.

Sugarman MA, Woodard JL, Nielson KA, Seidenberg M, Smith JC, Durgerian S, Rao SM (2012) Functional magnetic resonance imaging of semantic memory as a presymptomatic biomarker of Alzheimer's disease risk. Biochimica et biophysica acta 1822:442-456.

Suh J, Foster David J, Davoudi H, Wilson Matthew A, Tonegawa S (2013) Impaired Hippocampal Ripple-Associated Replay in a Mouse Model of Schizophrenia. Neuron 80:484-493.

Sutherland RJ, Lee JQ, McDonald RJ, Lehmann H (2020) Has multiple trace theory been refuted? Hippocampus 30:842-850.

Szalay G, Martinecz B, Lénárt N, Környei Z, Orsolits B, Judák L, Császár E, Fekete R, West BL, Katona G, Rózsa B, Dénes A (2016) Microglia protect against brain injury and their selective elimination dysregulates neuronal network activity after stroke. Nature Communication 7.

Talantova M et al. (2013) Aβ induces astrocytic glutamate release, extrasynaptic NMDA receptor activation, and synaptic loss. Proceedings of the National Academy of Sciences 110:E2518.

Tang W, Jadhav SP (2019) Sharp-wave ripples as a signature of hippocampal-prefrontal reactivation for memory during sleep and waking states. Neurobiology of Learning and Memory 160:11-20.

Tang W, Shin JD, Frank LM, Jadhav SP (2017) Hippocampal-Prefrontal Reactivation during Learning Is Stronger in Awake Compared with Sleep States. The Journal

of neuroscience : the official journal of the Society for Neuroscience 37:11789-11805.

Toledo JB, Arnold SE, Raible K, Brettschneider J, Xie SX, Grossman M, Monsell SE, Kukull WA, Trojanowski JQ (2013) Contribution of cerebrovascular disease in autopsy confirmed neurodegenerative disease cases in the National Alzheimer's Coordinating Centre. Brain : a journal of neurology 136:2697-2706.

Ulrich D (2015) Amyloid-beta Impairs Synaptic Inhibition via GABA(A) Receptor Endocytosis. The Journal of neuroscience : the official journal of the Society for Neuroscience 35:9205-9210.

Ulrich D (2016) Sleep Spindles as Facilitators of Memory Formation and Learning. Neural plasticity 2016:1796715.

Valero M, Averkin RG, Fernandez-Lamo I, Aguilar J, Lopez-Pigozzi D, Brotons-Mas JR, Cid E, Tamas G, Menendez de la Prida L (2017) Mechanisms for Selective Single-Cell Reactivation during Offline Sharp-Wave Ripples and Their Distortion by Fast Ripples. Neuron 94:1234-1247.e1237.

van Veluw SJ, Shih AY, Smith EE, Chen C, Schneider JA, Wardlaw JM, Greenberg SM, Biessels GJ (2017) Detection, risk factors, and functional consequences of cerebral microinfarcts. Lancet Neurology 16:730-740.

Venkat P, Chopp M, Chen J (2016) New insights into coupling and uncoupling of cerebral blood flow and metabolism in the brain. Croatian Medical Journal 57:223-228.

Verret L, Mann Edward O, Hang Giao B, Barth Albert MI, Cobos I, Ho K, Devidze N, Masliah E, Kreitzer Anatol C, Mody I, Mucke L, Palop Jorge J (2012) Inhibitory Interneuron Deficit Links Altered Network Activity and Cognitive Dysfunction in Alzheimer Model. Cell 149:708-721.

Walker Matthew P, Robertson Edwin M (2016) Memory Processing: Ripples in the Resting Brain. Current Biology 26:R239-R241.

Walsh DM, Klyubin I, Fadeeva JV, Cullen WK, Anwyl R, Wolfe MS, Rowan MJ, Selkoe DJ (2002) Naturally secreted oligomers of amyloid beta protein potently inhibit hippocampal long-term potentiation in vivo. Nature 416:535-539.

Wang B, Wang Z, Sun L, Yang L, Li H, Cole AL, Rodriguez-Rivera J, Lu HC, Zheng H (2014) The amyloid precursor protein controls adult hippocampal neurogenesis through GABAergic interneurons. The Journal of neuroscience : the official journal of the Society for Neuroscience 34:13314-13325.

Wang DV, Ikemoto S (2016) Coordinated Interaction between Hippocampal Sharp-Wave Ripples and Anterior Cingulate Unit Activity. The Journal of Neuroscience 36:10663.

Wang J, Fang Y, Wang X, Yang H, Yu X, Wang H (2017a) Enhanced Gamma Activity and Cross-Frequency Interaction of Resting-State Electroencephalographic Oscillations in Patients with Alzheimer's Disease. Front Aging Neurosci 9.

Wang L, Du Y, Wang K, Xu G, Luo S, He G (2016a) Chronic cerebral hypoperfusion induces memory deficits and facilitates Aβ generation in C57BL/6J mice. Experimental neurology 283:353-364.

Wang Q et al. (2020) The Allen Mouse Brain Common Coordinate Framework: A 3D Reference Atlas. Cell 181:936-953.e920.

Wang R, Reddy PH (2017) Role of Glutamate and NMDA Receptors in Alzheimer's Disease. J Alzheimers Dis 57:1041-1048.

Wang X, Zhang X-G, Zhou T-T, Li N, Jang C-Y, Xiao Z-C, Ma Q-H, Li S (2016b) Elevated Neuronal Excitability Due to Modulation of the Voltage-Gated Sodium Channel Nav1.6 by Aβ1−42. Frontiers in Neuroscience 10.

Wang Z, Jackson RJ, Hong W, Taylor WM, Corbett GT, Moreno A, Liu W, Li S, Frosch MP, Slutsky I, Young-Pearse TL, Spires-Jones TL, Walsh DM (2017b) Human Brain-Derived Aβ Oligomers Bind to Synapses and Disrupt Synaptic Activity in a Manner That Requires APP. The Journal of Neuroscience 37:11947.

Weiner MW, Veitch DP, Aisen PS, Beckett LA, Cairns NJ, Green RC, Harvey D, Jack CR, Jagust W, Liu E, Morris JC, Petersen RC, Saykin AJ, Schmidt ME, Shaw L, Siuciak JA, Soares H, Toga AW, Trojanowski JQ (2012) The Alzheimer's Disease Neuroimaging Initiative: a review of papers published since its inception. Alzheimers Dement 8:S1-68.

Whitesell JD et al. (2021) Regional, Layer, and Cell-Type-Specific Connectivity of the Mouse Default Mode Network. Neuron 109:545-559.e548.

Wiegand JP, Gray DT, Schimanski LA, Lipa P, Barnes CA, Cowen SL (2016) Age Is Associated with Reduced Sharp-Wave Ripple Frequency and Altered Patterns of Neuronal Variability. The Journal of neuroscience : the official journal of the Society for Neuroscience 36:5650-5660.

Wierzynski CM, Lubenov EV, Gu M, Siapas AG (2009) State-dependent spike-timing relationships between hippocampal and prefrontal circuits during sleep. Neuron 61:587-596.

Wilson MA, McNaughton BL (1994) Reactivation of hippocampal ensemble memories during sleep. Science 265:676.

Winship IR (2014) Laser speckle contrast imaging to measure changes in cerebral blood flow. Methods in Molecular Biology 1135:223-235.

Winship IR, Armitage GA, Ramakrishnan G, Dong B, Todd KG, Shuaib A (2014) Augmenting collateral blood flow during ischemic stroke via transient aortic occlusion. Journal of Cerebral Blood Flow & Metabolism 34:61-71.

Witton J, Staniaszek LE, Bartsch U, Randall AD, Jones MW, Brown JT (2016) Disrupted hippocampal sharp-wave ripple-associated spike dynamics in a transgenic mouse model of dementia. The Journal of physiology 594:4615-4630.

Wolansky T, Clement EA, Peters SR, Palczak MA, Dickson CT (2006) Hippocampal slow oscillation: a novel EEG state and its coordination with ongoing neocortical activity. The Journal of neuroscience : the official journal of the Society for Neuroscience 26:6213-6229.

Wu JW, Hussaini SA, Bastille IM, Rodriguez GA, Mrejeru A, Rilett K, Sanders DW, Cook C, Fu H, Boonen RACM, Herman M, Nahmani E, Emrani S, Figueroa YH, Diamond MI, Clelland CL, Wray S, Duff KE (2016) Neuronal activity enhances tau propagation and tau pathology in vivo. Nature neuroscience 19:1085-1092.

Wu X, Foster DJ (2014) Hippocampal Replay Captures the Unique Topological Structure of a Novel Environment. The Journal of Neuroscience 34:6459.

Xiong H, McCabe L, Costello J, Anderson E, Weber G, Ikezu T (2004) Activation of NR1a/NR2B receptors by soluble factors from APP-stimulated monocyte-derived macrophages: implications for the pathogenesis of Alzheimer's disease. Neurobiol Aging 25:905-911.

Xu W, Fitzgerald S, Nixon RA, Levy E, Wilson DA (2015) Early hyperactivity in lateral entorhinal cortex is associated with elevated levels of AbetaPP metabolites in the Tg2576 mouse model of Alzheimer's disease. Experimental neurology 264:82-91.

Xu Y, Yan J, Zhou P, Li J, Gao H, Xia Y, Wang Q (2012) Neurotransmitter receptors and cognitive dysfunction in Alzheimer's disease and Parkinson's disease. Prog Neurobiol 97:1-13.

Yamamoto K, Tanei ZI, Hashimoto T, Wakabayashi T, Okuno H, Naka Y, Yizhar O, Fenno LE, Fukayama M, Bito H, Cirrito JR, Holtzman DM, Deisseroth K, Iwatsubo T (2015) Chronic optogenetic activation augments abeta pathology in a mouse model of Alzheimer disease. Cell Rep 11:859-865.

Yeung JHY, Calvo-Flores Guzman B, Palpagama TH, Ethiraj J, Zhai Y, Tate WP, Peppercorn K, Waldvogel HJ, Faull RLM, Kwakowsky A (2020) Amyloid-beta1-42 induced glutamatergic receptor and transporter expression changes in the mouse hippocampus. J Neurochem 155:62-80.

Yoshizaki K, Adachi K, Kataoka S, Watanabe A, Tabira T, Takahashi K, Wakita H (2008) Chronic cerebral hypoperfusion induced by right unilateral common carotid artery occlusion causes delayed white matter lesions and cognitive impairment in adult mice. Experimental neurology 210:585-591.

Zhai Y, Yamashita T, Nakano Y, Sun Z, Shang J, Feng T, Morihara R, Fukui Y, Ohta Y, Hishikawa N, Abe K (2016) Chronic cerebral hypoperfusion accelerates Alzheimer's disease pathology with cerebrovascular remodeling in a novel mouse model. Journal of Alzheimer's Disease 53:893-905.

Zheng H, Koo EH (2011) Biology and pathophysiology of the amyloid precursor protein. Mol Neurodegener 6:27.

Zlokovic BV (2011) Neurovascular pathways to neurodegeneration in Alzheimer's disease and other disorders. Neuroscience 12:723-738.

Zott B, Busche MA, Sperling RA, Konnerth A (2018) What Happens with the Circuit in Alzheimer's Disease in Mice and Humans? Annu Rev Neurosci 41:277-297.

Zott B, Simon MM, Hong W, Unger F, Chen-Engerer H-J, Frosch MP, Sakmann B, Walsh DM, Konnerth A (2019) A vicious cycle of β amyloid–dependent neuronal hyperactivation. Science 365:559-565.